

Characterisation of the Morphological and Surface Properties of Organic Micro-Crystalline Particles

by

Siti Nurul'Ain Yusop

Submitted in accordance with the requirements for the degree of

DOCTOR OF PHILOSOPHY
(CHEMICAL ENGINEERING)

UNIVERSITY OF LEEDS
Institute of Particle Science & Engineering
School of Chemical and Process Engineering
December 2014

This copy has been supplied on the understanding that it is copyright material and that no quotation from the thesis may be published without proper acknowledgement

Declaration

The work reported in this thesis was carried out in the Institute of Particle Science and Engineering at the University of Leeds and Diamond Light Source, Oxfordshire between January 2011 and December 2014 under supervision of Prof. Kevin J. Roberts and Dr. Vasuki Ramachandran, together with Dr. Gwyndaf Evans from the Diamond Light Source. The candidate confirms that the work submitted is her own and that appropriate credit has been given where reference has been made to the work of others.

© 2015 The University of Leeds and Siti Nurul'Ain Yusop

Acknowledgements

I would like to thank my supervisors, Prof. Kevin J. Roberts, Dr. Vasuki Ramachandran and Dr. Gwyndaf Evans from Diamond Light Source for giving me the opportunity to carry out this PhD project at the University of Leeds. I much appreciate their constant support, outstanding help and valuable advice which has enabled me to complete this work.

I would like to acknowledge my research group members in Institute of Particle Science and Engineering, Dr. David R. Merrifield for his willingness to assist me on using Inverse Gas Chromatography instrument and his valuable advice on my work, Miss Thai Thu Hien Nguyen, Miss Siti Fatimah Ibrahim, Dr. Nornizar Anuar and Mr. Mohd Fitri Othman for their continual supports. I would also like to thank Microfocus beamline I24 team at Diamond Light Source, notably Dr. Anna Warren and Dr. Richard Gildea for their outstanding assistance in helping me to carry out the X-ray microdiffraction and microtomography experiments and analysis at Diamond. I would like to thank Dr. Roberts Docherty (Pfizer, Sandwich, UK) for helpful comments and advice concerning the urea simulations.

I would like to express my special appreciation to my thoughtful husband, Mr. Seth Iskandar bin Haji Abdul Majid, my beloved mother, Ms Halimah binti Hashim, and all my family members for their endless supports and prayers throughout this PhD journey. I would also like to acknowledge my late father, who was encouraged me to pursue this PhD.

Finally, I would like to thank to Diamond Light Source for providing funding research and synchrotron radiation beamtime associated with this project and Universiti Teknologi MARA, Malaysia and the Ministry of Higher Education, Malaysia for their overall sponsorship of this PhD programme.

Abstract

The surface properties of single and agglomerated micro-crystals are characterised using the micro-focus X-ray beams available at a third generation synchrotron light source together with other laboratory facilities. The influence of the crystallisation environment, on the resultant product crystals is studied by both varying the cooling rates during crystallisation and through the addition of impurities and cross-correlated with the morphology and size changes. Unmodified urea crystallised in 99% ethanol produce needle-like crystals whilst addition of 4% of biuret in crystallisation of urea produce a more prismatic crystal shape. At faster cooling rates smaller sized crystals are produced and vice versa. Dispersive surface energy analysis using inverse gas chromatography (IGC) shows that unmodified urea has lower dispersive surface energy than urea modified by biuret. The dispersive surface energy also increases as the cooling rates increased. Both the morphology changes and surface energy measurements are validated using molecular modelling. The morphological prediction intermolecular force calculations of unmodified urea and urea modified by biuret are used to calculate a weighted value for the whole crystals' dispersive surface energies. The results are in good agreement with experimental results from IGC. The sorption of urea crystals on water moisture showed that unmodified urea samples adsorbed water higher than urea modified by biuret by the observation of the percentage of mass change with respect to the relative humidity. The study of variability within powdered samples was found that no significant different in the unit cell parameters values of each single crystals. The orientation relationship between agglomerated micro-crystalline particles of aspirin showed the agglomerates tend to interact at the faces that have ability to form bonding. In urea samples, most of the agglomerates are mostly aligned due to epitaxy growth of the crystals. The XMT experiment also was carried out on agglomerated α -LGA and the 3-dimensional (3D) shape the samples were obtained.

Table of Contents

Acknowledgements.....	ii
Abstract.....	iii
Table of Contents.....	iv
List of Tables.....	viii
List of Figures.....	xi
Notation.....	xvii
Chapter 1 Introduction.....	1
1.1 Research Background.....	2
1.2 Research Objectives.....	4
1.3 Project Management.....	7
1.4 Structure of the Report.....	7
References.....	9
Chapter 2 Crystallography Crystallisation & Crystal	
Properties.....	10
2.1 Introduction.....	11
2.2 Basic Crystallography.....	11
2.2.1 Crystal Lattice.....	11
2.2.2 Crystallographic Directions & Planes.....	14
2.2.3 Crystal Projection.....	15
2.2.3.1 Constructions using a Wulff Net.....	17
2.2.4 Atomic Packing.....	19
2.2.5 Crystal Defects.....	23
2.3 Crystal Morphology & Habit.....	25
2.4 Polymorphism.....	26
2.5 Crystallisation.....	30
2.5.1 Supersaturation.....	30
2.5.2 Metastable Zone Width (MSZW).....	31
2.5.3 Nucleation.....	33
2.5.4 Crystal Growth.....	33
2.5.5 Types of Crystal Faces.....	35
2.6 Agglomeration.....	36
2.7 Closing Remarks.....	37

References.....	38
Chapter 3 Surface and Solid State Analysis and Characterisation of Micro-crystals.....	41
3.1 Introduction.....	42
3.2 Surface Analysis Techniques.....	42
3.2.1 Inverse Gas Chromatography (iGC) for Surface Energy Analysis.....	42
3.2.2 Dynamic Vapour Sorption.....	49
3.3 X-ray Techniques.....	50
3.3.1 X-ray Diffraction.....	50
3.3.1.1 Single Crystal X-ray Diffraction.....	54
3.3.1.2 Reciprocal Lattice.....	55
3.3.2 X-ray Tomography.....	56
3.3.3 Synchrotron Radiation.....	57
3.3.3.1 Development of Synchrotron Radiation.....	58
• First Generation of Storage Rings.....	58
• Second Generation of Storage Rings.....	58
• Third Generation of Storage Rings.....	58
3.3.3.2 Overview of Synchrotron Radiation Source.....	60
3.4 Closing Remarks.....	62
References.....	62
Chapter 4 Materials & Methods.....	68
4.1 Introduction.....	69
4.2 Materials.....	69
4.2.1 Urea.....	69
4.2.2 Biuret.....	71
4.2.3 Aspirin.....	71
4.2.4 L-Glutamic Acid.....	73
4.3 Experimental Methods.....	74
4.3.1 Crystallisation of Urea and Urea Modified by Biuret using AutoMATE.....	74
4.3.2 Particle Size & Shape Analysis using Morphologi G3.....	76

4.3.3 Surface Energy Analysis by using Inverse Gas Chromatography.....	77
4.3.4 Water Sorption Isotherm Measurement.....	78
4.3.5 Development of X-ray Microdiffraction (XMD) and X-ray Microtomography (XMT) Analysis from Synchrotron.....	79
4.3.5.1 Micromanipulator for Mounting Crystals.....	80
4.3.5.2 Sample Preparation.....	81
4.3.5.3 Diffraction data Collection and Processing.....	82
4.3.5.4 Calculation to Determine Unit Cell Constants of the Crystals.....	83
4.3.6 X-Ray Microtomography Instrument.....	84
4.4 Computational Modeling Methods.....	85
4.4.1 Calculation of Intermolecular Interaction Using HABIT98 and Visual Habit.....	85
4.4.2 Charges Calculation.....	87
4.4.3 Surface Energy Prediction.....	87
4.5 Closing Remarks.....	88
References.....	89
Chapter 5 Influence of Crystallisation Environment on Surface Properties of Urea.....	92
5.1 Introduction.....	93
5.2 Experimental Studies.....	93
5.2.1 Morphological Habit Measurement Using Morphologi G3.....	93
5.2.2 Surface Energy Analysis Study Using Inverse Gas Chromatography.....	99
5.2.3 Dynamic Vapour Sorption Studies.....	102
5.2.4 Integration of the Experimental Analysis.....	106
5.3 Surface Characterisation using Molecular Modeling.....	107
5.3.1 Morphology Prediction of Urea.....	108
5.3.1.1 Identification of Key Intermolecular Interactions.....	108

5.3.1.2 Attachment Energy Calculation for Morphology Prediction.....	110
5.3.2 Re-evaluation of Intermolecular Potential Selection for Dispersive Surface Energy Prediction..	113
5.3.3 Prediction of Dispersive Surface Energy.....	119
5.3.3.1 Calculations of Fractional Surface Areas based on Experimental Data.....	119
5.4 Discussion.....	123
5.5 Closing Remarks.....	124
5.9 References.....	124

Chapter 6 Characterisation of Micro-crystals and the Agglomerates using X-ray Microdiffraction

and Microtomography.....	125
6.1 Introduction.....	126
6.2 Justification on Selection of the Materials.....	126
6.3 Case Study 1: Variability in the Structure of Micro-crystals within Powdered Samples.....	126
6.3.1 Variation in aspirin powder samples.....	126
6.3.2 Variability in the structure of micro-crystals as a function of processing conditions.....	127
6.4 Case Study 2: Determination of the Orientation Relationship between Micro-crystals within Agglomerates.....	138
6.4.1 Development of a Stereographic Projection Method for Agglomerated Micro-crystals.....	139
6.4.2 Agglomerated Aspirin.....	142
6.4.3 Agglomerated unmodified urea and urea modified by Biuret as prepared at different cooling rates.....	148
6.5 Case Study 3: Studies of the Polymorphic forms and transformation of L-glutamic acid.....	164
6.5.1 Crystallisation of L-glutamic acid polymorphic forms.....	164
6.5.2 The Change of Unit Cell Parameters in Mediated	

Polymorphic Transformation Crystal of L-glutamic acid.....	165
6.5.3 Angle Calculations between the contacting two polymorphs resulting from the transformation between α - and β - forms of LGA.....	168
6.6 Case Study 4: Characterising the 3D shape of an Agglomerate of α -LGA using X-ray Microtomography.....	171
6.6.1 X-ray Microdiffraction data of agglomerated α -LGA.....	176
6.7 Discussion	178
6.8 Closing Remarks.....	178
References.....	178
Chapter 7 Conclusion & Future Works.....	181
7.1 Introduction.....	182
7.2 Conclusion of this Study	182
7.2.1 Influence of Crystallisation Environment on the Physico-chemical Properties of Urea Crystals.....	182
7.2.2 XMD and XMT Studies of the Structure and Orientation of Single Agglomerated Micro-crystals.....	183
7.3 Re-appraisal of Thesis Objective.....	184
7.4 Suggestion for Future Work.....	185
Appendix.....	xxviii

List of Tables

Table 2.1 Seven Crystal Systems	12
Table 2.2 Bravais lattice from seven main crystal systems	13
Table 4.1 The coordinates of the unit cell axis for aspirin crystals	83
Table 5.1 Surface energies calculation for set of urea samples at 0.1°C/min left overnight to undergo slow cooling crystallisation	100
Table 5.2 Summary of dispersive surface energy results for unmodified urea and urea modified by biuret at different cooling rates	101
Table 5.3 Debug analysis of intermolecular bonds in urea using Hagler force field with Hagler charges	109
Table 5.4 Summary of slice energy and attachment energy using bulk-isolated charges	111
Table 5.5 Attachment energies of four important faces of urea calculated using bulk-isolated charges model for prediction of polar morphology	112
Table 5.6 Description of types of atoms use in lattice energy calculations for three Hamiltonian parameters of MOPAC charges (AM1, MNDO, PM3), ab-anitio charges from CRYSTAL, and Hagler scaled charges from its own partial charges	114
Table 5.7 Types of charges use in lattice energy calculations. Three types of charges; empirical charges of MOPAC with different Hamiltanian parameters (AM1, MNDO,PM3), ab-anitio charges from CRYSTAL, and Hagler scaled charges	114
Table 5.8 Types of force-fields with their type of potential in calculating lattice energy	115
Table 5.9 Lattice energies values of urea using four different charges and force-fields. The bold columns in black is the values using Hagler potential with its scaled charges providing good match to the experimental	

lattice energy of -22.2 kcal/mol, however, provides an unrealistically low van der Waals component.

The bold columns in red is the values using Dreiding potential with CRYSTAL charges, which gives the highest value of van der Waals component

	116
Table 5.10 Percentage surface area of crystal faces obtained from Visual Habit	120
Table 5.11 Summary of prediction surface energy of unmodified urea and urea modified by biuret	121
Table 6.1 Summary of unit cell constant determination for aspirin crystals	128
Table 6.2 Unit cell constants of urea 0.1°C/min	131
Table 6.3 Unit cell constants of urea-biuret crystals 0.1°C/min	132
Table 6.4 Unit cell constants of urea 0.25°C/min	132
Table 6.5 Unit cell constants of urea-biuret crystals 0.25°C/min	133
Table 6.6 Unit cell constants of urea 0.5°C/min	133
Table 6.7 Unit cell constants of urea-biuret crystals 0.5°C/min	134
Table 6.8 Unit cell constants of urea 0.75°C/min	134
Table 6.9 Unit cell constants of urea-biuret crystals 0.75°C/min	135
Table 6.10 Unit cell constants of urea 1.0°C/min	135
Table 6.11 Unit cell constants of urea-biuret crystals 1.0°C/min	136
Table 6.12 Summary of unit cell parameters for unmodified urea and urea modified by biuret crystals at different cooling rates	136
Table 6.13 Angle calculation of agglomerated aspirin crystals using vector calculation	143
Table 6.14 Angle determination using stereographic projection method of agglomerated aspirin (sample 1)	143
Table 6.15 Angle determination using stereographic projection method of agglomerated aspirin (sample 2)	146
Table 6.16 Angle calculations between agglomerated unmodified urea 0.1°C/min using vector equation	149
Table 6.17 Angle calculations between agglomerated unmodified urea 0.1°C/min using stereographic projection	149

Table 6.18 Angle calculations between agglomerated urea modified by biuret 0.1°C/min using vector equation	151
Table 6.19 Angle calculations between agglomerated urea modified by biuret 0.1°C/min using stereographic projection	151
Table 6.20 Angle calculations between agglomerated unmodified urea 0.5°C/min using vector equation	153
Table 6.21 Angle calculations between agglomerated urea modified by biuret 0.5°C/min using stereographic projection	153
Table 6.22 Angle calculations between agglomerated unmodified urea 1.0 °C/min using vector calculation	155
Table 6.23 Angle calculations between agglomerated unmodified urea 1.0 °C/min using stereographic projection	155
Table 6.24 Angle calculations between agglomerated urea modified by biuret 1.0°C/min using vector calculation	159
Table 6.25 Angle calculations between agglomerated urea modified by biuret 1.0°C/min using stereographic projection	159
Table 6.26 Planes use for angle calculations determination	161
Table 6.27 Summary of angle calculations of the agglomerated unmodified urea and urea modified by biuret crystals. The samples summarised are chosen based on the smallest angle value to show the parallelism between crystals	162
Table 6.28 Unit cell constants results of 2 polymorphic forms of LGA. The value of unit cell constants of α -LGA indicates the data collected at α - crystal, near the interface of β -LGA, β -LGA indicates the data collected at β - crystal, interface indicates the data collected at the interface of α - and β - crystals, and inside α indicates the data collected at α - crystals, far away from the growing β - crystals	167
Table 6.29 Angles calculations of LGA crystals using vector calculations	169
Table 6.30 Angles calculations of LGA crystals using stereographic projections	169

Table 6.31 Unit cell parameters determination of two agglomerated α -LGA	176
Table 6.32 Angle determination using vector calculations and stereographic projection method	176

List of figures

Figure 1.1 Flow diagram of the proposed methodology of the single analysis	6
Figure 1.2 Schematic diagram of structure of the report	8
Figure 2.1 Diagram of lattice parameters determination of crystal Lattice	12
Figure 2.2 Designation of a crystal plane by Miller indices	14
Figure 2.3 Spherical projection of normal to crystal faces	15
Figure 2.4 (a) Construction of pole P normal to the crystal plane. (b) The angle between two planes is equal to the angle θ between the two poles	16
Figure 2.5 Construction of stereographic projection by defining the north and south poles in the circle	17
Figure 2.6 (a) The construction of Wulff net with projection of latitude and longitude on the sphere of projection, (b) Wulff net drawn with 2° intervals	18
Figure 2.7 (a) Stereographic projection with projection of two poles (P_1 and P_2), (b) measurement of the angle between two poles using Wulff net. The poles lie on great circle	19
Figure 2.8 Types of atoms arrangement in crystal lattice (a) ABABAB... arrangement (b) ABCABCABC... arrangement	20
Figure 2.9 The diagram of type of bonding forces exist in matter	21
Figure 2.10 Lennard-Jones potential diagram	22
Figure 2.11 Four types of point defects in a crystal lattice	24
Figure 2.12 Diagram of dislocations occur in crystal lattice	24
Figure 2.13 A twinning plane	25
Figure 2.14 Types of crystal shapes (a) needle-like shape (b) prismatic shape of snowflakes	26
Figure 2.15 Two polymorphs of paracetamol (a) form I and (b) form II show different arrangement of molecules for crystal packing	27

Figure 2.16 Solubility curves of two polymorphic forms according to Ostwald's rule	28
Figure 2.17 Schematic diagrams showing the relationship between the Gibbs free energy and the temperature T of two polymorphic inter-relationships A and B represent metastable and stable polymorphs: (a) monotropic. T_A is melting temperature of metastable A form and T_B is a melting temperature of stable B form (b) enantiotropic. Metastable A form transforms to B form when the temperature reaches T_t (transition temperature)	29
Figure 2.18 Metastable Zone Width diagram shows the metastable region is in between solubility line and supersolubility curve. Below solubility line, no crystallisation occurs, while above supersolubility curve, the crystal growth occurs instantaneous	32
Figure 2.19 Steps, terrace, kink sites and adsorbed molecule on crystal surface of crystal growth model	34
Figure 2.20 Step (S), kink (K), flat (F) faces	35
Figure 2.21 Schematic diagram of formation of agglomerates from a group of particles	36
Figure 3.1 Schematic representation of a $RT \ln V_N$ versus $a \cdot \sqrt{\gamma_L^d}$ plot for n-alkanes and polar probes	47
Figure 3.2 Propagation of an electromagnetic wave consisting of cojoined electric magnetic waves	52
Figure 3.3 Diagram of incident wavelength of Bragg's plane	53
Figure 3.4 Schematic diagram of XRD	53
Figure 3.5 The relationship between the crystal orientation and the diffraction pattern	55
Figure 3.6 Diagram of (a) diffraction patterns from two-dimensional arrays (b) relationship between crystal lattice and reciprocal lattice	56

Figure 3.7 An example of tomography method by slicing the object into several sections and obtained 3D images from reconstruction of the slice images	56
Figure 3.8 Schematic diagram of Synchrotron Radiation ring at Diamond Light Source	60
Figure 4.1 Molecular structure of urea	69
Figure 4.2 Morphology of urea showing the slower growing prismatic {110} faces and the faster growing {111} and {001} faces	70
Figure 4.3 Molecular structure of biuret	71
Figure 4.4 Molecular structure of aspirin	72
Figure 4.5 The formation of the aspirin-aspirin dimer due to hydrogen bonds between two carboxylic groups	73
Figure 4.6 Molecular Structure of (a) α - and (b) β -L-glutamic acid	73
Figure 4.7 The crystalliser system of AutoMATE (a) four parallel reactors (b) close-up image of a reactor showing inlets for the turbidity probe, a glass stirrer, a temperature detector and cooling jacket	75
Figure 4.8 The Morphologi G3 Malvern Instrument Unit	76
Figure 4.9 (a) The Inverse Gas Chromatography Instrument from SMS Co.UK Ltd with solvent oven on the left and column oven on the right (b) Schematic diagram of the instrument	77
Figure 4.10 Schematic diagram of dynamic vapour sorption instrument from SMS Co. UK Ltd	78
Figure 4.11 (a) Experimental hutch of beamline I24 (b) Schematic diagram of XMD	79
Figure 4.12 The stage developed for micromanipulator for mounting single crystals. (a) shows three adjustable directions for micromanipulator (b) adjustable joystick to pick up the selected crystals	81
Figure 4.13 Sample holder for mounting crystal	82
Figure 4.14 Schematic diagram of XMT on I04 beamline	84
Figure 4.15 Limiting radius determination for lattice energy calculation	86

Figure 5.1 Images of unmodified urea and urea modified by biuret crystals crystallised at 0.1°C/min left overnight taken from Morphologi G3	94
Figure 5.2 Graphs of (a) frequency curves and (b) undersize curves of unmodified urea and urea modified by biuret crystallised at 0.1°C/min for aspect ratio (blue:unmodified urea, green: urea modified by biuret)	95
Figure 5.3 Crystal images of unmodified urea and urea modified at different cooling rates	96
Figure 5.4 Particle size (aspect ratio) distribution of unmodified urea and urea modified by biuret at different cooling rates	97
Figure 5.5 Distribution of unmodified urea at different cooling rates indicates that the length of the crystals decreasing at the faster cooling rates	99
Figure 5.6 Dispersive surface energy plotted of unmodified urea and urea modified by biuret at different cooling rates	101
Figure 5.7 Graphs of percent in mass changes of (a) unmodified urea and (b) urea modified by biuret at different cooling rate at different relative humidity. Red line represents samples crystallised at cooling rate 0.1°C/min, green line is for samples crystallised at cooling rate 0.25°C/min, purple line is for samples crystallised at cooling rate 0.5°C/min, blue line is for samples crystallised at cooling rate 0.75°C/min, and orange line is for samples crystallised at 1.0°C/min	103
Figure 5.8 Graphs of percent in mass changes of unmodified urea and urea modified by biuret at (a) 0.1°C/min and (b) 1.0°C/min. Red line and blue line represent unmodified urea sample and urea modified by biuret, respectively	105
Figure 5.9 Atom-atom interaction (a) bond type a (b) bond type b from DM-analysis (c) the interaction between central molecule of urea (yellow) with its surrounding molecules	110
Figure 5.10 Graphs of slice energy of {111} and {-1-1-1}	112

Figure 5.11 Morphology prediction of urea using bulk-isolated charges to calculate the attachment energies of each faces including the polar faces of (111) and (-1-1-1)	113
Figure 5.12 Lattice energy plots and its component contributions of urea crystal using Hagler force field with its parameterised partial electronic charges	117
Figure 5.13 Lattice energy plots and its component contributions of urea crystal using Dreiding force field with Crystal charges	118
Figure 5.14 Comparison of morphology of unmodified urea and urea modified by biuret from experiment and modeling	119
Figure 5.15 Cleave surfacaes of urea with showing of hydrogen bonding interactions (a) (001) face, (b) (110) face, (c) (111) face, (d) ($\bar{1}\bar{1}\bar{1}$) face	122
Figure 6.1 Aspirin crystal structure visualised in CAMERON graphical tool plugged-in WinGX software	130
Figure 6.2 Diagram of Wulff net used for determine the angle between planes and directions of crystals	140
Figure 6.3 Example of stereographic projection result on agglomerated urea crystals. Blue and red spots indicate the projected plane for crystal 1 and 2. Green circles around the (110) plane of both crystals are selected planes to be used to calculate the angle between planes	141
Figure 6.4 Example of stereographic projection result on agglomerated urea crystals. Blue and red spots indicate the projected plane for crystal 1 and 2. Green circles around the (110) plane of both crystals are selected planes to be used to calculate the angle between planes. The Wulff net is overlayed on the projected plot and rotated to calculate the angle between the planes by aligning two planes on the great circle	142
Figure 6.5 Image of 2 agglomerated aspirin crystals taken at beamline 124 DLS	143

Figure 6.6 Image of 3 aspirin crystals agglomerated captured from beamline 124 DLS	143
Figure 6.7 Stereographic projection plots of agglomerated aspirin crystals sample no.1 (sample j and k)	144
Figure 6.8 Stereographic projection plots for aspirin crystals samples no.2 (sample m & n)	145
Figure 6.9 Sterographic projection plots for aspirin crystals samples no.2: (sample n and o)	145
Figure 6.10 Morphology prediction of aspirin based on attachment energy	147
Figure 6.11 The cleave surfaces of aspirin at (100), (b) (110), and (c) (001)	148
Figure 6.12 (a) Image of unmodified urea crystals recrystallised at 0.1°C/min (sample no.5 in Table 6.16 and 6.17). Blue and red boxes indicate the position of the agglomerated crystals. The yellow spots indicate the point where the beam hits the crystal during data collection, (b) stereographic projections plotted for sample no.5 (blue: crystal 5p & red: crystal 5q)	150
Figure 6.13 (a) Image of urea modified by biuret crystals recrystallised at 0.1°C/min (sample no.8 in Table 6.18 and 6.19) Blue and red boxes indicate the position of the agglomerated crystals. Yellow spots indicate the point where the beam hits the crystal during data collection, (b) stereographic projections plotted for sample no.8 (blue: crystal 8p & red: crystal 8q)	152
Figure 6.14 (a) Image of unmodified urea crystals recrystallised at 0.5°C/min (sample no.11 in Table 6.20 and 6.21). Blue and red boxes indicate the position of the agglomerated crystals. The yellow spots indicate the point where the beam hits the crystal during data collection, (b) stereographic projections plotted for sample no.11 (blue: crystal 11p & red: crystal 11q)	154

- Figure 6.15 Stereographic projection plots for sample no.12 in table 6.22 and 6.33 156
- Figure 6.16 (a) Image of unmodified urea crystals recrystallised at 1.0°C/min (sample no.13 in Table 6.22 and 6.23). Blue and red boxes indicate the position of the agglomerated crystals. The yellow spots indicate the point where the beam hits the crystal during data collection, (b) stereographic projections plotted for sample no.13 (blue: crystal 13p & red: crystal 13q). Blue dots cannot be seen in the plotted image because the plots overlapped with the red dots plotted 157
- Figure 6.17 (a) Image of unmodified urea crystals recrystallised at 1.0°C/min (sample no.15 in Table 6.22 and 6.23). Blue and red boxes indicate the position of the agglomerated crystals. The yellow spots indicate the point where the beam hits the crystal during data collection, (b) stereographic projections plotted for sample no.15 (blue: crystal 15p & red: crystal 15q). The blue dots cannot be seen in the plotted image because the plots overlapped with red dots plots 158
- Figure 6.18 (a) Image of urea modified by biuret crystals recrystallised at 1.0°C/min (sample no.17 in Table 6.24 and 6.25). Blue and red boxes indicate the position of the agglomerated crystals. The yellow spots indicate the point where the beam hits the crystal during data collection, (b) stereographic projections plotted for sample no.17 (blue: crystal 17p & red: crystal 17q) 160
- Figure 6.19 The crystals of LGA observed under hot stage microscope. Prismatic shape belongs to α -LGA and observable needle-like shape belongs to β -LGA (in red circles) 164

Figure 6.20 Samples of LGA with β – crystal grows from α -LGA. The arrow pointed on the point of the beam hits the interface: (a) sample 1, (b) sample 2, (c)sample 3.	166
Figure 6.21 Stereographic projection plotted for sample no.2 of alpha (blue) and beta (red) LGA crystals	169
Figure 6.22 Stereographic projection plotted for sample no.3 of alpha (blue) and beta (red) LGA crystals	170
Figure 6.23 Molecular packing at surface of (a) (021) of beta form, (b) (101) of α -form, (c) (111) of α -form	171
Figure 6.24 Image of XMT data collection: (a) image of the beam with the sample in, (b) flat field reference image, (c) image of the beam with sample after divided each images in (a) with image in (b). The sample is circled in red	172
Figure 6.25 The images cut into slices in z-direction during reconstruction	173
Figure 6.26 3D rendering image after reconstruction	174
Figure 6.27 Microscopic image of α -LGA crystals (captured by microscope camera from Morphologi G3)	175
Figure 6.28 Stereographic projection plots of two agglomerated α -LGA. Blue dots represent crystal a and red dots represent crystal b	177

Notation

Latin Letters

A	surface area of the face
AN	Acceptor number
c	solution concentration
c*	equilibrium concentration
C _e	equilibrium solubility
Δc	driving force
d _{hkl}	interplanar spacing
DN	Donor number
E	Energy , eV
E _{att}	attachment energy
E _{latt}	lattice energy
E _{sl}	slice energy
F _c	carrier gas flow rate, ml/min
ΔG ^{ads}	adsorption free energy
ΔG ^{DP}	dispersive interactions
ΔG ^{SP}	special (polar) interactions
h	Planck's constant, 4.135 x 10 ⁻¹⁵ eV.s
i	number of crystals
J	correction factor for the compressibility of the carrier gas
j	number of faces
K _A	acidity value of solid particle
K _D	basicity value of solid particle
M	Multiplicity
m	mass of stationary phase, g
N _A	Avogadro's constant, 6.023x10 ²³ mol ⁻¹
P _o	outlet pressure

P_i	inlet pressure
R	universal gas constant, 8.314 J/mol.K
r	radius of nucleus
r_c	critical radius of nucleus
S	Supersaturation
SA	fractional surface area of the (hkl) face
T	temperature of the column, K
T_m	melting point
T_1	undercooled temperature
t_G	time of first appearance of crystal growth
t_N	time of first formation of critical nucleus
t_r	residence time
t_o	hold-up time of non-retained compound (methane), min
t_1	time of first appearance of the crystal
V_B	Buckingham potential
V_{cell}	cell volume of the crystal, m ³
V_{LJ}	Lennard-jones potential
V_N	net retention volume
V_s	specific retention volume
W_a	work of adhesion
W_c	work of cohesion
Z	number of unit cell

Greek Letters

α	unit cell angle, °
β	unit cell angle, °
ϵ	depth of the potential well
σ	finite distance at which the inter-particle potential is zero
σ	relative supersaturation
θ	scattering angle of the diffraction wavelength
u	Frequency
γ	unit cell angle, °
γ	surface energy, mJ/m ²
γ^d	dispersive surface energy for non-polar components
γ^P	surface energy for polar components
γ_L^+	acidic parameter of the probe molecule
γ_L^-	basic parameter of the probe molecule
γ_s^+	acidic parameter of the solid surface
γ_s^-	basic parameter of the solid surface
γ_S^d	dispersive surface energy of solid
γ_L^d	dispersive surface energy of probe
λ	spreading coefficient
λ	Wavelength

Abbreviations

BFDH	Bravais-Friedel-Donnay-Harker
CCD	charge-coupled device
CCDC	Cambridge Crystallographic Data Centre
CIF	Crystallographic Information File
CSD	Cambridge Structure Database
DVS	Dynamic Vapour Sorption
hkl	milller indices
IGC	Inverse Gas Chromatography
LGA	L-glutamic acid
MSZW	metastable zone width
RF	radio frequency
RH	relative humidity
SDU	sample dispersion unit
XMD	X-ray microdiffraction
XMT	X-ray microtomography
XDS	X-ray Detector Software
XRD	X-ray diffraction

CHAPTER I

INTRODUCTION

1.1 Research Background

Crystallisation is a separation process for preparing fine chemical products. In the pharmaceutical industry, for example, it is a routine process used to produce pharmaceutical drug powders. The product performance of the crystallisation process is dependent on the key processing parameters such as supersaturation of the solute in the solvent, types of solvent, temperature, pH, hydrodynamics, cooling rates, etc. These parameters control the crystallisation process and may affect the polymorphism, size and shape of the crystals. The surface interfacial properties of the crystals affect the morphological habit because of the hydrophilic and hydrophobic characteristics on the individual surface itself. The properties of crystals can be determined by measuring the powder itself. However, to understand its surface interfacial properties, it is crucial to measure at the single particle level. It is because it effects on the physico-chemical properties, that it also influences the stability and product performance. The characteristics of individual faces of the crystal determine the surface energy of the crystal. Each individual facet of the crystal may have different surface energies, depending upon the relative hydrophilicity and hydrophobicity of the surface. Traditionally, surface analysis techniques for powder characterisation such as inverse gas chromatography (IGC) and dynamic vapour sorption (DVS) analyse surface properties of all the surfaces on the crystals and a net value which lacks the granularity to be able to assess how process induced changes to the external shape might impact on the powder's surface energy. Theoretically, the surface energy of a sample of faceted crystalline particles can be defined as (Hammond, *et al.*, 2006):

$$\text{Surface energy of a particle, } \gamma = \sum_i \sum_j M_j A_j S_j \quad (1.1)$$

Where i is a number of crystals

j represents a unique crystallographic forms on a faceted crystal
number of faces

M_j is a multiplicity of the individual forms

A_j is fractional surface area of the j^{th} face

S_j is a surface energy of the j^{th} face

Many pharmaceutical and fine chemical manufacturing processes produce micron-sized crystals. In previous studies, the investigation of surface properties of crystals has been restricted to study on single large crystals (York, 1983). However, in industry, the particles produced can be quite small as 20 μm and, the particles undergo processes such as milling, granulation, and compression their surfaces are not always well defined. For example, these downstream processes may break the crystals, thus the surface properties may change (Ho *et al.*, 2012). However, there is still a gap to relate the properties of molecular crystals of single particles, particularly micro-crystals with the bulk powders which normally produced in the fine industry. Therefore, it is important to study the characteristics of the small particulates to understand their surface properties. The surface properties of single crystals can be characterized by using single crystal X-ray diffraction (XRD). However, in a normal laboratory XRD, a large beam size is present which is more suitable for large crystal sizes. Hence, to understand the structure of agglomerates of micron-sized crystals, a small beam size is highly preferable as the beam should be smaller than sample to avoid unwanted air scattering (Evans, 1999). The micro-focus beams available at third generation of synchrotron radiation facilities provide a higher intensity and much brighter source of X-rays which is very suitable for small molecules size crystals (Harding, 1995). In particular, the small beam sizes (ca 5-10 μm) provided enable X-ray microdiffraction (XMD) technique to be used to study the individual crystals structure within microcrystalline agglomerates. This technique has been proved in preliminary study of microcrystalline organic crystals of aspirin done by Merrifield *et al.*, 2011.

In a similar manner X-ray microtomography (XMT) has been used previously for the characterisation of small particles. Mostly, though, its use has been restricted to inorganic systems and at a particle size somewhat larger than the size of particles envisaged for this study. In previous research small particle characterisation is well explored (Marks, 1994). However, there is still a lack of understanding about the structure of particulate assemblies in particular the relative orientation behaviour between the constituent crystals. The attractive combination of XMT and

XMD has the potential to characterise the external shape of the crystal, its internal structure and its crystal orientation of within micron-sized agglomerated crystals (ca. 20-50 μ m).

1.2 Research Aims and Objectives

In this project, a new holistic approach (see figure 1.1) for the characterisation micro crystalline samples has been developed encompassing a combination of XMT and XMD using the Diamond synchrotron radiation source used in combination with laboratory characterisation facilities and molecular modelling. Synchrotron radiation is chosen because it has micron-sized beams that are precisely focused as well as higher fluxes than laboratory sources enabling the characterisation of smaller particles. The research question underlying this PhD study is as follows:

“How the crystal morphology can influence the surface properties of micro-crystalline particles and how the interactions between particles can be measured, hence compared between single micro-particle and powdered samples?”

Delivery of the thesis’s aim will be enabled through a number of key objectives:

- Developing a handling system to help in selection of the samples and to mount samples on the goniometer for the analysis. Using this, it is possible to measure the crystal shape, structure, and orientation, thus, avoiding the problem of selecting new samples, or time consuming transfer of the sample from one instrument to another.
- Examining the morphological habit, particle size and shape distribution, water sorption effect on the crystals and the surface energetic nature of crystals using Morphologi G3, Dynamic Vapour Sorption (DVS) and Inverse Gas Chromatography (iGC).

- Analysis of surface interfacial properties of micro-crystalline particles, being the shape, structure and relative orientations of the particles when they are in agglomerated state using new developing technique of XMT and XMD in synchrotron radiation source beamline I24, Diamond Light Source UK.
- Assessment of the relationship between bulk properties of the crystals and the single molecular crystals using molecular modelling of the intermolecular interactions within the crystal.

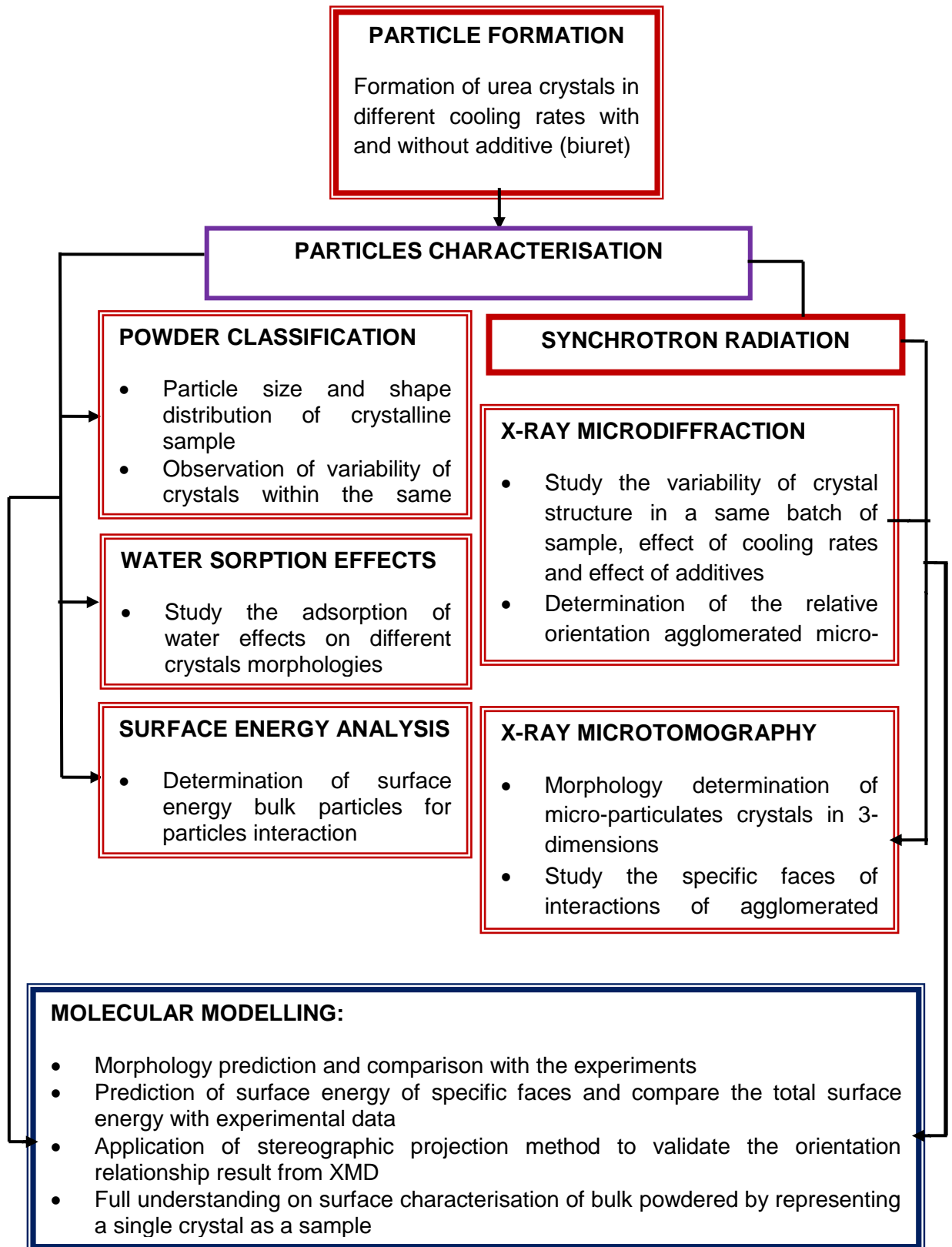


Figure 1.1: Flow diagram of the proposed methodology of the single particle analysis

1.3 Project Management

This research project was supervised by Prof. Kevin J. Roberts and Dr. Vasuki Ramachandran at the University of Leeds, UK in collaboration with Dr. Gwyndaf Evans at the Synchrotron Radiation Institute, Diamond Light Source (DLS), Didcot, Oxfordshire, UK. The latter provided a research grant and synchrotron radiation time at the beamline I24 and I04. The main idea of this project is to develop a high novelty combination technique of XMD and XMT at microfocus beamline I24. This project is supervised by:

1. Prof. Kevin J. Roberts, University of Leeds, UK
2. Dr. Gwyndaf Evans, DLS
3. Dr. Vasuki Ramachandran, University of Leeds, UK

The research also involved the team from beamline I24, at the Diamond Light Source, Dr. Anna Warren for XMD and XMT data collection and Dr. Richard Gildea who developed the stereographic projection program for agglomeration data analysis. The laboratory work for surface analysis was involved Dr. David R. Merrifield who supported in work using inverse gas chromatography and dynamic vapour sorption. The funding for the study in four years period funded by Ministry of Higher Education of Malaysia and Universiti Teknologi MARA (UiTM), Malaysia.

1.4 Structure of the Report

The report is divided into seven chapters (figure 1.2). Chapter I describes the research background and the aims and objectives of the research. Chapter II and III explain the fundamental of crystallography and crystallisation and also the principles of the techniques used in this study. Chapter IV provides information about the materials and methods used in this study. Chapter V discusses the experimental results and molecular modelling simulation on the effect of morphology of urea influenced by different process conditions. Chapter VI discusses the XMD and XMT

analysis of powdered samples and relative orientation of the agglomerates of micro-crystals, and the external 3D shape of agglomerated α -LGA. Chapter VII summarises the conclusions of this work and suggestion of future work for research development. A schematic diagram of the layout for the report is shown in the figure 1.2 below:

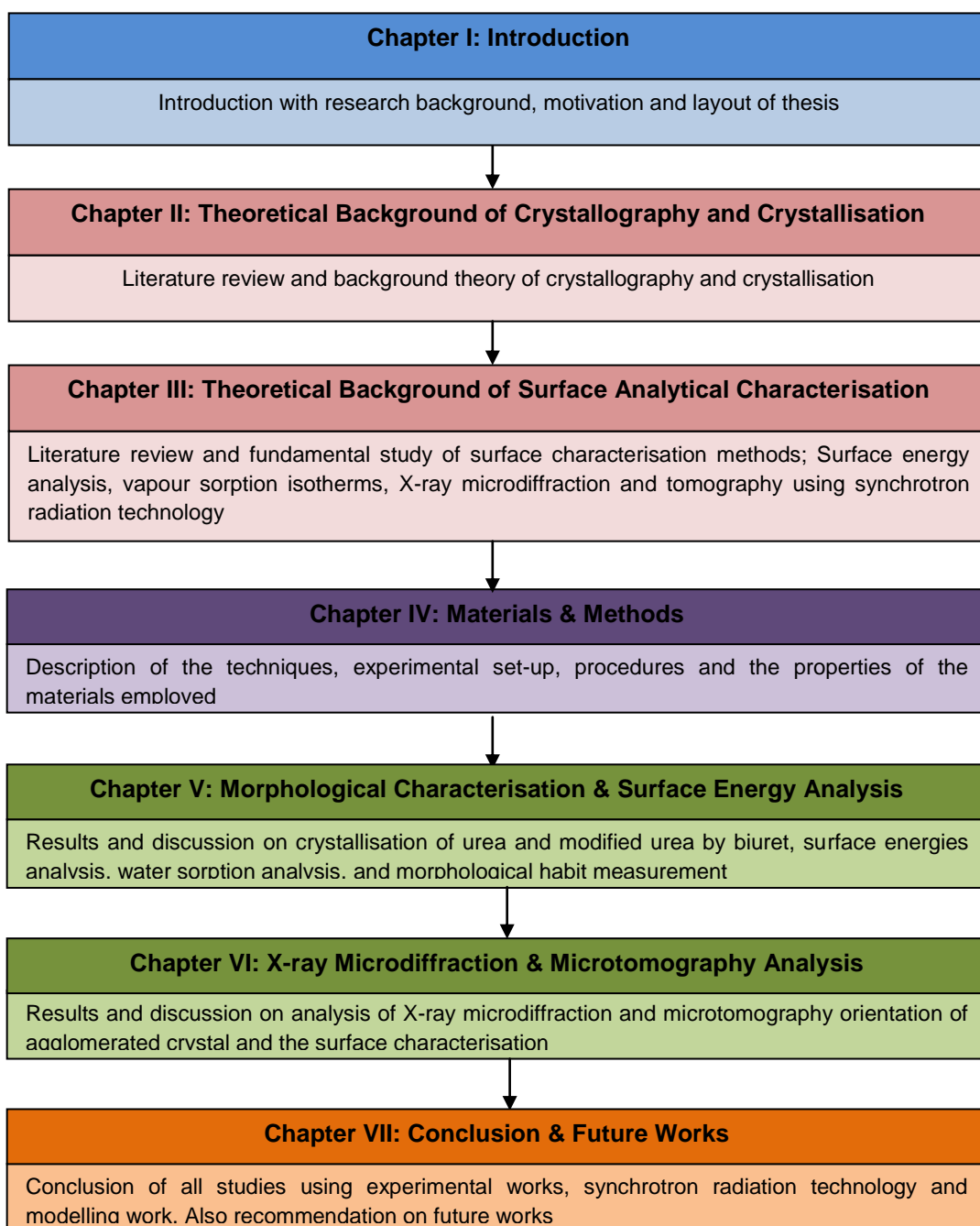


Figure 1.2: Schematic diagram of structure of the report

References

1. Evans, P.R., (1999). Some Notes on Choices in Data Collection. *Act. Cryst. (D)* (55):1771-1772.
2. Harding, M.M., (1995). Synchrotron Radiation-New Opportunities for Chemical Crystallography. *Act Crystallogr. B.* (51):432-446.
3. Ho, R., Naderi, M., Heng, J.Y.Y., Williams, D.R., Thielmann, F., Bouza, P., Keith, A.R., Thiele, G., Burnett, D.,J., (2012). Effect of Milling on Particle Shape and Surface Heterogeneity of Needle-Shaped Crystals. *Pharm. Res.* (29) 2806-2816.
4. Merrifield, D.R., Ramachandran, V., Roberts, K.J., Armour, W., Axford, D., Basham, M., Connolley, T., Evans, G., McAuley, K.E., Owen, R.L., Sandy, J., (2011). A Novel Technique Combining High-Resolution Synchrotron X-ray Microtomography and X-ray Diffraction for Characterisation of Micro-particulates. *Meas. Sci.Technol.* (22).
5. York, P., (1983). Solid-state Properties of Powders in the formulation and processing of solid dosage forms. *Int. J. Pharm.* (14) 1-28.

CHAPTER II

CRYSTALLOGRAPHY, CRYSTALLISATION & CRYSTAL PROPERTIES

2.1 Introduction

This chapter discusses the background to the basics of crystallography, the structure of crystals, how molecules arrange themselves in a crystal lattice and the bonding forces involved. It also discusses the crystallisation process which is important in producing particles with desired crystal morphology and polymorphic form.

2.2 Basic Crystallography

The understanding of the atom distribution in the crystalline state was discovered by Max Von Laue, W.H. and W.L. Braggs in 1912 (Braggs, 1913). The first X-ray diffraction experiments were carried out by them to work out the structure of rock salt, whilst W. H. Bragg discovered the wavelength of monochromatic X-ray beams (Barret & Massalski, 1980). An ordered arrangement of atoms or molecules which repeats in three-dimensions forms a crystal. Crystalline materials contain a regular repeating pattern of atoms or molecules, the smallest repeat of which is known as a unit cell. A crystal is the most stable form since the energy of the atomic interaction is at its lowest state compared amorphous material which has a random arrangement of atoms or molecules. Each crystal has its own shape, in facets which grow naturally during crystallisation, the shape and faces of the crystal are dependent on the atoms and molecules inside the crystal.

2.2.1 Crystal Lattice

Crystalline solids form by the long range ordering of atoms in a repeating pattern called a unit cell. The atoms arrangement is repeated in a specific direction and distance (Glusker & Trueblood, 2010). The unit cell contains the information about the atoms coordinates, types of atoms and site occupancy. The repetition of the unit cell can be represented by the geometry of the repetition. The lengths (a, b, c) of the unit cell are measured

in Angstrom, (\AA , $1 \text{\AA} = 10^{-10} \text{ m}$), and a set of lattice constants and the angles between them (α , β , γ) are called the lattice parameters (figure 2.1).

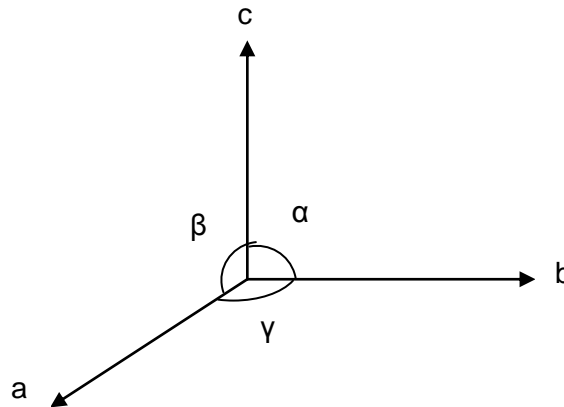


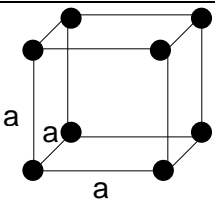
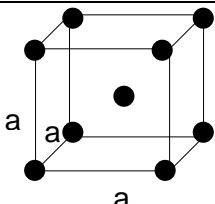
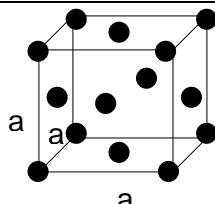
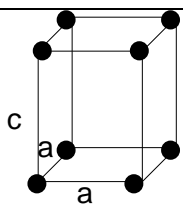
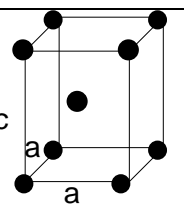
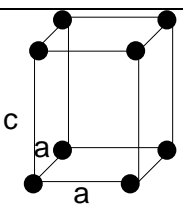
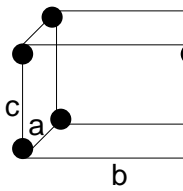
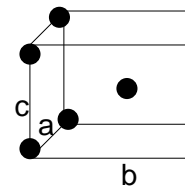
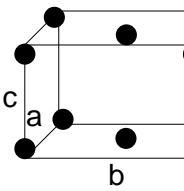
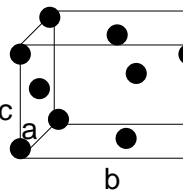
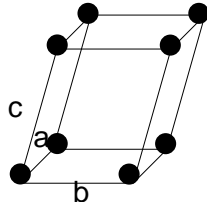
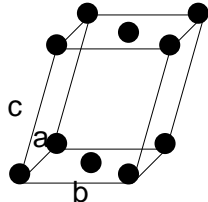
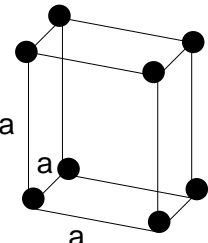
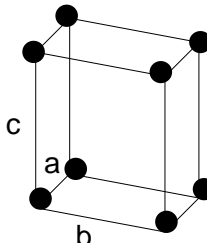
Figure 2.1: Diagram of lattice parameters determination of crystal lattice

There are seven basic crystal systems each having their own characteristics. However, Bravais discovered that there are fourteen types of unit cell that can be formed from these seven basic crystal systems. Table 2.1 lists the seven crystal systems and Table 2.2 lists the derivation of fourteen Bravais lattice from the main crystal systems.

Table 2.1: Seven Crystal Systems

Crystal System	Unit Cell
Cubic	$a = b = c$ $\alpha = \beta = \gamma = 90^\circ$
Tetragonal	$a = b \neq c$ $\alpha = \beta = \gamma = 90^\circ$
Orthorhombic	$a \neq b \neq c$ $\alpha = \beta = \gamma = 90^\circ$
Rhombohedral	$a = b = c$ $\alpha \neq \beta \neq \gamma \neq 90^\circ$
Hexagonal	$a = b \neq c$ $\alpha = \beta = 90^\circ, \gamma = 120^\circ$
Monoclinic	$a \neq b \neq c$ $\alpha = \gamma = 90^\circ \neq \beta$
Triclinic	$a \neq b \neq c$ $\alpha \neq \beta \neq \gamma \neq 90^\circ$

Table 2.2: 14 Bravais lattices from seven main crystal systems

Cubic			
			
Primitive (P)	Body-centred (I)	Face-centred (F)	
Tetragonal		Hexagonal	
			
Primitive (P)	Body-centred (I)	Primitive (P)	
Orthorhombic			
			
Primitive (P)	Body-centred (I)	Base-centred (C)	Face-centred (F)
Monoclinic			
			
Primitive (P)		Base-centred (C)	
Rhombohedral		Triclinic	
			

2.2.2 Crystallographic Directions and Planes

All crystal structures have different faces as described as a plane with specific directions. In crystallography Miller indices form a notation for planes within a crystal lattice. Figure 2.2 shows a determination of crystal plane in crystal lattice system (Millburn, 1973).

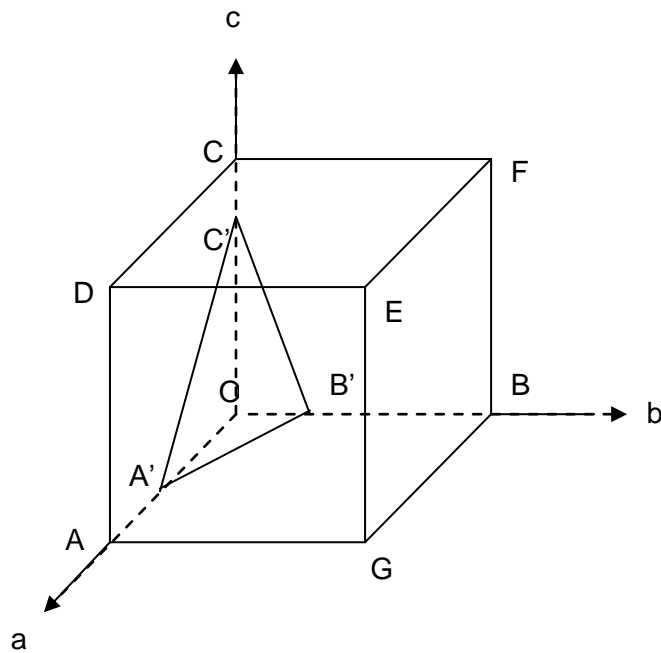


Figure 2.2: Designation of a crystal plane by Miller indices

The $A' B' C'$ plane is denoted by:

$$\begin{array}{ccc} A' = \frac{OA'}{OA} & B' = \frac{OB'}{OB} & C' = \frac{OC'}{OC} \end{array}$$

The plane of Miller indices for the unit cell can be expressed as

$$\frac{a}{h} , \frac{b}{k} , \frac{c}{l}$$

Where h , k , l can be rational numbers including zero. These are called as indices of the face in which denotes by $(h\ k\ l)$ while for the directions of the plane, or also known as vector components of the direction along the axes are denoted by $[h\ k\ l]$.

2.2.3 Crystal Projection

In crystallography, crystal planes can be represented in two dimensions by crystal projection on the flat sheet of plain paper. Each plane represents by a dot, in which the angular relationships can be determined from each dot with respect to other dots. Crystal projection is very useful to get information of the angles between planes or directions for the planes that unrepresent or hidden at the back of other faces. The projection from three dimensions to two dimensions normally used in crystallography is known as stereographic projection (Phillips, 1963). Theoretically, the stereographic projection can be explained by placing a crystal in the centre of sphere as known as spherical projection (Figure 2.3). Each dot marked on the sphere represents crystal faces.

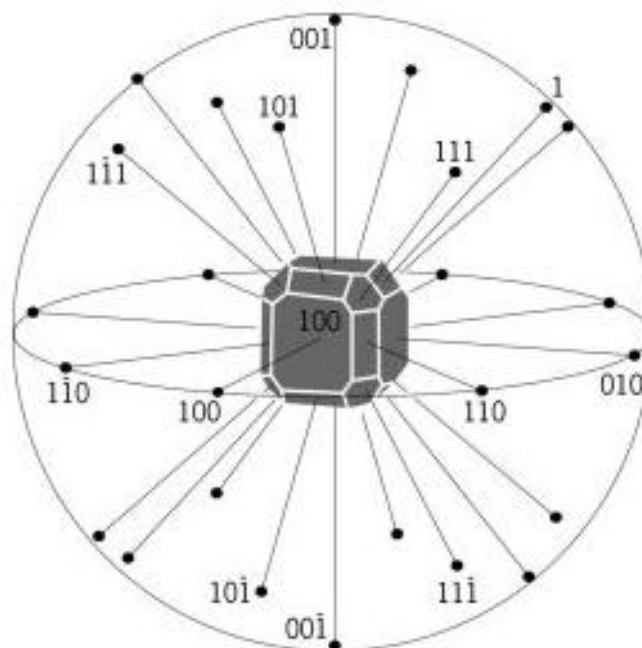


Figure 2.3: Spherical projection of normals to crystal faces (Collins, 2005)

The construction of normal to crystal faces can be drawn as in Figure 2.4 (a). The normal to crystal faces is drawn through centre of the sphere to intersect with the sphere, called as P. P is a pole of the plane of which OP is normal. The line that intersects with the sphere with such a plane is called a great circle. The great circle is a circle on the surface of sphere which has radius equal to radius of the sphere. The poles represent the directions in the crystal which is normal to the lattice planes of lattice directions. Figure 2.4 (b) shown the construction between two poles to determine the angles between planes (with OP and OQ as normal to the crystal planes in which the angle between planes equal to the angle between OQ and OP (constructed by the arc, noted as ϕ).

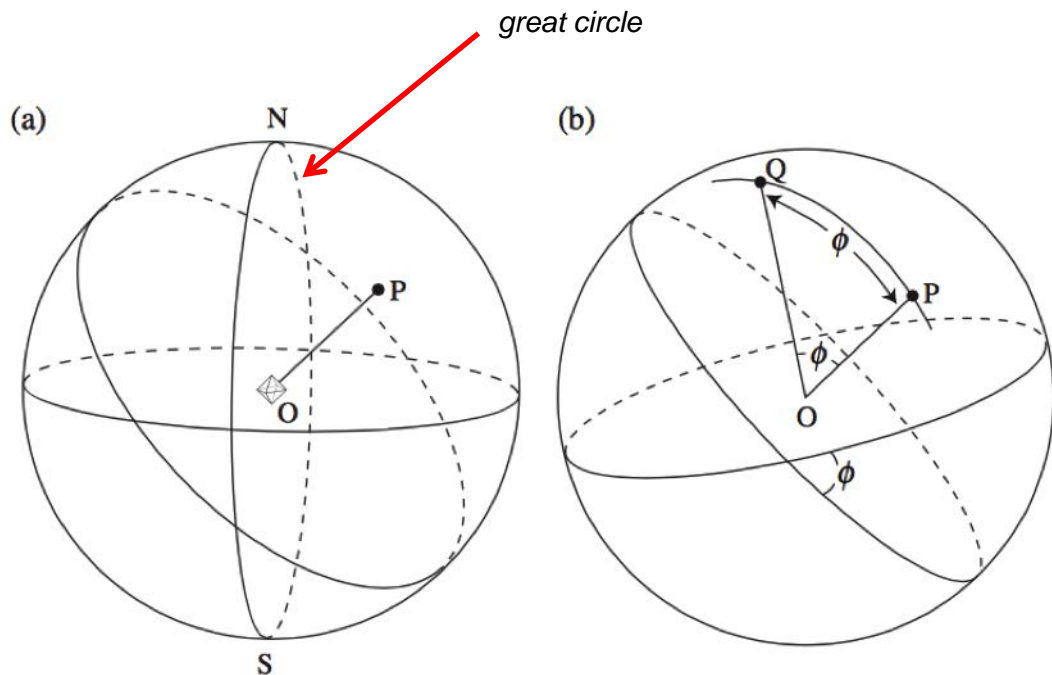


Figure 2.4: (a) Construction of pole P normal to the crystal plane, (b) The angle between two planes is equal to the angle ϕ between the two poles (Kelly and Knowles, 2012).

From the construction of the poles in Figure 2.4, to represent clearly the angular relationships between crystal planes, the constructed poles projected on the piece of flat plain paper as shown in Figure 2.5. The two dimensions projection can be explained by defining the north and south

poles, N and S, respectively. The line passes through the sphere normal to line NS and cuts the great circle is called an equator. In the construction of stereographic projection, the great circle is known as primitive circle. Projection of pole P_1 on the north pole produced P'_1 inside the primitive circle. The poles positioned in the north always projected inside primitive circle. For the south pole, the projection of P_2 is outside the primitive circle (P'_2). However, the projection outside the primitive circle is normally inconvenient to work on it, therefore, the projection of pole P_2 could be projected in the primitive circle by projected it from the north pole, as marked in the Figure 2.5 as P''_2 to distinguish from the P'_2 .

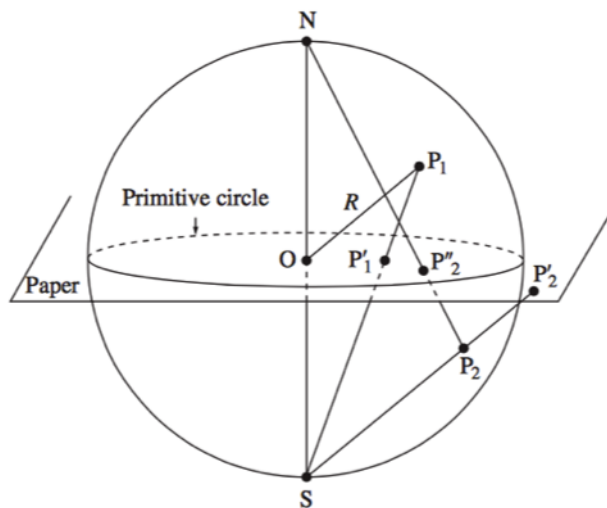


Figure 2.5: Construction of stereographic projection by defining the north and south poles in the circle.

2.2.3.1 Constructions using a Wulff Net

Another method to construct the stereogram is by a method called as a Wulff net. The Wulff net is very usable to calculate the angular measurement between planes. The diagram of Wulff net is shown in Figure 2.6. Wulff net is the projection of one half of the globe, with lines of latitude and longitude marked upon its surface while the north and south poles lie on the plane of projections.

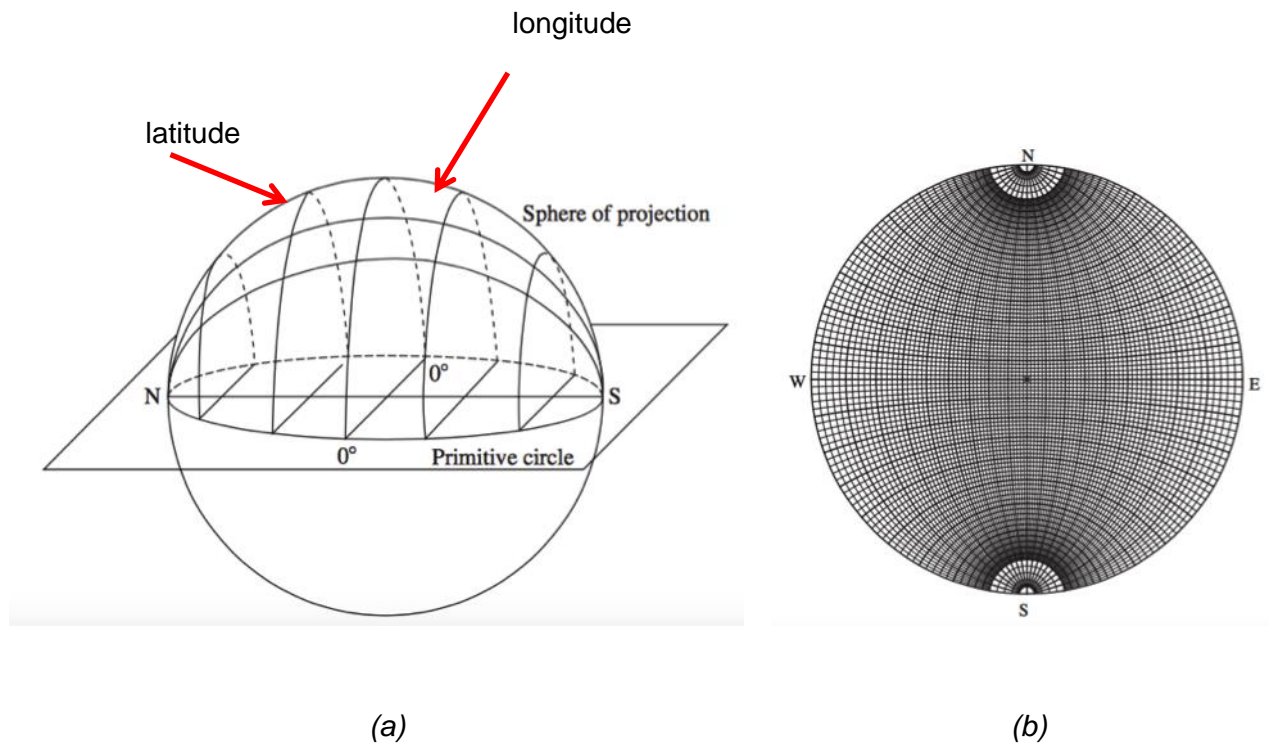


Figure 2.6: (a) The construction of Wulff net with projection of latitude and longitude on the sphere of projection, (b) Wulff net drawn with 2° intervals (Kelly and Knowles, 2012).

The net can be used together with the stereogram by placing one on top of another by using transparent tracing paper in order to measure the angular relationships between crystal planes, with the equal radius between both sphere and the location of the centre. The angle between poles within the primitive circle can be measured by rotating the stereogram until the two poles lie on the same great circle and the angles measured by counting the small circles between the poles. The measurement is explained in Figure 2.7.

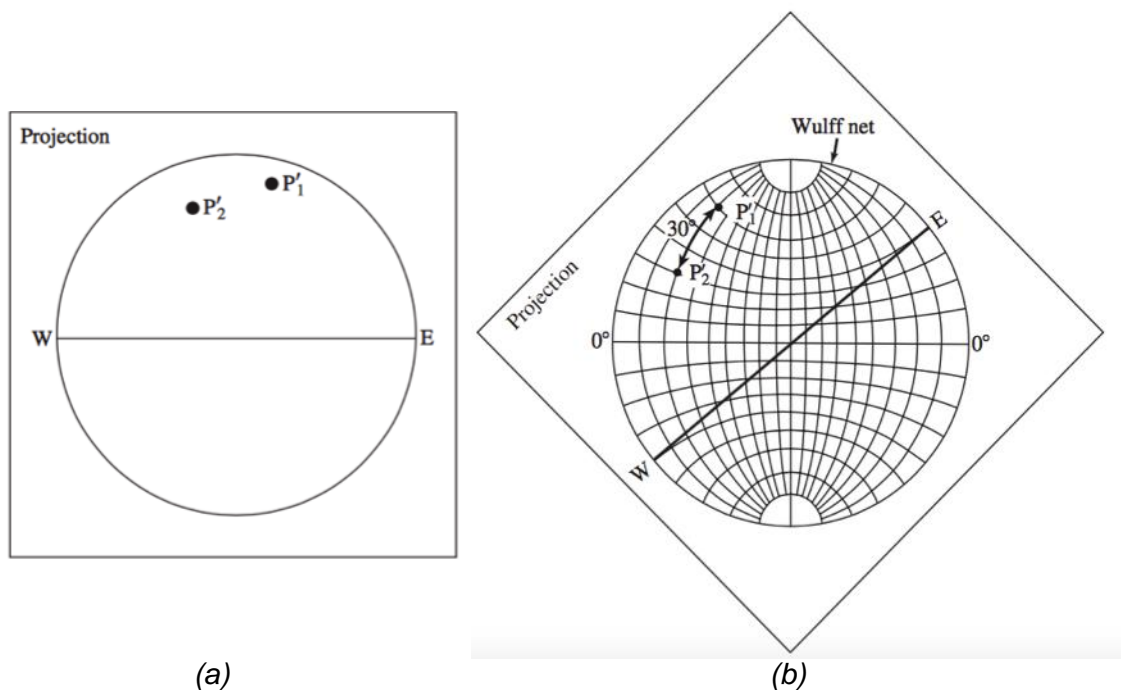


Figure 2.7: (a) Stereographic projection with projection of two poles (P_1 and P_2), (b) measurement of the angle between two poles using Wulff net. The poles lie on great circle.

2.2.4 Atomic Packing

In the crystal lattice, the atomic packing is stacked together with the existence of intermolecular bonding. In the solid state, the atoms are spherical in shape, rigid spheres, and identical in size. These atoms pack as close as possible to form a very stable crystal. In simple atomic structures, at the first single layer, the atoms arrange themselves in a hexagonal close packed array with six nearest neighbours. From this first layer, it offers the atoms the chance to build a second layer by occupying the X sites or Y sites (the sites show in figure 2.8). The atoms then build up the third layer in which at this layer, the atoms have the option either to make a layer vertically to the first layer or occupy positions at the Y sites. If the atoms at the third layer arrange themselves vertically to the first layer, thus a hexagonal close packed structure (h.c.p) is formed with the stacking arrangement $ABABAB \dots$ (figure 2.8 (a)). If the atoms arrange themselves

at the Y sites for the third layer, a face centred cubic structure is built up with the stacking arrangement of $ABCABCABC \dots$ (figure 2.8 (b)).

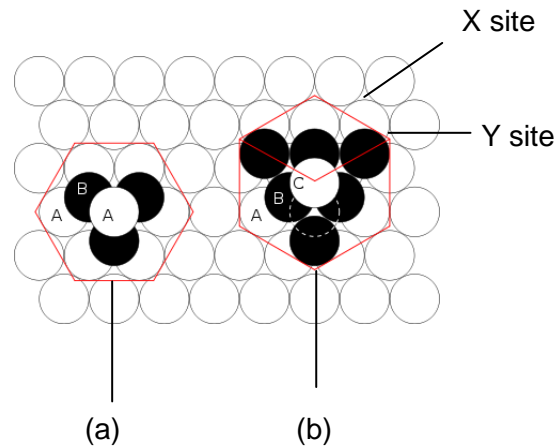


Figure 2.8: Types of atoms arrangement in crystal lattice (a) $ABABAB\dots$ arrangement (b) $ABCABCABC\dots$ arrangement.

The arrangement of the atomic packing in the unit cell is influenced by the interatomic bonding. The bonding is very important to hold the atoms in this arrangement. In order to have the most stable crystal structure, attractive and repulsive forces are needed. According to Pauli's Exclusion Principle, when two forces that hold the atoms become equal, it means the atoms more stable, at their lowest potential energy (Cramer, 2002). There are three types of bonding that influence the atomic packing and molecular arrangement as shown in Figure 2.9

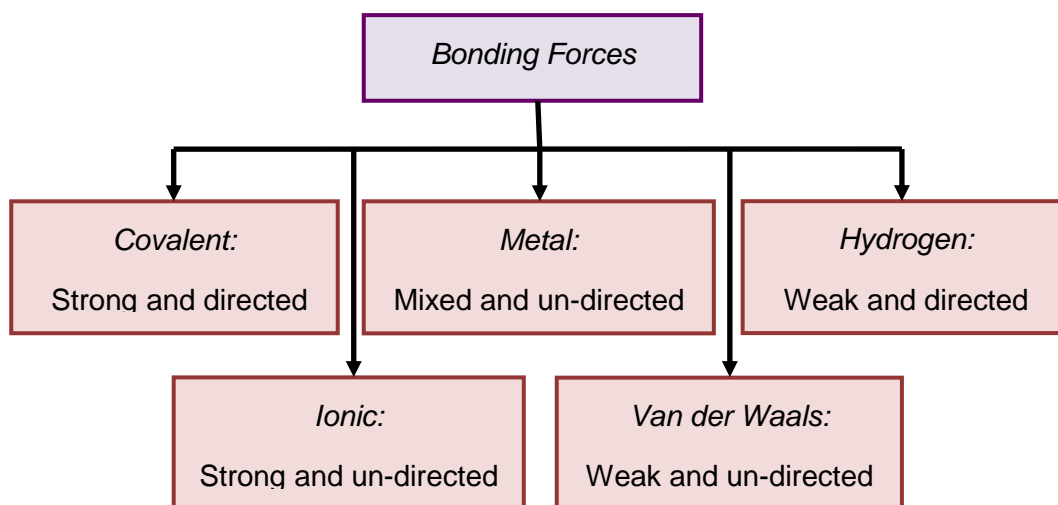


Figure 2.9: The diagram of type of bonding forces exist in matter

Covalent bonding is a chemical bond in which the atoms share the electrons to complete the outer valency shell. The bond is affected by the electronegativity of the atoms in which the sharing of electrons between equal electronegative atoms forms non-polar bonding while unequal electronegativity causes polar bonding.

Ionic bonding is an attractive force between two different electron charges; known as cations and anions. The ionic bonding occurs when the electronegative charged atom releases its electron to achieve a stable electron configuration while the electropositive charges atom accepts the released electronegative charges to achieve its stable electron configuration.

The non-bonded interaction, called van der Waals is the weakest among the three types of bonding and is an intermolecular interaction. It exists because of the polarisability of an electron orbital. Van der Waals bonding balances the electronic charge imbalance of ionic and covalent bonding. There are three types of van der Waals forces:

- (i) Keesom force (dipole- dipole interactions)
- (ii) Debye force (dipole-induced dipole interactions)
- (iii) London dispersion force (induced dipole-induced dipole interactions)

Another type of non-bonded interaction is hydrogen bonding. It is the strongest bonding in intermolecular interactions compared to van der Waals interaction, where hydrogen atoms have the ability to form bridges between highly electronegative atoms such as F, O, and N (Ladd, 1979). In organic materials, this non-bonded interaction plays the important role in terms of determining the strength of the molecules in the crystal lattice. In molecular models, Lennard-Jones (Oobatake & Ooi, 1972) and Buckingham potentials models (Buckingham, 1938) can be used to calculate the non-bonded interaction. In Lennard-Jones (6-12) potential, the calculation considers the short range, r^{-12} (repulsion) due to overlapping electrons orbital (the first term in the equation) and long range, r^{-6} (attraction) due to van der Waals forces (the second term in the equation). The equation can be described as follow:

$$V_{LJ}(r) = 4\epsilon \left[\left(\frac{\sigma}{r} \right)^{12} - \left(\frac{\sigma}{r} \right)^6 \right] \quad (2.1)$$

Where ϵ is depth of the potential well,

σ is finite distance at which the inter-particle potential is zero,

r is distance between particles

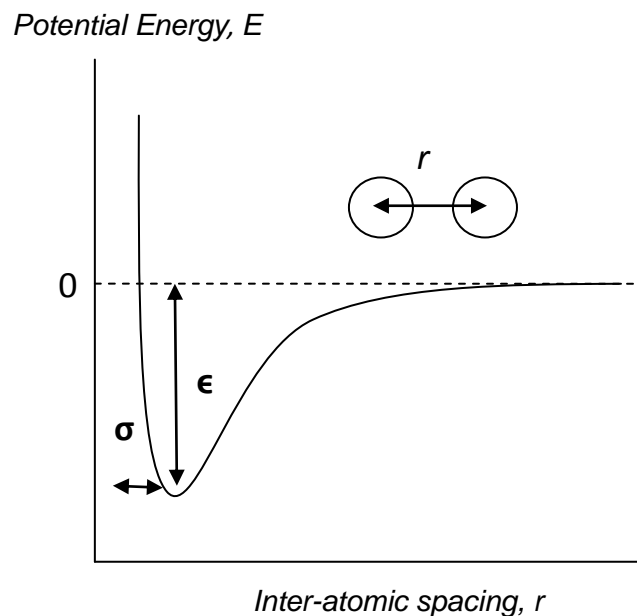


Figure 2.10: Lennard-Jones potential diagram

Figure 2.10 represents Lennard-Jones potential which the potential energy diagrams against the inter-atomic distance, r between the atoms.

Buckingham potential is alternative equation of Lennard-Jones which it does not take into account the short-range term of the repulsion, thus, the equation becomes

$$V_B(r) = -\frac{A}{r^6} + Be^{-Cr} + q_i q_j / r \quad (2.2)$$

2.2.5 Crystal Defects

An ideal crystal is one which contains no defects, however, in reality, defects in crystals always occur. The distortion or irregularity in atomic arrangement can cause a crystal lattice defect. Defects in crystals are not always disadvantageous. Defects in crystal lattice can intentionally be introduced to improve the mechanical properties of a material. There are four types of crystal defects; (i) point defects (0-D), (ii) linear defects (1-D), (iii) planar defects (2-D), (iv) bulk defects (3-D).

Point defects (as shown in figure 2.11) occur when an atom is missing or irregularly placed in the lattice structure. Point defects can occur in four conditions:

- lattice vacancies when the atoms are absent (also called Schottky defect)
- self-interstitials when atoms occupy the positions between ideal lattice atomic position
- substitution impurity atoms in which the atoms replace the host atoms in specific sites within the crystal lattice
- interstitial impurity atoms in which the atoms occupy the interstitial place in the crystal lattice.

However, it is also possible for the two point defects to occur simultaneously. For example, the lattice vacancy and self-interstitial atom defects can occur

in pairs when the atom moves out to an interstitial position and vacates its original position. This pair of defects is also called a Frenkel defect.

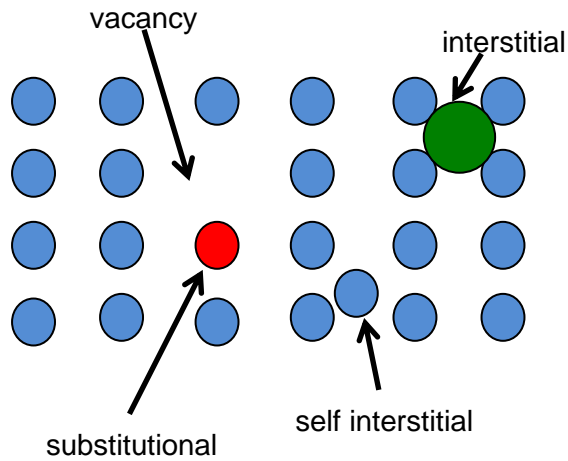


Figure 2.11: 4 types of point defect in a crystal lattice

Linear defects, commonly known as ‘dislocations’, are defects occur when some of the atoms are not in their positions in the crystal structure. There are two primary types of dislocations; (i) edge dislocations (figure 2.12 (i)), (ii) screw dislocations (figure 2.12 (ii)). Sometimes, a combination of both dislocations may occur, as which is also a common situation in crystal defects (figure 2.12 (iii)). Burgers vector is used to describe the magnitude of distortion of the plane. Edge dislocations occur when a line of atoms terminate its plane in the middle of the crystal lattice. In edge dislocations, Burgers vector is perpendicular to the line of direction. A screw dislocation occurs when Burger’s vector is parallel to the dislocation line.

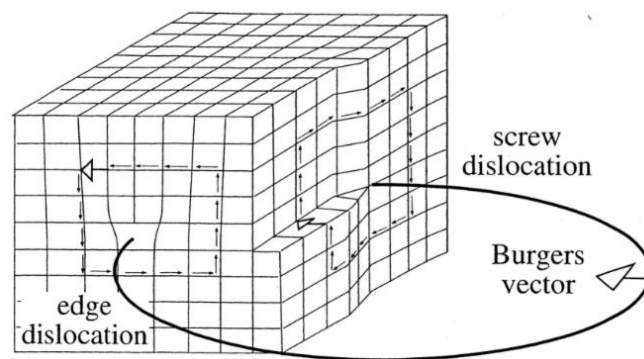


Figure 2.12: Diagram of dislocations occur in crystal lattice

Planar defects are an imperfection that occurs when the orientation of atomic planes at an interface is changed. Grain boundaries normally occur during crystal growth or by subsequent mechanical deformation. Other type of planar defect is when two different domains develop during crystal growth which has a distinct orientational arrangement with respect to each other. This is effect called twinning, with a twinning plane between the two (figure 2.13).

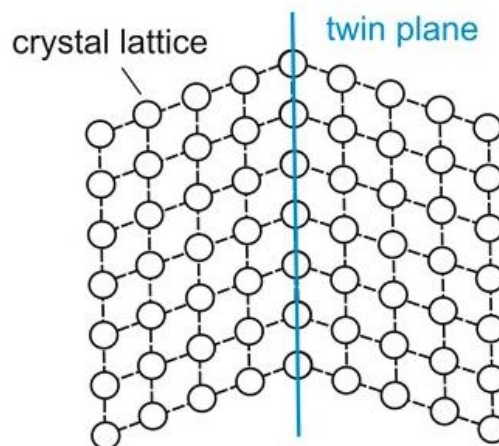


Figure 2.13: A twinning plane

2.3 Crystal Morphology & Habit

From a crystallographic view, the arrangement of atoms in crystal lattice and the symmetry of the crystal lattice determine the shape of crystals. The external shape of the crystal is called its morphology or habit. From a crystal chemistry perspective, the crystal habit depends on the relative growth rates of the faces of the crystal. However, both of these are inter-related to each other. The growth rates of the faces may differ depending on the process conditions due to the fact that this individual growth rates may be different. Hence, different shapes of crystals can be produced. Changing the degree of the driving force (supersaturation), solvent and impurities (Davey, *et al.*, 1986) can significantly affect the crystal growth rates and also the shape. For example, in L-glutamic acid crystallisation, different supersaturation tends to convert the prismatic meta-stable α - form to long needle-like stable

β -form at specific temperature (Ferrari and Davey, 2004). The solvent effect in crystallization of aspirin shows that if different solvents are used for crystallisation, hence, may produce different shapes of crystals i.e aspirin (Watanabe *et al.*, 1982).

The most common crystal shapes are (a) plate-like, (b) prismatic, (c) needle-like shape (Figure 2.14). During the crystallization process, crystals will form the shape that has the lowest free surface energy (Cardew, 1985). The morphology of the crystal is important as it determines the surface properties of the crystal. It has a significant effect on the physico-chemical properties of the crystal during downstream processing, and therefore careful control must be taken in order to retain its properties.

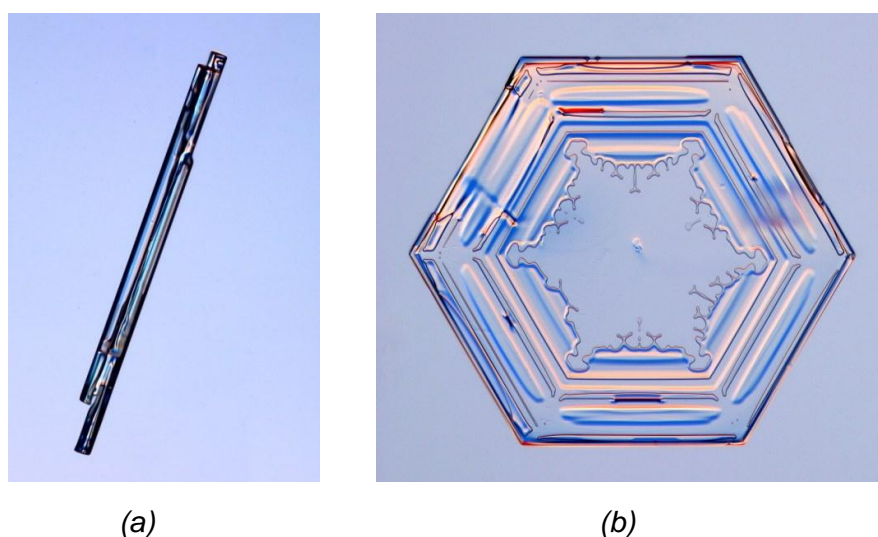


Figure 2.14: Types of crystal habits: (a) needle-like shape; (b) hexagonal plate shaped of snowflakes. (<http://www.its.caltech.edu/~atomic/snowcrystals>).

2.4 Polymorphism

Polymorphism occurs when the same molecular species with the same chemical composition in more than one crystal structure. Polymorphism can occur in two ways:

- (1) Packing polymorphisms in which the molecules have different crystal packing between two polymorphs (Braun, *et al.*, 2008). Figure 2.15 shows the packing polymorphism of paracetamol form I and II.
- (2) Conformational polymorphisms in which the molecules flexibly change their conformation arrangements of the molecules, for example change in torsion angles of the bonding between atoms or functional group (Cabeza & Bernstein, 2014).

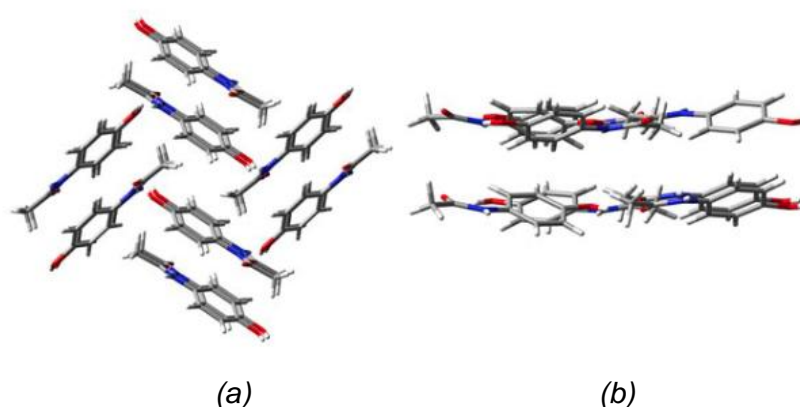


Figure 2.15: Two polymorphs of paracetamol (a) form I and (b) form II show different arrangement of molecules for crystal packing (Redinha *et al.*, 2013).

The formation of different polymorphs can be effected example by recrystallisation of the compound in different solvents and or through variation of crystallisation conditions such as temperature, concentration and pH. (Byrn *et al.*, 1995). For example, crystallisation of hydrocetrizine from different solvents can form crystals with different polymorphs. Different conditions such as supersaturation and the temperature of crystallisation process will also affect the crystal morphology even if the same solvents used (Chen *et al.*, 2008). Polymorphism can also be controlled by using “tailor made additives”, being either solvents or additives which have similar molecular structure as the host molecule (Roberts *et al.*, 1994), (Graham *et al.*, 2013).

The formation of polymorphs is important in pharmaceutical processing as the difference in physical properties can have an impact on the performance of the pharmaceutical drugs. This is because different polymorphs can have different physical properties such as molar density, hygroscopicity, melting temperature, heat capacity, solubility, dissolution rate, stability, habit, hardness, and compactibility. Thus, fully controlling the process is very crucial to ensure that only the desired polymorph will form. Another different case exists when the crystal has incorporated solvent molecules in its structure (non-solvated crystal). On first examination such a situation would appear as if polymorph had been produced. However, it would not be polymorph but is often called a pseudo-polymorph because the chemical compositions of the non-solvated and solvated crystals differ (Giron, 2001).

The existence of polymorphic forms can be affected by either thermodynamics or kinetics. If the thermodynamic factor determines the polymorphic formation, the polymorph produced depends on the stability of the crystal. The most stable form of a polymorph is that which has the lowest free energies. This can often be characterised by the lowest solubility, highest density and highest melting point. According to the Ostwald's rule (Mullin, 2001), if the formation of polymorphs is affected by kinetic factors, then the compound will be likely to crystallise in its least stable form (metastable) first followed by its conversion to its most stable form.

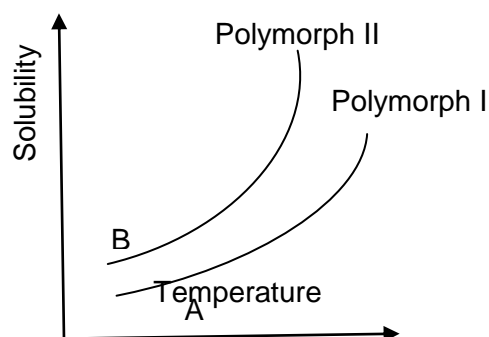


Figure 2.16: Solubility curves of two polymorphic forms according to Ostwald's rule (Roberts, 2011).

Figure 2.16 above gives an example of the formation of polymorphs I and II by Ostwald's rule. Consider that the compound is crystallised in two different solvents, A and B. Solvent A is supersaturated to polymorph I but not II, while solvent B is supersaturated with respect to both polymorphs. In certain conditions, the least stable polymorph form which is polymorph II will transform to polymorph I which is the most stable form (Mullin, 2001). The anti-viral HIV drug, Stavudine, has two polymorphic forms. During the crystallisation, the effect of supersaturation was studied. In agreement with Ostwald's rule, Stavudine form I which is is the least stable polymorph formed first, followed by its conversion to the more stable form II (Mirmehrabi & Rohani, 2006).

There are two types of structural inter-relationship between polymorphs:

- (1) Monotropic: In this system only one polymorph can form along the temperature range below the melting point, T_m . For this system, the free energy curve does not cross the solubility curve, Figure 2.17 (a).
- (2) Enantiotropic: In here, one polymorph forms in one temperature range and the other polymorph forms in the other temperature range. A transition temperature exists at which the first polymorphic form will transform to another polymorphic form. For this system, the free energy curve does cross the solubility curve before the melting point (Figure 2.17 (b)).

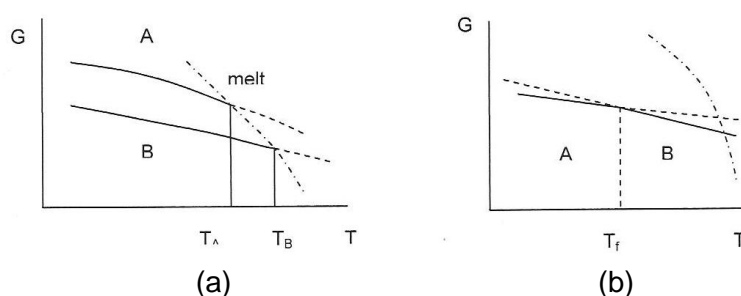


Figure 2.17: Schematic diagrams showing the relationship between the Gibbs free energy and the temperature T of two polymorphic inter-relationships. A and B represent metastable and stable polymorphs: (a) monotropic. T_A is melting temperature of metastable A form and T_B is a melting temperature of stable B form (b) enantiotropic. Metastable A form transforms to B form when the temperature reaches T_f (transition temperature) (Brittain, 1999).

2.5 Crystallisation

Crystallisation from solution phases is a purification process using liquid/solid separation techniques which separates a solid from its 'mother' solution. In this process, the solution can be formed by the addition of a solid to the solvent. Depending on the solubility of the solid in the solvent, at certain temperature and pressure, a homogenous solution can be produced. When the maximum amount of solute is dissolved in a given volume, the solution is said to be saturated. Cooling of such a solution can result in crystallisation process that involves three stages:

- (1) Supersaturation
- (2) Nucleation
- (3) Crystal Growth

2.5.1 Supersaturation

The crystallisation process is dependent on a suitable driving force, i.e supersaturation. A supersaturated solution is one in which the solute concentration is higher than solution's the equilibrium solubility at a given temperature. Δc is denoted as the driving force. S , the supersaturation, is the ratio of actual (c) to equilibrium (c^*) solubilities given by:

$$\Delta c = c - c^* \quad (2.3)$$

and

$$S = \frac{c}{c_e} \quad (2.4)$$

Thus, the absolute or relative supersaturation, σ , can be expressed by:

$$\sigma = \frac{\Delta c}{c} = S - 1 \quad (2.5)$$

There are a number of ways that can be used to supersaturation to occur:

- the temperature of the solution can be changed depending on the sign of the solubility coefficient.
- solution pH can be changed in cases where the solution is an electrolyte.
- evaporation of the solvent. This is a simple technique often used in the production of non-speciality bulk chemicals.
- using a mixture of solvents in which the second added solvent has a low solubility but highly miscible than the saturating solution prepared from the first solvent.

2.5.2 Metastable Zone Width (MSZW)

Measurement of the metastable zone width (MSZW) is often used to assess the nucleation behaviour and solubility of the solute in a specified solvent in the crystallisation process (Mullin, 2001). The MSZW value can be highly dependent on process conditions. Factors that influence the value of MSZW are cooling / supersaturation rate, the purity of the solution and the nature of the crystals themselves. The presence of nucleation suppressing impurities can affect the MSZW value which commonly widens the metastable zone. Changes in temperature can also make the MSZW become broader. For example, the nucleation behaviour may vary if the temperature of the solution is maintained at a higher temperature than the equilibrium temperature for a long period of time, in comparison to the case where the solution temperature is maintained just above the saturation temperature. Solution agitation can also be used to narrow the MSZW.

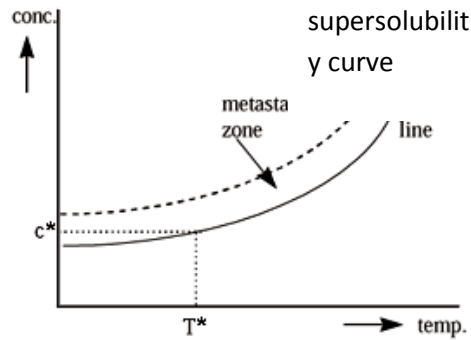


Figure 2.18: Metastable Zone Width Diagram shows the metastable region is in between solubility line and supersolubility curve. Below solubility line, no crystallisation occurs, while above supersolubility curve, the crystal growth occurs instantaneous (Giulietti et al., 2001).

At a given supersaturation, critical nucleus will occur. The time of the first formation of critical nucleus is called t_N . As it is difficult to see the appearance of critical nucleus in the solution, thus the appearance of the first crystal growth after time t_G . The MSZW can be measured only if $t_N > t_G$. Otherwise, crystallisation will not occur and MSZW cannot be considered in the system.

The nucleation behaviour within MSZW can be characterised either by the isothermal or polythermal method. In an isothermal method, the saturated solution is agitated until it becomes saturated. To attain constant supersaturation, it is undercooled to a certain temperature, called T_1 and maintained until the first crystals appear at time t_1 . For the polythermal method, the MSZW is determined by measuring the location of the supersolubility curve as a function of cooling rate.

2.5.3 Nucleation

Nucleation is the process in which a solid phase is initially formed from a supersaturated solution through the process of forming clusters from the dispersed solute molecules in the solvent. In order to reach a critical size of the nuclei, the nuclei have to be stable from a free energy stand point otherwise they will redissolve and the nucleation process will fail. The nucleation process can be divided into two types: primary nucleation and secondary nucleation.

In primary nucleation, the solute solubility tends to be low, thus supersaturation is high. This is very important in pharmaceuticals, photographic chemicals, pigments and catalysts industries. Within this, there are sub-types of nucleation: homogeneous and heterogeneous nucleation. Homogeneous nucleation occurs in a totally random way with nuclei being homogeneously formed throughout the mother phase. Heterogeneous nucleation occurs when the mother phase has a large number of microparticulates (foreign particles) within it with this encouraging nucleation within the solution.

Secondary nucleation can be intrinsic or extrinsic in nature. Nucleation by intrinsic particles occurs by mechanical action or through particle-particle collisions with the agitator or impeller where the small particles break off the primary nuclei; this generates a new growth centre. The nucleation by extrinsic particles however occurs when e.g: seed materials are added into the solution to initiate the crystallisation process. The purpose of adding seeds to the solution is in particular to control the nucleation process through this particle size and its better distribution.

2.5.4 Crystal Growth

As nucleation process proceeds, the cluster formed continues into the crystal growth process. In the mechanism of crystal growth, an atom or

molecule is incorporated at the surface of the crystal which increases the size of the crystal. There are stages to the crystal growth process:

- (1) Transport of molecules through solution
- (2) Attachment of molecules to the surface
- (3) Movement of molecules on the surface
- (4) Attachment of molecules to edges and kinks

The Kossel model (see figure 2.19) of crystal growth is helpful to understand the interfacial kinetics at the growing crystal surfaces. It is a simple model developed from cubic units where surface layers are formed with four sites being of specific interest (Mullin, 2001):

- (a) Steps
- (b) Terraces between steps
- (c) Kink sites on the steps
- (d) Terrace-adsorbed molecules

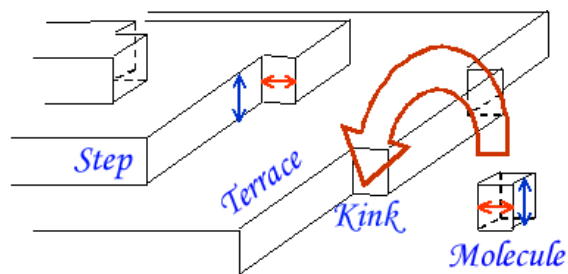


Figure 2.19: Steps, terrace, kink sites and adsorbed molecule on crystal surface of crystal growth model

When atoms are attached to the surface or terrace, one bond will form. In contrast the atoms that attach to steps will form two bonds whereas three bonds will form when the atoms attach to kinks sites. Obviously, kink sites give the most stable configuration of crystal growth, as at these sites the three neighbouring atoms that are attracted to the atoms decrease the surface energies of the sites. At the edge sites, the attachment of the atoms leads to the completion of the entire crystal plane. At the completion of this plane, the

new stable nucleus is formed on the plane surface. This nucleus increases the surface energy at the edges to attract other atoms whilst decreasing the surface energy in the interior. The stability of the nucleus depends on the ratio of volume to surface in which if the critical radius of the nucleus, (r_c), $r_c < r$, the nucleus is stable and the growth can continually proceed but if $r_c > r$, the nucleus is unstable and growth is impossible.

2.5.5 Types of Crystal Faces

As the crystal completes the growing process, three different types of faces can be formed: F- (flat) faces; S- (stepped) faces; and K- (kink) faces (Figure 2.20). K-faces grow fast and are rough at the molecular level. K faces will be incorporated and become part of crystal. However, only a few can be incorporated directly at the K faces but many desorb at the K faces before they are incorporated. Most will be adsorbed at the S faces. The rate of growth at the S faces is much slower than at the K faces. F faces have the slowest growing rate compared to S and K faces as they need some mechanism to grow at all the steps. During the crystal growing process, the growth rate of different types of faces can be expected to differ, e.g., the fast growing S-faces and K-faces are likely to become smaller in terms of their surface area when compared to the slowest growing F-faces and finally disappear. Thus, only the slow growing faces tend to exist as the crystal develops in size. (Roberts, 2011).

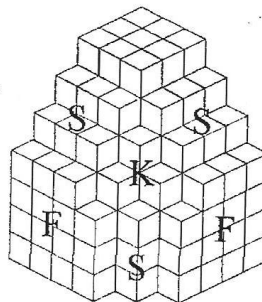


Figure 2.20: Step (S), kink (K), flat (F) faces (Roberts, 2011)

2.6 Agglomeration

Agglomeration is the sticking of particles to one another resulting in the forming caking through the bridges or lumps. In fine chemical industries for example in the pharmaceutical industry, agglomeration is desired in order to improve powder properties i.e, the flowability, compaction behaviour, increasing the surface area of particles, and reducing the dusting problem during the handling process (Jeck, 2006). The agglomeration occurs by the binding mechanism that holds the particles together. Binding occurs by adhesion forces between particles. These forces determine the strength of the agglomeration. During agglomeration, new particle sizes form, with larger sizes than single particle. Agglomerates can be in the form of tablets, granules, bricks or compaction of particles. The formation of new particle sizes does not change the original solid particles, size and shape. Jeck, 2006 also explained that agglomeration tends to occur at the fast growing faces of the crystals.

There are two primary types of agglomerates; (i) soft agglomerates and (ii) hard agglomerates. The first type of agglomerates may influence the bulk powder properties as mild forces occur during processing that have a tendency to break the agglomerates. The latter type normally form larger size of particles than the primary particles before the agglomeration (Figure 2.21) , thus the breakage can happen if large forces are applied to the particles such as may take place during the milling process (Nichols, *et al.*, 2002).

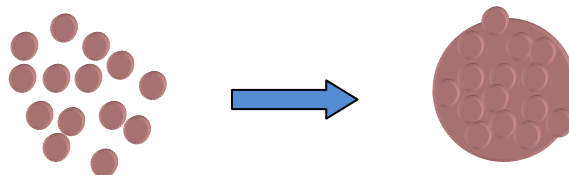


Figure 2.21: Schematic diagram of formation of agglomerates from a group of particles.

In Brunsteiner *et al.*, 2005, a study had been carried out to understand the agglomeration process at the molecular level by simulating surface interactions between agglomerates particles. In their study, inorganic and organic materials had been used to observe the respective differences between the agglomeration processes for these two types of material. They discovered that the extent of supersaturation influenced the strength of the agglomeration.

Using fundamental approaches, the characterisation of particle-particle interactions forms an important interest in this study. Several methods have been selected for the characterisation of the agglomerates; surface energy analysis to determine the average dispersive energy for the batch crystals, X-ray diffraction to determine the orientation relationship between crystals and molecular modelling simulation to fully understand the surface chemistry of the compounds. These methods are described in chapter 3 and 4 of this thesis.

2.7 Closing Remarks

This chapter has reviewed and discussed the fundamental theories of crystallography and crystallization process including the basic crystallography, crystal chemistry and the stages in crystallization process including nucleation and growth process, mechanism of crystal growth and morphology of the crystals.

References

1. Barret, C., Massalski, T.B., (1980). Structure of Metals. Crystallographic Methods, Principles and Data In: International Series on Materials Science and Technology. Third revised ed., vol 35. *Pergamon*, Oxford.
2. Bragg, W.H., Bragg, W.L., (1913). The Reflection of X-rays by Crystals. *Proc. R. Soc. Lond A*: (88) 428-438.
3. Braun, D.E., Gelbrich, T., Kahlenberg, V., Laus, G., Wieser, J., Griesser, U.J., (2008). Packing Polymorphism of a Conformationally Flexible Molecule (Aprepitant). *New J. Chem.* (32) 1677-1685.
4. Britain, H. G. (1999). Polymorphism in Pharmaceutical Solids. Vol 95. *Marcel Dekker, Inc.* New York.
5. Brunsteiner, M., Jones, A.G., Pratola, F., Price, S.L., Simon, S.J.R., (2005). Toward A Molecular Understanding of Crystal Agglomeration. *J. Cryst. Growth Des.* (5) 3-6.
6. Buckingham, R.A.,(1938). The Classical Equation of State of Gaseous Helium, Neon, and Argon. *Proc. R. Soc. Lond A: Mathematical, Physical and Engineering Sciences* (168) 264-283.
7. Cardew, P.T., (1985). The Growth Shape of Crystals. *J. Cryst. Growth.* (73) 385-391.
8. Chen, J., Wang, J., Ulrich, J., Yin, Q., Xue, L., (2008). Effect of Solvent on the Crystal Structure and Habit of Hydrocortisone. *J. Cryst. Growth Des.* (8) 1490-1494.
9. Crystallography. (n.d.) *Collins Discovery Encyclopedia*, First ed. (2005).
10. Cramer, C.J., (2002). Essentials of Computational Chemistry: Theories and Models. First ed. *John, Wiley & Sons*, England.
11. Curz-Cabeza, A.J., Bernstein, J., (2014). Conformational Polymorphism. *Chem. Rev.* (114) 2171-2190.
12. Davey, R., Fila, W., Garside, J., (1986). The Influence of Biuret on the Growth Kinetics of Urea from Aqueous Solutions. *J. Cryst. Growth.* (79) 607-613.

13. Ferrari, E.S., Davey, R.J., (2004). Solution-mediated Transformation of α - to β - L-Glutamic Acid: Rate Enhancement Due to Secondary Nucleation. *J. Cryst. Growth Des.* (4) 1061-1068.
14. Giron, D., (2001). Investigations of Polymorphism and Pseudopolymorphism in Pharmaceuticals by Combined Thermoanalytical Techniques. *J. Therm. Anal. Cal.* (64) 37-60.
15. Giulietti, M., Seckler, M.M., Derenzo, S., Re, M.I., Cekinski, E., (2001). Industrial Crystallisation and Precipitation from Solutions: States of the Technique. *Brazilian Journal of Chemical Engineering.*
16. Glusker, J.P., Trueblood, K.N., (2010). Crystal Structure Analysis. Third ed. *Oxford University Press.*
17. Graham, K.R., Stalder, R., Wieruszewski, P.M., Patel, D.G., Salazar, D.H., Reynolds, J.R., (2013). Tailor-Made Additives for Morphology Control in Molecular Bulk-Heterojunction Photovoltaics. *ACS Appl. Mater Interfaces.* (5) 63-71.
18. Hilfiker, R., (2006). Polymorphism: In the Pharmaceutical Industry.
19. Jeck, S. (2006) Molecular Modeling of Particle-Particle Interactions Relevant in Understanding Pharmaceutical Formulation Design: A Case Study of Acetylsalicylic Acid and Ascorbic Acid. *Student Exchange Project Thesis, University of Leeds.* Associated paper:
Hammond, R.B., Jeck, S., Ma, C.Y., Pencheva, K., Roberts, K.J., Auffret, T., (2009). *J. Pharm. Sci.* (98) 4589-4602.
20. Ladd, M.F.C., (1979). Structure and Bonding in Solid State Chemistry. (Ellis Horwood Series in Chemical Science). *Ellis Horwood Ltd, New York.*
21. Kelly, A., Knowles, K.M., (2012). Crystallography and Crystal Defects. Second ed. *John Wiley & Sons, Ltd, Chichester, UK.*
22. Milburn, G.H.W., (1973). X-ray Crystallography. First Ed. *Butterworths and Co. Ltd., London.*
23. Mirmehrabi, M., Rohani, S., (2006). Polymorphic Behaviour and Crystal Habit of an Anti-Viral/ HIV Drug: Stavudine. *J. Cryst. Growth Des.* (6) 14-149.
24. Mullin, J.W., (2001). Crystallisation. Fourth ed. *Butterworth-Heinemann, Oxford.*

25. Nichols, G., Byard, S., Bloxham, M.J., Botterill, J., Dawson, N.J., Dennis, A., Diart, V., North, N.C., Sherwood, J.D., (2002). A Review of the Terms Agglomerate and Aggregate with Recommendation for Nomenclature Used in Powder and Particle Characterisation. *J. Pharm. Sci.*, (91) 10.
26. Oobatake, M., Ooi, T., (1972). Determination of Energy Parameters in Lennard-Jones Potentials from Second Virial Coefficients. *Prog. Of Theoretical Physics*.(48) 2132-2143.
27. Phillips, F.C., (1963). An Introduction to Crystallography. Third ed. *Longmans, Green and Co. Ltd*, London.
28. Redinha, J.S., Jesus, .A.J.L., Pais, A.A.C.C., Almeida, J.A.S., (2013). Crystallisation: From the Conformer to the Crystal. Book Article: Advanced Topics on Crystal Growth. *Dr. Sukarno Ferreira (Ed.)*
29. Roberts, K.J., (2011). Pharmaceutical Product Formulation. *PEME5360M Course Notes, School of Process, Environmental and Materials Engineering*, University of Leeds.
30. Roberts, K.J., Sherwood, J.N., Yoon, C.S., (1994). Understanding the the Solvent-Induced Habit Modification on Benzophenone in Terms of Molecular Recognition at the Crystal / Solution Interface. *Chem. Mater.* (6) 1099-1102.
31. Watanabe, A., Yamaoka, Y., Kozo, T., (1982). Crystal Habits and Dissolution Behaviour of Aspirin. *Chem. Pharm. Bull.* 30 (8) 2958-2963.

CHAPTER III

SURFACE AND SOLID-STATE ANALYSIS AND CHARACTERISATION OF MICRO-CRYSTALS

3.1 Introduction

This chapter discusses the theoretical background to the solid-state and surface characterisation techniques used in this work. It includes the investigation of surface energy analysis of solid particles conducted by inverse gas chromatography (IGC), the use of dynamic vapour sorption (DVS) for characterisation of water sorption effect to the surface of solid particles, the measurement of the size and shape of the crystals and the technology of synchrotron radiation for the measurement of the crystal structure, crystal aggregation and 3-D morphology use in X-ray micro-diffraction and X-ray micro-tomography techniques.

3.2 Surface Analysis Techniques

3.2.1 Inverse Gas Chromatography (IGC) For Surface Energy Analysis

The determination of the surface free energy in particles processing is very important in order to determine the stability, adhesion and cohesion between particles and also the interactions among the molecules in the crystal packing. These properties are important to understand to ensure the final products meet their specification. The results from surface characterisation of solid particles help the related industries to improve the surface properties and whether to do some modifications to increase product performance. It also helps to fundamentally understand the surface chemistry of the particles. Surface free energy characterisation is important in pharmaceutical dosage and pharmaceutical processing and to help determine the granule strength, morphology, failure process, and the formation of film on the binders (Hooton *et al.*, 2006).

In surface energetic studies, the interactions between solid surfaces and the external environment occur due to the termination of the bulk crystal structure at the crystal surfaces with the resultant surface energies reflecting the nature and strength of the 'broken bond' component of the existence of

intermolecular forces between the constituent molecules within the crystal packing. Two types of interactions are important: dispersive and acid-base interactions which results from the London dispersion forces and the electrons sharing of the charged atoms, respectively. Surface free energy or surface energy, γ , (mJ/m^2) is defined as amount of energy that is required to increase 1m^2 per unit area of surface,

$$\gamma = \gamma^P + \gamma^D \quad (3.1)$$

Where γ^P is the surface energy for polar components and γ^D is the dispersive surface energy for non-polar components.

A dispersive surface energy is due to the non-polar components which are, in turn, the intermolecular energy that arises from van der Waals forces interactions between molecules. A polar surface energy can be calculated from the Lewis acid (γ_s^+) to characterise basic properties (γ_s^-) while Lewis base (γ_s^-) can be used to characterise the acidic properties (γ_s^+) of the solid surface of the material studied.

$$\gamma^P = 2N_A \cdot a \cdot ((\gamma_L^+ \gamma_s^-)^{1/2} + (\gamma_L^- \gamma_s^+)^{1/2}) \quad (3.2)$$

Where N_A is the Avogadro's constant,

a is the cross sectional area of the probe molecule,

γ_L^+ is the acidic parameter of the probe molecule,

γ_L^- is the basic parameter of the probe molecule,

γ_{s+} is the acidic parameter of the solid surface, and

γ_{s-} is the basic parameter of the solid surface

The term of surface free energy is referring to the interactions of atoms or molecules at interfaces, since this energy differs from the bulk. The surface energy is influenced by several factors such as wettability and work of adhesion and cohesion of the substance. The interfacial surface energy is the energy that exists when two individual surfaces interact with each other. The interfacial interactions include the work of adhesion (W_a) between two

phases and work of cohesion (W_c) of one phase. The subtraction of the work of adhesion from the work of cohesion gives the value for the spreading coefficient, λ , which is an important parameter in determining the granule strength. A positive value of the spreading coefficient is indicative of strong granules whilst a negative value is more consistent of weak granules (Rowe, 1989a), thus:

$$\lambda = W_a - W_c \quad (3.3)$$

In the earlier studies of the surface energetic nature of solid particles, contact angle measurements were a popular method in determining the surface energy of the solid. The contact angle between liquid and solid is measured by dropping a small drop of liquid on the solid surface and measuring the interaction between the liquid and solid by using Young's equation (Zisman, 1964). There are several methods that have used contact angle techniques to measure the surface energy of the solid, including the sessile drop method (Nizhenko *et al.*, 1964), Wilhelmy method (Heertjes *et al.*, 1971), and powder contact angle method using a static capillary rise technique (Dunstan & White, 1986). However, the results obtained from contact angle techniques can be affected by the compression of the powder on the disk in which the compression may change the surface properties, affecting the accuracy of the measurement (Grimsey *et al.*, 2002). In the early 1970s, inverse gas chromatography (IGC) had been introduced for surface energy determination. In 1989, this technique had been used to study the water binding on egg solid (Demertzis & Kontominas, 1989). Dove *et al.*, 1996 did a comparison study between contact angle techniques and inverse gas chromatography. The two methods of contact angle measurement used were compressing a plate of powder and sticking uncompressed powder on the plate. From this investigation, they found that the inverse gas chromatography technique gave similar values to the contact angle measurement techniques. The first authors to introduce inverse gas chromatography method in pharmaceutical field were Huu-Phouc *et al.*, in 1986 in who used IGC to determine the partial solubility parameters of lactose.

The surface energy of powder materials can also be determined by IGC. Generally, IGC determines the thermodynamic parameters of the solids, specifically the partition and solubility coefficients, enthalpies of adsorption, free energy of adsorption and also the sorption isotherms of the adsorbate. The utility of IGC in measuring the surface properties of the materials have made it very useful in the pharmaceutical, food, dyeing or painting industries. In the food industry, for example, the thermodynamic properties of aromatic-starch interactions (Boutboul *et.al*, 2002) have been determined. In other studies, the polar and total surface energy distributions of lactose from the known dispersive surface energy has been obtained from the IGC calculation (Das *et al.*, 2011).

In IGC, the solid material is packed in a long, thin packed column which acts as an adsorbent and is a stationary phase while the volatile probes pass through the column as the adsorbate. To determine the dispersive surface energy, a series of n-alkanes can be used as non-polar solutes while polar probes such as alcoholic solvents to study the acid-base interactions of the solid particles for polar surface energy determination. The probe residence time, t_r (min) can be calculated as the probes passed through the column and hence the shape of the resultant chromatogram indicate the characteristics of the stationary phase and its interaction with the probes. From the residence time, the net retention volume, V_N can be calculated by using the equation 3.4:

$$V_N = F_c \cdot J (t_r - t_o) \quad (3.4)$$

From the net retention volume, the specific retention volume can be obtained from the following equation 3.5:

$$V_S = \frac{V_N \cdot 273}{m \cdot T} \quad (3.5)$$

Where,

F_c is the carrier gas flow rate, ml/min,

t_o is the hold-up time of non-retained compound (methane), min,

m is the mass of stationary phase, g,

T is the temperature of the column, K, and

J is the correction factor for the compressibility of the carrier gas.

J can be obtained from the equation 3.6 below:

$$J = \frac{3}{2} \times \frac{\left(\frac{P_i}{P_o}\right)^2 - 1}{\left(\frac{P_i}{P_o}\right)^3 - 1} \quad (3.6)$$

where, P_i and P_o are inlet and outlet pressures respectively.

In IGC, there are two methods of dispersive surface energy calculation have been commonly used are Dorris-Gray and Schultz methods. Different values had been obtained, with the larger value coming from the Doris-Gray method compared to Schultz method (Shi *et al.*, 2002). The dispersive surface energy can be calculated from the adsorption free energy of the probes, ΔG^{ads} which can be calculated by the following equation 3.7. Thus:

$$\Delta G^{ads} = -RT \cdot \ln V_N + C \quad (3.7)$$

where, R is a universal gas constant, T is the temperature of the column, V_N is a net retention volume of the n -alkane probes with the carbon number, n , and C is a constant, depending on the reference state absorption.

Injection of polar probes into the column causes an interaction between dispersive and special interaction of molecules probes with the solid samples in the column. Thus, ΔG^{ads} is given by equation 2.8:

$$\Delta G^{ads} = \Delta G^{DP} + \Delta G^{SP} \quad (3.8)$$

Where ΔG^{DP} is a dispersive interactions while ΔG^{SP} is a special interactions.

The dispersive surface energy is calculated by using Fowkes equation which takes into consideration the work of adhesion and the dispersive component

of surface energy of solid and the probes. This can be obtained from equation 3.9, thus;

$$RT \ln V_N = 2N_A \cdot a \cdot \sqrt{\gamma_S^d} \cdot \sqrt{\gamma_L^d} + C \quad (3.9)$$

Where a is surface area of the probe molecule and γ_S^d and γ_L^d are the dispersive surface energy of solid and probe molecules, respectively. From equation (3.9), a graph of $RT \ln V_N$ versus $a \cdot \sqrt{\gamma_L^d}$ can be plotted (figure 3.1).

The dispersive surface energy can be calculated from the slope of the graph, i.e. $2N_A \sqrt{\gamma_S^d}$.

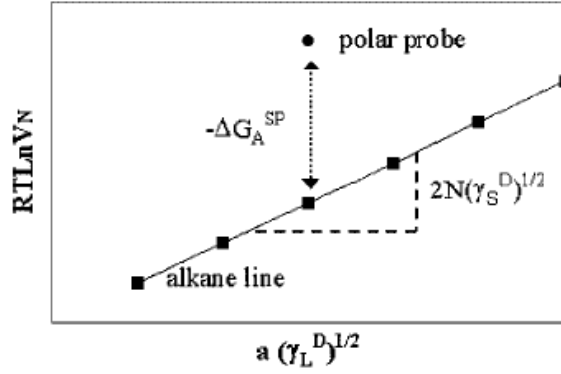


Figure 3.1: Schematic representation of a $RT \ln V_N$ versus $a \cdot \sqrt{\gamma_L^d}$ plot for n -alkanes and polar probes. (Grimsey et al., 2002)

The vertical distance between polar probe and the n -alkane line represents the specific polar component of the free energy of adsorption of the powder (ΔG_A^{SP}). Plotting ΔG_A^{SP} at different temperatures allows the specific enthalpy (ΔH^{SP}) and the specific entropy (ΔS^{SP}) of adsorption to be calculated as shown in the following expression:

$$(\Delta G_A^{SP}) = (\Delta H^{SP}) - T(\Delta S^{SP}) \quad (3.10)$$

However, measuring the free energy of adsorption at different temperatures always give very small effects to the entropy, therefore the entropy effects can be ignored (Telko & Hickey, 2007). Therefore,

$$\Delta G_A^{SP} = \Delta H^{SP} \quad (3.11)$$

Acid-base properties of the surface energy of solid particles can be obtained by using Gutmann's equation (Comte, *et al.*, 2005), thus:

$$-\Delta H_A^{SP} = K_B AN^* + K_A \cdot DN \quad (3.12)$$

Where ΔG is the specific interaction adsorption surface energy of solid particle,

K_A is the acidity value of solid particle,

K_B is the basicity value of solid particle,

AN^* is the acceptor number, and

DN is the donor number

The determination of acid-base properties in the surface energy determination is important to understand the surface properties of particles. The interaction of electron acceptors and donors (Lewis acid-base) gives information on the acidity and basicity of the solid particles (Panzer and Schreiber, 1992, Donnet *et al.*, 1991). Furthermore, the calculation of surface energy and acid-base interactions of particles, determines the surface thermodynamic properties of solid particles (Chehimi *et al.*, 1995). From previous studies it is now known that the morphology of the substrate materials has a significant effect on the surface energy determination of the crystal. Storey carried out experimental work using several ibuprofen crystals that were recrystallised in different solvents; hexane, acetonitrile and methanol which produced different shaped crystals. This, in turn, was found to change the dispersive surface energy due to the different intermolecular interactions involved for the different surface chemistries of the crystal habit faces (Storey, 1997). The IGC has also been used for thermal analysis and has been shown to give highly accurate results as it has been found to be very sensitive to changes in the relative humidity of the probe vapours. These changes of relative humidity have been changed the surface energy

of solid particles. As the relative humidity increased, the surface energies were found to decrease. This is was found to be consistent with the adsorbed water molecules competing for the same sites as the probes decreasing their interaction with the surface (Sunkersett *et al.*, 2001). To demonstrate that IGC gives the accurate vapour sorption results, a comparison study between isothermal microcalorimetry and IGC was carried out (Buckton *et al.*, 1999). In this, three samples of saquinavir mesylate an anti-viral drug at different drying conditions was used to determine the dispersive surface energies and the water sorption of the samples. As both methods were found to be highly accurate in terms of measuring the changes between samples that IGC can be as good as isothermal calorimetry in terms of its sensitivity even when small changes in the sample occurred.

3.2.2 Dynamic Vapour Sorption

Besides IGC, this work showed an alternative approach to study the sorption isotherm for solid particles is dynamic vapour sorption (DVS). DVS has been developed from gravimetric techniques and measures how much a sample adsorbs and desorbs water vapour. In a similar to IGC, DVS is also widely used in fine and a powder industry due to the very sensitive measurements it provides only requires 1-100 mg of sample. Sorption isotherm analysis is mainly used to characterise solid-vapor interactions. It measures the vapour absorbed or desorbed to and from the samples as a function of vapour pressure (Smith *et al.*, 2004). In water sorption analysis, three methods have been used; (i) the weighing bottle and salt solution method, (ii) the gravimetric method, (iii) the volumetric method (McLaren & Rowen, 1951).

The weighing bottle and salt solution method is the oldest technique. However, the sensitivity of this technique is low and it can take a long time to reach the equilibrium state because of the gases interference in the system and the associated inaccuracies that need to be eliminated. In DVS, the gravimetric method is used in which a high sensitive microbalance is used to

weigh the sample. Because of high sensitivity, it gives high accuracy and also gives rapid results (Williams & Levoguer, 2006). This technique is widely used in the polymer, food, pharmaceutical, building materials industries etc. In pharmaceutical processing, it is very important to measure the water sorption isotherms of the powders because of the concern of bioavailability of the pharmaceutical products when administered to the human body and also their tendency to changes in their polymorphic form during the storage. For example, after the spray drying process in drugs formulation, the stability of the products in absorbing water must be observed (Tzannis and Prestrelski, 1998). During the processing of pharmaceutical solids, the amorphous materials may be produced which will affect the products stability and producibility. This is because amorphous materials are highly unstable due to the random arrangement of molecules. Thus, DVS can also be used to determine the amorphous content in the drugs powder (Mackin *et al.*, 2002), (Columbano *et al.*, 2002). In amorphous materials the glass transition temperature, T_g , is important which is the starting temperature for crystalline materials to change to the amorphous state or vice versa. Thus, it is important to know the T_g for pharmaceutical compounds that easily transform in amorphous form state. Such a study had been carried out on amorphous lactose to determine its T_g , thus enabling the effective control over the crystallization process to prevent the formation of the amorphous phase (Buckton & Darcy, 1996).

3.3 X-ray Techniques

3.3.1 X-Ray Diffraction

X-ray diffraction (XRD) is a technique to determine the structure of the matter. It gives information on molecular packing in the unit cell, coordinates of each atom and intermolecular interactions. Including this information, the orientation of the crystal can also be determined using this technique. As in real crystal products, most of the crystals have defects, thus, by using XRD, defects in crystal can also be characterised. It can also determine whether

the solid is in the crystal or amorphous form. There are two types of popular XRD techniques that have been used, powder XRD and single crystal XRD. In powder XRD, powdered sample is used, with a large number of crystallites. An X-ray beam is impinged on the powder sample, which will diffract and produce diffraction planes with different angles depend on the crystal orientation, size and strain. As the particle size decreases, the peak width becomes larger due to the decrease in destructive interference close to the Bragg angles associated with the increase in surface to bulk ratio of the particle. Powder XRD can also be used to determine the existence of polymorphs within a sample. Each polymorph has a different crystal structure with different atomic positions, size and shape, thus, the diffraction patterns of each will be different. However, the result of powder XRD is not as precise as in single crystal XRD, where it is possible to obtain more structural detail including bond lengths and angles. In a similar manner to powder XRD, in single crystal XRD, the X-ray beams is impinged on the sample, however, in this case, only one single crystal would be used for examination by the beam with the sample being rotated to select different crystal planes for diffraction.

In XRD, electromagnetic radiation waves are used. The electromagnetic radiation accelerates in a vacuum very close with the velocity of light. The energy produced by the moving charged particles or electrons are called photons in an electric field, E . The vectors electric field and magnetic field, H , are both orthogonal to the direction of wave propagation (figure 3.2). As the wave is incident on the atoms in the crystal lattice, it scatters the X-ray waves in all directions. As a result, the X-ray waves give a diffraction pattern dependent on the crystal structure and interplanar spacing, d , of the lattice. The interplanar spacing is dependent on the lattice parameters, a , b , and c of the unit cell. The electromagnetic radiation is measured by energy, E , wavelength, λ or frequency, ν . All these parameters are related each other in the equation 3.13 and 3.14:

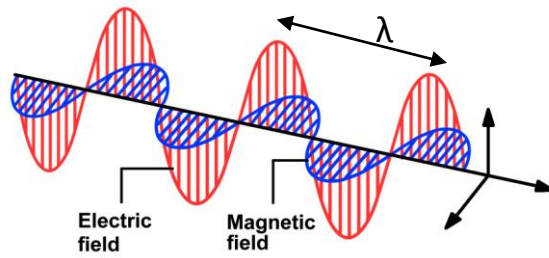


Figure 3.2: Propagation of an electromagnetic wave consisting of cojoined electrical and magnetic waves (<http://mysite.du.edu/~lconyers/SERDP>)

$$\lambda = \frac{c}{\nu} \quad (3.13)$$

$$E = h\nu \quad (3.14)$$

where c is a speed of light, and h is a Planck's constant (4.135×10^{-15} eV.s). By combining both equations, the energy can be obtained by expression in equation 3.15,

$$E = \frac{hc}{\lambda} \quad (3.15)$$

X-ray radiation energy is not necessarily calculated in Joules, J, as often it is calculated in electron volts in which $1\text{eV} = 1.602 \times 10^{-19}$ J. To calculate the wavelength with knowing the selected energy, it can be expressed by;

$$\lambda = \frac{hc}{eV} = 12398/V \quad (3.16)$$

From equation (3.16), the minimum value for the wavelength can be obtained by the function of the voltage accelerating the electrons. In general, the range of X-ray wavelengths is between the ultraviolet region and the region of γ -rays emitted by radioactive substances. The wavelengths usually used in crystallography generally range between $0.4 - 2.5\text{\AA}$.

In crystal diffraction analysis, Bragg's Law is applied. The X-ray diffraction intensity patterns are produced from the diffraction of the X-ray beam to the Bragg's plane of the sample (Doyle *et al.*, 1988). The incident and diffracted X-rays fulfilling Bragg's law are shown in figure 3.3:

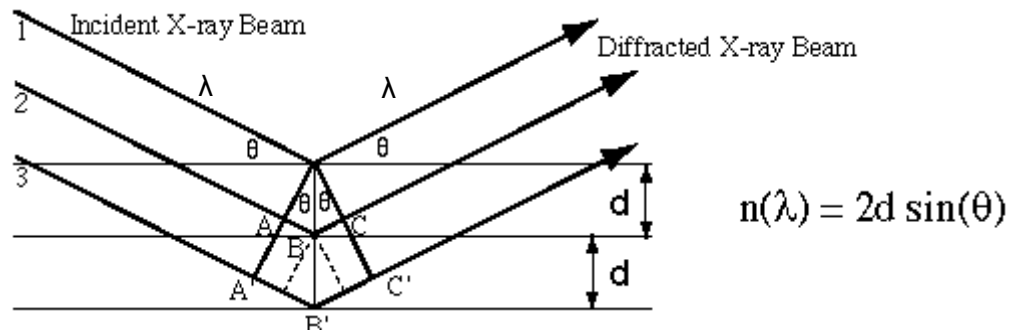


Figure 3.3: Diagram of incident wavelength of Bragg's plane (Analytical Chemistry Instrumentation Distance Education, 2009)

$$n\lambda = 2d_{hkl} \sin\theta \quad (3.17)$$

In which n is an integer, λ is the wavelength of the incident wave, d is the plane spacing and θ is the scattering angle of the diffraction wavelength to be measured. The diffraction result is collected on the X-ray detector as in figure 3.4 below:

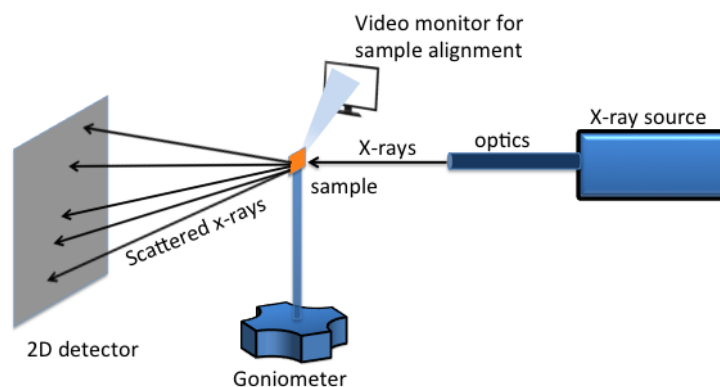


Figure 3.4: Schematic diagram of XRD. (Adapted from B. B. He, U. Preckwinkel, and K. L. Smith, *Advances in X-ray Analysis*, 2000, **43**, 273)

3.3.1.1 Single Crystal X-ray Diffraction

Single XRD gives more detailed information about the crystal structure including bond lengths, bond angles, and details of site ordering. It can also determine the cation-anion coordination in the molecular structure of crystals. It is also possible to obtain structures of the high temperature and pressure and also low temperature phases of crystals using dedicated environmental equipment. These methods are widely used in chemical and biological research for understanding of the molecular conformation of substances. In biological research, diffraction analysis is commonly used for the determination of protein crystal structures (Owen and Garman, 2005). There are three basic elements in the equipment for single crystal XRD experiments:

- (i) X-ray tube (source)
- (ii) a sample holder
- (iii) X-ray detector

An X-ray tube is the main element of the XRD equipment, used to generate the X-rays. It is generally a cathode X-ray tube, where the electrons are generated when they have sufficient energy to be dislodged from an inner shell by heating the filament in the tube and accelerating the electrons to a target material by applying a voltage. Molybdenum, Mo is the most common target material used to produce monochromatic K_{α} radiation for diffraction. In normal laboratory XRD, only a discrete number of possible wavelengths can be selected for experimental use. This is one of the differences between normal laboratory X-ray generators and synchrotron radiation X-ray source (Giacovazzo *et al.*, 2002). A 3- or 4-circle goniometer is commonly used in single crystal diffractometer. Generally, the sample is mounted on a thin glass fibre which is attached to the goniometer which allows rotation within the collimated X-ray beam. The diffraction that is satisfied by the Bragg equation will be measured at the X-ray detector. From the diffracted X-rays, the diffraction pattern and the crystal orientation can be related to each other. Figure 3.5 shows the relationship between crystal orientation and the diffraction pattern.

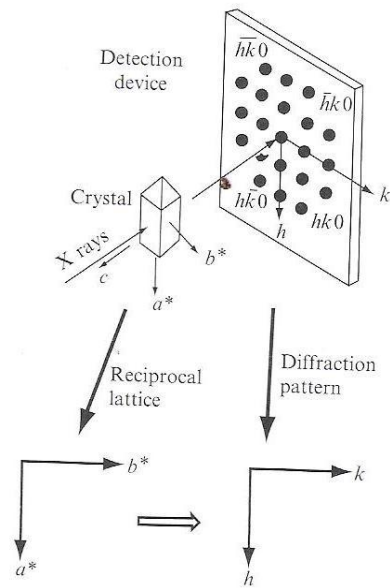


Figure 3.5: The relationship between the crystal orientation and the diffraction pattern (Glusker & Trueblood, 2010)

3.3.1.2 Reciprocal Lattice

In figure 3.5, the diffraction pattern of the crystal is the relative orientation of reciprocal lattice. The reciprocal lattice is denoted as a^* , b^* and c^* . From the figure above, the indexed diffraction patterns, h and k are respect to a^* and b^* . The reciprocal lattice is derived from the Fourier transform of the direct lattice (Ashcroft & Mermin, 1976). It is perpendicular to the crystal lattice. The reciprocal lattice point, (hkl) is at a distance of $1/d_{hkl}$ (from the direct beam at origin (000) and perpendicular to the distance between the (hkl) lattice planes (figure 3.6(a)). The importance of reciprocal lattice in crystal diffraction is to show that the arrangement of diffraction patterns on the lattice is reciprocal to the structure arrangement on the given lattice (figure 3.6(b)).

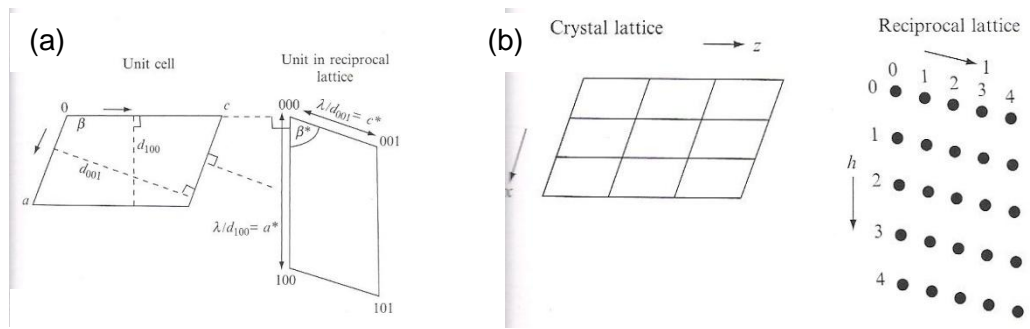
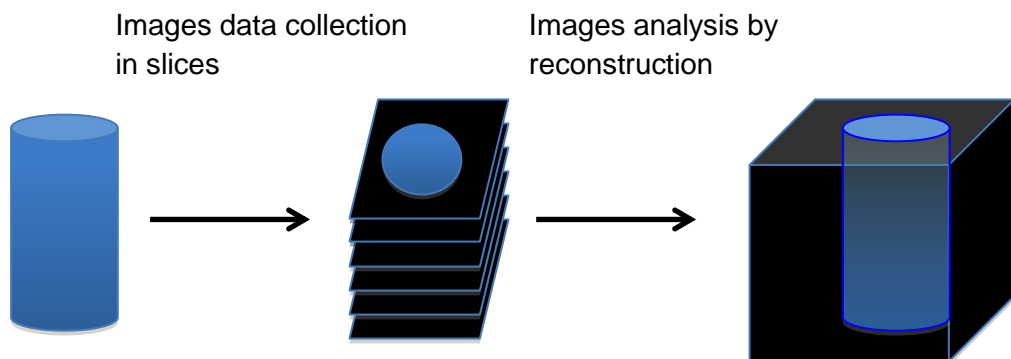


Figure 3.6: Diagram of (a) diffraction patterns from two-dimensional arrays (b) relationship between crystal lattice and reciprocal lattice (Shmueli, 2007).

Many XRD studies have been used to determine the internal structure of the crystal and this technique has been widely used in many areas that involved small particles (Korsunsky *et al.*, 2011).

3.3.2 X-Ray Tomography

Tomography is a method for imaging an object by creating cross-sectional of 3-dimensional (3D) objects. It is a non-destructive method to create a virtual model of material in 3D without destroying the original image. Figure 3.7 shows an example of the tomography method.



Real object Slice of images from tomography 3D image obtained from reconstruction

Figure 3.7: An example of tomography method by slicing the object into several sections and obtained 3D image from reconstruction of the slice images.

This technique is widely used in medicine as a computed-tomography (CT) scan for bone imaging, tumour imaging and infant imaging (Davis & Wong, 1996, Beckman *et al.*, 1999). It is also used in geology to determine the porosity of the soil, space study of meteorites (Ebel & Rivers, 2007), food industries, and electronic industries. The advantage of this technique is that it is possible for the high intensity of the light to penetrate the dense objects. The effect of cracks and voids in carbon/carbon composites which are used in the aerospace industry also use X-ray tomography (XMT) to visualise the microcracking in the samples (Paris *et al.*, 2001). The images that are obtained from the projection of the light will be reconstructed using algorithms to get a clear or structural shape of the particles. Some software can be used for the image analysis. ImageJ is used to define the region of interest of the images obtained from the raw data (Collin, 2007), filter and threshold for reducing noise and determine a pixel and produce the binary image. The image analysis can be carried out by mathematical analysis, Landis & Keane, (2010) reviewed these analytical methods. In tomographic reconstruction mathematics, the information is obtained from two-dimensional absorption of light images and it is reconstructed to produce a three-dimensional digital image. The absorption of light is an algorithmic function of how the materials absorbed the light and the distance through which the light must travel.

3.3.3 Synchrotron Radiation

Synchrotron radiation (SR) is a technique that generates high electromagnetic radiation energy (Ivanenko & Pomeranchuk, 1944) by accelerating electrons that are moving along a bending magnetic field that causes the electron beam to travel in a circular path. Synchrotron light is one type of Radio Frequency (RF) accelerator, in which the electric field is not static but oscillates at some frequency. The first discovery of synchrotron light occurred from the experimental observation that the light observed from 70MeV with a small spot but bright light visibly can be seen from the output machine (Elder *et al.*, 1947).

3.3.3.1 Development of Synchrotron Radiation Source

- **First Generation of Storage Rings**

In the earliest development of synchrotron radiation, the first generation of synchrotron radiation sources was a development of electron storage rings, which is an important part of the synchrotron radiation source because the electrons accelerate in this medium (Bilderback *et al.*, 2005). However, in the earliest work, it was operated in a parasitic mode, primarily for high energy physics research. The first major development of storage rings to be dedicated to synchrotron radiation was developed at the University of Wisconsin called Tantalus I, with 3.45 m diameter of storage ring, 8 bending magnets had been used, producing 240MeV electron energy with 10 beamlines. This enabled some of the early pioneering research into synchrotron radiation studies to be carried out. The synchrotron beam circulated continuously with repeated sequences of injection, acceleration, and extraction up to 50 Hz. The synchrotron radiation source provided high flux, high beam stability and a reduced radiation hazard (Rowe & Mills, 1973).

- **Second Generation of Storage Rings**

In the second generation storage rings, dedicated synchrotron sources were designed and were used in various applications. Large numbers of beamlines and experimental stations has been produced to serve many users. However, bending magnets were still the main source of electron beam acceleration the electrons for producing the SR light.

- **Third Generation of Storage Rings**

In synchrotron radiation light sources, the high flux alone was not felt to be sufficient as many synchrotron radiation studies relied on the brightness of the light. The brightness is defined as (3.18),

$$\text{Brightness} = \frac{\text{Number of photons produced in given times}}{\text{Source area} \times \text{Source divergence} \times \text{Spread of colours}} \quad (3.18)$$

To achieve high brightness, a large number of photons need to be produced in a given time and small area. A small area is produced by little beam divergence, and the photon energies also have to be concentrated. Therefore, to increase the brightness, the vertical slits are required to narrow the angular divergence; hence a smaller beam size is produced. A small beam size is necessary in a crystallography experiment when a sample of small crystals is used. It is beneficial to have a matching incident beam to the crystal size, whilst still maintaining the angular resolution for diffracted spots because it maximises the signal to noise ratio. Many developments had occurred from time to time to improve the light sources to ensure they give a high performance. The major improvement that had been done in third generation sources to achieve high brightness was by using insertion devices. These insertion devices are placed at the empty straight sections between the bending magnets in the storage rings. Along the trajectory path, insertion devices are placed that are arrays of magnets such as “undulators” and “wigglers” to produce the wiggling movement of electrons along the path that gives highly intense and tunable light. The insertion devices create a sinusoidal magnetic field, to force the particles to oscillate around the mean orbit. The light circulating the ring then travels into the beam lines in which the experiments are carried out. The wavelength of the synchrotron light that pass into the beam lines differ depending on the application and the requirements of the experiments. The tunable wavelengths allow the use of ultraviolet waves or soft or hard X-rays depending on the experiments to be carried out. Third generation synchrotrons have achieved a mature stage in which the high brightness and intensities of light have been produced effectively (Winick, 1998).

3.3.3.2 Overview of Synchrotron Radiation Source

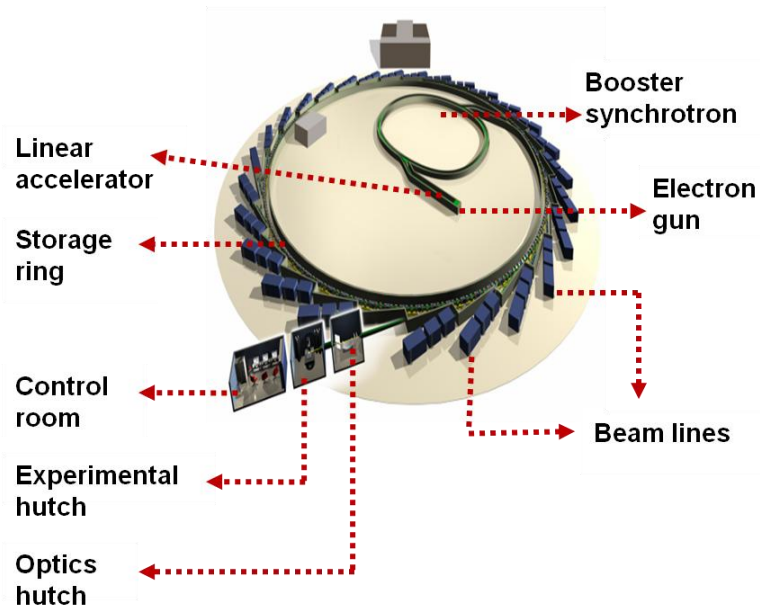


Figure 3.8: Schematic diagram of Synchrotron Radiation ring at Diamond Light Source.

In this thesis work the Diamond Light Source (DLS) was used to carry out the XRD experiments. Figure 3.8 shows the schematic diagram of the synchrotron ring at DLS. The main elements of synchrotron radiation facilities are the electron gun, linear accelerator, booster synchrotron, and synchrotron ring itself. The ring is not truly in a circular shape, but it is actually a multi-sided polygon. The electrons are generated in the electron gun, in which the electrons are produced using a high voltage cathode under vacuum then accelerated to about 90keV. The electrons are further accelerated using the first particle accelerator, the Linac to give extremely high energy at about 100MeV using radio frequency (RF) cavities. The second particle accelerator called the booster synchrotron helps the electrons to move in a circular track in which bending magnets are inserted to bend the electrons to ensure they move in right path. Here, the electrons are accelerated further to achieve of 3 GeV. The charged particles moving along a circular orbit emit electromagnetic radiation. The parameter of

interest to compare with different synchrotron source is the source size, which is how effective cross-section of the emitting particle beam, the beam, the beam emittance which is a constant along the particle path, and the divergence of the emitted X-ray beam (Giacovazzo, *et al.*, 2002). These beam lines guide the beams of light to the experimental stations. Each beam lines have 3 main parts:

- (1) Optics hutch
- (2) Experimental lab
- (3) Control cabin

In the optics hutch, the X-ray beam from the storage ring has the relevant energy selected and is then focused in this section towards the sample. The sample is placed in the experimental hutch on the goniometer, in which the beam interacts with the sample. The control cabin is the room where the experiments are controlled via computers that are connected to the equipment where data is collected from the experiment. There are many uses of synchrotron radiation. The beam lines support experiments such as diffraction, imaging and spectroscopy with different wavelengths depending on the type of experiments that are carried out. Synchrotron radiation single crystal XRD has been widely used in many areas to determine the crystal structures and confirmation of the lattice parameters such as in the mineralogy processing industry (Pluth *et al.*, 1997), in biology to find complex protein crystal structures (Cusack *et al.*, 1998) and also in the pharmaceutical industry to determine the small molecules of pharmaceutical drug crystals (Sharff and Jhoti, 2003). In the pharmaceutical industry, the determination of the shape of the particles using X-ray tomography has become a major interest to be studied since it is important to understand the effect of surface/surface interactions between particles on the performance of the powder after it has processed.

3.4 Closing Remarks

This chapter has described about the theoretical principles of the methods used in this research including the surface characterization using IGC, DVS, X-ray diffraction and tomography, and the technology of synchrotron radiation.

References

1. Analytical Chemistry Instrumentation Distance Education, Chemical Instrumentation Facility, *Department of Chemistry, IOWA State University*,(2009):<http://www.acide.chem.iastate.edu/xrd/high%20school/xrd012006.htm>
2. Ashcroft, N.W., Mermin, N.D., (1976). *Solid State Physics. Holt, Rinehart and Winston*, New York.
3. Beckman, F. Heise, K., Kolsch, B., Bonse, U., Rajewsky, M.F., Bartscher, M., Biermann, T., (1999). Three-dimensional of Nerve Tissue by X-ray Phase-Contrast Microtomography. *Biophys. J.* (76) 98-102.
4. Bilderback, D.H., Elleaume, P., Weckert, E., (2005). Review of Third and Next Generation Synchrotron Light Sources. *J. Phys. B: At. Mol. Opt. Phys.* (38) S773-S797.
5. Boutboul, A., Lenfant, F., Giampaoli, P., Feigenbaum, A., Ducruet, V., (2002). Use of Inverse Gas Chromatography to Determine Thermodynamic Parameters of Aroma-Starch Interactions. *J. Chromatogr A.* (969) 9-16.
6. Buckton, G., Darcy, P., (1996). Water Mobility in Amorphous Lactose below and Close to the Glass Transition Temperature. *Int. J. Pharm.* (136) 141-146.

7. Buckton, G., Dove, J.W., Davies, P., (1999). Isothermal Microcalorimetry and Inverse Gas Chromatography to Study Small Changes in Powder Surface Properties. *Int. J. Pharm.* (193) 13-19.
8. Chehimi, M., Lascelles, S., Armes, P., (1995). Characterisation of Surface Thermodynamic Properties of p-Toluene Sulfonate-doped Polypyrrole by Inverse Gas Chromatography. *Chromatographia.* (41) 671-677.
9. Collin, T.J, 2007. Image for Microscopy. *BioTechniques.* 43, 25-30.
10. Columbano, A., Buckton, G., Wikeley, P., (2002). A Study of the Crystallisation of Amorphous Salbutamol Sulphate using Water Wapour Sorption and Near Infrared Spectroscopy. *Int. J. Pharm.* (237) 71-178.
11. Comte, S., Calvet, R., Dodds, J.A., Balard, H., (2005). Surface Properties of Low Specific Surface Powders using Inverse Gas Chromatography. *Powder Technol.* (157) 39-47.
12. Cusack, S., Belrhali, H., Bram, A., Burghammer, M., Perrakis, A. & Riekkel, C., (1998). Small is Beautiful: Protein Micro-crystallography. *Nat. Struct. Biol.* 634-637.
13. Das, S.C., Larson, I., Morton, D.A.V., Stewart, P.J., (2011). Determination of the Polar and Total Surface Energy Distributions of Particulates by Inverse Gas Chromatography. *Langmuir Letter.* (27) 521-523.
14. Davis, G.R., Wong, F.S.L., (1996). X-ray Microtomography of Bones and Teeth. *Physiol. Meas.* (17) 121-146.
15. Demertzis, P.G., Kontominas, M.G., (1989). Water Binding on Egg Powders by Inverse Gas Chromatography–Water Cluster–Analysis. *Lebensmittel-Wissenschaft Technol.* (22) 228-232.
16. Donnet, J.B., Park, S.J., Balard, H., (1991). Evaluation of Specific Interactions of Solid Surfaces by Inverse Gas Chromatography: A New Approach Based on Polarizability of the Probes. *Chromatographia.* (31) 434-440.
17. Dove, J.W., Buckton, G., Doherty, C., (1996). A Comparison of Two Contact Angle Measurement Methods and Inverse Gas

- Chromatography to Assess the Surface Energies of Theophylline and Caffeine. *Int. J. Pharm.* (138) 199-206.
18. Doyle, S., Roberts, K.J., Sherwood, J.N., Clark, S.M., (1988). Application of Synchrotron Radiation Energy Dispersive Diffraction to the In-Situ Observation of Wax Crystallisation from Solution. *J. Cryst. Growth.* (88) 306-310.
 19. Dunstan, D., White, L.R., (1986). A Capillary Pressure Method for Measurement of Contact Angles in Powders and Porous Media. *J. Colloid Interface Sci.* (111) 60 – 64.
 20. Ebel, D.S., Rivers, M.L., (2007). Meteorite 3-D Synchrotron Microtomography: Methods and Applications. *Meteoritics & Planetary Science.* (42) 1627-1646.
 21. Elder, F.R., Gurewitsch, A.M., Langmuir, R.V., Pollock, H.C., (1947). A 70 MeV Synchrotron. *J. Appl. Phys.* (18) 810.
 22. Gerson, A.R., (2008). 3D-microdiffraction. A Facility for the Australian Synchrotron. *Current Appl. Phys.* (8) 463-466.
 23. Giacovazzo, C., Monaco, H.L., Artioli, G., Viterbo, D., Ferraris, G., Gilli, G., Zanotti, G., Catti, M., (2002). Fundamental of Crystallography, Second ed. *IUCr, Oxford Science Publications.*
 24. Glusker, J.P., Trueblood, K.N., (2010). Crystal Structure Analysis, A Primer, 3rd Ed. *IUCr, Oxford Science Publications.*
 25. Grimsey, I.M., Feeley, J.C., York, P., (2002). Analysis of the Surface Energy of Pharmaceutical Powders by Inverse Gas Chromatography. *J. Pharm. Sci.* (91) 571-583.
 26. Heertjes, P.M., Smet, E.C., Witvoet, W.C., (1971). The Determination of Interfacial Tensions with the Wilhelmy Plate Method. *Chem. Eng. Sci.* (26) 1479 – 1480.
 27. Hooton, J.C., German, C.S., Davies, M.C., Roberts, C.J., (2006). A Comparison of Morphology and Surface Energy Characteristics of Sulfathiazole Polymorphs Based Upon Single Particle Studies. *European J. Pharm. Sci.* (28) 315-324.
 28. Huu-Phouc, N., Luu, R.P.T., Munafo, A., Ruelle, P., Namtran, H., Buchmann, M., Kesselring, U.W., (1986). Experimentally Optimized

- Determination of Partial Solubility Parameters of Lactose by Gas-Solid Chromatography. *J. Pharm. Sci.* (75) 68-72.
29. Ivanenko, D., Pomeranchuk, I., (1944). On the Maximal Energy Attainable in Betatron. *Phys. Rev.* (60) 53.
 30. Korsunsky, A.M., Hofmann, F., Abbey, B., Song, X., Belnoue, J.P., Mocuta, C., Dolbnya, I., (2012). Analysis of the internal structure and lattice (mis)orientation in individual grains of deformed nickel polycrystals by synchrotron X-ray micro-diffraction and microscopy. *Int. J. Fatigue.* (42) 1-13.
 31. Landis, E.N., Keane, D.T., (2010). X-Ray microtomography, *Mater. Charact.* 61, 1305-1316.
 32. Mackin, L., Zanon, R., Park, J.M., Foster, K., Opalenik, H., Demonte, M. (2002). Quantification of Low Levels (10%) of Amorphous Content in Micronised Active Batches Using Dynamic Vapour Sorption and Isothermal Microcalorimetry. *Int. J. of Pharm.* (231) 227-236.
 33. McLaren, A.D., Rowen, J.W., (1951). Sorption of Water Vapor by Proteins and Polymers: A Review. *J. Polym. Sci.* VIII, 289-324.
 34. Nizhenko, V.I., Eremenko, V.N., Sklyarenko, L.I., (1965). Application of the Sessile Drop Method to the Determination of the Surface Energy and Density of the Liquids Wetting of the Backing Material. *Soviet Powder Metallurgy and Metal Ceramics.* (4) 463 – 466.
 35. Owen, R.L., Garman, E., (2005). A New Method for Predetermining the Diffraction Quality of Protein Crystals: Using SOAP as a Selection Tool. *Acta Crystallogr. D.* (61) 13-140.
 36. Panzer, U., Schreiber, H.P., (1992). On the Evaluation of Surface Interactions by Inverse Gas Chromatography. *Macromolecules.* (25) 3633-3637.
 37. Paris, O., Peterlik, H., Loidl, D., Rau, C., Weitkamp, T., (2001). Microcracks in Carbon/Carbon Composites: A Microtomography Investigation using Synchrotron Radiation, *Mat. Res. Soc. Symp. Proc.* 678.
 38. Pluth, J.J., Smith, J.V., Pushcharovsky, D.Y., Semenov, E.I., Bram, A., Riekkel, C., Weber, H.P., Robert, W.B., (1997). Third-generation Synchrotron X-ray Diffraction of 6 μ m crystal of raite,

- $\approx \text{Na}_3\text{Mn}_3\text{Ti}_{0.25}\text{Si}_8\text{O}_{20}(\text{OH})_2 \cdot 10\text{H}_2\text{O}$, Opens Up New Chemistry and Physics of Low-temperature Minerals. *Proc. Natl. Acad. Sci. USA.* (94) 12263-12267.
39. Rowe, M.E., Mills, F.E., (1973). Tantalus I: A Dedicated Storage Ring Synchrotron Radiation Source. *Particle Accelerators* (4) 211-227.
 40. Rowe, R.C., (1989a). Binder–substrate interactions in granulation: a theoretical approach based on surface free energy and polarity. *Int. J. Pharm.* (52) 149–154.
 41. Sharff, A., Jhoti, H., (2003). High-throughput Crystallography to Enhance Drug Discovery. *Chem. Biol.* (7) 340-345.
 42. Shi, B., Wang, Y., Jia, L., (2002). Comparison of Dorris-Gray and Schultz methods for the calculation of surface dispersive free energy by inverse gas chromatography. *J. Chromatogr. A.* (1218) 860-862.
 43. Shmueli, U., (2007). Theories and Techniques of Crystal Structure Determination. *IUCr, Oxford Science Publications.*
 44. Smith, A.L., Mulligan, R.B., Shirazi, H.M, (2004). Determining the Effects of Vapor Sorption in Polymers with the Quartz Crystal Microbalance/Heat Conduction Calorimeter. *J. Polym. Sci., Part B. Polym. Phys.* (42) 3893-3906.
 45. Storey, R.A., (1997). The nucleation, growth, and solid state properties of particulate pharmaceuticals. *PhD Thesis, University of Bradford, UK.*
 46. Sunkersett, M.R., Grimsey, I.M., Doughty, S.W., Osborn, J.C., York, P., Rowe, R.C., (2001). The Changes in Surface Energetics with Relative Humidity of Carbamazepine and Paracetamol as measured by Inverse Gas Chromatography. *Eur. J. Pharm. Sci.* (13) 219-225.
 47. Tzannis, S.T., Prestrelski, S.J., (1999). Moisture Effects on Protein-Excipient Interactions in Spray-Dried Powders. Nature of Destabilizing Effects of Sucrose. *J. Pharm. Sci.* (88) 360-370.
 48. Thompson, A.C., Vaughan, D., (2001). X-ray Data Booklet. Center for X-ray Optics Advanced Light Source. Second ed. *Lawrence Berkeley National Laboratory, USA.*

49. Williams, D.R., Levoguer, C.L., (2006). The Characterisation of Pharmaceutical Materials by Dynamic Vapour Sorption. *Surface Measurement Systems Ltd*, UK.
50. Winick, H., (1994). Synchrotron Radiation Sources, A Primer. Series on Synchrotron Radiation Techniques and Applications. Vol.1. *World Scientific*, Singapore.
51. Winick, H., (1998). Fourth Generation of Synchrotron Radiation. *IEEE*.
52. Zisman, W.A., (1964). Relation of the Equilibrium Contact Angle to Liquid and Solid Constitution In: Contact Angle, Wettability, and Adhesion. *Adv. in Chemistry*, ACS, Washington.

CHAPTER IV

MATERIALS & METHODS

4.1 Introduction

This chapter describes the materials, experimental methods, instrumentation that has been used in this study. These relate to the research into understanding the morphological changes when impurities are added during the crystallisation of urea. In addition, the qualitative measurement of their surface properties using IGC and DVS reported in chapter 5 together with details concerning the molecular modelling techniques used to predict molecular interactions in the bulk crystals and crystal surfaces are described and explained. The chapter also describes methodologies used in respect of the X-ray microdiffraction and microtomography reported in chapter 6.

4.2 Materials

4.2.1 Urea

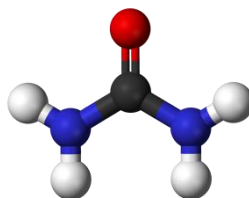


Figure 4.1: molecular structure of urea

Urea or carbamide ($\text{CH}_4\text{N}_2\text{O}$), molecular weight of 60.06 g/mol and density of 1.32g/cm^3 with 98% purity was purchased from Sigma Aldrich. Figure 4.1 shows the molecular structure of urea. Its melting point is 132°C (Zha *et al.*, 1995). It is an organic compound with two amide functional groups ($-\text{NH}_2$) joined by a carbonyl group ($\text{C}=\text{O}$). It has a tetragonal structure, ($P-42_1m$) with two molecules in the unit cell with dimensions $a = 5.565\text{\AA}$ and $c = 4.684\text{\AA}$ (Docherty, 1989). The nitrogen atoms make it very soluble in water with a solubility of 121g urea/100g water at 25°C (Lee and Lahti, 1972). The solubility of urea in alcoholic solvents and alcohol/water mixtures has been

reported by Rajalakshmi *et al.*, 1993, Geddes, 2003, and Lee & Lahti, 1972 who measure urea solubility in methanol, ethanol, isopropanol, water/methanol, water/ethanol, and water/isopropanol. The enthalpy of solution for urea was found to be mostly independent of the temperature and the concentration of urea (Kustov & Smirnova, 2010). In the agricultural industry, urea is commonly used as a fertiliser as it is a very convenient source of nitrogen. It is formed from the reaction of ammonia, NH_3 and carbon dioxide, CO_2 either in solid or liquid form. Figure 4.2 shows the morphology of urea crystals. Urea crystals recrystallised from an alcoholic solution form long needle-like shaped crystals, which agree well with the morphology prediction (Docherty, 1989). Urea crystals have a slow growing face at (110) face as shown in figure 4.2 but faster growing faces at $\{001\}$ and $\{111\}$. Previous research by Davey *et al.*, 1986 has shown the addition of biuret in urea may inhibit the growth of these fast growing faces.

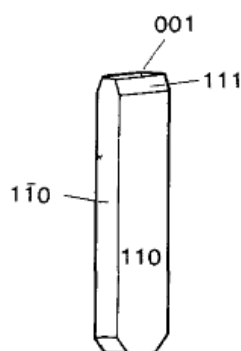


Figure 4.2: Morphology of urea showing the slower growing prismatic $\{110\}$ faces and the faster growing $\{111\}$ and $\{001\}$ faces (Davey *et al.*, 1986)

4.2.2 Biuret

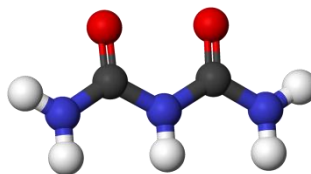
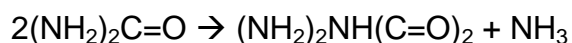


Figure 4.3: Molecular structure of biuret

Biuret is a decomposition product of urea, in which two molecules of urea combine together (as shown in figure 4.3) and release one molecule of ammonia, NH_3 , thus:



The decomposition of urea easily occurs as the melting point (132.7°C) of urea is close to its decomposition temperature (143.3°C). Thus, industrially it can be important to control the decomposition of urea because it leads to the release of ammonia which must be controlled because it can destroy not only plants, but is also harmful to animals. In the industrial crystallisation of urea, many experimental procedures have been patented to achieve higher yield of urea production and reduce the biuret content (Cook, 1964).

4.2.3 Aspirin

Acetylsalicylic acid or 2-(acetyloxy)-benzoic acid is commonly known as aspirin ($\text{C}_9\text{H}_8\text{O}_4$), molecular weight of 180.16g/mol with a density of 1.40g/cm^3 . It has a melting point of 135°C . This molecule has an acetyl group and a carboxyl group attached to the phenyl group (as shown in figure 4.4). It is a monoclinic structure, with $P2_1/c$ space group with unit cell parameters: $a = 11.233\text{ \AA}$, $b = 6.544\text{ \AA}$, $c = 11.231\text{ \AA}$, and $\beta = 95.890$ (Harrison *et al.*, 2002). It is an anti-inflammatory drug which is used to treat minor aches and

pains to rheumatic fever. It is also used to help prevent heart attacks, as it acts as a blood thinning agent.

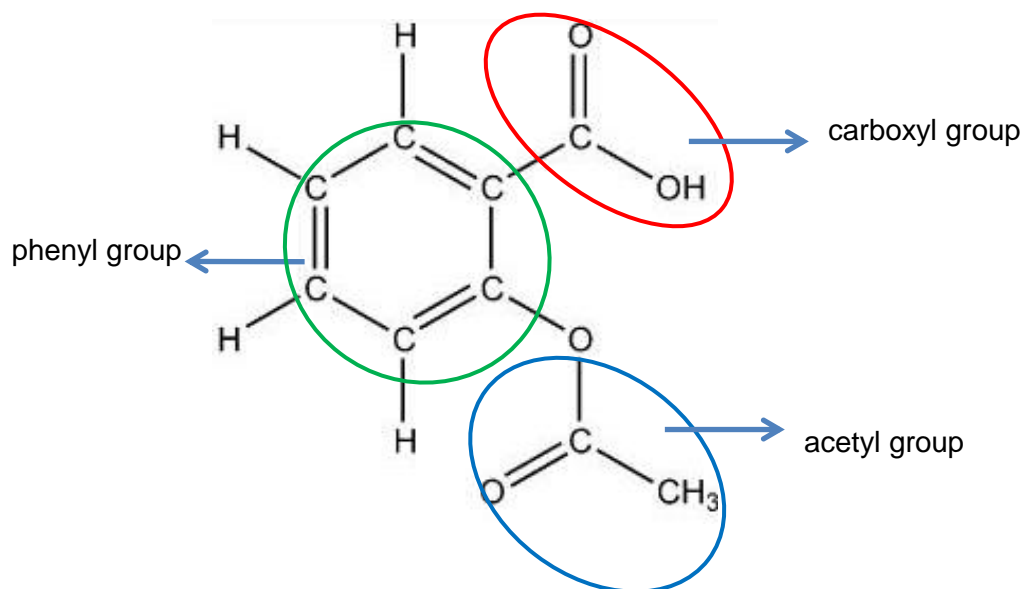


Figure 4.4: Molecular structure of aspirin. Red circle is a carboxyl group, green circle shows the phenyl group and blue circle is an acetyl group in aspirin molecule (Chemistry Matters)

In the crystallographic packing of aspirin the carboxylic groups of two aspirin molecules form a centro-symmetric dimer due to the hydrogen bonding between both carboxylic groups as shown in figure 4.5. No polymorphism has been convincingly shown to exist since Vishweshwar *et al.*, 2005 claimed there was a second polymorph of aspirin which could be obtained from the recrystallisation of aspirin from levetiracetam or acetamide solutions. However, Bond *et al.*, 2007, disputed this work and showed from their single crystal X-ray diffraction work that aspirin only formed one structure of polymorph. In this work, however the aspirin crystals were prepared from 38% v/v of a water-ethanol mixture that crystallised at 0.7°C/min.

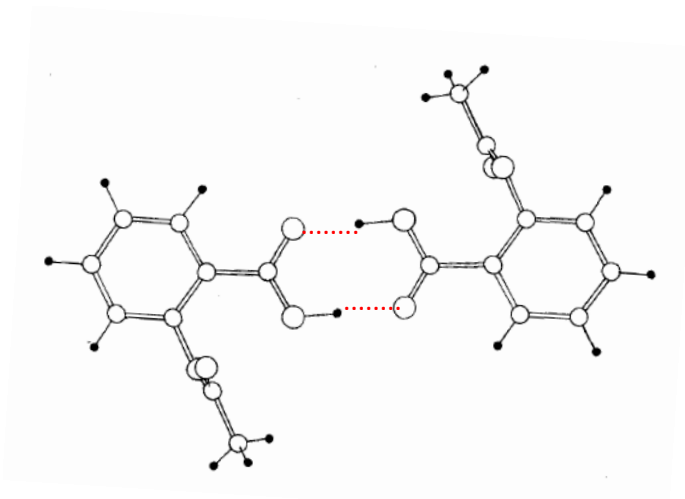


Figure 4.5: The formation of the aspirin-aspirin dimer due to hydrogen bonds between two carboxylic groups (Kim et al., 1985).

4.2.4 L-Glutamic Acid

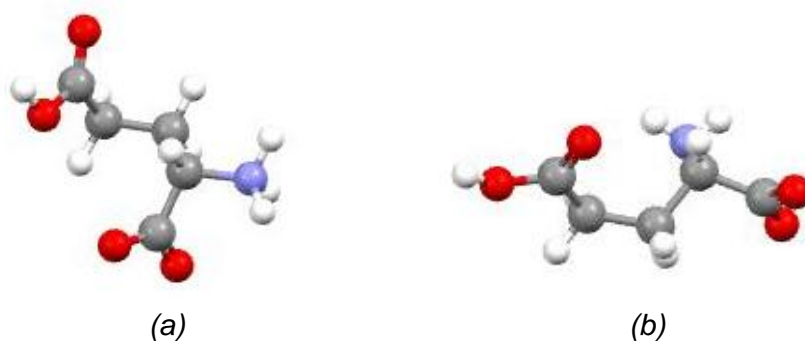


Figure 4.6: Molecular Structure of (a) α - and (b) β -L-glutamic acid

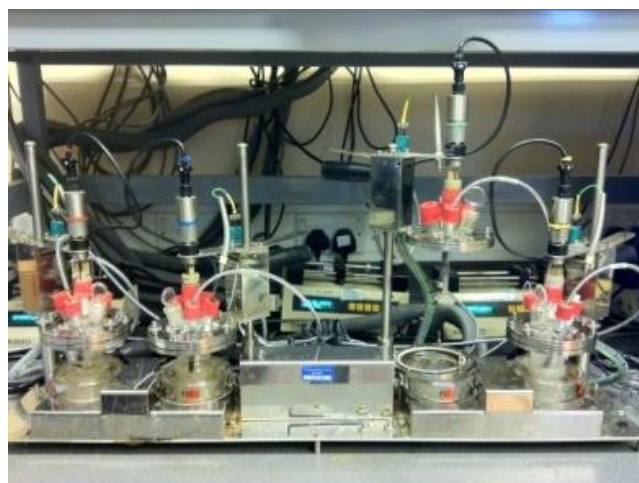
L-glutamic acid (LGA), ($C_5H_9NO_4$) has a molecular weight of 147.13g/mol and density of 1.46 g/cm^3 at 20°C . It is a non-essential amino acid. It is one of two amino acids that have a carboxylic acid group as a side chain. It is also known as glutamate as the carboxylic acid side chain can become protonated, thus giving the carboxyl group a negative charge. In the human body, this amino acids acts as neurotransmitter in which it helps nerve cells to receive information from and to other cells. LGA has two polymorphs, the

& β form, which are the metastable and stable form, respectively. Both polymorphs have orthorhombic $P2_12_12_1$ unit cells with $a = 10.282$, $b = 8.779$, and $c = 7.068$ for the α -form while for the β -form, the unit cell parameters are $a = 5.159$, $b = 17.30$, and $c = 6.948$ (Lehman *et al.*, 1972), (Lehman & Nunes, 1980). The stable β -form is needle-like in shape, while the metastable α -form is prismatic in shape. The α form can be produced by rapid cooling of the LGA recrystallised in aqueous solution. Heating up a saturated solution of LGA in water with some α form crystals present in the solution to 45°C will transform α to β -LGA (Kitamura, 1989).

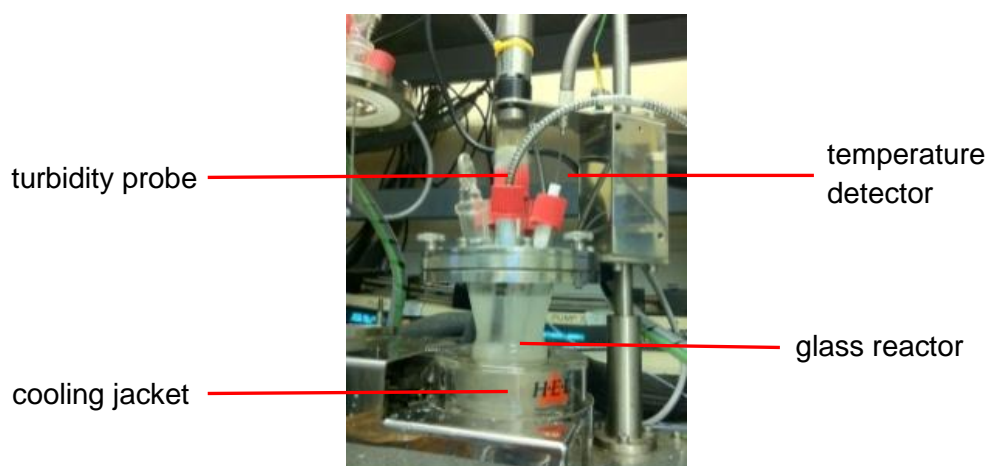
4.3 Experimental Methods

4.3.1 Crystallisation of Urea and Urea Modified by Biuret using AutoMATE crystalliser

The crystallisation experiment of urea was carried out by AutoMATE from HEL Ltd (as shown in figure 4.7). It is a crystalliser system consisting four jacketed reactors equipped with stirrer, temperature detectors and turbidity probes. All reactors can operate simultaneously with different conditions since each reactor temperature can be controlled independently. At first, two samples of urea were prepared and crystallised at a cooling rate of $0.1^\circ\text{C}/\text{min}$ and left overnight to observe the formation of urea crystals without and with biuret. 12g of urea was prepared in two glass flask reactors with a capacity of 100ml while 0.5g of biuret added in one of them. 100ml ethanol was used as a solvent to dissolve the samples. The solutions were heated up to 60°C to ensure all the solids dissolved and then cooled down to 35°C . Later, five sets of urea solutions were prepared with the same conditions as the previous sets, and crystallised at five different cooling rates (0.1, 0.25, 0.5, 0.75, and $1.0^\circ\text{C}/\text{min}$). Another five sets of samples were also prepared with the addition of biuret and five cooling rates.



(a)



(b)

Figure 4.7: the crystalliser system of AutoMATE (a) four parallel reactors (b) close-up image of a reactor showing the inlets for the turbidity probe, a glass stirrer, a temperature detector and a cooling jacket.

The crystallised samples were then filtered out from the reactor and dried in the oven at temperature of 60°C. The crystal samples were used for morphology characterization, surface energy analysis and water sorption effect measurements using Morphologi G3, Inverse Gas Chromatography and Dynamic Vapour Sorption respectively.

4.3.2 Particle Size & Shape Analysis using Morphologi G3

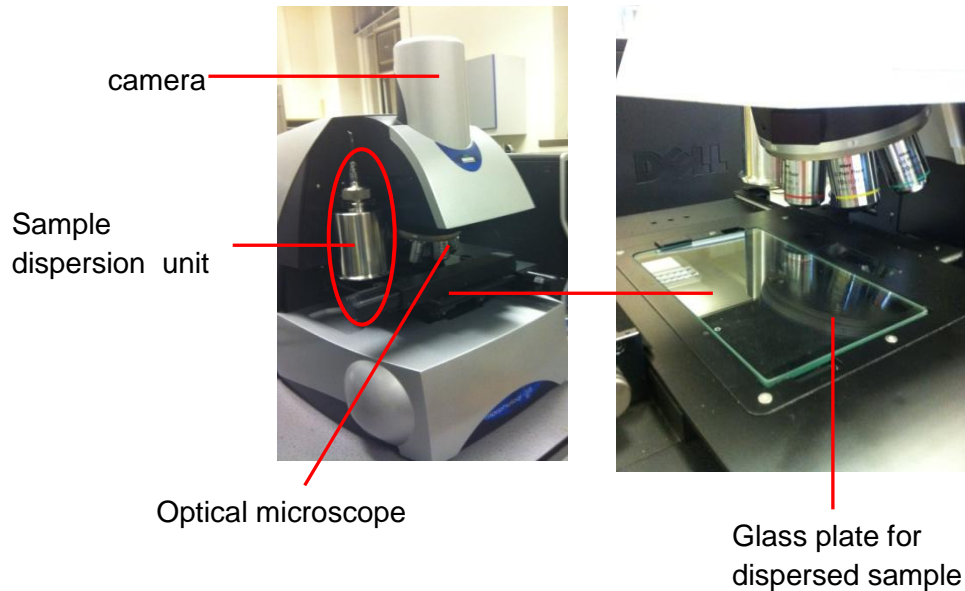


Figure 4.8: the Morphologi G3 Malvern Instrument Unit

The morphological characterisation of pure urea and urea modified by biuret crystals was analysed by using the Morphologi G3 (figure 4.8) from Malvern Instruments Ltd. The Morphologi G3 instrument consists of several main units:

- (1) Sample dispersion unit (SDU): - The SDU consists of two aluminium foils which cover the sample holder in the SDU. A nitrogen gas supply is applied to the foils to burst them and the sample to disperse on the sample holder.
- (2) Sample carrier holder: - Four slides and the SDU glass plates which the sample is placed on this carrier holder after it bursts.
- (3) Camera: - This is located at the top of the instrument and used to capture the particle images.
- (4) Optical Microscope: - it consists of 4 different objectives (5x, 10x, 20x, 50x) to look on the particles.

In this work, two methods in Morphologi G3 were used. First is the method of dry dispersion which explained above. Second, as the urea crystals were sticky and agglomerated, it was not suitable to use this dispersion method. In order to reduce the agglomeration, 3 mm³ samples were dispersed in 0.01% lecithin in a iso-octane mixture in a 5 ml vial which went through ultrasound vibration to ensure the samples did not agglomerate. 5x magnification of the optical microscope was chosen since the urea crystals were large (ca. 3mm) and can be observed by the naked eye.

4.3.3 Surface Energy Analysis by using Inverse Gas Chromatography

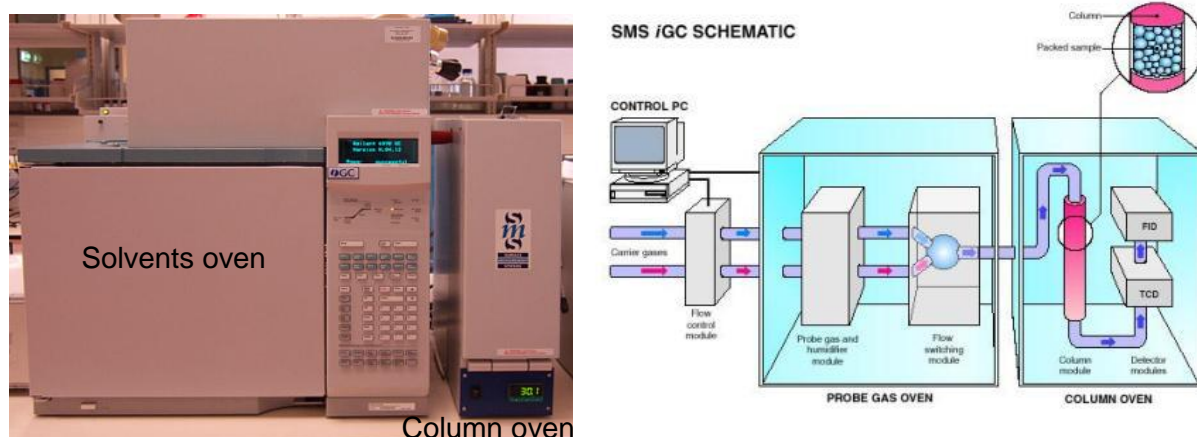


Figure 4.9: The Inverse Gas Chromatography Instrument from SMS Co. UK Ltd with solvent oven on the left and column oven on the right

The pure urea and urea modified by biuret crystals were packed in columns with 4mm I.D. and 300mm in length then placed in the column oven. The ends of the columns were plugged with glass wool. Helium and methane gas have been used as a carrier gas and for dead volume determination respectively. Nine probes were used as elutants which five of them are series of n-alkanes (octane, nonane, decane, undecane, dodecane) supplied by Fisher Scientific UK while the other four are polar probes for measuring polar surface energies (ethanol, 1-propanol, chloroform, 1,4-dioxane). A flame ionization detector (FID) was used to determine the retention times of

elutants and methane. The Dorris-Gray and Schultz approaches were used to determine surface energy determination. The surface energy calculations were calculated using SMS-iGC Analysis Macros (version 1.8). All the theories of calculations have been described in chapter 3. All the experiments were undertaken at 35°C and 0% relative humidity.

4.3.4 Water Sorption Isotherm Measurement using Dynamic Vapour Sorption

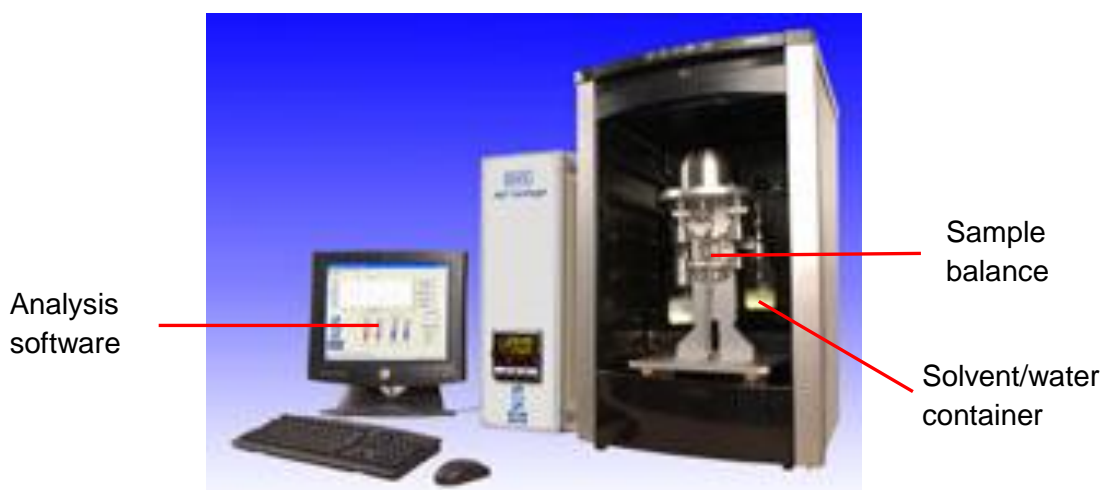


Figure 4.10: Dynamic Vapour Sorption Unit from Surface Measurement System Co. UK Ltd.

The quantification of water sorption effect to the surface layer of urea samples was measured by Dynamic Vapour Sorption (figure 4.10) using equipment obtained from Surface Measurement System Co. UK Ltd. The samples were weighed onto a sample cup in the range of 15-10 mg using Cahn D-200 ultra-sensitive recording microbalance. The microbalance was placed in a fully temperature controlled incubator with $\pm 0.1^{\circ}\text{C}$ temperature stability. Because it is very sensitive to sorption and desorption of moisture, and to avoid condensation of vapour occurring on the balance, a constant flow rate of dry gas was supplied to purge the balance head to ensure the baseline stability of the balance. A carrier gas, nitrogen, was used to

measure moisture uptake and loss at a specific relative humidity (RH) with pressure at about 1-2 bar. A rapid humidity ramping method to observe the water uptake and loss at a certain time in was used. The relative humidity ramped from 0-90%, at 10% per hour at 25°C for one full cycle. The data obtained were analysed using DVS Standard Analysis Suite version 4.3 which runs using Microsoft Excel.

4.3.5 X-Ray Microdiffraction (XMD) and X-Ray Microtomography (XMT) Analysis using Synchrotron Radiation

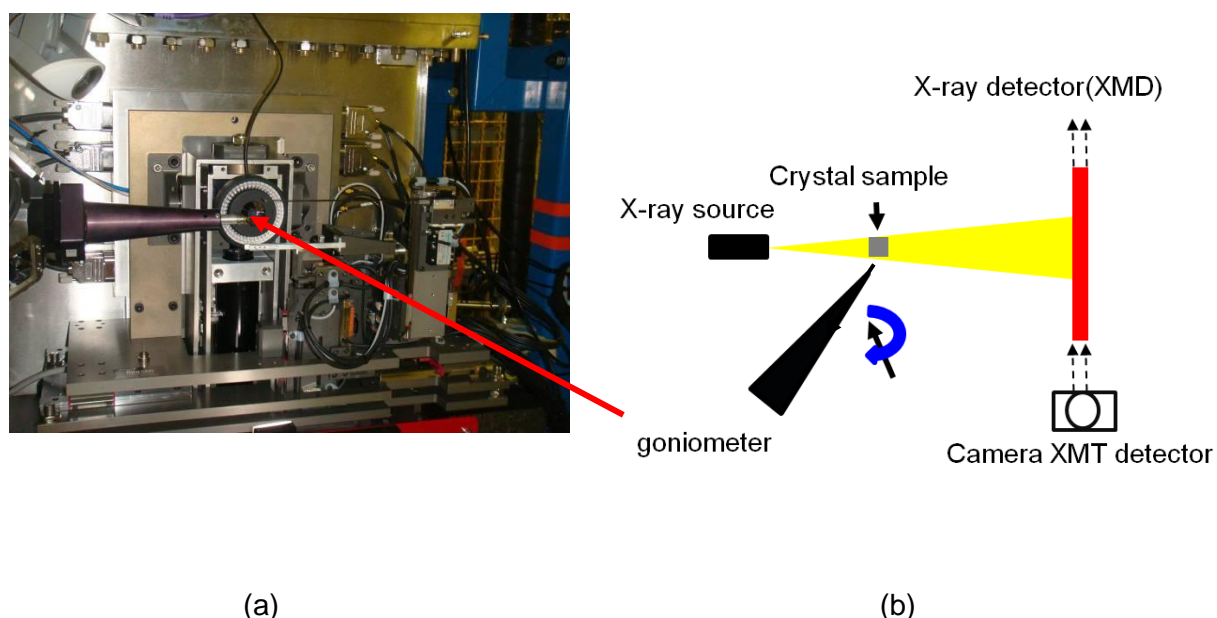


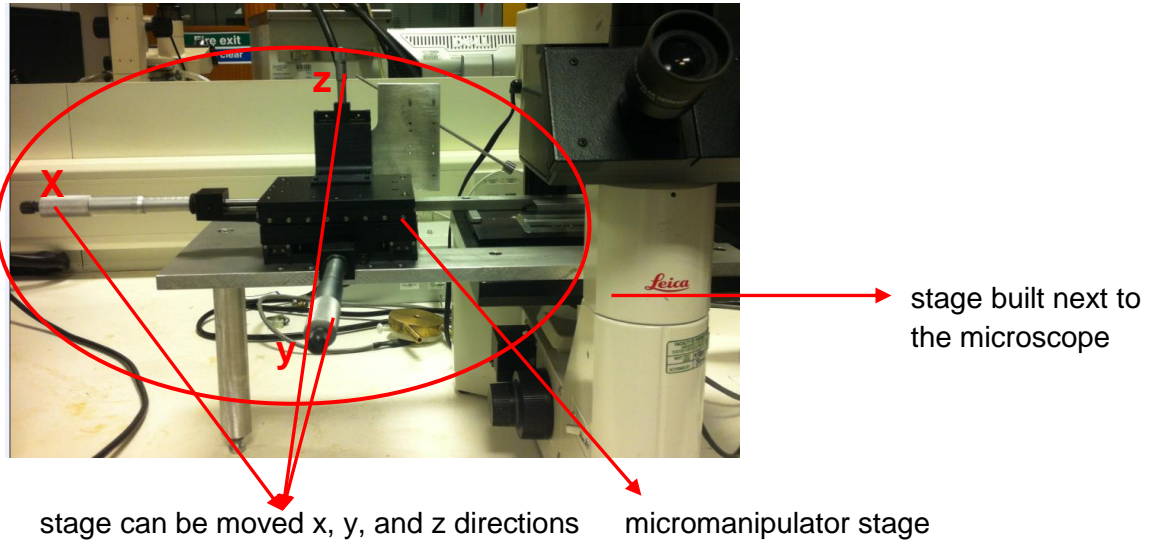
Figure 4.11: (a) Experimental hutch of beamline I24, (b) schematic diagram of XMD

Single crystals and agglomerated crystals for analysis by XMD were carried out at the Diamond Light Source Ltd, Diamond House, Didcot, Oxfordshire, UK at beamline I24 (Figure 4.11(a)) and its schematic diagram in figure 4.11(b). The I24 beamline is a tunable wavelength energy (6.4-25keV) undulator beamline with vertical and horizontal focusing mirrors to align the accelerating electrons from storage ring direct to the sample beam. The available wavelengths were in the range of 0.7-2.0Å. After several tests to choose the best wavelength to obtain good data collection, the suitable

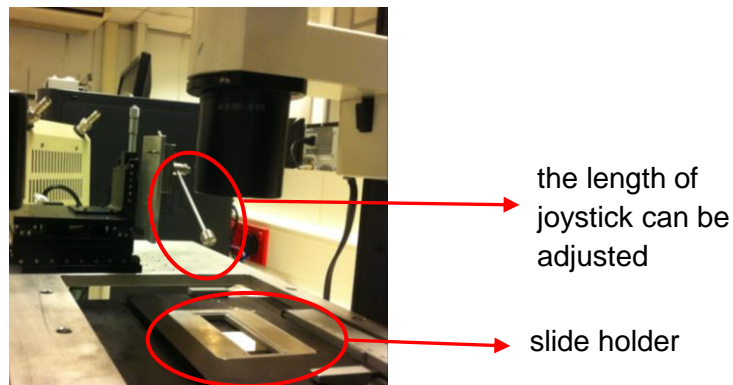
wavelength used was 0.5904. The sample was placed on the goniometer, which can be rotated through 360° with movable X, Y and Z directions. The rotation of the sample for the data collection depends on the position of the crystals that are attached together. This was to ensure that during data collections, there was no overlap of diffraction that occurs between the agglomerated samples. During data collections, each sample was rotated by a small angle, typically between 0.2° to 1.0°. In this work, after several tests to determine the best diffraction images, a 0.2° oscillation angle was selected. In this experiment, the energy was 21keV. All data collections were carried out at a temperature of 100K. This lower temperature was selected because the atoms in the crystal lattice are at their most stable condition.

4.3.5.1 Micromanipulator for Mounting Crystals

The development of the mounting crystals stage for single micron-sized single crystals was developed at IPSE laboratory, University of Leeds. The stage was integrated with a inverted optical microscope. In figure 4.12 (a), it shows the micromanipulator has three adjustable directions, x, y, and z. These adjustable three directions are to move the micromanipulator stage. The crystals placed on the slide holder (figure 4.12 (b)). In figure 4.12 (b) also shows the joystick in which the sample holder (figure 4.12) placed at the tip of the joystick. The length of the joystick can be adjusted depending on the location of the interested crystals to be picked up.



(a)



(b)

Figure 4.12: The stage developed for micromanipulator for mounting single crystals. (a) shows three adjustable directions for micromanipulator (b) adjustable joystick to pick up the selected crystals.

4.3.5.2 Sample preparation

Single and agglomerated crystals were picked under a microscope using a spine standard sample holder (with HamptonTM pin) with a goniometer mount (the magnet holds the sample holder on the goniometer) (figure 4.13). After the selection of crystals, the sample holder was mounted onto the goniometer head. To make sure the sample was placed at the centre of the

X-ray beam, the goniometer was adjusted x, y and z directions. This was adjusted remotely by the computerised program.

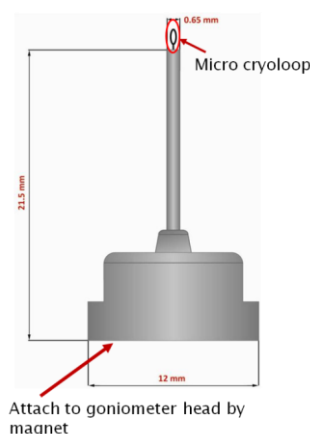


Figure 4.13: Sample holder for mounting crystal

4.3.5.3 Diffraction data Collection and Processing

The diffraction data were recorded on a Pilatus3 6M, (100Hz max. frame rate), a hybrid pixel detector from Dectris. The wavelength used in this work was 0.5904 Å with detector distance of 220mm. There are several software can be used to process the diffraction data for indexing and integrating to determine the space group and the unit cell parameters. In this work, as the samples were small molecules, the suitable softwares are X-ray Detector Software (XDS) (Kabsch, 2001) and Xprep (Bruker, 2004) for integrating and indexing of the diffraction data obtained from the crystal. The data obtained was refined using Shelx (Sheldrick, 2008), a process delivering the structure solution and refinement.

4.3.5.4 Calculation to Determine Unit Cell Constants of the Crystals

From the diffraction data, it gives information of the coordinates of unit cell axis a, b, and c. This information can be used to determine the unit cell parameters of crystals. Table 4.1 is the example of the unit cell axis information obtained from diffraction data of aspirin crystals.

Table 4.1: The coordinates of the unit cell axis for aspirin crystals.

Crystals \ Coordinates	x	y	z
Aspirin crystal			
unit cell a – axis	-2.239	9.240	-6.225
unit cell b – axis	-6.396	-1.544	0.009
unit cell c – axis	-1.230	5.156	10.109

The unit cell of a, b, and c is the basis vector of unrotated crystals along x, y, and z coordinates (Å) or called as orientation matrix of the crystals. From this information, unit cell parameters can be calculated. Generally unit cell parameter of crystal calculates from the square root of dot product of the vector:

$$\| a \| = \sqrt{(a \cdot a)} \quad (4.1)$$

From the general equation, the calculation for unit cell constants determination is followed the equation below:

$$\| a \| = \sqrt{(a^2 + b^2 + c^2)} \quad (4.2)$$

4.3.6 X-ray Microtomography Instrument

In X-ray Microtomography work, beamline I04 was used. The tomography camera was installed below the beam to capture the single rotation snapshots images of the crystal. The camera model is a pco 1600 (pco, Germany) integrated with advanced CCD (charge-coupled device). The CCD system is suitable for fluorescence imaging and microscopy. The camera is enabled to record images in 160MB/s with high resolution (1600x1200 pixels). The images were recorded in its software called pco camware. This experiment was carried out on I04 beamline.

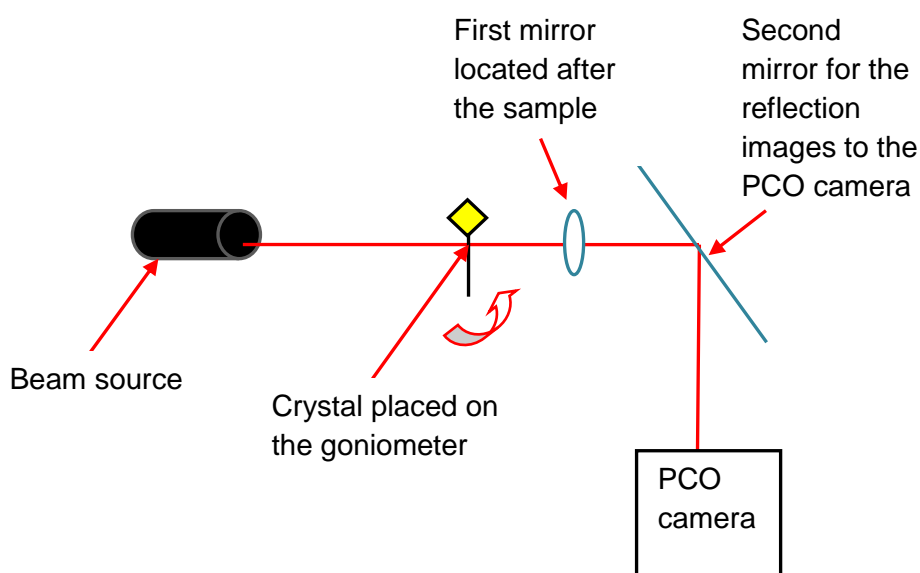


Figure 4.14: schematic diagram of XMT on I04 beamline

From the image captured by the camera, the images were analysed and processed using ImageJ (Ferreira & Rasband, 2012) and TomoJ (Messaoudil *et al.*, 2007). The reconstruction of the image gave the 3-dimensional (3D) view of the crystal and thus through this analysis the full 3D crystal shape was determined.

4.4 Computational Modelling Methods

4.4.1 Calculation of Intermolecular Interaction Using HABIT98 and Visual Habit

The HABIT98 (Clydesdale, *et al.*, 1998) were used to calculate the strength of intermolecular interactions and these were, in turn, used to predict the morphology of the urea crystals. Using this program, it calculates the energies of solid state crystallised particles. This program predicts the morphology of the crystal by using the Crystallographic Information File (CIF file) that can be obtained from Cambridge Structure Database (CSD). Based on this information, the program does not only consider the symmetry operations of the crystal, but it also calculates the energies between molecules based on the atomic charges calculated from quantum chemistry calculations. In HABIT98, bonded and non-bonded forces in molecules are used to calculate the energies of the structure. This program considers all inter-atomic interactions between molecules both within the unit cell and the extended lattice. These van der Waals interactions between each pair of non-bonded atoms involved both repulsion and attraction interactions and were calculated using either Lennard-Jones(Oobatake & Ooi, 1972) and Buckingham potentials (Buckingham, 1938). The electrostatic energy, also involving both repulsion and attraction interactions, was also taken into account to give a summation of the total atom-atom energy. The total interaction energy is calculated by defining the limiting radius of a sphere. In this study, the limiting radius was chosen to be 30Å. The summation of all the interaction energies is the lattice energy of the crystal (E_{latt}) which consists of the slice energy (E_{sl}) and attachment energy (E_{att}). The interaction of molecules that are close enough to the origin molecule considered to be inside a growth layer, or slice, of thickness d_{hkl} , in which hkl is the growth face, and attachment energy for molecules outside of this slice.

$$E_{latt} = E_{sl} + E_{att} \quad (4.3)$$

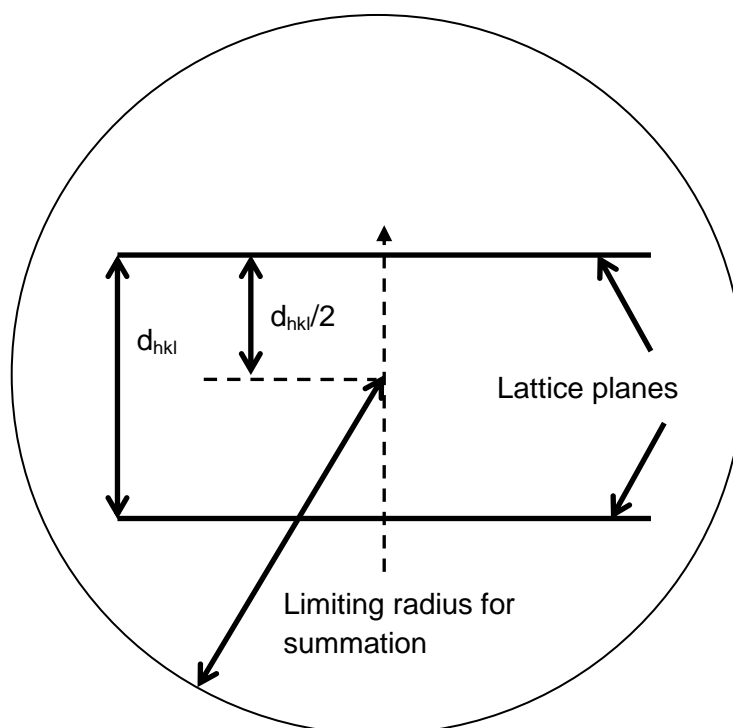


Figure 4.15: Limiting radius determination for lattice energy calculation

In HABIT98, the lattice energy can be calculated by choosing the lattice (LATT) mode, while to get information of the bonding analysis of atom-atom interactions, the FULL mode was chosen. However, for the urea crystals, because it is a polar molecule, to obtain attachment energy of each face of the crystal, the polar (POLR) mode was chosen. Details of HABIT98 program is in a manual by Clydesdale *et al.*, 1998. In prediction of the urea crystals, Lifson and Hagler force-field was used to calculate the lattice and attachment energies. Because of the polarity of the molecule, two charges have been used in order to calculate the attachment energy of the faces, which were bulk charges and isolated charges that the charges of incoming molecule to the growth layer. The charges obtained from Docherty, 1989, calculated again using Lifson & Hagler potential set and scaled charges for the isolated charges.

Visual Habit is the newer version of the HABIT98 program and one in the process of being integrated within the CCDC's materials Mercury module. It has been design to be more users friendly as it has an integrated ability to do visualisations of the crystal morphology. As in HABIT98, it calculates the attachment energy, which uses SHAPE program to visualise the morphology prediction based on the attachment energy values. However, there is a limitation for this software in that it currently only has few force-fields available to calculate the lattice energy, which Hagler force-field is not available for the calculation. Thus, in prediction of morphology of urea and urea modified by biuret, both morphologies were predicted by giving the input files with values of centre to face distance for each faces.

4.4.2 Charges Calculation

In this study, three types of determining urea charges were used to calculate the lattice energy of urea, and determine the most highest dispersive interactions contributed in the energy, in which in later calculation would be used for dispersive surface energy prediction. All the charges produced from MOPAC for three different Hamiltonian parameters (AM1, MNDO, and PM3), ab-initio quantum charges from CRYSTAL, and Hagler scaled charges.

4.4.3 Surface Energy Prediction

In surface energy prediction calculation, the surface energy, γ for each form (hkl) is calculated using equation 4.4. The attachment energy value obtained from HABIT98 calculation (Hammond, *et al.*, 2006).

$$\gamma_{hkl} = \left(\frac{Z \cdot E_{att} \cdot d_{hkl}}{2 \cdot N_A \cdot V_{cell}} \right) \quad (4.4)$$

Where γ_{hkl} is the surface energy of (hkl) face, (kcal/m²),
 E_{att} is the attachment energy of the (hkl) face, (kcal/mol),
 d_{hkl} is the interplanar spacing of (hkl) plane, (Å),
 Z is the number of molecule in unit cell,
 N_A is the Avogadro number, and
 V_{cell} is the cell volume of the crystal, m³

The total surface energy for the crystal was predicted from:

$$\gamma_{total} = \sum \gamma_{hkl} \cdot M \cdot SA \quad (4.5)$$

Where M is the multiplicity of the same form of the (hkl) faces and SA is the fractional surface area of the (hkl) face. The value of multiplicity, M, together with fractional surface area, SA, was calculated using Visual Habit. In order to determine respectively dispersive component of the surface energies and electrostatic energy of the crystal, the calculated values for the attachment energy were partitioned into their van der Waals (dispersive) and electrostatic (polar) components.

4.5 Closing Remarks

In this chapter, the materials and instruments used in this study were discussed. The description of materials which are urea, biuret, and aspirin were described. The methods used in preparation of the samples and the surface analytical techniques and development of X-ray diffraction and tomography methods also were described in detail. Additionally, the computational methods for morphology prediction using HABIT98 and Visual Habit and was described in this chapter.

References

32. Bond, A.D., Boese, R., Desiraju, G.R., (2007). On the Polymorphism of Aspirin. *Angew. Chem. Int. Ed.* (46) 615-617.
33. Bruker (2004). *APEX2, SAINT-Plus, XPREP and SADABS*. Bruker AXS Inc., Madison, Wisconsin, USA.
34. Buckingham, R.A., (1938). The Classical Equation of State of Gaseous Helium, Neon, and Argon. *Proc. R. Soc. Lond. A: Math., Phys. Eng. Sci.* (168) 264-283.
35. Clydesdale, G., Hammond, R.B., Roberts, K.J., Docherty, R., (1998). HABIT98 - A Program for Predicting the Morphology of Molecular Crystals as a Function of the Growth Environment. *Program Manual*.
36. Cook, L.H., (1964). Urea Crystallisation. *United States Patent Office*. 3124612.
37. Davey, R., Fila, W., Garside, J., (1986). The Influence of Biuret on the Growth Kinetics of Urea Crystals from Aqueous Solution. *J. Cryst. Growth.* (79) 607-613.
38. Docherty, R. (1989). Modelling the Morphology of Molecular Crystals. *Ph.D Thesis*, University of Strathclyde, Glasgow.
39. Docherty, R., Roberts, K.J., Saunders, V., Black, S., Davey, R.J., (1993). Theoretical Analysis of the Polar Morphology and Absolute Polarity of Crystalline Urea. *Faraday Discuss.* (95) 11-25.
40. Ferrari, E.S., Davey, R. J., (2004). Solution-Mediated Transformation of α -to β -L-glutamic acid: Rate Enhancement Due to Secondary Nucleation. *J. Cryst. Growth Des.* (4) 1061 – 1068.
41. Ferreira, T., Rasband, W., (2012). *ImageJ User Guide (Revised Edition)*.
42. Geddes, A., (2003). The Filtration and Drying Behaviour of Organic Crystals with Varied Morphologies following their Batch Crystallisation. *PhD Thesis*, University of Leeds.
43. Hammond, R.B., Pencheva, K., Roberts, K.J., (2006). A Structural-Kinetic Approach to Model Face-Specific Solution/Crystal Surface Energy Associated with the Crystallisation of Acetyl Salicylic Acid

- from Supersaturated Aqueous/Ethanol Solution. *J. Cryst. Growth Des.* (6) 1324-1334.
44. Hammond, R.B., Jeck, S., Ma, C.Y., Pencheva, K., Roberts, K.J., Auffret, T., (2009). An Examination of Binding Motifs Associated with Inter-Particle Interactions between Facetted Nano-Crystals of Acetylsalicylic Acid and Ascorbic Acid through the Application of Molecular Grid-Based Search Methods. *J. Pharm. Sci.* (98) 4589-4601.
45. Hammond, R.B., Pencheva, K., Roberts, K.J., (2007). Molecular Modeling of Crystal-Crystal Interactions Between the α - and β -L-glutamic acid Using Grid-Based Method. *J. Cryst. Growth Des.* (7) 875 -884.
46. Harrison, A., Ibberson, R., Robb, G., Wittaker, G., Wilson, C., Youngson, D., (2002). In-situ Neutron Diffraction Studies of Single Crystals and Powders during Microwave Irradiation. *Faraday Discuss.* (122) 363-379.
47. Kabsch, W. (2001). Chapter 25.2. 9 in International Tables for Crystallography, Volume F. *Crystallography of Biological Macromolecules*, (Rossmann, MG, and Arnold, E., eds) Kluwer Academic Publishers, Dordrecht, The Netherlands.
48. Kim, Y., Machida, K., Taga, T., Osaki, K., 1985. Structure Redetermination and Packing Analysis of Aspirin Crystal. *Chem. Pharm. Bull.* (33) 2641-2647.
49. Kitamura, M., (1989). Polymorphism in the Crystallisation of L-Glutamic Acid. *J. Cryst. Growth.* (96) 541-546.
50. Kustov, A.V., Smirnova, N.L., (2010). Temperature and Length Scale Dependence of Tetraalkylammonium Ion Solvation in Water, Formamide, and Ethylene Glycol. *J. Phys. Chem. B.* (115) 14551-14555.
51. Lee, F., Lahti, L.E., (1972). Solubility of Urea in Water-Alcohol Mixtures. *J. Chem. Eng. Data.* (17) 304-306.
52. Lehmann, M.S., Nunes, A.C., (1980). A short hydrogen bond between near identical carboxyl groups in the α - modification of L-glutamic acid. *Act. Crystallogr. B* (36) 1621-1625.

53. Messaoudil, C., Boudier, T., Sorzano, C.O.S., Marco, S., (2007). TomoJ: tomography software for three-dimensional reconstruction in transmission electron microscopy. *BMC Bioinformatics*. (8) 288.
54. Oobatake, M., Ooi, T., (1972). Determination of Energy Parameters in Lennard-Jones Potentials from Second Virial Coefficients. *Prog. Theor. Phys.* (48) 2132-2143.
55. Rajalakshmi, T., Dhanasekaran, R., Ramasamy, P., (1993). The Growth and Perfection of Urea Single Crystals from Solution. *J. Mater. Sci. Lett.* (12) 1797-1799.
56. Sheldrick, G.M., 2008. A short history of SHELX. *Acta Crystallogr. A*. (64) 112-122.
57. Vishweshwar, P., McMahon, J.A., Oliveira, M., Peterson, M.L., Zaworotko, M.J., (2005). The Predictably Elusive Form II of Aspirin. *J. Am. Chem. Soc.* (127) 16802-16803.
58. Zha, M., Franszosi, P., Zanotti, L., Zuccalli, G., Paorici, C., Capelletti, R., Razzetti, C., (1995). Crystal Growth and Characterisation of Urea by Physical Vapour Transport in Semi-open Cells. *J. Cryst. Growth*. (146) 29-36.

CHAPTER V

INFLUENCE OF CRYSTALLISATION ENVIRONMENT ON SURFACE PROPERTIES OF UREA

5.1 Introduction

This chapter discusses the results obtained from the crystallisation experiments for urea and the effect of biuret on the formation of the urea crystals. The aim is to understand how the addition of biuret molecules changes the urea morphology, and also how the solution cooling rate effect the size of particles. The analysis of the resultant size and shape using Morphologi G3 will be presented and discussed. The effect of morphology on surface energy of the urea and how this change for urea modified by the presence of biuret also will be presented, together with the characterisation of these materials propensity for water sorption using Dynamic Vapour Sorption (DVS). To understand and rationalise the experimental results, the molecular modelling work is used to predict crystal morphology and molecule to surface binding of solvents and biuret interactions were used. The work is integrated at the particle level through quantitative calculations of surface energy of each of the crystal faces present in crystal morphology.

5.2 Experimental Studies

5.2.1 Morphological Habit Measurement Using Morphologi G3

Urea has been chosen to be studied as it has unique characteristic, as it is a polar molecule, with different polarity at different ends. Crystallisation of urea itself in ethanol solvent without any additive expected to produce long needle-like crystal. However, the addition of biuret expected to change its morphology, hence, it is an interest to understand the effect of biuret on the morphology of urea, hence its surface properties, in this study is the surface energy and the potential of the crystals in the water adsorption. Here, in this experimental work, the differences of morphological habits as in size and shape of the crystals among all the samples sets were characterised using the Morphologi G3 instrument. The morphology differences between two

samples can be observed directly from the images obtained and indirectly following further data analysis from the distribution graphs of size and shape.

Figure 5.1 shows the images of particles taken from Morphologi G3 for the first set of samples, being unmodified urea and urea modified by biuret, crystallised at 0.1°C/min and left overnight.

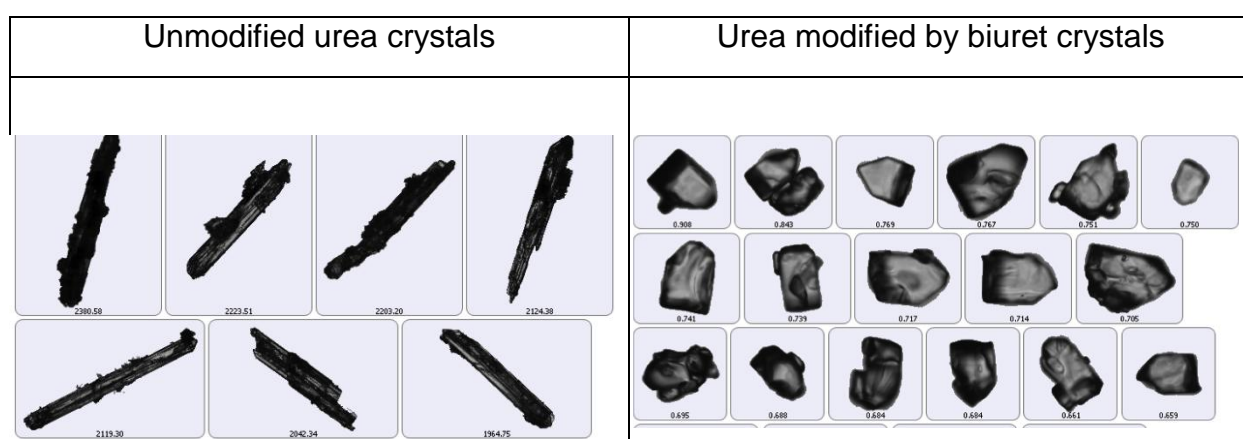


Figure 5.1: Images of some crystals of unmodified urea and urea modified by biuret crystals crystallised at 0.1°C/min left overnight taken from Morphologi G3.

In figure 5.1, the images show that the morphology of urea changed when biuret was added in urea solution from needle-like crystals to prismatic shape. The difference in shape can be quantified and expressed in terms of aspect ratio. The large changes in length and width are clearly observed. Thus, aspect ratio is the best parameter to explain the difference. In Morphologi G3, aspect ratio is defined as,

Aspect ratio = width / length, in which the value has to be in the range 0 to 1.

In the case of unmodified urea, the aspect ratio would be lower, (close to zero) while urea modified with biuret as it has bulkier shape, will have value

close to 1. It can be shown in the frequency and undersize curves comparing the aspect ratio of unmodified urea and urea modified by biuret in figure 5.2:

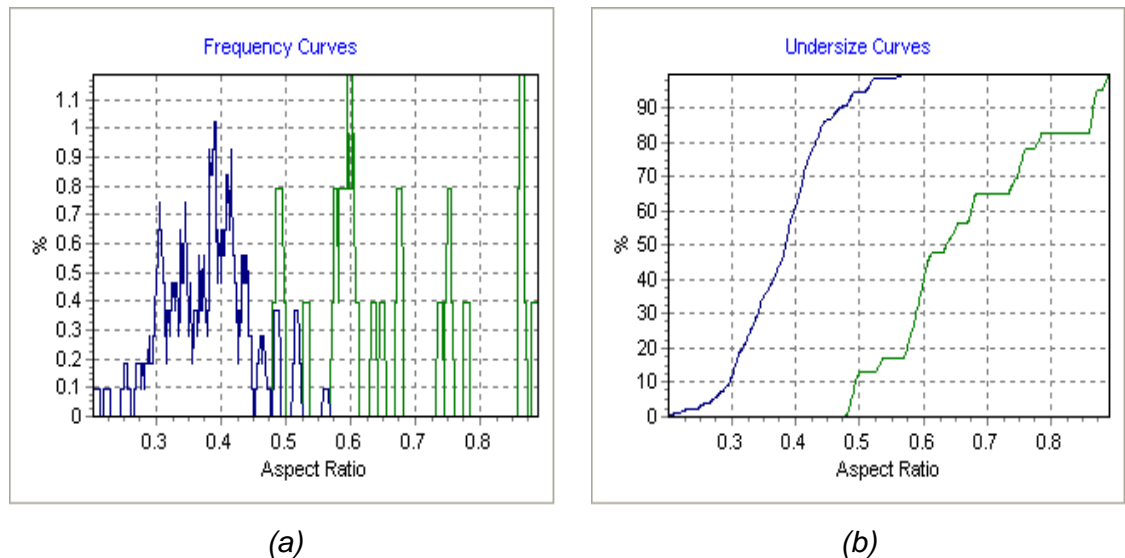


Figure 5.2: Graphs of (a) frequency curves and (b) undersize curves of unmodified urea and urea modified by biuret crystallised at $0.1^{\circ}\text{C}/\text{min}$ for aspect ratio (blue: unmodified urea, green: urea modified by biuret) Frequency curves represent the percent of distribution of particles and undersize curves represent the cumulative percent of distribution of particles.

In Figure 5.2, the graphs of frequency curves (a) represent the percent of distribution of particles and undersize curves (b) represent the cumulative percent of distribution of the particles. The x-axis for both graphs represents the aspect ratio of the particles while the y-axis represents the percentage of the particles. Here, the blue curve represents the unmodified urea while green curve represent urea modified by biuret. The results obtained were between hundreds number of particles. Both samples show the aspect ratio will be higher as the crystals become shorter. The curves show that unmodified urea has a low aspect ratio (in range of 0.3 to 0.5) and have the maximum number of percentage of distribution at 0.4, while urea modified by biuret lies between 0.5 and 1.0. The undersize curves also show that the cumulative distribution of the unmodified urea lies below 0.5 while urea modified by biuret above 0.5. This means unmodified urea has long crystals compared to urea modified by biuret which has a higher aspect ratio.

Later, the crystals were crystallised at different cooling rates to observe the effect of cooling rates on the crystals' formation. Figure 5.3 shows the data as a function of solution cooling rate associated with crystallisation at five different cooling rates (0.1, 0.25, 0.5, 0.75, and 1.0°C/min).

Cooling rates (°C/min)	Unmodified urea	Urea modified by biuret
0.1		
0.25		
0.5		
0.75		
1.0		

Figure 5.3: Crystal images of some of particles on samples of unmodified urea and urea modified at different cooling rate (the number displayed on the each single images is CE diameter number which just used for selection of single particle image)

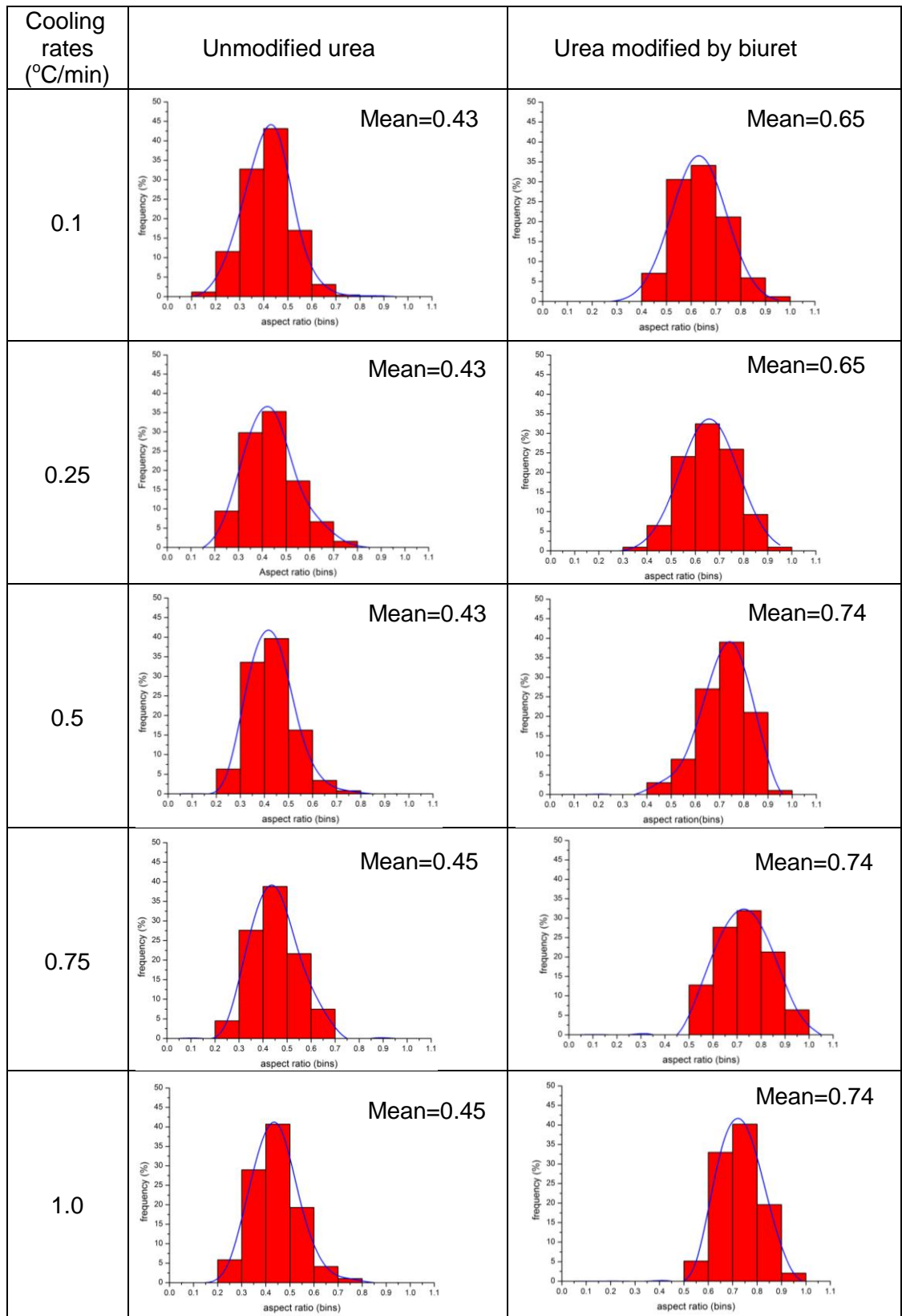


Figure 5.4: Particle size (aspect ratio) distribution of unmodified urea and urea modified by biuret at different cooling rates.

Figure 5.4 gives the distribution images of unmodified urea and urea modified by biuret crystals at different cooling rates, while figure 5.4 shows the histogram and distribution of the crystals at different cooling rates in term of aspect ratio. The x-axis represents the aspect ratio from 0 to 1, while y-axis represents the percentage of number of particles. In figure 5.3, the unmodified urea observed to have long needle-like crystals at all cooling rates, and prismatic shape can be observed for urea modified by biuret at all cooling rates. In unmodified urea crystals, the average aspect ratio for crystals crystallised at different cooling rates only 2% different which is 0.43 for 0.1, 0.25 and 0.5°C/min, while 0.45 for 0.75 and 1.0°C/min. In urea modified by biuret, the average aspect ratio value for 0.1 and 0.25°C/min is 0.65 while for 0.5, 0.75 and 1.0°C/min is 0.74. It is only 9% difference in which too small different of changes can be observed in different cooling rates of urea modified by biuret. This shows that cooling rates does not particularly influence the crystals morphology but it does impact on the size of the crystals. Figure 5.5 for unmodified urea supports the fact that the size changed at different cooling rates. The crystals produced at the slowest cooling rates grown larger (in length) between 225 up to more than 300µm whilst the length reduced when the crystals crystallised at higher cooling rates. It can be observed by looking at crystals that produced at 1.0°C/min which have length between 75 and 100µm. The effect of cooling rates happened to the growth rates of the crystals in which slower cooling rates produced larger crystals, while faster cooling rates produced smaller crystals.

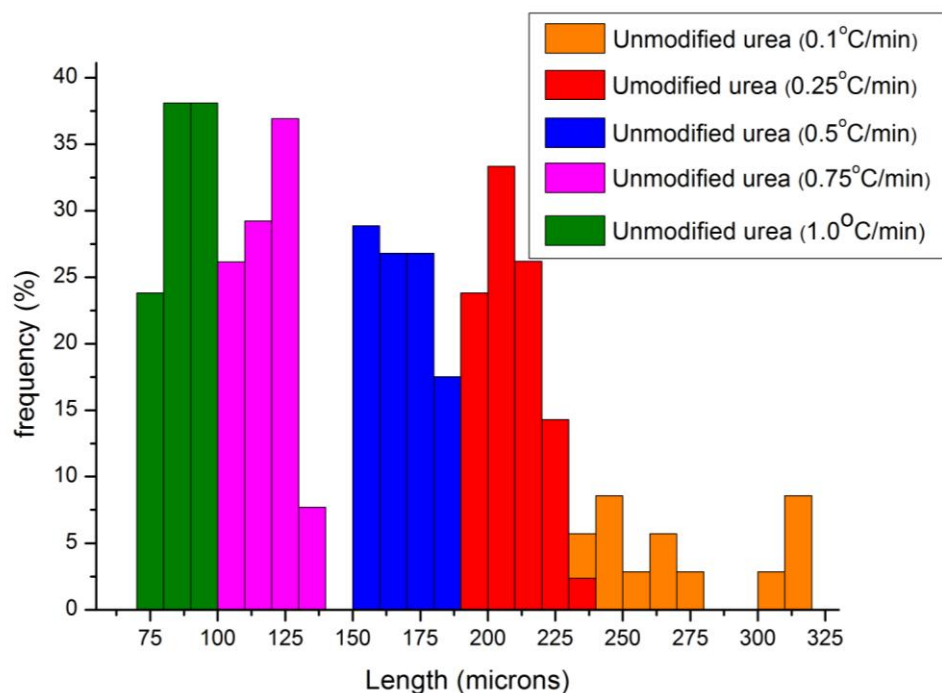


Figure 5.5: Distribution graph of unmodified urea at different cooling rate indicates that the length of the crystals decreasing at the faster cooling rates.

5.2.2 Surface Energy Analysis Study Using Inverse Gas Chromatography

The study of surface energies of urea and urea modified by biuret has been carried out using IGC using several organic solvents as probes in order to determine the dispersive surface energies of the samples. In the first case, sets of samples of unmodified urea and urea modified by biuret at 0.1°C/min which were left in the reactors overnight to undergo uncontrolled crystallisation were prepared. Each sample was measured three times to obtain reproducible results. The surface energy results obtained are tabulated in table 5.1:

Table 5.1: Surface energies calculation for set of urea samples crystallised at cooling rate of 0.1°C/min and left in the reactor overnight to undergo slow cooling crystallisation

Set	Set I (mJ/m ²)	
	Unmodified urea	Urea modified by biuret
Exp 1	41.43	47.60
Exp 2	41.23	44.22
Exp 3	40.23	46.19
Avg	40.96	46.00

In the above results, it shows that the dispersive surface energy of unmodified urea is lower than that for urea modified by biuret. The morphological changes of the crystals affected the dispersive surface energy (Thielmann, *et al.*, 2007). As the urea modified by biuret form prismatic shape, the total surface area of the crystals is increasing. It is because the increasing the surface area of {111}, which gives high contribution in dispersive surface energy due to more energetic sites of the crystals. While needle-like shape crystals have lower total surface area than prismatic shape, therefore less number of energetic sites of the crystals can be measured for the surface energy. In the second case, the surface energy analysis had been done for the sets of unmodified urea and urea modified by biuret at different cooling rates. The summary of the results obtained from inverse gas chromatography is tabulated in table 5.2.

Table 5.2: Summary of dispersive surface energy results for unmodified urea and urea modified by biuret at different cooling rates

Samples	Unmodified urea					Urea modified by biuret				
Cooling rates (°C/min)	0.1	0.25	0.5	0.75	1.0	0.1	0.25	0.5	0.75	1.0
Run 1	39.51	42.2	43.57	44.33	45.62	43.00	43.2	45.85	46.69	47.11
Run 2	40.79	42.18	43.78	44.47	45.32	42.28	43.72	45.07	46.67	47.35
Run 3	41.80	42.99	44.19	44.19	45.52	42.15	43.31	45.28	46.6	46.35
Avg Surface energy (mJ/m ²)	40.7	42.5	43.9	44.3	45.5	42.5	43.4	45.4	46.7	46.9

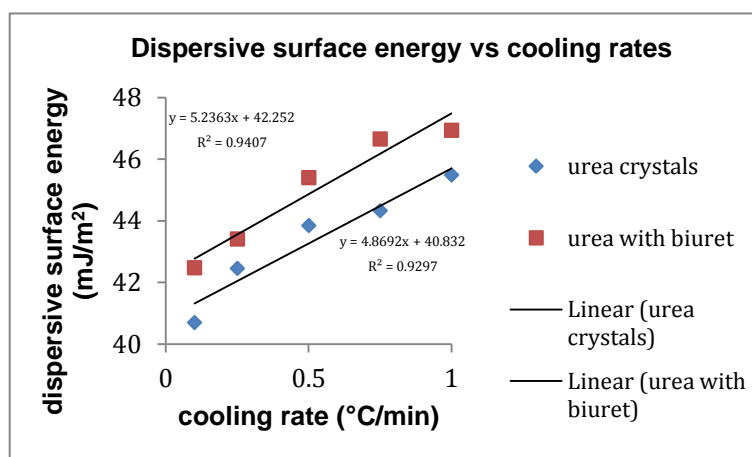


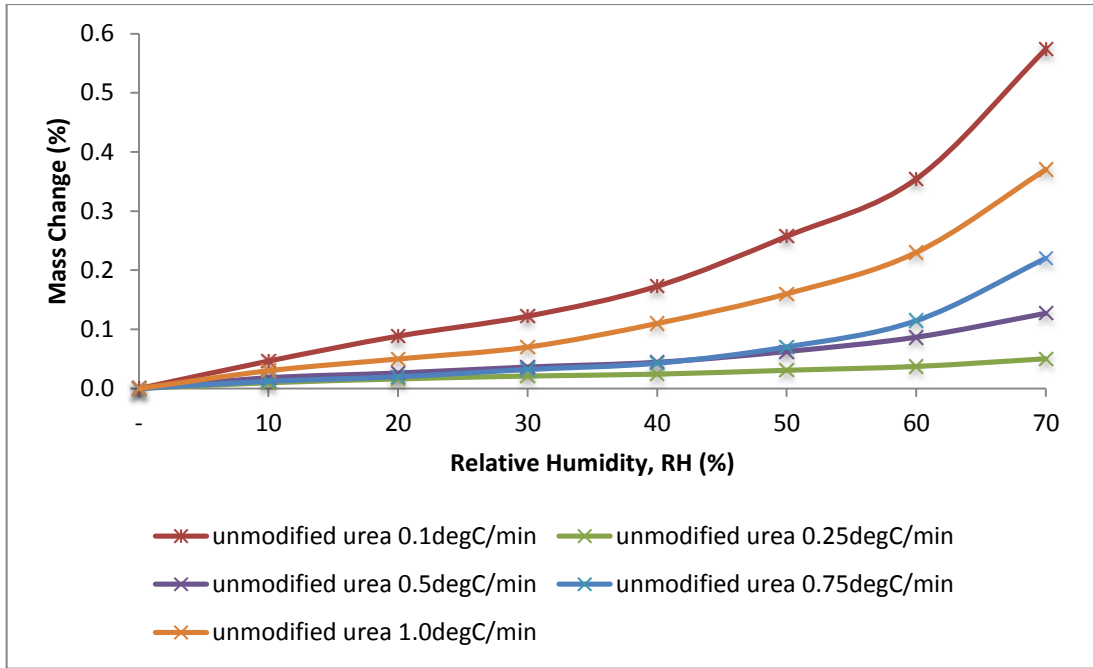
Figure 5.6: Dispersive surface energy plotted of unmodified urea and urea modified by biuret at different cooling rates.

The data presented in Table 5.2 and plotted as a graph in Figure 5.6, shows that increasing cooling rate for crystallisation to occur, the surface energy becomes higher. The same trend of increasing in surface energy can be observed for unmodified urea and urea modified by biuret samples. As

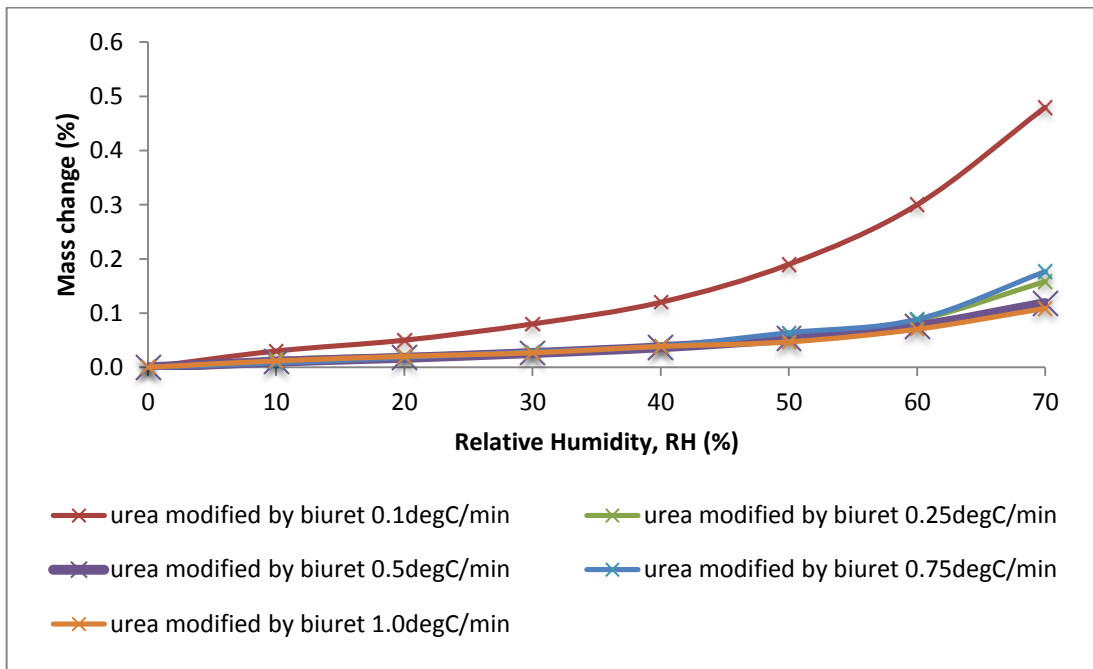
increasing the cooling rates to allow the crystallisation to occur, the crystals produced were smaller. This is because the time for the crystals to grow completely is too fast at the higher cooling rates, in consequence, small crystals were produced and give impact to the surface area of the crystals. In contrast, at slower cooling rates, for example crystals crystallised at cooling rate of $0.1^{\circ}\text{C}/\text{min}$, the crystals produced were larger. Therefore, changes in cooling rates affect the value of dispersive surface energy because of increasing in surface area per volume of the crystals.

5.2.3 Dynamic Vapour Sorption Studies

Data from the water sorption experiments and analysis using DVS to observe the effect of water taken in unmodified urea and urea modified by biuret samples is shown in Figure 5.7. These reveal the percentage of mass changes of unmodified urea and urea modified by biuret crystals at different cooling rates. The mass changes of the samples were observed at different relative humidity. Results from 0 to 70% relative humidity are showed in figure 5.7 and figure 5.8. Cut off at 70% relative humidity had been chosen because of at higher relative humidity than 70%, the water sorption on the samples are high and rapidly increase (up to 40% water uptake), which showing that the absorption of water in samples had taken part. Graphs in figure 5.7 are shown to discuss the effect of crystals crystallised at different cooling rates on the rates of adsorption. Figure 5.8 shows the comparison curves of unmodified urea and urea modified by biuret at 0.1 and $1.0^{\circ}\text{C}/\text{min}$ to compare the rates of adsorption between unmodified urea and urea modified by biuret crystals.



(a)

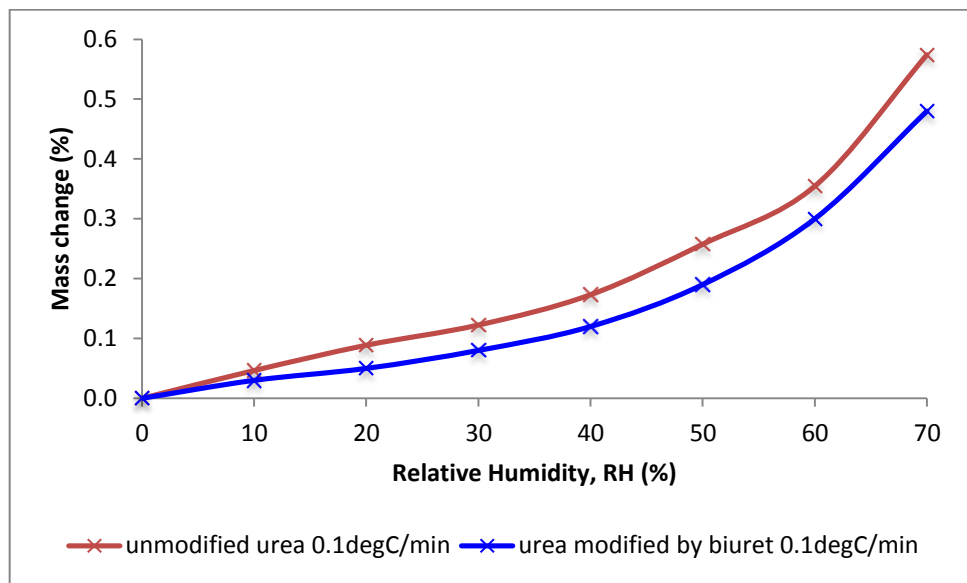


(b)

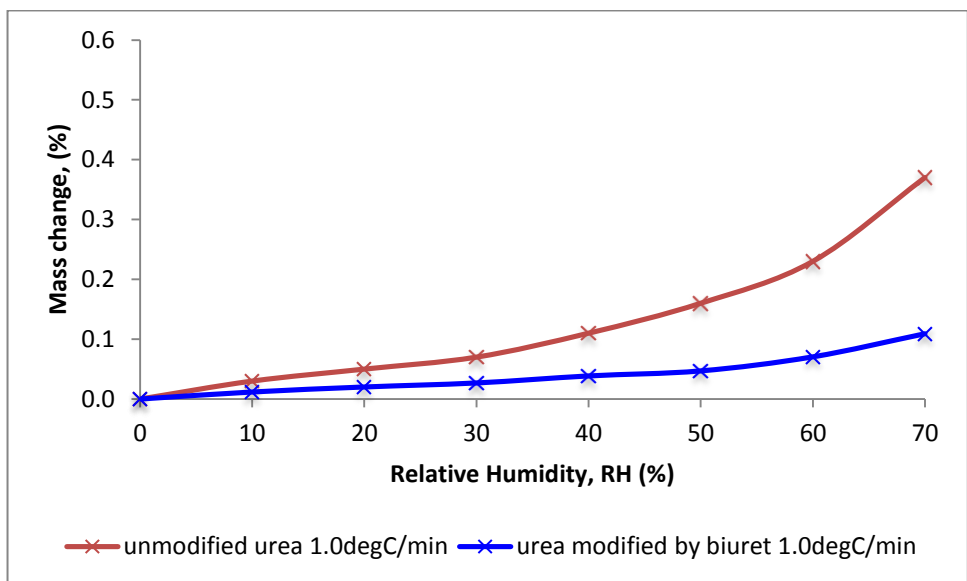
Figure 5.7: Graphs of percent in mass changes of (a) unmodified urea and (b) urea modified by biuret at different cooling rates at different relative humidity. Red line represents samples crystallised at cooling rate $0.1^{\circ}\text{C}/\text{min}$, green line is for samples crystallised at cooling rate $0.25^{\circ}\text{C}/\text{min}$, purple line is for samples crystallised at cooling rate $0.5^{\circ}\text{C}/\text{min}$, blue line is for samples crystallised at cooling rate $0.75^{\circ}\text{C}/\text{min}$, and orange line is for samples crystallised at cooling rate $1.0^{\circ}\text{C}/\text{min}$.

In figure 5.7(a), unmodified urea at five different cooling rates was examined for their water sorption effect. Unmodified urea at 0.1°C/min has the highest water sorption. For unmodified urea at 0.1°C/min (red line), it can be seen in the graph that the mass change slowly increase from 0 to 40% RH (up to 0.2% mass change), however, the mass started to increase in higher rate above this RH as the slope slightly steep until it reach 70% RH (up to 0.6%). For the other four different cooling rates, the mass change are lower than unmodified urea recrystallised at 0.1°C/min. Samples recrystallised at 0.75 and 1.0°C/min also show the mass change started to increase in higher rate when it reaches 40% RH. However, the mass change is only 0.2 and 0.4% at 70% RH. For samples recrystallised at 0.25 and 0.5°C/min, the percentage of mass change is much lower (about 0.1%) and increasing the RH also does not give significant changes to the mass change.

The urea modified by biuret crystals at different cooling rates also were observed (figure 5.7(b)). The trend of increasing percentage of mass changes is similar to unmodified urea crystals in which small percentage of mass changed were observed up to 40% RH, but the mass change increased rapidly above this relative humidity. Similar to unmodified urea samples, the urea modified by biuret recrystallised at the slowest cooling rate, 0.1°C/min, also has the highest percentage mass change as the relative humidity increase, however, the value is lower than unmodified urea sample (0.5%). The other four different cooling rates also have the similar trend to the unmodified urea samples, as the percentage of mass change is much lower than sample recrystallised at 0.1°C/min. The high increase in mass change can be observed clearly when the relative humidity reaches 60%.



(a)



(b)

Figure 5.8: Graphs of percent in mass changes of unmodified urea and urea modified by biuret at (a) $0.1^{\circ}\text{C}/\text{min}$ and (b) $1.0^{\circ}\text{C}/\text{min}$. Red line and blue line represent unmodified urea sample and urea modified by biuret sample, respectively.

Figure 5.8 (a) and (b) show the graphs for unmodified urea and urea modified urea by biuret at $0.1^{\circ}\text{C}/\text{min}$ and $1.0^{\circ}\text{C}/\text{min}$ respectively. Comparing both graphs show that unmodified urea adsorbs water much higher than

urea modified by biuret. It can be seen from graph that up to 70% RH, the percentage of mass change is 0.6 and 0.5, respectively, even though only 0.1% difference. For unmodified urea at 0.1°C/min At 1.0°C/min (figure 5.7(b)), it also shows unmodified urea increased its mass higher than urea modified by biuret. The difference is larger than samples recrystallised at 0.1°C/min., which is about 0.3% difference. Urea is expected to have very hygroscopic characteristic (Werner, 1937). Its {110} face is known to have hydrophilic characteristics. As unmodified urea has large surface area of {110}, therefore has ability to adsorb water molecules from its surrounding very easily, and hold the water molecules strongly, also, further increase in relative humidity makes the crystals absorbed water rather than only adsorption process. However, as the crystals become more prismatic, the {110} face is shrinking, while the {111} face which less hydrophilic grew larger. Hence, less water adsorbed at the whole surfaces of the crystals.

5.2.4 Integration of the Experimental Analysis

Crystallisation of urea in ethanol solvent produced long needle-like crystals. This result is consistent with reports that urea crystals grow rapidly on [001] direction, thus identifying the (001) face as the fastest growing face (Davey, *et al.*, 1986) crystallised in water and (Huang, *et al.*, 1990) crystallised urea in different solvents.

In figure 5.1, the size of unmodified urea and urea modified biuret at 0.1°C/min cooling rates showed the size became smaller. The size of unmodified urea is long needle-like shape. However, addition of biuret to the urea solution for crystallisation, it can be seen that the crystal become shorter and produce smaller block shaped crystals. The difference between size distributions of the two samples can be observed from the frequency and undersize curves of aspect ratio of the crystals in Figure 5.2. The crystal size of urea crystallised at 0.1°C/min were long up to 2.6 mm while the urea modified by biuret at 0.1°C/min has average crystal size length of 100 µm. The addition of biuret on the crystal habit affecting the relative growth rates

is consistent for the different faces of urea crystals. In particular, the results would suggest that the biuret molecules attach at the fast growing faces which are the {001}, {111} and ($\bar{1}\bar{1}\bar{1}$) faces and retards their growth with respect to the {110} form. Thus, the retardation of fastest growing face caused the face to grow slowly; hence making the crystal become bulkier. This study also gives an understanding about the effect of cooling rate on crystal growth. As at slower cooling rate, it produced longer sizes of crystal as mentioned in section 5.2. It is due to the time of the crystals to undergo complete crystal growth process is much higher than at faster cooling rates. The surface energy studies using IGC shows that the trend of the data with respect to the increase in cooling rate is much same. The urea modified by biuret has a higher surface energy when compared to the unmodified urea crystals.

Considering initially the higher surface energies for the urea crystals modified by biuret when compared to unmodified urea it can be seen that by looking at the urea and biuret structure, as discussed in Davey *et al.*, (1986), one biuret molecule would be expected to replace two urea molecules at {001} face. The replacement by biuret leaves this face with available hydrogen bonding linkages. Now considering the different surface energies of different cooling rates, it can be seen that this relates to the smaller particle sizes and hence higher surface area, which are produced due to enhanced nucleation at the faster cooling rates. Hence, these data demonstrate the impact of crystallisation processing conditions, in this case solution cooling rate and the action of impurities on the physico-chemical properties of the crystals.

5.3 Surface Characterisation using Molecular Modelling

Molecular modelling was used to complement the experimental work as well as to give a better and molecule-centred understanding for validating the experimental analysis. In this work, prediction of morphology of urea and modified urea by biuret is discussed in this section and compared with the

experimental results. In addition, prediction of surface energy also calculated using attachment energy approach.

5.3.1 Morphology Prediction of Urea

In routine work of morphology prediction of urea, attachment energy of each crystal faces was calculated. As urea has a polar morphology with different ends of (111) being polar, BFDH and classical attachment energy methods cannot be directly used because BFDH method predicts the morphology only based on the crystal geometry while the second approach does not consider polar faces and will give the same value of attachment energy for the polar faces (Docherty, 1989). Thus, the polar attachment energy calculation method developed by Docherty (1989) was used to predict the morphology of urea. In this work, the attachment energy calculation by Docherty was initially reproduced as a reference point for these studies. In latter calculations, the force field chosen was by Lifson and Hagler (Lifson *et al.*, 1979) which has good description for amides. Also, this force field has its own charges distribution that suitable to use for urea compound. In Docherty's work, for self-consistency, he scaled the charges provided by Lifson and Hagler. There were two types of charges that had been considered for the polar morphology calculation which were the bulk isolated charges and surface isolated charges. Bulk isolated charges are charges that distributed by the molecule in the bulk crystal while surface isolated charges are the charges from incoming molecule to the surface of the bulk crystal.

5.3.1.1 Identification of Key Intermolecular Interactions

In order to predict crystal morphology, the intermolecular interactions of the crystals need to be understand. The intermolecular interactions determine the value of the attachment energy of the crystals faces. Figure 5.9 shows the strongest intermolecular interactions exist in urea crystal. From bonding

analysis calculation in HABIT98, it shows that two hydrogen bonding exists in urea crystal (type a and b). Table 5.3 shows the intermolecular bonding analysis in urea crystal. Figure 5.9(c) shows one molecule of urea forms hydrogen bonds with molecules surrounding it. By taking one molecule of urea as a central molecule (noted in yellow colour), the oxygen atom from the central molecule can form four hydrogen bonds with the hydrogen atoms from the surrounding molecules, while the hydrogen atoms from amides form hydrogen bond with the oxygen atom from the molecules surround it.

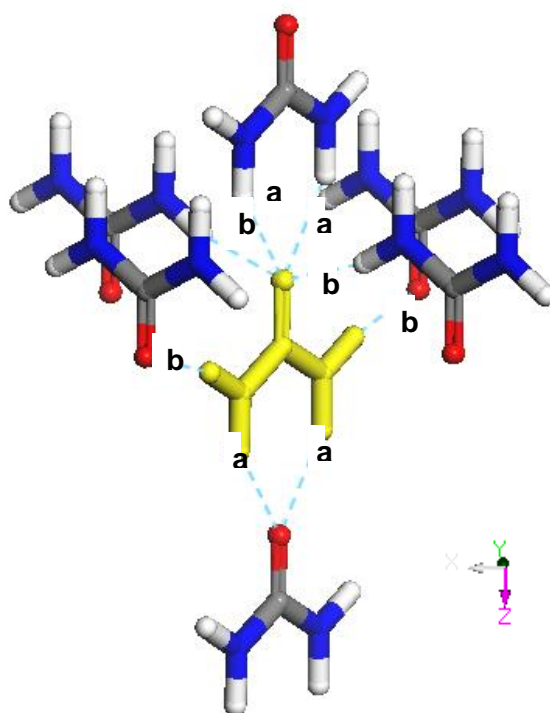
Table 5.3: Debug analysis of intermolecular bonds in urea using Hagler force field with Hagler charges.

Bond type	multiplicity	Distance (Å)	van der Waals		van der Waals (total)	COU	Total
			ATT	REP			
a	4	4.68	-2.02	2.10	0.08	-3.74	-3.66
b	8	4.3	-1.74	1.26	-0.48	-2.52	-3.00



(a) bond type a

(b) bond type b



(c)

Figure 5.9: Atom-atom interaction (a) bond type a (b) bond type b from DM-analysis (c) the hydrogen bonding interaction between central molecule of urea (yellow) with its surrounding molecules.

5.3.1.2 Attachment Energy Calculation for Morphology Prediction

As urea is a polar molecule, the attachment energy calculation needs also to consider the slice energy of each face. Consideration of the growth slice position and energy for the faces is important in order to obtain the most

stable value for each of the unique habit faces. Here, four faces were taken into account in order to predict the morphology, which is (001) as the fastest growing face, (110) as the slowest growing face, (111) and ($\bar{1}\bar{1}\bar{1}$) as polar faces. The slice energies that need to be considered are for the polar faces. Thus, the calculations of the slice energy must reach the most stable energy, and then the value of attachment energy is selected. From the calculations of the slice energy as a function of its position, the value of the attachment energy of -4.6 and -4.9 kcal/mol for {111} and {-1-1-1} respectively calculated to give the most stable slice energy values for both faces as plotted in graphs Figure 5.10.

Table 5.4: Summary of slice energy and attachment energy using bulk-isolated charges

slice shift	E _{slice} (kcal/mol)		E _{att} (kcal/mol)	
	(1 1 1)	(-1 -1 -1)	(1 1 1)	(-1 -1 -1)
0	-6.57	-6.57	-6.8	-6.8
0.1	-6.57	-6.57	-6.8	-6.8
0.2	-9.09	-9.09	-5.4	-5.9
0.3	-10.55	-10.55	-4.9	-5.4
0.4	-10.94	-10.94	-4.7	-5
0.5	-11.13	-11.13	-4.6	-4.9
0.6	-11.13	-11.13	-4.6	-4.9
0.7	-11.13	-11.13	-4.6	-4.9
0.8	-11.16	-11.16	-4.6	-4.9
0.9	-11.16	-11.16	-4.6	-4.9
1	-11.16	-11.16	-4.6	

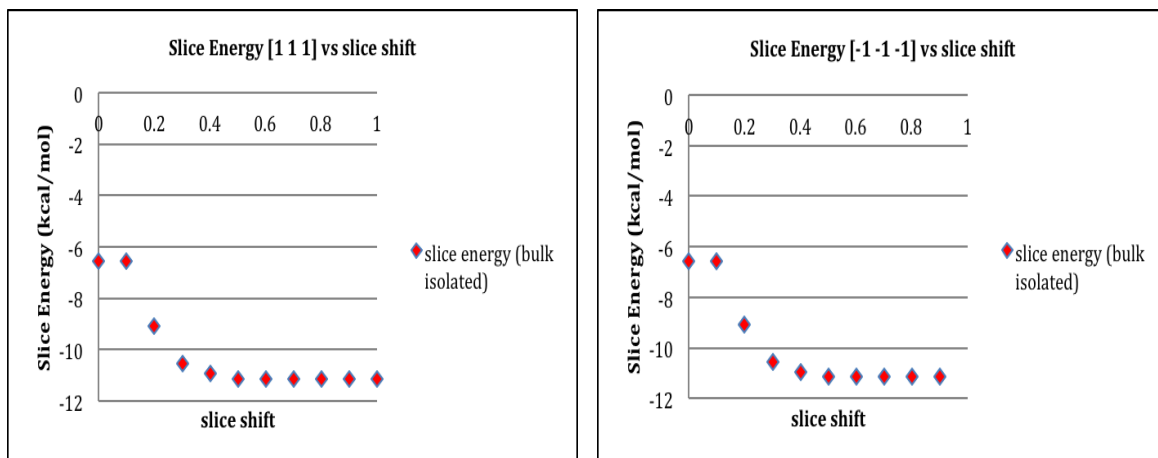


Figure 5.10: Graphs of slice energy of $\{111\}$ and $\{-1-1-1\}$

Table 5.5 shows the attachment energies values of four important faces of urea to predict its polar morphology using Hagler force field together with bulk-isolated charges of Hagler charges. Figure 5.11 is the figure of morphology prediction of urea based on this calculation.

Table 5.5: Attachment energies of four important faces of urea calculated using bulk-isolated charges model for prediction of polar morphology

Face (hkl)	Attachment energy bulk-isolated charges model (kcal/mol)
(110)	-4.2
(001)	-4.5
(111)	-4.5
(-1-1-1)	4.9

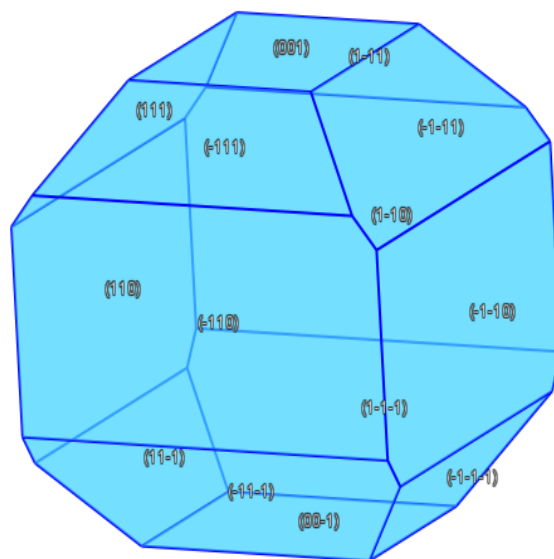


Figure 5.11: Morphology prediction of urea using bulk-isolated charges to calculate the attachment energies of each faces including the polar faces of (111) and $(\bar{1}\bar{1}\bar{1})$.

5.3.2 Re-evaluation of Intermolecular Potential Selection for Dispersive Surface Energy Prediction

It is important to predict the lattice energy to ensure that the value is close to the known experimental sublimation enthalpy for urea. In the previous Docherty (1989) work, the lattice energy calculation was determined using Hagler potential set, together with its scaled charges, which gives -22.57 kcal/mol. In this work, the parameters were widened by using five types of force fields to model the van der Waals component used to calculate the lattice energy of urea (Hagler, Momany, Dreiding, Nemethy, and Tripos force fields). These force fields were chosen based on their ability in terms of calculating the hydrogen bonding and van der Waals interactions needed for the carboxyl and amide groups that exist within the urea structure. The van der Waals components are important for the simulation of dispersive surface energy in the next section. These calculations also used three different sets of partial electron charges as calculated using MOPAC (AM1, MNDO, and

PM3 implementations), CRYSTAL and those taken from Hagler (Docherty, 1989) as well as the case without the charges on the molecule being considered. The description of each types of charges used in lattice energy calculations and lists of charges for all types of atoms are listed in table 5.6 and 5.7 respectively.

Table 5.6: Description of types of atoms use in lattice energy calculations for three Hamiltonian parameters of MOPAC charges (AM1, MNDO, PM3), ab-initio charges from CRYSTAL, and Hagler scaled charges from its own partial charges.

Types of charges	Descriptions
AM1	Austin Model 1. Use for C, H, N, O. It is suitable for many chemical functionalities. (Dewar <i>et al.</i> , 1985)
MNDO	Modified Neglect of Differential Overlap Model 2. The parameters calculate the atomic orbital ionisation, van der Waals and electrostatic interactions (Dewar & Thiel, 1977)
PM3	Parameterised Model 3. Optimise simultanously C, H, N, O, F, Al, Si, P, S, Cl, Br, I. Use two parameters of Gaussian functions (Stewart, 1989)
CRYSTAL	Ab-initio quantum mechanicals charges calculations
HAGLER	Hagler own calculated charges. Use for carboxylic and amide groups
* Full descriptions of each types of charges can be obtained from Cramer, 2002	

Table 5.7: Types of charges use in lattice energy calculations. Three types of charges; empirical charges of MOPAC with different Hamiltonian parameters (AM1, MNDO, PM3), ab-initio charges from CRYSTAL, and Hagler scaled charges

Atoms	Types of charges				
	MOPAC			CRYSTAL	HAGLER
	AM1	MNDO	PM3		
Carbon (C)	0.401	0.467	0.168	0.426	0.380
Oxygen (O)	-0.439	-0.455	-0.480	-0.425	-0.380
Nitrogen (N)	-0.450	-0.408	0.011	-0.467	-0.830
Hydrogen (H)	0.251	0.215	0.089	0.219	0.415
Hydrogen (H)	0.218	0.187	0.057	0.196	0.415
Nitrogen (N)	-0.450	-0.408	0.011	-0.467	-0.83
Hydrogen (H)	0.251	0.215	0.089	0.219	0.415
Hydrogen (H)	0.218	0.187	0.057	0.196	0.415

Table 5.8: Types of force-fields with their type of potential in calculating lattice energy

Force Fields	Types of potential
Hagler	Parameterised for H, C, N, O: carboxylic acid and amides. Use its own partial charges to calculate lattice energy
Momany	General hydrogen bond potential. Parameterised for H, C, N, O: carboxylic acid and amides. Take into account the van der Waals interactions
Dreiding	Van der Waals interactions in combination of 2 and 3 body in term of hydrogen bond
Nemethy	General hydrogen bond potential. Parameterised for H, C, N, O: carboxylic acid and amides.
Tripos	Scaling factors for hydrogen bond. Parameterised for H, C, N, O, Cl, F, S. H-bond acceptor atoms: N, O, F, Cl, S

Table 5.9: Lattice energies values of urea using four different charges and five different force fields. The bold columns in black is the values using Hagler potential with its scaled charges providing a good match to the experimental lattice energy of -22.2kcal/mol, however, provides an unrealistically low van der Waals component. The bold columns in red is the values using Dreiding potential with CRYSTAL charges, which gives the highest value of van der Waals component.

Force Fields	Lattice Energy (kcal/mol)															
	Mopac									CRYSTAL			HAGLER			No charges
	AM1			MNDO			PM3			VdW	Coul	Total	VdW	Coul	Total	VdW
VdW	Coul	Total	VdW	Coul	Total	VdW	Coul	Total	VdW							
Hagler	-5.8	-10.6	-16.4	-5.9	-9.1	-15.0	-5.9	-8.6	-14.5	-5.9	-8.8	-14.7	-5.9	-16.7	-22.6	-5.9
Momany	-11.4	-5.3	-16.7	-11.4	-4.5	-15.9	-11.4	-4.3	-15.6	-11.4	-4.6	-16.0	-11.4	-8.3	-19.7	-11.4
Dreiding	-13.1	-10.6	-23.8	-13.1	-9.1	-22.2	-13.1	-8.6	-21.7	-13.1	-8.8	-21.9	-13.1	-16.7	-29.8	-13.1
Nemethy	-4.5	-10.6	-15.1	-10.8	-4.5	-15.3	-10.7	-4.3	-15.0	-10.7	-4.4	-15.1	-10.7	-8.3	-19.1	-10.7
Tripos	-4.5	-10.6	-15.1	-4.5	-9.1	-13.6	-4.4	-8.6	-13.0	-4.5	-8.8	-13.3	-4.5	-16.7	-21.2	-4.5

The sublimation enthalpy of urea is -22.8 kcal/mol (Acree Jr. & Chickos, 2010), (Zaitsau, *et al.*, 2003), which gives the experimental lattice energy -22.2 kcal/mol. From table 5.9, the closest value of the lattice energy of urea was calculated using the Hagler force field with its scaled charges (-22.57 kcal/mol) (Docherty, 1989). The Hagler scaled charges with this force field was used in prediction of lattice energy of urea because of the polarity of the urea molecule and the ability of the oxygen atom in urea molecule to form four hydrogen bonds with four hydrogen atoms of urea make it somewhat a special case in terms of determining its lattice energy (see figure 5.9: hydrogen bonding interaction). Figure 5.12 shows the plot of lattice energy as a function of intermolecular interaction as calculated with the Hagler force field showing the respective contributions from the van der Waals and electrostatic interactions. Urea is known to have strong hydrogen bonds interactions. In HABIT98 calculation, the hydrogen bonding interaction inclusively counted in vdW interaction. However, in figure 5.12, the van der Waals interaction is lower than electrostatic interactions. This is a reflection of the polarity of urea molecule and the strong electrostatic interactions.

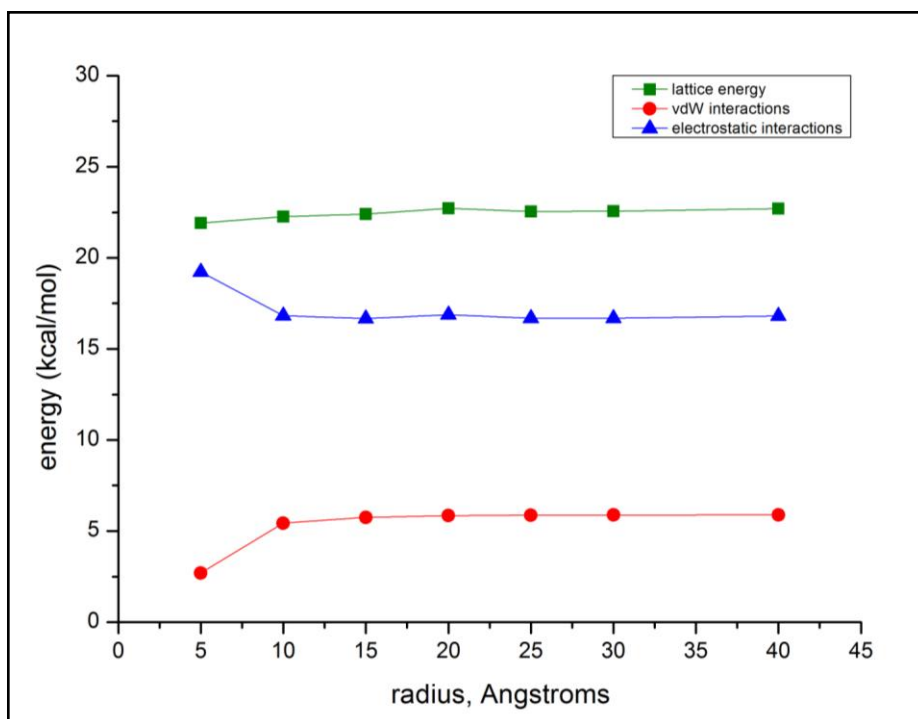


Figure 5.12: Lattice energy plots and its component contributions of urea crystal using Hagler force field with its parameterised partial electronic charges.

However, even though the Hagler force field agrees well with experimental lattice energy, the selection of the suitable force field to be used for the calculation of the dispersive surface energy needs a rigorous calculation of the dispersive interactions. Examination of table 5.9 shows that the dispersive component calculated is unrealistically low for a close packed molecular crystal such as urea. The sharp differences between the partial electronic calculations provided by Hagler and those calculated ab-initio as shown in table 5.7. The Hagler charges for all the urea atoms are much higher compared to CRYSTAL charges and the empirical charges using AM1 and MNDO parameters. The combination of Dreiding force field with the CRYSTAL charges gives the highest van der Waals interactions compared to other force fields, thus the value was selected to be used for dispersive surface energy simulation. It can be seen in the figure 5.13. The graph shows the van der Waals interactions are higher than electrostatic interactions using combination of Crystal charges and Dreiding force field. Comparing the value of van der Waals interactions using Hagler force field and the re-evaluated value, the re-evaluated value is more reliable to be used to predict the dispersive surface energy.

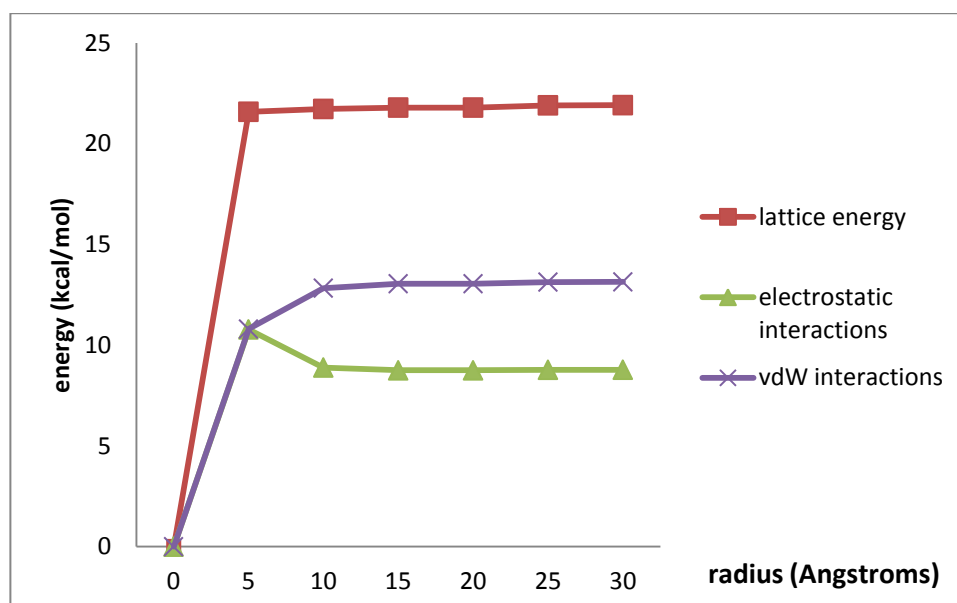


Figure 5.13: Lattice energy and its component contributions of urea crystal using Dreiding force field with Crystal charges

5.3.3 Prediction of Dispersive Surface Energy

5.3.3.1 Calculations of Fractional Surface Areas based on Experimental Data

In this section, the prediction morphology of unmodified urea and urea modified by biuret is presented. Figure 5.14 shows the comparison of simulated morphology of unmodified urea and modified urea by biuret optimised to match the experimental data from micrograph images. The prediction of unmodified urea and urea modified by biuret are seen to be in good agreement with experimental observations. The fractional surface area was obtained from the Visual Habit program tabulated in table 5.10. The prediction of both crystals agrees with the crystals produced during crystallisation process. Fractional surface area of modified urea by biuret crystals for the {111} form increased while that for the {110} form decreased. These are consistent with the effect of biuret being to retard the fastest growing face (111), in which make the (111) face become larger whilst (110) face becomes smaller.

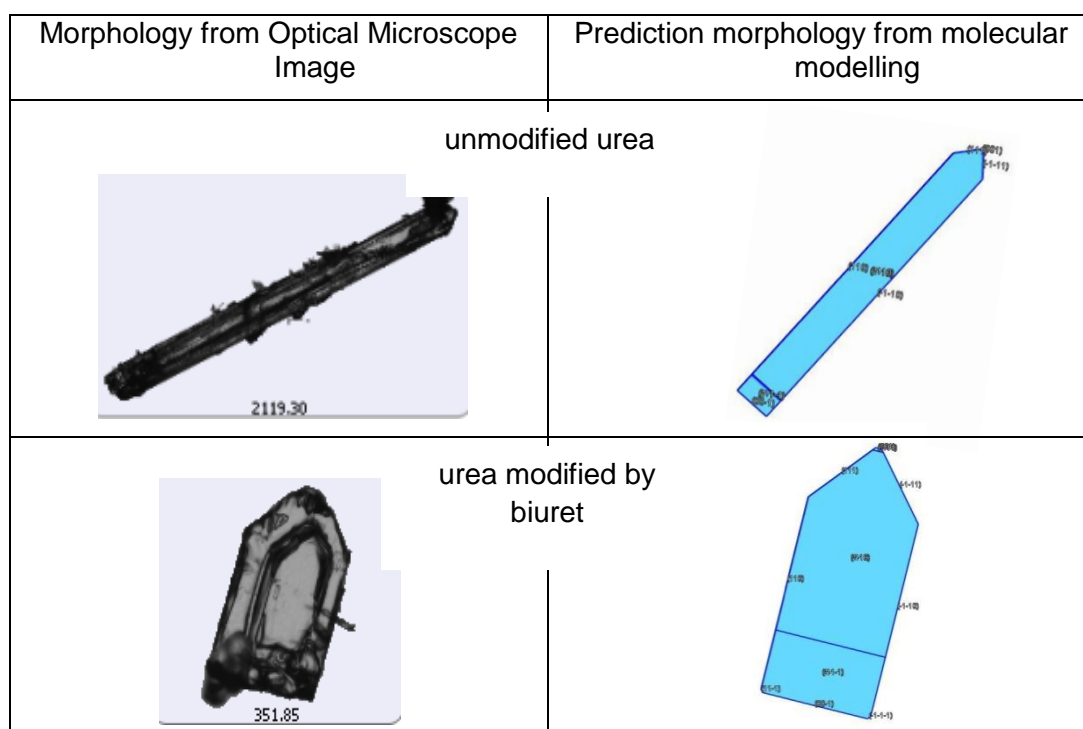


Figure 5.14: Comparison of morphology of unmodified urea and urea modified by biuret from experiment and modelling

Table 5.10: Percentage surface area of crystal faces obtained from Visual Habit

Crystal Face			% Surface Area	
h	k	l	Unmodified urea	Urea Modified by biuret
1	1	0	22.84	16.58
1	-1	0	22.84	16.58
-1	-1	0	22.84	16.58
-1	1	0	22.84	16.58
1	1	1	2.04	8.12
1	-1	-1	2.04	8.12
-1	-1	1	2.04	8.12
-1	1	-1	2.04	8.12
total			100	100

The fractional area obtained in previous section was used to calculate the total dispersive surface energy of unmodified urea and urea modified by biuret using surface energy prediction (equation 4.2) and its molecular scale rationalisation. The summary of dispersive surface energy prediction is tabulated in table 5.11. In dispersive energy prediction, the calculations were made using all five forces. The prediction result using Dreiding force field provided the best results for dispersive surface energy. Using dreiding force field, the dispersive surface energy prediction gives 45.51 and 53.27 mJ/m² for unmodified urea and urea modified urea by biuret respectively (table 5.11). The values are higher than the experimental values, which 40.96 and 46.00, respectively. However, the prediction values provided the same trends as the experimental surface energy results, in which the modified urea by biuret has a higher predictive dispersive surface energy when compared to that of the unmodified urea. The stronger dispersive interactions give by the dreiding force field are consistent with this force field being more suitable for modelling the van der Waals interactions for a strongly hydrogen bonded system such as urea.

Table 5.11: Summary of prediction surface energy of unmodified urea and urea modified by biuret

Form	Multiplicity (M)	Unmodified urea (mJ/m ²)				Urea modified by biuret			
		Fractional surface area (SA)	Dispersive Surface Energy	Electrostatic Surface Energy	Total Surface Energy	Fractional surface area (SA)	Dispersive Surface Energy	Electrostatic Surface Energy	Total Surface Energy
{1 1 0}	4	0.228	39.29	40.21	79.50	0.166	28.51	29.18	57.69
{1 1 1}	4	0.020	6.22	6.85	13.07	0.081	24.76	27.25	52.01
Total surface energy (mJ/m ²)			45.51	47.06	92.57		53.27	56.43	109.70

As shown in table 5.11, the $\{111\}$ form is well known as the fastest growing face, gives the largest contributions in dispersive surface energy. As crystals become bulkier (urea modified by biuret), the dispersive surface energy of each faces increased. Thus, the value of the surface energy increased. The $\{111\}$ increased in fractional surface area whilst 110 decreased. The electrostatic energy gives significant values in which the energy at $\{001\}$, $\{111\}$, and $\{-1-1-1\}$ are high as these faces have polar atoms at the surfaces while $\{110\}$ is expected to have low electrostatic energy as the polarity of this face is very low. Figure 5.15 shows the surface chemistry for the important faces of urea crystals.

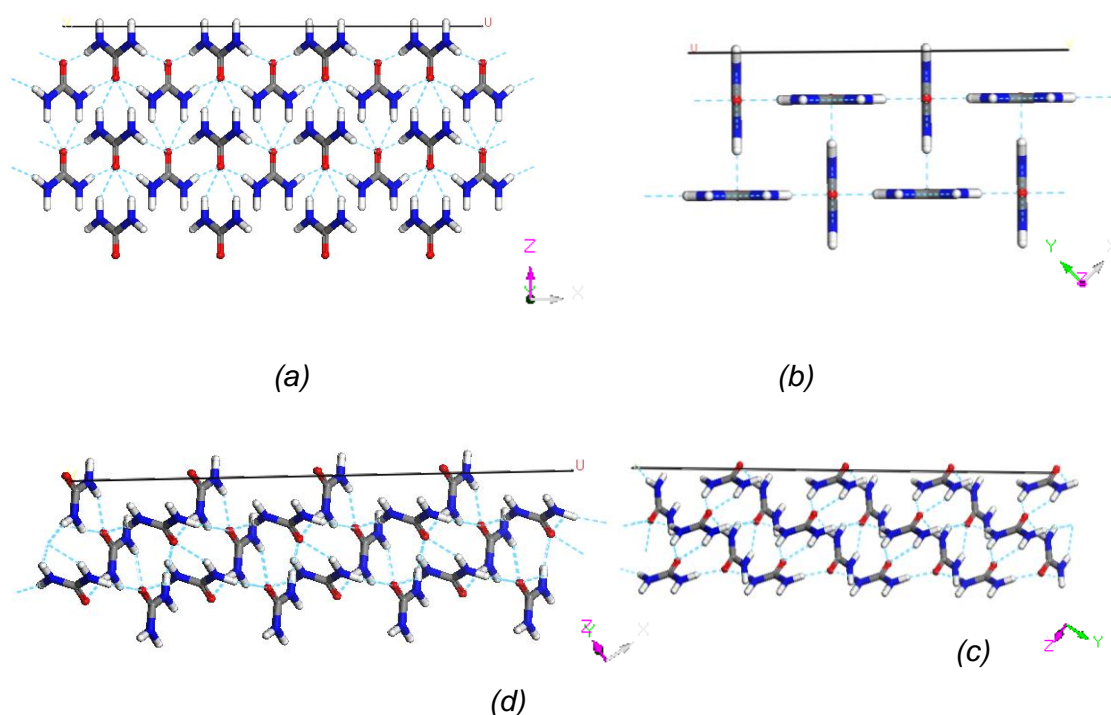


Figure 5.15: cleave surfaces of urea with showing of hydrogen bonding interactions (a) (001) face, (b) (110) face, (c) (111) face, (d) $(\bar{1}\bar{1}\bar{1})$ face.

Figure 5.15 (a) is a (001) face, which the fastest growing face. Hydrogen atoms from amides exposed at the surface, however, the carbonyl oxygen that show up to the surface provides the hydrogen bonding to the incoming molecule at the surface. This explains the strongest interactions occur on this face. Differ for (110) face, the urea molecule lays flat to the other

molecule, therefore, the interactions to the incoming molecules are very weak. For the polar faces, at $(\bar{1}\bar{1}\bar{1})$ face, the carbonyl oxygen exposed at the surface, however, hydrogen from amides be on the (111) face.

5.4 Discussion

From all the experimental and molecular modelling analysis, the results show that modification of crystallisation of urea by addition of biuret changed its morphology from needle-like shape to prismatic shape. Also, the crystallisation of both unmodified urea and urea modified by biuret at different cooling rates gave effect to the crystals size. The change in crystal morphology and crystal size further analysed using dynamic vapour sorption for water sorption analysis as reveal that urea is a comparatively hygroscopic material. Unmodified urea was found to adsorbed water to a higher degree than urea modified by biuret. It is confirmed that crystallisation of urea in water solution produced very needle-like shape, in which the crystal growth at c-axis (001) is very fast. The study on dispersive surface energy was carried out using inverse gas chromatography to understand the effect to the dispersive surface energy. The addition of biuret increased the dispersive surface energy while smaller crystal size gives higher dispersive surface energy value compared to the larger crystal. The experimental work validated using molecular modelling based upon predictions of the urea morphology. From the attachment energy calculations and fractional surface area determination, the prediction morphology of urea was found to agree with the morphology observed in experimental work. The dispersive surface energy prediction using Dreiding force field with CRYSTAL charges agrees well with the experimental results.

5.5 Closing Remarks

All the experimental and molecular modelling work helps to understand the effect of biuret to the urea crystals. The surface energy simulation analysis give good agreement with the value obtained from experimental data. This comparison gives understanding that the changed morphology of the actual crystal, it also changed the overall surface properties of the crystals.

References

1. Acree, Jr, W., Chickos, J.S., (2010). *J. Phys. Chem. Ref. Data Vol 39*.
2. Davey, R., Fila, W., Garside, J., (1986). The Influence of Biuret on the Growth Kinetics of Urea Crystals from Aqueous Solution. *J. Cryst. Growth.* (79) 607-613.
3. Huang, B., SU, G., HE, Y., (1990). Growth of Large Size Urea Crystals. *J. Cryst. Growth.* (102) 762-764.
4. Lifson, S., Hagler, A.T., Dauber, P. (1979). Consistent Force Field Studies of Intermolecular Forces in Hydrogen-Bonded Crystals. 1. Carboxylic Acids, Amides, and the C=OH-Hydrogen Bonds. *J. Am. Chem. Soc.* (101) 5111.
5. Thielmann, F., Burnett, D.J., Heng, J.Y.Y., (2007). Determination of the Surface Energy Distributions of Different Processed Lactose. *Drug Development and Industrial Pharmacy.* (33):1240-1253.
6. Werner, E.A., (1937). Urea as a Hygroscopic Substance. *Nature Publishing Group.* 512.
7. Zaitsau, D., Kabo, G.J., Kozyro, A.A., Sevruk, V.M., (2003). *Thermochim. Acta.* (406) 17-28

CHAPTER VI

CHARACTERISATION OF MICRO-CRYSTALS AND THE AGGLOMERATES USING X-RAY MICRODIFFRACTION AND MICROTOMOGRAPHY

6.1 Introduction

This chapter discusses the results collected from XMD and XMT experiment at the Diamond Light Source using the microfocus beamline I24 and the macrocrystallography beamlike I04. There are four case studies describe in this work. Firstly, a study the variability of crystals in powders by observing the difference in unit cell parameters. Also, from this study, the capability of carrying out diffraction experiment on micro-crystals of small molecules using microfocus beamline can be explained. Three compounds were chosen for investigation: (i) aspirin, (ii) urea and its modification by biuret (iii) polymorphic transformation of α - to β -L-glutamic acid. Secondly an examination aimed to understand the relationship of relative orientation between agglomerated particles of the aspirin and urea. Angle calculation using vector calculations and using the method of stereographic projection to determine the angles between crystals will be discussed in this chapter. Thirdly, is an examination of the interfacial development of the β -form microcrystal of LGA on the surface of the α -form. Fourthly a study aimed of understanding the external morphology of agglomerated micro-crystal and to correlate it with the XMD result by using single XMT. This was carried out on an agglomerated sample of α -LGA.

6.2 Justification on Selection of the Materials

As this research is focused on work on the ability of using a micro-focus beam in order to determine the structure and orientation of the micron sized small molecule particles, examination of other system is also important in order to test and to produce sufficient results to prove the ability of the overall approach itself. In this, aspirin crystals were selected as they have smaller particles than urea, less than 50 μm , which are suitable for the micro-focus beam used at synchrotrons. Furthermore, the aspirin crystals like urea also formed agglomerates.

Urea is a polar molecule is the primary material chosen for study in this thesis. It is a unique molecule in which one oxygen atom can form four hydrogen bonds with hydrogen atoms surrounds it. Crystallisation of urea in water and alcoholic solvents, such as methanol and ethanol forms long-needle like crystals. By adding biuret to the process, the morphology changes from long-needle shape crystals to prismatic crystals. There are published works on the experimental study of crystallisation of urea and how biuret affects the urea morphology (Davey, *et al.*, 1986), and modelling work Docherty, 1991), (Salvalaglio, *et al.*, 2012). However, during the process itself, the crystals often form agglomerates. Thus, it is of interest to understand the surface chemistry properties of the urea crystals and the difference between the urea crystals and urea modified by biuret crystals.

LGA was also chosen to be one of the systems to be studied because it has polymorphs. The polymorphs change from metastable form of α -LGA to stable β -LGA when the temperature increases above 45°C. Polymorphism of LGA is also well published in which the (101) face of β -LGA crystal grew from the (111) face of the α -LGA crystal (Ferrari & Davey, 2004), (Hammond, *et al.*, 2007). Thus, in this case LGA provides an opportunity to get a better understanding on how these two polymorphs are orientated each other during crystal growth.

6.3 Case study 1: Variability in the structure of microcrystals within Powdered Samples

From X-ray diffraction data collection, the routine work that needs to be done from the data collection is to process the data to determine the unit cell parameters and the space group of the crystals. For this routine, in general, it is not necessary to have complete diffraction images data set from the crystal sample. Unit cell parameters can be determined from coordinates of unit cell a, b, and c-axis. Variation in aspirin crystals and urea and urea modified by biuret were observed.

6.3.1 Variation in aspirin powder samples

Table 6.1 is the results of unit cell parameters of aspirin for each crystals obtained from the processed data collection with the standard deviation (std. dev.) in the bracket.

Table 6.1: Summary of unit cell constant determination for aspirin crystals

Crystals	Unit cell (Å°)	a	b	c	β	mosaicity
Crystal 1		11.251	6.530	11.237	95.87	0.301
Crystal 2		11.238	6.539	11.244	95.92	0.298
Crystal 3		11.239	6.543	11.242	95.91	0.282
Crystal 4		11.240	6.541	11.242	95.91	0.265
Crystal 5		11.239	6.541	11.245	95.92	0.288
Crystal 6		11.240	6.541	11.242	95.92	0.276
Crystal 7		11.261	6.518	11.256	95.86	0.268
Crystal 8		11.241	6.539	11.239	95.90	0.256
Crystal 9		11.239	6.541	11.238	95.91	0.289
Crystal 10		11.239	6.547	11.242	95.92	0.279
Crystal 11		11.240	6.543	11.238	95.92	0.283
Crystal 12		11.241	6.537	11.244	95.89	0.289
Average value		11.242	6.539	11.242	95.90	0.281
(Std Dev)		(0.007)	(0.007)	(0.005)	(0.02)	(0.013)
Unit cell constants of aspirin from literature : a = 11.242, b = 6.539, c = 11.245 (Aubrey <i>et al.</i> , 2007)						

In this work, the objective is to observe the variability of unit cell constants for sample to sample within a powdered sample. For most studies to determine the unit cell constants of single crystal, large single crystals were used. By using synchrotron technology, it is possible to use small single micro-crystal to measure the unit cell constants. In this study, twelve aspirin single micro-crystals had been mounted for data collection. From the processed data of these single crystals of aspirin, the space group was determined to be $P2_1/c$ and monoclinic with 4 molecules per unit cell, in which agreed with other aspirin crystal structure determination (Wheatley, 1964). In the experiment that was carried out, the structure of aspirin had been solved and compared with several literatures. Solving the aspirin structure is to do comparison on the result of data collection using microfocus beamline X-ray microdiffraction and conventional X-ray diffraction (Wheatley, 1964 and Kim *et al*, 1984), also other diffraction method such as neutron diffraction (Harrison, 2002). Figure 6.1 shows the molecular structure of aspirin sample as solved using SHELX in the WinGX program (Farrugia, 2012). The R-factor value for this solving structure is 0.05. The literature value of R-factor was 0.18 and 0.04 respectively for X-ray diffraction and 0.09 for neutron diffraction. The unit cell constants values were found to be very similar to each other. The average unit cell constants for all collected data was found to be $a = 11.242$, $b = 6.539$, $c = 11.242$, and $\beta = 95.90$. The values of a and c axes were found to be almost the same and to all intents and purpose can be concluded to be identical. These values were compared with literature (bottom column in table 6.1) with which only a very small difference was observed. The values were determined from single crystal XRD. The unit cell constants also compared with different method such as neutron diffraction to determine crystal structure of aspirin and the results were also found to agree with it (Harrison *et al.*, 2002). The percentage error obtained from results of the data processing show only a very small error in the unit cell constants values. Thus this work showed that there was no significant change in unit cell constants of crystals in a batch of powder crystals.

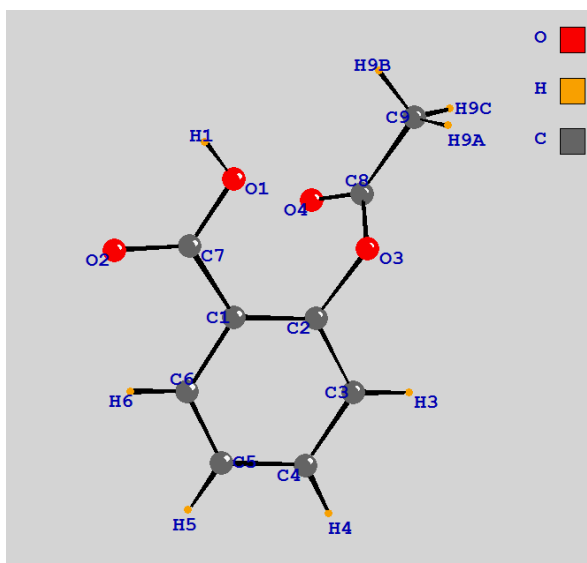


Figure 6.1: Aspirin crystal structure visualise in CAMERON graphical tool plugged-in WinGX software.

6.3.2 Variability in the Structure of Micro-crystals as a Function of Processing Conditions

The second material studied using XMD was urea. In this XMD data was collected from unmodified urea and urea modified by biuret micro-crystals prepared at five different cooling rates. Table 6.2 to 6.11 shows the unit cell constants for all the samples, urea and urea with addition of biuret at 0.1, 0.25, 0.5, 0.75 and 1.0 °C/min respectively. The unit cell parameters of urea crystal structure from literature to be used as comparison was $a = b = 5.565\text{\AA}$, $c = 4.684\text{\AA}$ and $\alpha, \beta, \gamma = 90^\circ$. This material has a tetragonal structure with a $P-42_1m$ space group.

Table 6.2: Unit cell constants of urea 0.1°C/min

Crystals \ Unit cell (Å)	a	b	c	mosaicity
Crystal 1	5.620	5.620	4.688	0.226
Crystal 2	5.626	5.626	4.693	0.286
Crystal 3	5.623	5.623	4.691	0.210
Crystal 4	5.622	5.622	4.690	0.194
Crystal 5	5.564	5.564	4.679	0.148
Crystal 6	5.571	5.571	4.677	0.377
Crystal 7	5.565	5.565	4.679	0.144
Crystal 8	5.566	5.566	4.679	0.220
Crystal 9	5.566	5.566	4.679	0.284
Crystal 10	5.570	5.570	4.679	0.218
Crystal 11	5.577	5.577	4.683	0.197
Crystal 12	5.567	5.567	4.679	0.140
Average Unit Cell Parameters and std dev ()	5.586 (0.027)	5.586 (0.027)	4.683 (0.006)	0.220 (0.069)

Table 6.3: Unit cell constants of urea-biuret crystals 0.1 °C/min

Unit cell (Å) Crystals	a	b	c	mosaicity
Crystal 1	5.566	5.566	4.678	0.374
Crystal 2	5.569	5.569	4.681	0.148
Crystal 3	5.575	5.575	4.682	0.224
Crystal 4	5.571	5.571	4.682	0.214
Crystal 5	5.567	5.567	4.681	0.248
Crystal 6	5.566	5.566	4.676	0.147
Crystal 7	5.567	5.567	4.679	0.266
Crystal 8	5.566	5.566	4.679	0.260
Crystal 9	5.566	5.566	4.678	0.204
Crystal 10	5.567	5.567	4.683	0.144
Crystal 11	5.565	5.565	4.678	0.178
Crystal 12	5.565	5.565	4.678	0.124
Average Unit Cell Parameters and std dev ()	5.567 (0.003)	5.567 (0.003)	4.679 (0.002)	0.211 (0.071)

Table 6.4: Unit cell constant of urea crystals 0.25 °C/min

Unit cell (Å) Crystals	a	b	c	mosaicity
Crystal 1	5.570	5.570	4.682	0.145
Crystal 2	5.572	5.572	4.682	0.162
Crystal 3	5.571	5.571	4.682	0.142
Crystal 4	5.574	5.574	4.683	0.145
Crystal 5	5.571	5.571	4.684	0.145
Crystal 6	5.575	5.575	4.691	0.152
Average Unit Cell Parameters and std dev ()	5.572 (0.002)	5.572 (0.002)	4.684 (0.004)	0.149 (0.007)

Table 6.5: Unit cell constant of urea-biuret crystals 0.25degC/min

Unit cell (Å) Crystals	a	b	c	mosaicity
Crystal 1	5.574	5.574	4.684	0.151
Crystal 2	5.571	5.571	4.681	0.365
Crystals 3	5.569	5.569	4.681	0.142
Crystal 4	5.567	5.567	4.681	0.393
Crystals 5	5.571	5.571	4.678	0.167
Crystal 6	5.569	5.569	4.681	0.146
Crystal 7	5.576	5.576	4.685	0.147
Crystal 8	5.572	5.572	4.682	0.160
Average Unit Cell Parameters and std dev ()	5.571 (0.003)	5.571 (0.003)	4.682 (0.002)	0.209 (0.106)

Table 6.6: Unit cell constants of urea crystals 0.5°C/min

Unit cell (Å) Crystals	a	b	c	mosaicity
Crystal 1	5.565	5.565	4.678	0.155
Crystal 2	5.566	5.566	4.678	0.143
Crystals 3	5.563	5.563	4.677	0.166
Crystal 4	5.565	5.565	4.679	0.147
Average Unit Cell Parameters and std dev ()	5.565 (0.001)	5.565 (0.001)	4.678 (0.001)	0.152 (0.010)

Table 6.7: Unit cell constants of urea-biuret crystals 0.5°C/min

Unit cell (Å) Crystals	a	b	c	mosaicity
Crystal 1	5.566	5.566	4.679	0.161
Crystal 2	5.562	5.562	4.675	0.156
Crystal 3	5.562	5.562	4.675	0.149
Crystal 4	5.567	5.567	4.679	0.147
Average Unit Cell Parameters and std dev ()	5.564 (0.003)	5.564 (0.003)	4.677 (0.002)	0.153 (0.006)

Table 6.8: Unit cell constants of urea crystals 0.75°C/min

Unit cell (Å) Crystals	a	b	c	mosaicity
Crystal 1	5.574	5.574	4.683	0.266
Crystal 2	5.563	5.563	4.679	0.242
Crystal 3	5.571	5.571	4.682	0.143
Crystal 4	5.570	5.570	4.683	0.143
Average Unit Cell Parameters and std dev ()	5.570 (0.005)	5.570 (0.005)	4.682 (0.002)	0.199 (0.065)

Table 6.9: Unit cell constants of urea-biuret crystals 0.75°C/min

Unit cell(Å) Crystals	a	b	c	mosaicity
Crystal 1	5.567	5.567	4.681	0.372
Crystal 2	5.572	5.572	4.682	0.246
Crystal 3	5.566	5.566	4.680	0.412
Crystal 4	5.566	5.566	4.680	0.443
Crystal 5	5.567	5.567	4.677	0.143
Crystal 6	5.570	5.570	4.682	0.272
Crystal 7	5.562	5.562	4.676	0.262
Crystal 8	5.563	5.563	4.675	0.147
Crystal 9	5.564	5.564	4.679	0.167
Crystal 10	5.568	5.568	4.679	0.142
Crystal 11	5.568	5.568	4.679	0.163
Crystal 12	5.567	5.567	4.679	0.160
Crystal 13	5.566	5.566	4.678	0.140
Average Unit Cell Parameters and std dev ()	5.567 (0.003)	5.567 (0.003)	4.679 (0.002)	0.236 (0.110)

Table 6.10: Unit cell constants of urea crystals 1.0°C/min

Unit cell(Å°) Crystals	a	b	c	mosaicity
Crystal 1	5.574	5.574	4.682	0.413
Crystal 2	5.571	5.571	4.679	0.446
Crystal 3	5.579	5.579	4.697	0.272
Crystal 4	5.569	5.569	4.694	0.333
Average Unit Cell Parameters and std dev ()	5.573 (0.004)	5.573 (0.004)	4.688 (0.009)	0.366 (0.079)

Table 6.11: Unit cell constants of urea-biuret crystals 1.0degC/min

Unit cell (Å) Crystals	a	b	c	mosaicity
Crystal 1	5.565	5.565	4.679	0.146
Crystal 2	5.569	5.569	4.681	0.163
Crystal 3	5.626	5.626	4.691	0.174
Crystal 4	5.626	5.626	4.691	0.151
Crystal 5	5.624	5.624	4.691	0.152
Crystal 6	5.623	5.623	4.691	0.172
Crystal 7	5.622	5.622	4.690	0.152
Crystal 8	5.625	5.625	4.692	0.124
Crystal 9	5.623	5.623	4.691	0.142
Crystal 10	5.622	5.622	4.690	0.146
Average Unit Cell Parameters and std dev ()	5.613 (0.024)	5.613 (0.024)	4.689 (0.005)	0.152 (0.015)

Table 6.12: Summary of unit cell parameters for unmodified urea and modified urea by biuret crystals at different cooling rates

Cooling rates (°C/min)	Unit Cell Parameters					
	Unmodified Urea			Urea Modified by Biuret		
	a	b	c	a	b	c
0.1	5.586	5.586	4.683	5.567	5.567	4.679
0.25	5.572	5.572	4.684	5.571	5.571	4.682
0.5	5.565	5.565	4.678	5.564	5.564	4.677
0.75	5.570	5.570	4.682	5.573	5.573	4.688
1.0	5.567	5.567	4.679	5.613	5.613	4.689
Average and std dev ()	5.572 (0.008)	5.572 (0.008)	4.681 (0.002)	5.578 (0.02)	5.578 (0.02)	4.683 (0.005)

Table 6.2 to 6.11 listed the unit cell constants of unmodified urea and urea modified by biuret crystallised at different cooling rates. The values in the brackets are the standard deviation of unit cell values for each crystal and the average of the unit cell constants with their standard deviation stated in bold. Table 6.12 summarised the average of unit cell parameters of the unmodified urea and urea modified by biuret at different cooling rates. The average values were calculated to enable a comparison to be made between the different cooling rates and urea crystals modification with biuret. In terms of the variability of unit cell constants at different cooling rates, the standard deviation values were found to range from 0.001 to 0.024. The small differences in the unit cell constants were not found to change the crystal lattice and crystal symmetry significantly. Addition of biuret as impurities in urea crystallisation was not found to change the urea crystal lattice significantly with only small changes being observed (5.572 to 5.578) and (4.681 to 4.683) for a and c axis of unmodified urea and urea modified by biuret, respectively. The variability of the micro-crystals within the powder samples was also observed through measurement of their mosaic spread (mosaicity). The mosaicity of crystals is a measure of the quality and the perfection of the crystals. The lowest degree of mosaicity gives indication that the high perfection of crystals (Evans, 1999). In unmodified urea and urea modified by biuret crystals, the degree of mosaicity was found to be between 0.10° and 0.44° .

The measurement of the degree of mosaicity may also be influenced by the X-ray beam environment and is good to use lower temperature to collect the diffraction data for solving crystal structures, as the molecules in crystal lattice can be better stabilised at the lower temperature. However, lowering the temperature increased the degree of mosaicity of the crystals. In this study, the temperature set to 100K for data collection. The degree of mosaicity of crystals at 100K was normally found to lie between 0.3° and 1° . From the results above, they show that there are no significant differences in unit cell parameters of unmodified urea and urea modified by biuret. Also, the urea modified by biuret has the same space group as unmodified urea

crystal structure. The degree of mosaicity of the crystals can be considered to be quite a low degree of mosaicity.

In this section, using synchrotron radiation technology for determining unit cell parameters and crystal structure by using micro-crystals samples are showing that the results obtained are agreed with the literature study, in addition with good structure determination R-factor. In structure determination, the lower value of R-factor determine the good structure solving. The mosaicity of the micro-crystals also had been analysed and from the data collection, the values show that the mosaicity value for both samples, aspirin and urea, without and with addition of biuret are low, as low value of mosaicity is the value that shows the high perfection of crystals. From the results of unit cell parameters determination, degree of mosaicity and structure determination which all agree well with the literatures, with small deviation in unit cell parameters of urea samples show that the microfocus beam size used for this experiment is capable to carry out for micro-crystals small molecules samples. Other factors that influenced to produce high quality results besides selection of the beam size in respect to sample size are the chosen right wavelength that determine the energy use for the experiment (Evans *et al*, 2011).

6.4 Case Study 2: Determination of the Orientation Relationship between Micro-crystals within Agglomerates

The interest to determine the angles between crystals is to understand the relationship between agglomerated crystals, whether they are preferably orientated or only randomly orientated. The angle calculations had been done for agglomerated aspirin, unmodified urea and urea modified by biuret at different cooling rates. The entire angle calculated using vector equation and stereographic projection methods. In this section, the development of stereographic projection is discussed in section 6.4.1.

6.4.1 Development of a Stereographic Projection Method for Agglomerated Micro-crystals

In crystallography, stereographic projection method is well known as a technique for use in characterisation of crystal orientation, in particular for understanding the angular relationship between different crystal faces. Fundamentally, the stereographic projection is a projection of planes normal sphere onto a sphere. It is a method to represent the planes of faces in crystal to recognise the zones to which they belong and determine the angles between the planes without repetitive calculations. In this the information within sphere can be projected onto any pre-define plane which appears at the centre of the resulting projection circle. This method overcomes the problem in viewing the crystal faces that cannot be seen in crystal drawing (the hidden faces).

In this study, the stereographic projection method was applied to determine the orientation relationship between agglomerated crystals. From the diffraction data collection, the information of orientation matrices of each individual micro-crystal was used to produce a projection in which the central pole direction was co-linear with the synchrotron radiation beam direction. By overlaying separate projections obtained from different micro-crystals within agglomerates the orientation inter-relationship between the component micro-crystals could be determined. The development of this specific stereographic projection program was proposed and led from this PhD study and implemented through collaborative work with Dr. Richard Gildea at the Diamond Light Source. The projection produced enabled the measurement of interplanar angles between two crystals to calculate the angle using Wulff net (Figure 6.2). The method was based on Stokes *et al.*, 1986.

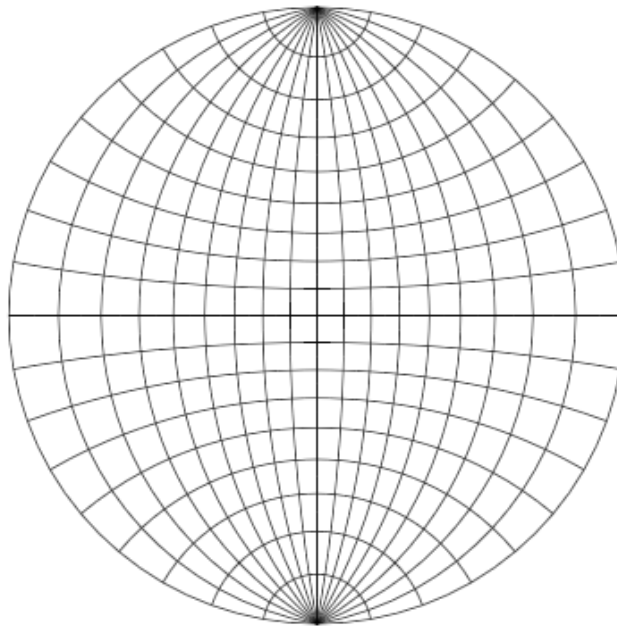


Figure 6.2: Diagram of Wulff net used for determine the angle between planes and directions of crystals.

The program produced the projection of the planes of the crystals. Figure 6.3 shows the example of the stereographic projection of agglomerated urea that consists of two projection of the urea crystals planes. These two projection of crystals can be differentiate by the colours of the spots which blue and red colours indicate projection of crystal 1 and crystal 2. Each spot projects each plane that exist in the crystal. Therefore, from the spots, the angle can be calculated by selecting one spot from crystal 1 and 2, e.g., plane (110) which highlighted in green circle in figure 6.3. After the selection of the planes to calculate the angle, the Wulff net is overlaid onto the stereographic projection plot.

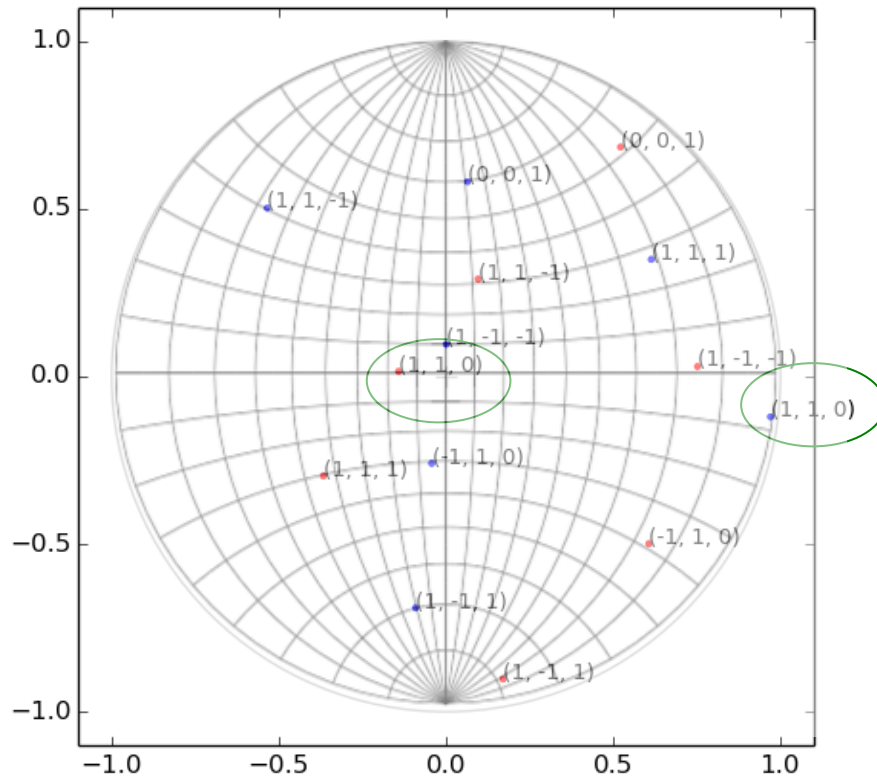


Figure 6.3: Example of stereographic projection result on agglomerated urea crystals. Blue and red spots indicate the projected plane for crystal 1 and 2. Green circles around the (110) plane of both crystals are selected planes to be used to calculate the angle between planes.

The Wulff net is rotated until the both two planes aligned at the great circle, as shown in figure 6.4. The space between line of the great circle is 10° . Therefore, the angle between plane (110) crystal 1 and (110) crystal 2 is 110° .

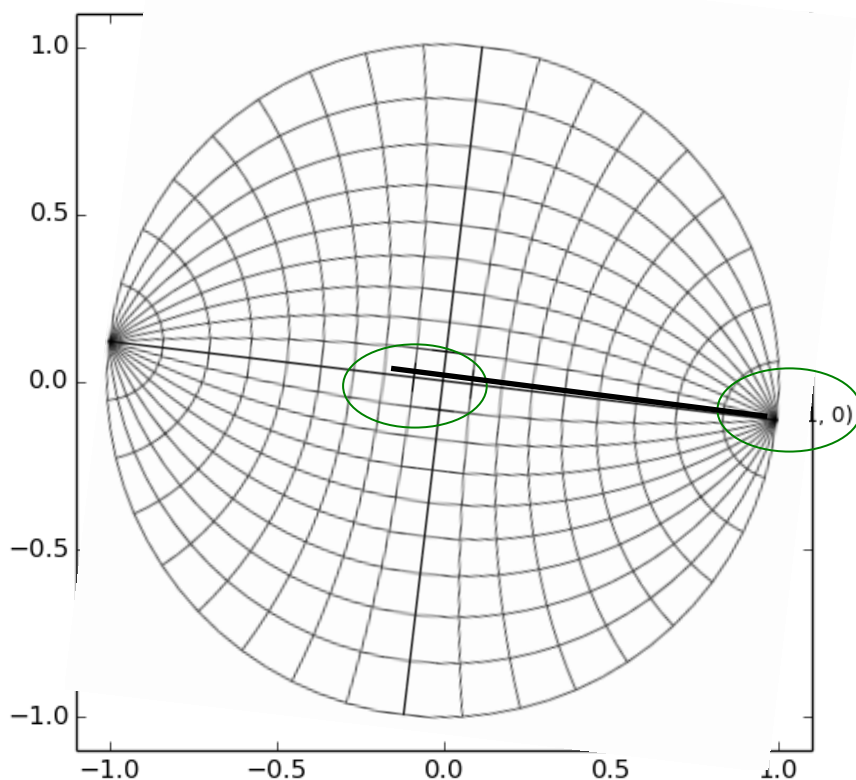


Figure 6.4: Example of stereographic projection result on agglomerated urea crystals. Blue and red spots indicate the projected plane for crystal 1 and 2. Green circles around the (110) plane of both crystals are selected planes to be used to calculate the angle between planes. The Wulff net is overlaid on the projected plot and rotated to calculate the angle between the planes by aligning two planes on the great circle.

6.4.2 Agglomerated Aspirin

The agglomerated aspirin crystals shown in figure 6.5 and 6.6 were analysed for orientation relationship study. The orientation was analysed between morphological importance faces of aspirin, which in this case (100), (110), and (011), based on MORANG calculations (Docherty & Roberts, 1988) and based on literature in which determined using BFDH method (Docherty *et al.*, 1991) to determine its morphology prediction (Meenan, 1997), (Aubrey *et al.*, 2007). The angle calculation using vector equation shown in table 6.13 while table 6.14 and 6.15 listed the angle determined using stereographic projection method for both agglomerated aspirin crystals.

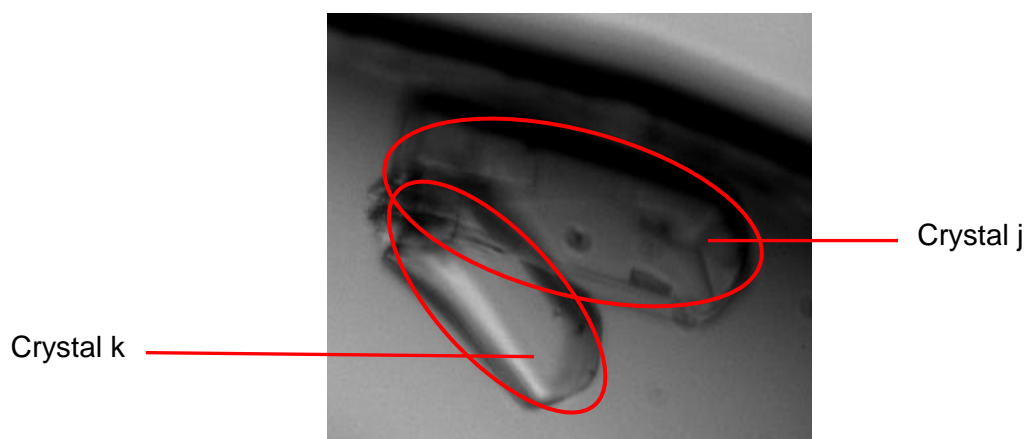


Figure 6.5: Image of 2 agglomerated aspirin crystals taken at beamline I24 DLS

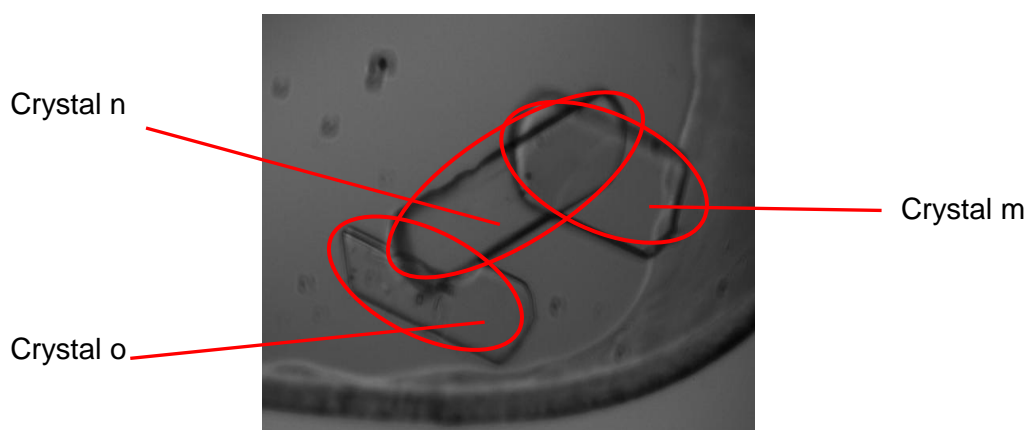


Figure 6.6: Image of aspirin crystals agglomerated captured from beamline I24 DLS

Table 6.13: Angle calculation of agglomerated aspirin crystals using vector equation

Agglomerated Aspirin Sample	Angle between crystals :	Angle in Unit Cell Axis		
		a (°)	b (°)	c (°)
1 (2 crystals)	1j & 1k	112.4	43.2	130.4
2 (3 crystals)	2m & 2n	21.3	45.5	46.9
	2n & 2o	154.8	135	109.5
	2m & 2o	171.3	179	2.7

Table 6.14: Angle determination using stereographic projection method of agglomerated aspirin (sample 1)

Planes for crystals 1		(angle, θ ($^{\circ}$))
j	k	
(1 0 0)	(1 0 0)	68
(1 1 0)	(1 1 0)	84
(0 1 1)	(0 1 1)	70
(1 0 0)	(1 1 0)	43
(0 1 1)	(0 -1 1)	14
(-1 1 0)	(-1 1 0)	10

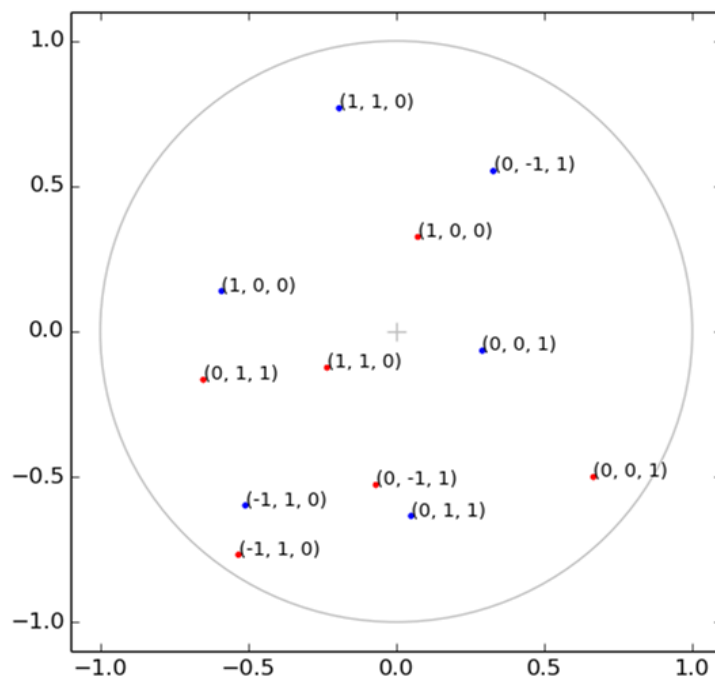


Figure 6.7: Stereographic projection plots of agglomerated aspirin crystals sample no.1: (sample j and k)

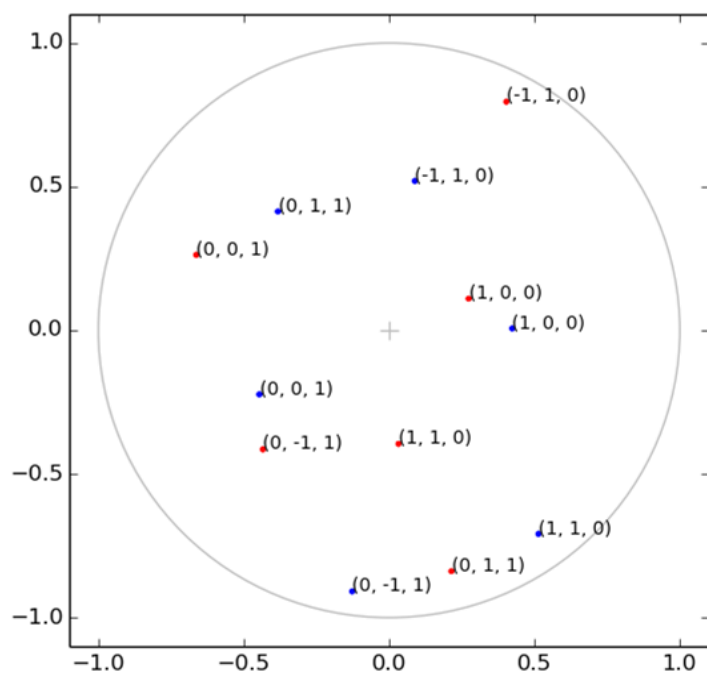


Figure 6.8: Stereographic projection plots for aspirin crystals samples no.2: (sample m & n)

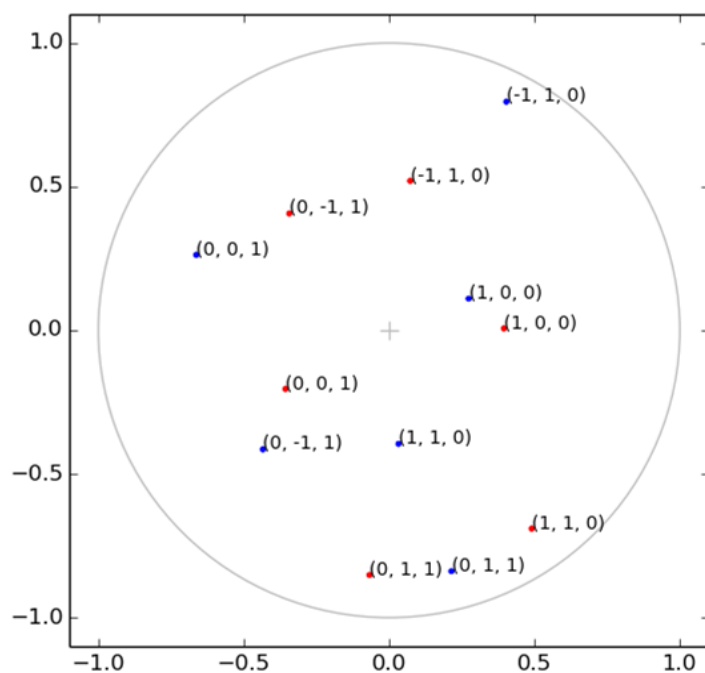


Figure 6.9: Stereographic projection plots for aspirin crystals sample no.2: (sample n and sample o)

Table 6.15: Angle determination using stereographic projection method of agglomerated aspirin (sample 2)

Planes for crystals 2			(angle, θ (°))
m	n	o	
(1 0 0)	(1 0 0)		18
(1 1 0)	(1 1 0)		47
(0 1 1)	(0 1 1)		132
(1 0 0)	(1 1 0)		58
(0 -1 1)	(0 1 1)		22
(-1 1 0)	(-1 1 0)		32
	(1 0 0)		(1 0 0)
	(1 1 0)	(1 1 0)	44
	(0 1 1)	(0 1 1)	20
	(1 0 0)	(1 1 0)	74
	(0 -1 1)	(0 1 1)	42
	(-1 1 0)	(-1 1 0)	32
(1 0 0)		(1 0 0)	2
(1 1 0)		(1 1 0)	2
(0 1 1)		(0 -1 1)	2
(1 0 0)		(1 1 0)	60
(-1 1 0)		(-1 1 0)	2

In this section, first, the discussion is on comparison between the results from vector equation calculations and stereographic projection method. To compare between both methods, the (100) plane was chosen as it is from the a-axes of table 6.13. The results from both showed the same angle determined (68°) in which 112° equivalent to 68° . The smallest angle that can be observed was between the (-110) planes which is 10° and between the (011) planes which is 14° . In sample 2 (figure 6.6), which involves three agglomerated aspirin crystals, the angles between crystals m-n, n-o, and m-o were determined. The angle between m-o was determined just to confirmed the angles obtained agree with the image in figure 6.5 that show the parallelism of the crystals gives very small angle values ((100), (110) and (011) planes) shown in table 6.15. Figure 6.10 shows the predicted morphology of aspirin based on attachment energy model (Hammond *et al.*,

2007). From this morphology prediction, the (100) face was found to be the largest face, thus the most morphological important face.

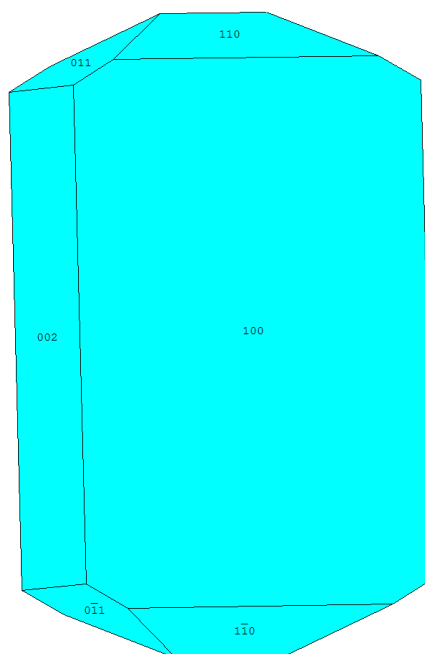


Figure 6.10: Morphology prediction of aspirin based on attachment energy

For more understanding about the surface chemistry of the aspirin crystal, at their faces, figure 6.11 shows the cleaved surfaces of (100), (011) and (110). At (100) surface, the carboxyl group is facing up at the face. Thus, it gives contribution to the hydrophilic characteristic. At this surface, it has possibility to form hydrogen bonding to other molecule that can have interaction with this face. It has been known that the cleaved plane always occurs at (100) due to the hydrogen bonding between two aspirin molecules that formed dimer. This intermolecular interactions has the weakest interaction energy, therefore the cleave plane easily occurs at (100) (Umiyama *et al*, 1979) . At (011) face, the carboxyl group one of the aspirin molecule exposed to the surface, while another molecule exposed its methyl group to the surface. In figure 6.8, the (110) face only has phenyl group exposed at the surface. Therefore, from the XMD results of angle calculations, the faces that has possibility to form hydrogen bonding tends to interact each other, as shown in the angles which very small angles between the planes was found.

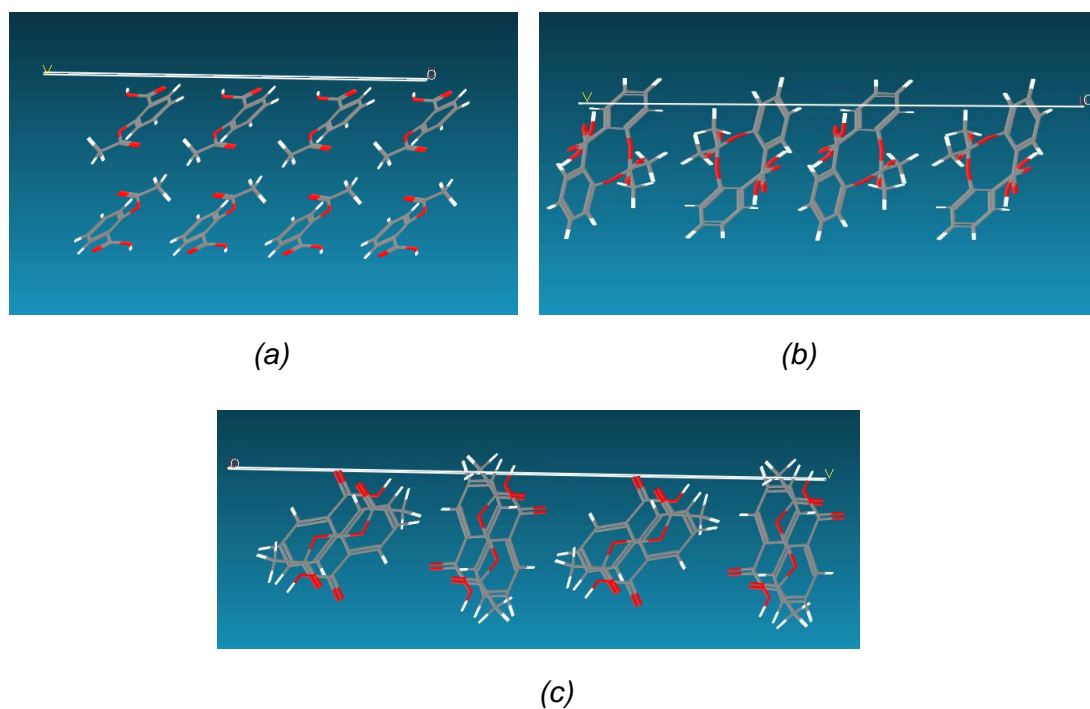


Figure 6.11: The cleave surfaces of aspirin at (a) (100), (b) (110), and (c) (001)

6.4.3 Agglomerated unmodified urea and urea modified by biuret as prepared at different cooling rates

In this section, the agglomerated unmodified urea and urea modified by biuret were analysed for orientation relationship between the agglomerated component micro-crystals. The results for angle calculated using vector equation and stereographic projection method was tabulated in table 6.16 to 6.25.

Table 6.16 and 6.17 show the values of angles for unmodified urea and urea modified by biuret recrystallised at $0.1^{\circ}\text{C}/\text{min}$. Figure 6.12 shows the image of sample no.5 as stated in table 6.16 and 6.17 for the agglomerated unmodified urea crystals together with the stereographic

projection plots for the agglomerates. Images for sample no.1 to sample no.4 are attached in the appendix as Figure 1 to 4.

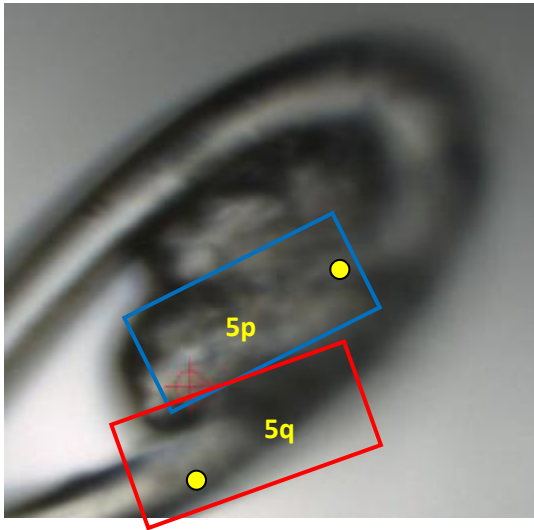
Table 6.16: Angle calculations between agglomerated unmodified urea 0.1°C/min using vector equation

Agglomerated Urea Sample No.	Angle between crystals :	Angle in Unit Cell Axis		
		a (°)	b (°)	c (°)
1 (2 crystals)	1p & 1q	69.2	93.2	35.3
2 (2 crystals)	2p & 2q	44.4	102.8 (77.2)	82.2
3 (2 crystals)	3p & 3q	65.3	82.0	60.0
4 (2 crystals)	4p & 4q	53	50.1	24.3
5 (2 crystals)	5p & 5q	1.8	1.2	1.3

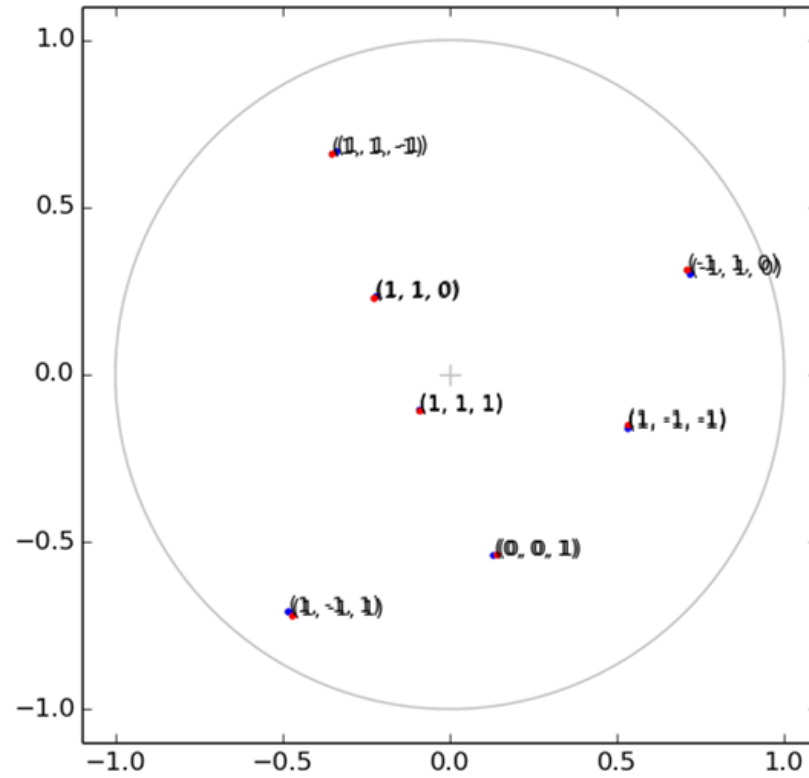
Table 6.17: Angle calculations between agglomerated unmodified urea 0.1°C/min using stereographic projection

Planes for crystals		angle, θ (°) for samples:				
P	q	1	2	3	4	5
(0 0 1)	(0 0 1)	36	82	60	154 (26)	0
(1 1 0)	(1 1 0)	32	74	88	44	0
(0 0 1)	(1 1 0)	63	68	34	66	90
(1 1 1)	(1 1 1)	120	95	66	30	0
(1 1 1)	(1 1 0)	83	64	54	36	40
(0 0 1)	(1 1 1)	100	69	16	26	50

The values of angles in table 6.17 were determined from the stereographic plots by using the Wulff net to determine the orientation angles between two crystals. Sample no.5 gives the significant interest as the value of the angles shows the parallelism between the crystals.



(a)



(b)

Figure 6.12: (a) Image of unmodified urea crystals recrystallised at $0.1^{\circ}\text{C}/\text{min}$ (sample no.5 in Table 6.16 and 6.17). Blue and red boxes indicate the position of the agglomerated crystals. The yellow spots indicate the point where the beam hits the crystal during data collection, (b) stereographic projections plotted for sample no.5 (blue: crystal 5p & red: crystal 5q).

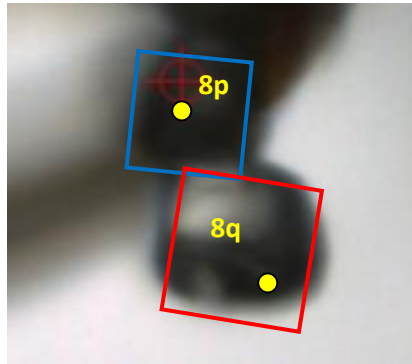
Table 6.18 and 6.19 show the angle calculations between agglomerated urea modified by biuret crystals recrystallised at 0.1°C/min using vector equation and stereographic projection methods. Figure 6.13 is the image of the agglomerated crystals for the sample no.8 which tabulated in the mentioned tables. Images for samples no.6, 7, and 9 are attached in the appendix as Figure 5 to 8.

Table 6.18: Angle calculations between agglomerated urea modified by biuret 0.1°C/min using vector equation.

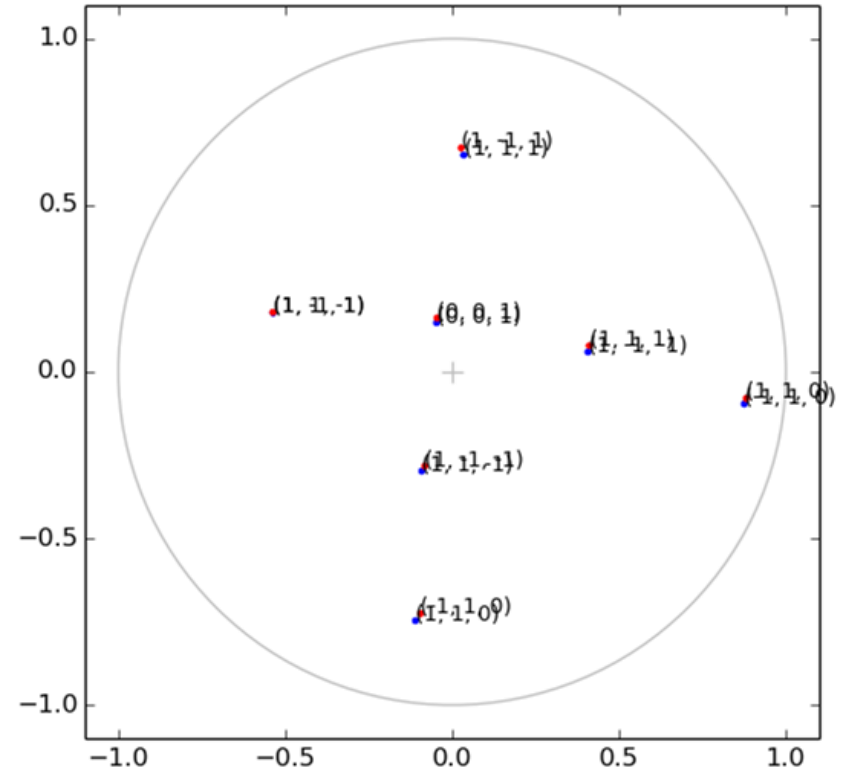
Agglomerated Urea Biuret Sample No.	Angle between crystals :	Angle in Unit Cell Axis		
		a (°)	b (°)	c (°)
6 (2 crystals)	6p & 6q	14.1	11.7	16.6
7 (2 crystals)	7p & 7q	34.2	26.1	34.7
8 (2 crystals)	8p & 8q	89.1	89.1	1.7
9 (2 crystals)	9p & 9q	35.9	60.4	72.2

Table 6.19: Angle calculations between agglomerated urea modified by biuret 0.1°C/min using stereographic projection

Planes for crystals		angle, θ (°) for samples:			
P	q	6	7	8	9
(0 0 1)	(0 0 1)	102	34	0	72
(1 1 0)	(1 1 0)	128	39	90	16
(0 0 1)	(1 1 0)	44	56	90	21
(1 1 1)	(1 1 1)	90	34	64	45
(1 1 1)	(1 1 0)	90	16	90	28
(0 0 1)	(1 1 1)	134	15	50	109



(a)



(b)

Figure 6.13: (a) Image of urea modified by biuret crystals recrystallised at $0.1^{\circ}\text{C}/\text{min}$ (sample no.8 in Table 6.18 and 6.19) Blue and red boxes indicate the position of the agglomerated crystals. Yellow spots indicate the point where the beam hits the crystal during data collection, (b) stereographic projections plotted for sample no.8 (blue: crystal 8p & red: crystal 8q).

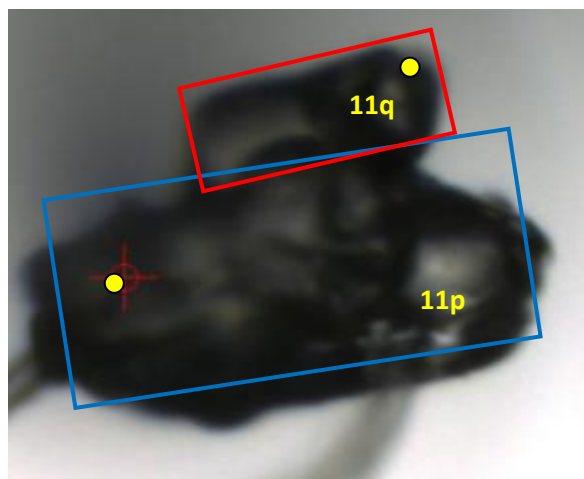
Table 6.20 and 6.21 show the angle calculations between agglomerated urea modified by biuret crystals recrystallised at 0.5°C/min using vector equation and stereographic projection methods. Figure 6.14 is the image of the agglomerated crystals for the sample no.11 which tabulated in the mentioned tables. Images for samples no.10 is attached in the appendix.

Table 6.20: Angle calculations between agglomerated unmodified urea 0.5°C/min using vector equation

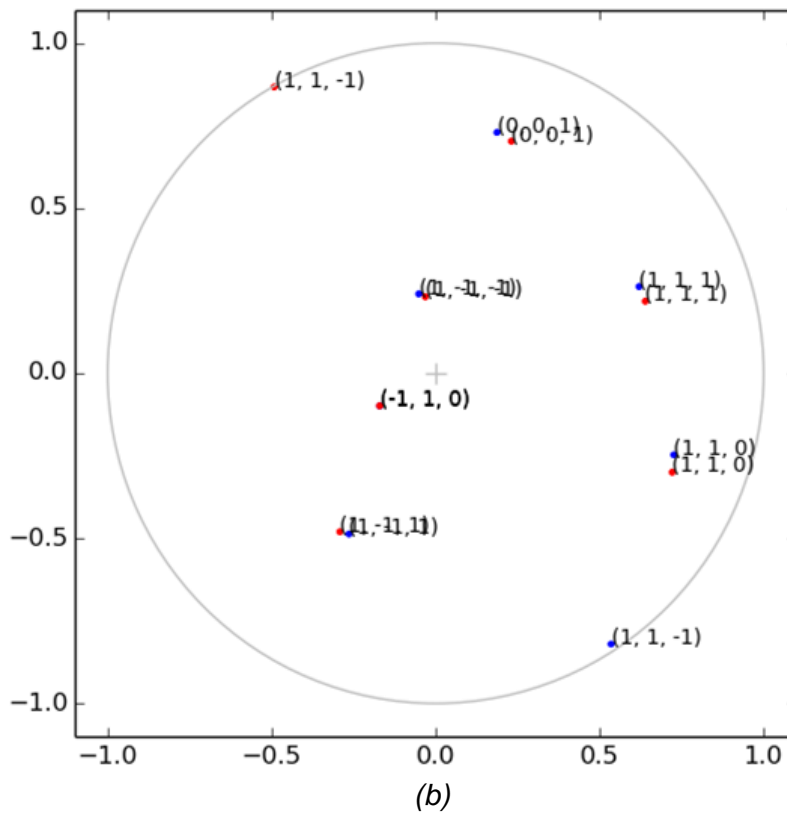
Agglomerated Urea Sample No.	Angle between crystals :	Angle in Unit Cell Axis		
		a (°)	b (°)	c (°)
10 (2 crystals)	10p & 10q	91.3	89.1	16.1
11(2 crystals)	11p & 11q	12.3	2.6	3.8

Table 6.21: Angle calculations between agglomerated unmodified urea 0.5°C/min using stereographic projection

Planes for crystals		angle, θ (°) for samples:	
p	q	10	11
(0 0 1)	(0 0 1)	16	4
(1 1 0)	(1 1 0)	90	4
(0 0 1)	(1 1 0)	104	94
(1 1 1)	(1 1 1)	74	4
(1 1 1)	(1 1 0)	100	44
(0 0 1)	(1 1 1)	66	54



(a)



(b)

Figure 6.14: (a) Image of unmodified urea crystals recrystallised at $0.5^{\circ}\text{C}/\text{min}$ (sample no.11 in Table 6.20 and 6.21). Blue and red boxes indicate the position of the agglomerated crystals. The yellow spots indicate the point where the beam hits the crystal during data collection, (b) stereographic projections plotted for sample no.11 (blue: crystal 11p & red: crystal 11q).

Table 6.22 and 6.23 show the angle calculations between agglomerated unmodified urea crystals recrystallised at 1.0°C/min using vector equation and stereographic projection methods. Figure 6.15 shows the stereographic projection plots for sample no. 12 while Figure 6.16 and 6.17 show the images of the agglomerated crystals together with the stereographic projection plots for sample no. 13 and 15. Image of sample no. 14 is attached in the appendix.

Table 6.22: Angle calculations between agglomerated unmodified urea 1.0 °C/min using vector equations

Agglomerated Urea Sample No.	Angle between crystals :	Angle in Unit Cell Axis		
		a (°)	b (°)	c (°)
12 (2 crystals)	1p & 1q	0.1	0.1	0.1
13 (2 crystals)	2p & 2q	0	0	0
14 (2 crystals)	3p & 3q	30.7	85.7	78
15 (2 crystals)	4p & 4q	0.3	0.2	0.2

Table 6.23: Angle calculations between agglomerated unmodified urea 1.0 °C/min using stereographic projections

Planes for crystals		Samples (angle, θ (°))			
p	q	12	13	14	15
(0 0 1)	(0 0 1)	0	0	78	0
(1 1 0)	(1 1 0)	0	0	68	0
(0 0 1)	(1 1 0)	90	90	26	90
(1 1 1)	(1 1 1)	0	0	95 (85)	0
(1 1 1)	(1 1 0)	39	40	106 (74)	40
(0 0 1)	(1 1 1)	50	50	126 (54)	130 (50)

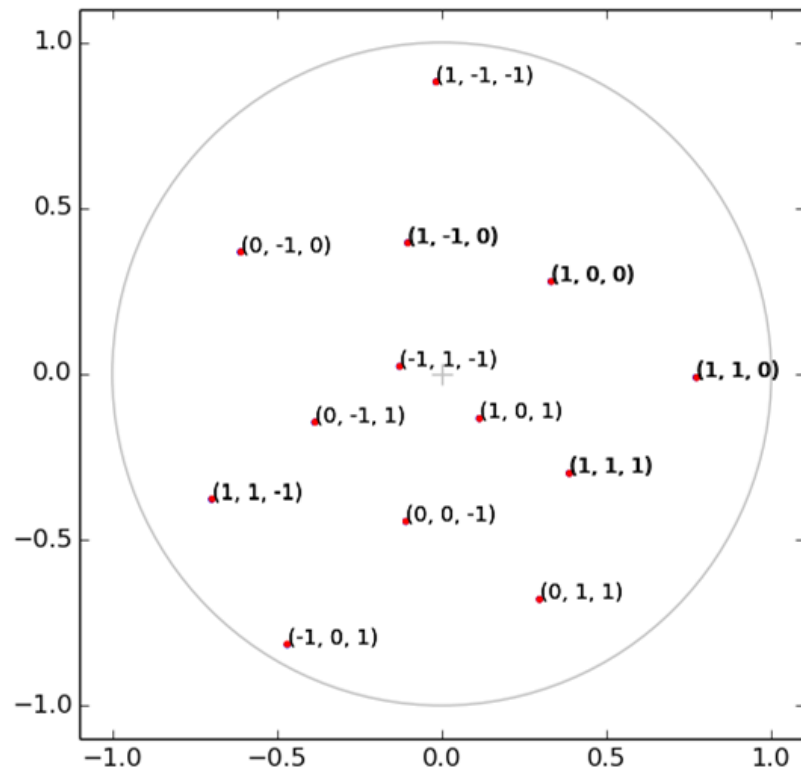
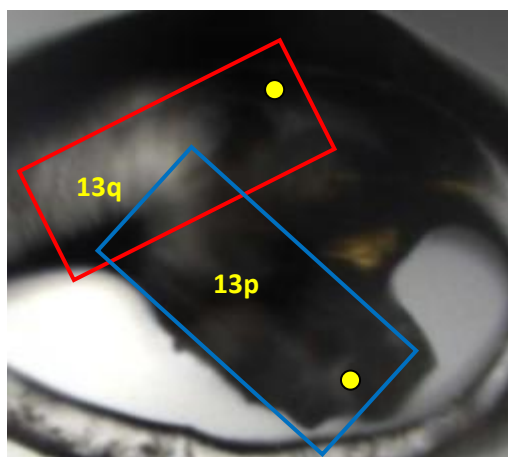
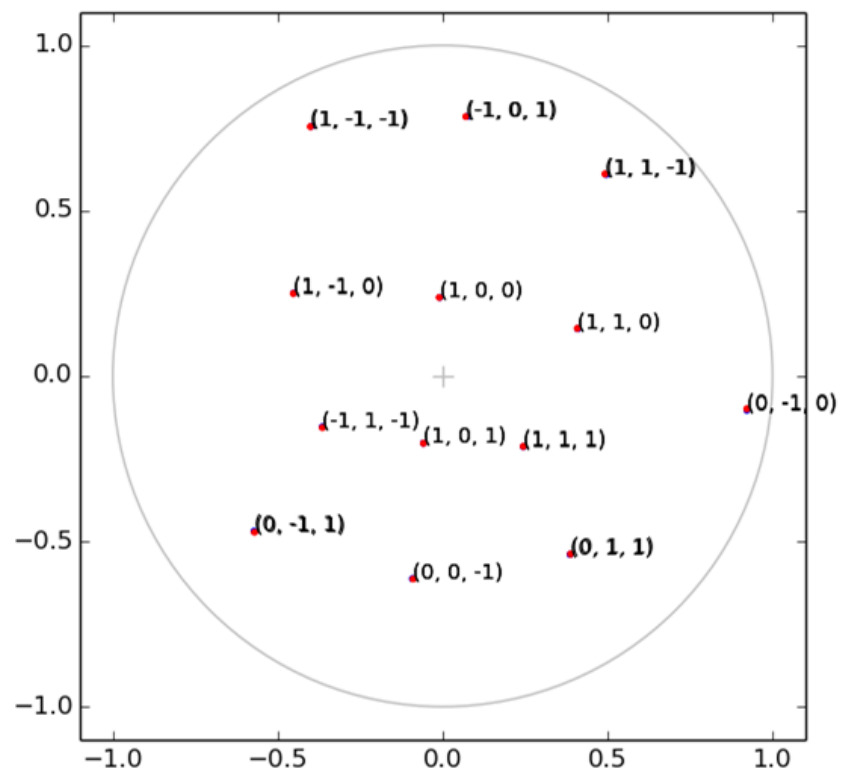


Figure 6.15: Stereographic projection plot for sample no. 12 in table 6.22 and 6.23

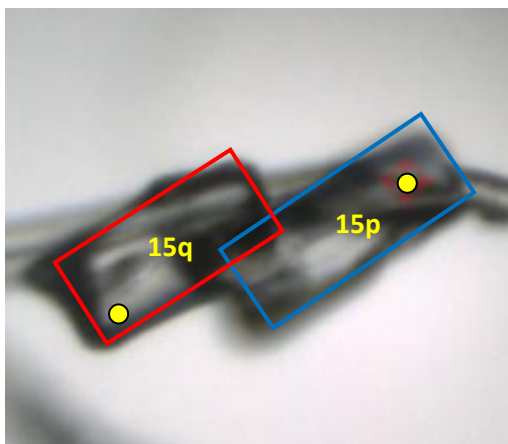


(a)

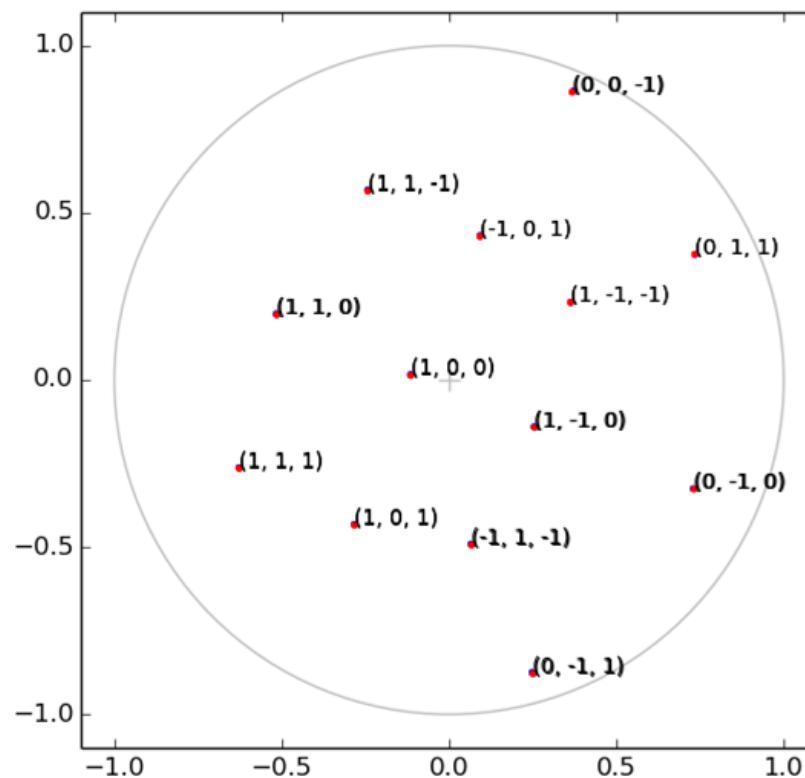


(b)

Figure 6.16: (a) Image of unmodified urea crystals recrystallised at $1.0^{\circ}\text{C}/\text{min}$ (sample no.13 in Table 6.22 and 6.23). Blue and red boxes indicate the position of the agglomerated crystals. The yellow spots indicate the point where the beam hits the crystal during data collection, (b) stereographic projections plotted for sample no.13 (blue: crystal 13p & red: crystal 13q). Blue dots cannot be seen in the plotted image because the plots overlapped with the red dots plotted.



(a)



(b)

Figure 6.17: (a) Image of unmodified urea crystals recrystallised at $1.0^{\circ}\text{C}/\text{min}$ (sample no.15 in Table 6.22 and 6.23). Blue and red boxes indicate the position of the agglomerated crystals. The yellow spots indicate the point where the beam hits the crystal during data collection, (b) stereographic projections plotted for sample no.15 (blue: crystal 15p & red: crystal 15q). The blue dots cannot be seen in the plotted image because the plots overlapped with red dots plots.

Table 6.24 and 6.25 show the angle calculations between agglomerated unmodified urea crystals recrystallised at 1.0°C/min using vector equation and stereographic projection methods. Figure 6.18 shows the image of the agglomerated crystals together with the stereographic projection plots for sample no.17. Image for sample no. 16 is attached in the appendix.

Table 6.24: Angle calculations between agglomerated urea modified by biuret 1.0 °C/min using vector equation

Agglomerated Urea-biuret Sample No.	Angle between crystals :	Angle in Unit Cell Axis		
		a (°)	b (°)	c (°)
16 (2 crystals)	1p & 1q	91.3	91	51.1
17 (2 crystals)	2p & 2q	78.4	79.4	11

Table 6.25: Angle calculations between agglomerated urea modified by biuret 1.0 °C/min using stereographic projection

Planes for crystals		Samples (angle, θ (°))	
p	q	16	17
(0 0 1)	(0 0 1)	130 (50)	12
(1 1 0)	(1 1 0)	80	80
(0 0 1)	(1 1 0)	56	94
(1 1 1)	(1 1 1)	(100) (80)	54
(1 1 1)	(1 1 0)	112 (68)	86
(0 0 1)	(1 1 1)	90	54

In stereographic projection analysis, angle between planes were determined. The angles values of agglomerated unmodified urea and modified urea by biuret crystals were compared. First, this work is discussed on the validation of the angle calculations using vector equation and using stereographic projection method. Three planes were chosen which $\{100\}$, $\{0-10\}$ and $\{00-1\}$ from stereographic projection plots. This is to compare the values obtained from the vector calculations in which it calculates the angle between planes by the vector of a- , b- and c- axes with the angles values determined by streographic projection method. From all the values obtained, it is confirmed that the values are same and validate the results. To explain clearly the orientation relationship between the agglomerated crystals, the planes that were chosen to determine the relationship are listed in table 6.26. There are many planes that can be used to determine the angles between crystals plane, however, to simplify it; those planes in table 6.26 were chosen.

Table 6.26: Planes use for angle calculations determination

Planes for crystals	
p	q
(0 0 1)	(0 0 1)
(1 1 0)	(1 1 0)
(0 0 1)	(1 1 0)
(1 1 1)	(1 1 1)
(1 1 1)	(1 1 0)
(0 0 1)	(1 1 1)

Table 6.27 summarises the angle determination of the agglomerated urea crystals.

Table 6.27: Summary of angle calculations of the agglomerated unmodified urea and urea modified by biuret crystals. The samples summarised are chosen based on the smallest angle value to show the parallelism between crystals.

Planes		*Actual angle between planes	Samples (°)						
			5	8	11	12	13	15	17
(0 0 1)	(0 0 1)	0	0	0	4	0	0	0	12
(1 1 0)	(1 1 0)	0	0	0	4	0	0	0	80
(0 0 1)	(1 1 0)	90	90	90	94	90	90	90	94
(1 1 1)	(1 1 1)	0	0	64	4	0	0	0	54
(1 1 1)	(1 1 0)	40	40	40	44	39	40	40	86
(0 0 1)	(1 1 1)	50	50	50	54	50	50	50	54

**Actual angle between planes calculated by using MORANG program*

In this study, the comparison between the same crystals in the same batch, for example five samples of unmodified urea crystallised at 0.1°C/min in table 6.16 and 6.17 showed the values of the angles were in random numbers. The same results for unmodified urea crystals at other cooling rates, and urea modified urea by biuret crystals. However, there were seven samples that show they are parallel to each other (as shown in table 6.27). The samples number 5, 8, 12, 13 and 15 show the perfect parallelism occurred between two agglomerates urea crystals. Samples number 11 and 17 are slightly misoriented for small degrees. Overall, these seven results from the agglomerated urea crystals show the crystals are aligned to each other. The results show good example of preferred orientation with parallel agglomeration. Outside this experiment, the observation on agglomeration of

urea crystals under microscope showed that the agglomerated urea crystals are mostly parallel and align to each other, either parallel at the same orientation or at opposite direction. This perhaps reflects the epitaxial nature of the growth process for many crystals (Chemla, 2012). In general, the epitaxy growth occurs by forming a new layer film on top of the growing surface. In the case of urea, the epitaxy growth occurs on the same materials known as homoepitaxy. It shows the epitaxially grown crystals that occur at its {110} interface. It is could be because of the fastest growth occurs at [001] direction, therefore the epitaxial growth selectively occurs at the most stable growing face which is {110} form. It is apparently the crystals grown in parallel to each other during crystal growth, regardless the crystals growth at different conditions of cooling rates and with the impurities. The surface chemistry of urea has been explained in detail in chapter 5 in molecular modelling section.

In both cases, aspirin and urea agglomerates, the results confirmed that the angles obtained from vector calculations and stereographic projections agreed each other with additional proof by observing the agglomerates micro-crystals samples images that the angles determined are similar to the orientation of the crystals in the images. In this study, the application of stereographic projection in crystallography, specifically the combination of it with the information obtained from X-ray diffraction data can be a platform to understand the relationship between agglomerated particles. As the basic application of this method is to determine the angular relationships within one crystal faces, it had been applied to determine the relationships between twinning planes of twinned crystal (Dechamps *et al*, 2000), and understand defects occur in crystal (Salje, 1995). From this study, the relationships of homoepitaxy growth on agglomerates micro-crystals can be understood and helps to further use of the stereographic projection.

6.5 Case study 3: Studies of the Polymorphic forms and transformation of L-glutamic acid

6.5.1 Crystallisation of L-glutamic acid polymorphic forms

In this case study, the polymorphic transformation of α - to β - LGA had been examined. The crystallisation of these polymorphs was done by dropping 0.1ml of LGA solution on to the glass slide and seeding this with α -LGA added to droplet and left overnight to observe the transformation in room temperature under hot stage microscope. Typical results are shown in figure 6.19:

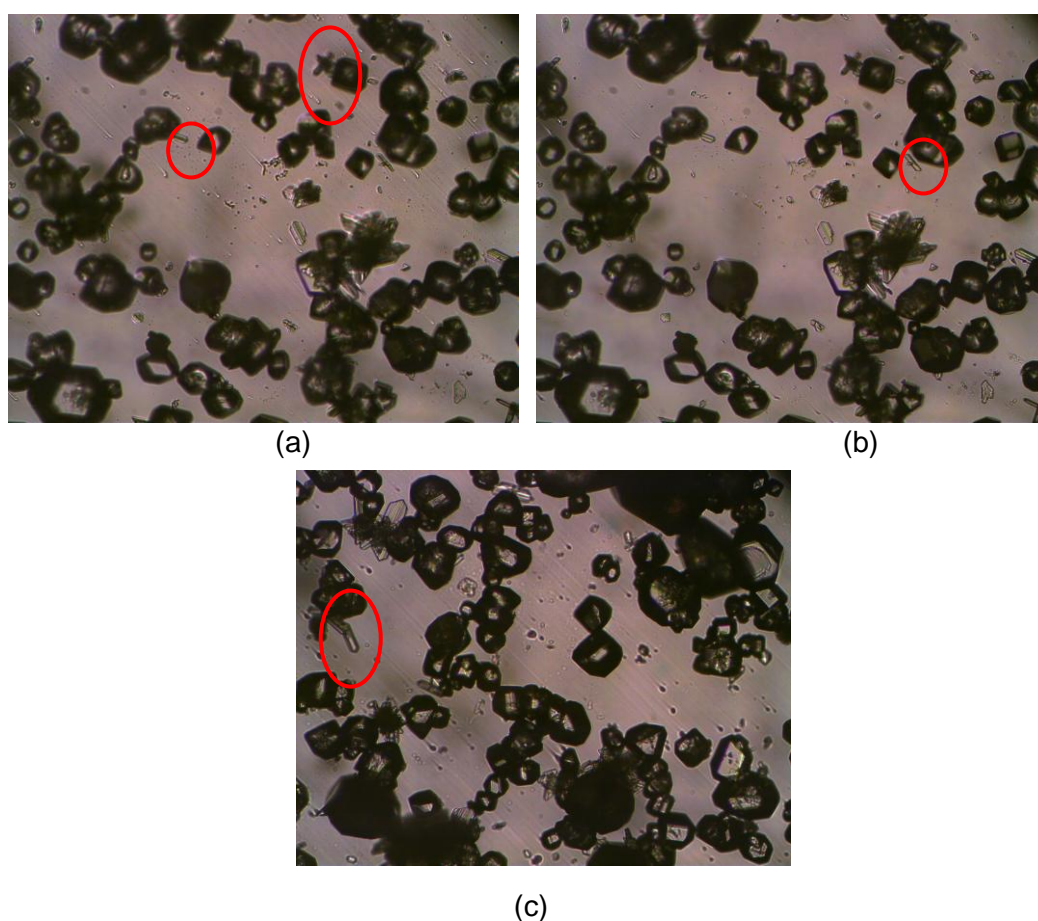


Figure 6.19: The crystals of LGA observed under hot stage microscope. Prismatic shape belongs to α -LGA and observable needle-like shape belongs to β -LGA (in red circles).

From the observation, the transformation of α - to β -LGA was achieved. At room temperature, the transformation occurred slowly. Figure 6.19 shows the formation of β - forms from the α -forms. At room temperature, the polymorphic transformation was observed to occur quite slowly and the rate also found to depend on the concentration of the solution. In this work, the concentration that was chosen was close to that for saturation of the α - form. In this way polymorphic transformation to the β - form was carefully controlled. Such is important in order to achieve the presence of the both polymorphic forms that β - form growth from α - form (as observed in the figure 6.19 in the red circle). These partly transformed crystals then subsequently further used for XRD analysis and through this to study the interfacial relationship between the two polymorphic forms.

6.5.2 The Change of Unit Cell Parameters in Mediated Polymorphic Transformation Crystal of L-glutamic acid

The unit cell parameters of the contacting micro-crystals of the two polymorphic forms of L-Glutamic acid (LGA) α - and β - form were measured. The data was collected at different points of the two crystal agglomerates. Table 6.28 shows the results of unit cell constants of two polymorphic forms of α - and β -LGA. Image for sample one, two and three are shown in Figure 6.17. All three samples are crystals of LGA with β -LGA grown topotaxically growing out of the α -form.

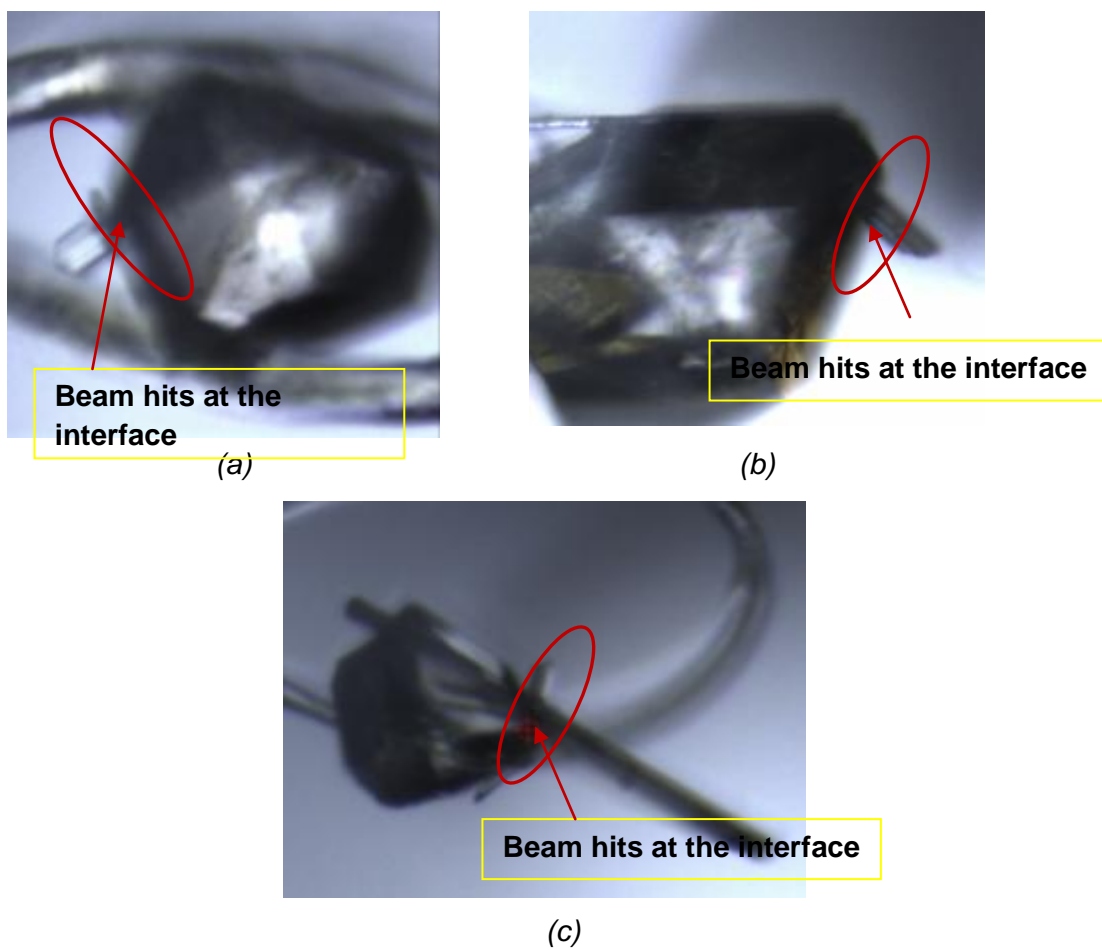


Figure 6.20: Samples of LGA with β – crystal grows from α -LGA. The arrow pointed on the point of the beam hits the interface: (a) sample 1, (b) sample 2, (c) sample 3.

Table 6.28: Unit cell constants results of 2 polymorphic forms of LGA. The value of unit cell constants of α -LGA indicates the data collected at α - crystal, near the interface of β -LGA, β -LGA indicates the data collected at β - crystal, interface indicates the data collected at the interface of α - and β - crystals, and inside α indicates the data collected at α - crystals, far away from the growing β - crystals.

Crystals	Unit cell	a	B	c
Sample 1	α - LGA	10.243	8.732	6.980
	β - LGA	-	-	-
	interface	10.235	8.737	6.977
		5.134	6.894	17.236
	Inside α	10.259	8.748	6.996
Sample 2	α - LGA	10.267	8.754	6.998
	β - LGA	5.133	6.888	17.233
	interface	10.241	8.738	6.979
		5.126	6.878	17.213
	Inside α	10.266	8.755	6.998
Sample 3	α - LGA	10.245	8.745	6.985
	β - LGA	5.133	6.889	17.239
	interface	5.133	6.882	17.232
	Inside α	5.136	6.888	17.235
<p>Unit cell constants for α-form from literature: $a=10.282$, $b=8.779$, $c=7.068$ and all α, β, and γ values are 90° (Lehmann & Nunes, 1980).</p> <p>Unit cell constants for β-form from literature: $a=5.154$, $b=6.942$, $c=17.274$ and α, β, and $\gamma = 90^\circ$ (Marcoin, et al., 1999)</p>				

Firstly, the discussion will be on α -LGA. For all three samples, data collections for α -LGA were collected around the large area of the crystal (as noted in the table as α -LGA). As shown in Table 6.28, it clearly shows the correct unit cell parameter to be consistent with the published structure of α -LGA. The crystal is $P2_12_12_1$, with orthorhombic. The values were compared with literature: $a=10.282$, $b=8.779$, $c=7.068$ and all α , β , and γ values are 90°

(Lehmann & Nunes, 1980). A slight difference with respect to the literature was observed associated with a percentage difference of 0.4%, 0.8%, and 1% for each a, b, and c values, respectively. Data collection at inside α -LGA means the data area of data was being collected close to the interface, but still in area of α -form. For this area, the values obtained are expected to have lattice parameter of α -form for sample 1 and 2. However, sample 3 gives value of lattice parameter of β form. The explanation for this is that perhaps because of the area is closed to the interface, in which the β -form started to grow; therefore, it may already to have arrangement of β -form. For data collection at β -form crystal, the beam hit the tip of the crystal. However, the result for sample 1 of β -LGA could not be determined as it failed to be indexed, thus further data processing could not proceed. The reason for this failure in indexing was not clear but this may reflect the fact that the β -LGA did not grow perfectly as β , therefore, the reflection data obtained has some incorrect mapping from the diffraction spot. The other two samples give consistent lattice parameters of β -LGA, which are $a=5.154$, $b=6.942$, $c=17.274$ and α , β , and $\gamma = 90^\circ$ (Marcoin, *et al.*, 1999). The percentage variation for published data was 0.4%, 0.7%, and 0.2% for a, b, and c values respectively.

6.5.3 Angle calculations between the contacting two polymorphs resulting from the transformation between α - and β -forms of LGA

The orientation relationship between polymorphic transformations of α - to β -LGA was determined using both vector equation and stereographic projection methods. Two samples of LGA crystals were used for analysis. The important faces were selected in this study are {001}, {101}, and {111} of α -form and {101}, {020}, and {021} of β -form (Hammond, *et al.*, 2007). The results for both methods are tabulated in the Table 6.29 and 6.30:

Table 6.29: Angles calculations of LGA crystals using vector calculations

LGA Sample No.	Angle between crystals :	Angle in Unit Cell Axis		
		a (°)	b (°)	c (°)
1 (2 crystals)	alpha & beta	98.6	90.2	51.1
2 (2 crystals)	alpha & beta	59.8	47.6	70.6

Table 6.30: Angles calculations of LGA crystals using stereographic projections

Planes for crystals		Samples (angle, θ (°))	
Alpha	beta	Sample 2	Sample 3
(1 0 1)	(0 2 1)	8	70
(1 1 1)	(0 2 1)	28	2
(1 1 1)	(1 0 1)	64	26

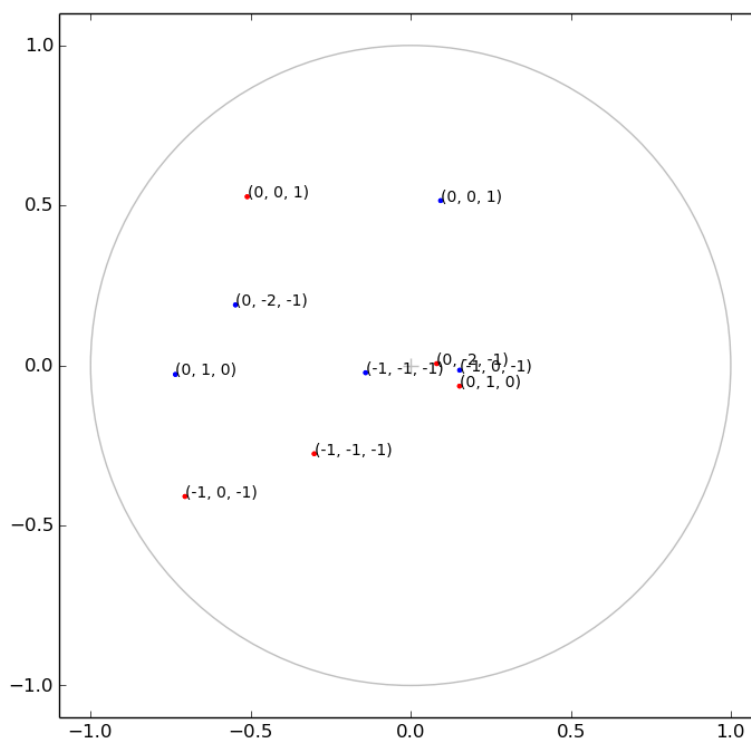
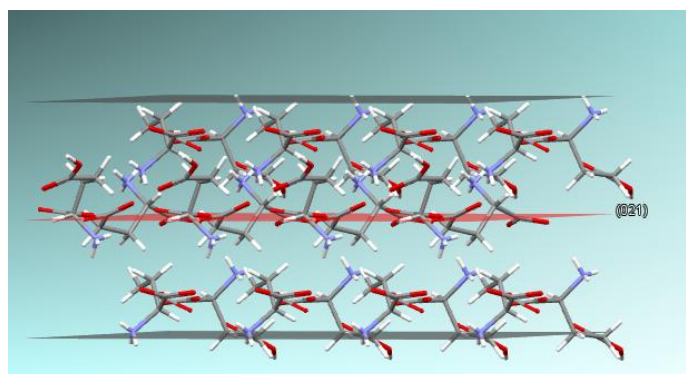
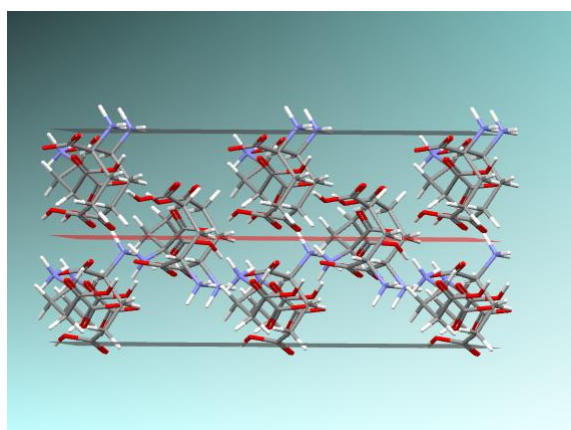


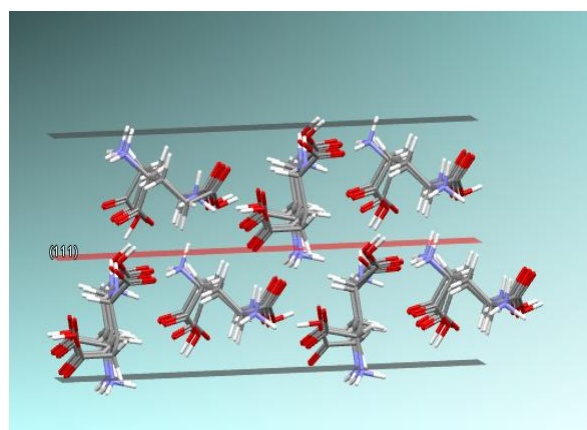
Figure 6.21: Stereographic projection plotted for sample no.2 of alpha (blue) and beta (red) LGA crystals



(a)



(b)



(c)

Figure 6.23: Molecular packing at surface of (a) (021) of beta form, (b) (101) of α -form, (c) (111) of α -form.

6.6 Case Study 4: Characterising the 3D shape of an Agglomerate of α -LGA using X-ray Micro-tomography

X-ray microtomography (XMT) work was conducted on I04 beamline at the Diamond Light Source. An agglomerated of α -LGA sample was used for XMT analysis with the aim to understand the morphology of 3D image. Absorption contrast mode was used to perform the XMT. The sample was

rotated between 0° to 180° for data collection to obtain the views of the projection at different angle. One of the images of the beam showing the projected sample image from the data collection is shown in Figure 6.24(a).

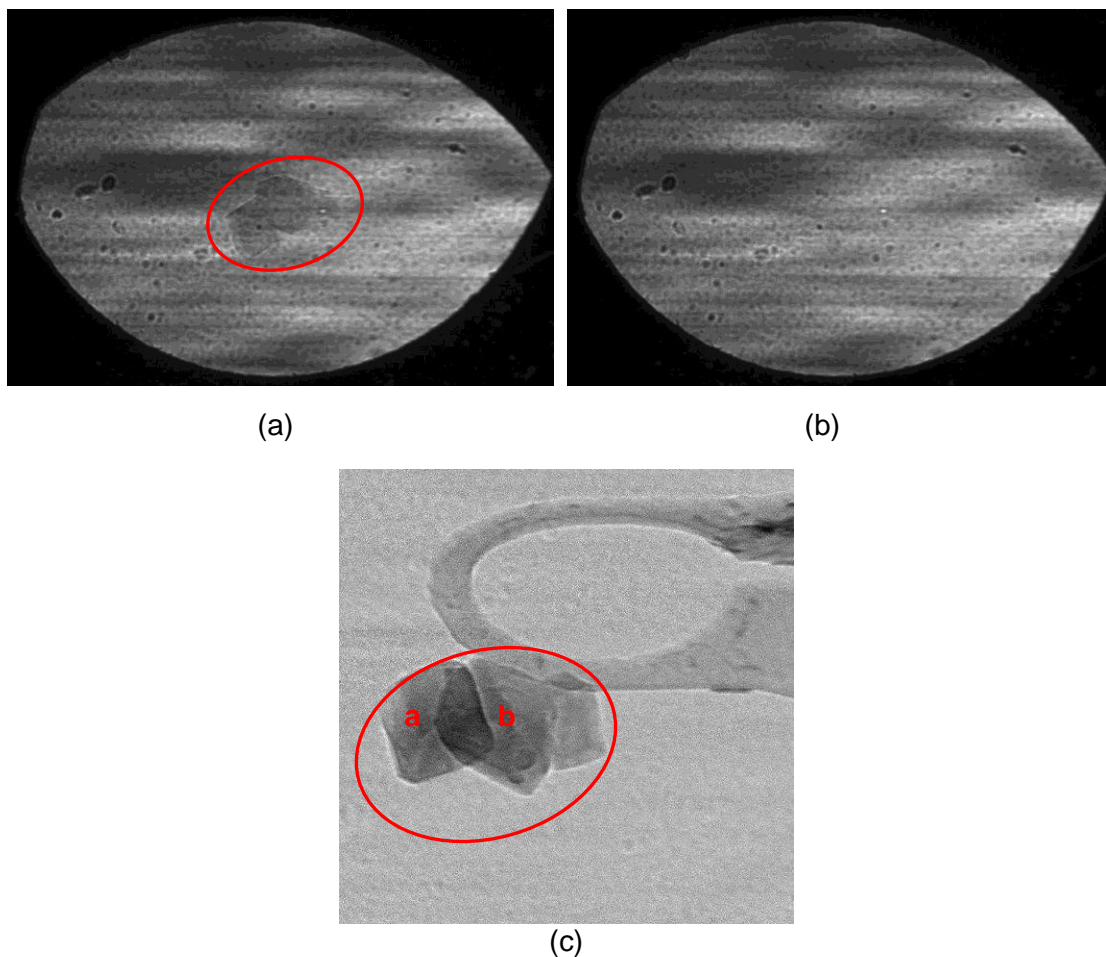


Figure 6.24: Image of XMT data collection: (a) image of the beam with the sample in, (b) flat field reference image, (c) image of the beam with sample after divided each images in (a) with image in (b). The sample is circled in red.

Using the ImageJ software (Ferreira & Rasband, 2012), the raw data images (example in Figure 6.24 (a)) were background subtracted with respect to the flat field reference image (Figure 6.24 (b)) i.e without sample to obtain just the absorption contrast of the sample itself (Figure 6.24 (c)). This process enables the acquisition of good quality images before the reconstruction process was carried out. The flat field reference image is the

image of field view without any sample exposed to the beam. Consistent beam intensity is important to produce good quality image as if the beam intensity were to change during the data collection period then good quality images with high absorption contrast could not be obtained.

After obtaining flat field correction images, reconstruction process was done using TomoJ software. In this process, the algorithms used were alignment of the tilt series, determination of the tilt axis and application of the ART (Algebraic Reconstruction Technique) using 10 iterations and a relaxation coefficient of 0.1. Alignment of the tilt series was found to be useful for shift and rotation correction of the images to produce good quality of the reconstruction volume tomogram. The ART is a suitable technique to be used to reconstruct tomography images for single particle analysis. A detail about the method used is explained in Messaoudill *et al.*, 2007. Figure 6.25 shows few slices of the reconstructed images.

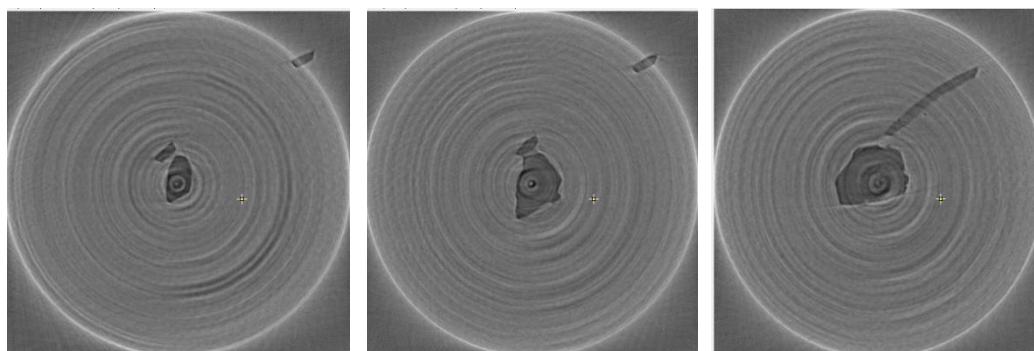


Figure 6.25: The images cut into slices in z-direction during reconstruction.

From the set of slices from reconstruction results, the two dimensional projections of the slice can be viewed as a full three-dimensional 3D image through a process called volume rendering. The resultant 3D image of agglomerated α -LGA sample so produced is shown in Figure 6.26.



Figure 6.26: 3D rendering image after reconstruction.

In XMT analysis, the 3D image of the agglomerated α -LGA sample was obtained. Using tomography analysis, morphology of crystals, specifically micron-sized particle can be obtained. This technique helps to get full understanding on determination of crystal morphology, as in 2D image, for example from conventional microscopy. Furthermore, from 3D image, the external faces of the crystal can be well determined, and provide a more effective way to define the crystal faces and external morphology of a micro-crystal. For this specific α -LGA sample, the 3D image can also be compared with the 2D image obtained from microscopic image (Figure 6.27).



Figure 6.27: Microscopic image of α -LGA crystals (captured by microscope camera from Morphologi G3).

There were researched on polymorphic transformation observation of α - and β -LGA done by Jacques *et al.*, 2005 and Pile *et al.*, 2006, which they used also novel in-situ imaging technique by synchrotron source as well. It was called Tomographic Energy Dispersive Diffraction Imaging (TEDDI), which the diffraction tomographic data collected in-situ in the model reactor. The samples were bulk crystallites. From the diffraction peaks and the mapping from tomographic imaging, the technique provides the information of the significant planes to determine the crystal alignment, and the intensity mapping of the concentration of the polymorphs in the reactor. Dharmayat *et al.*, 2006, also was done work on these polymorphs using combined XRD and on-line video microscopy. Again, this work done in slurries samples in-situ during transformation process occurs, which XRD can determine the structural differences when polymorphic transformation occurs from the diffraction pattern, while on-line video microscopy to detect the morphology changed when the transformation occurred. These two methods only showed the differences between two polymorphs in the slurries. However,

they were not be able to reveal the relationship in terms of how the transformation occurs from α - to β -LGA. There have been also been molecular modelling studies in which have attempted to show how this transformation can occur and on what the specific faces. (Hammond, *et al.* 2007).

6.6.1 X-ray microdiffraction data of agglomerated α -LGA

The diffraction experiment was carried out on the two agglomerated α -LGA shown in Figure 6.24 (as denoted a and b). Table 6.31 shows the routine data in diffraction work which is the unit cell parameters determination. Table 6.32 presents the angle calculation results from vector calculation and stereographic projection.

Table 6.31: Unit cell parameters determination of two agglomerated α -LGA

unit cell parameters	a	b	c	β
crystal j	6.996	8.758	10.265	90
crystal k	7.002	8.763	10.268	90

Table 6.32: Angle determination using vector calculations and stereographic projection method

Angle calculation based on vector calculations			
Angle between crystals :	Angle in Unit Cell Axis (°)		
	a	b	c
a & b	14	6	49.344
Angle calculated from stereographic projection			
Planes for crystals		Angle (°)	
a	b		
(101)	(101)	80	
(111)	(111)	80	
(101)	(02-1)	28	

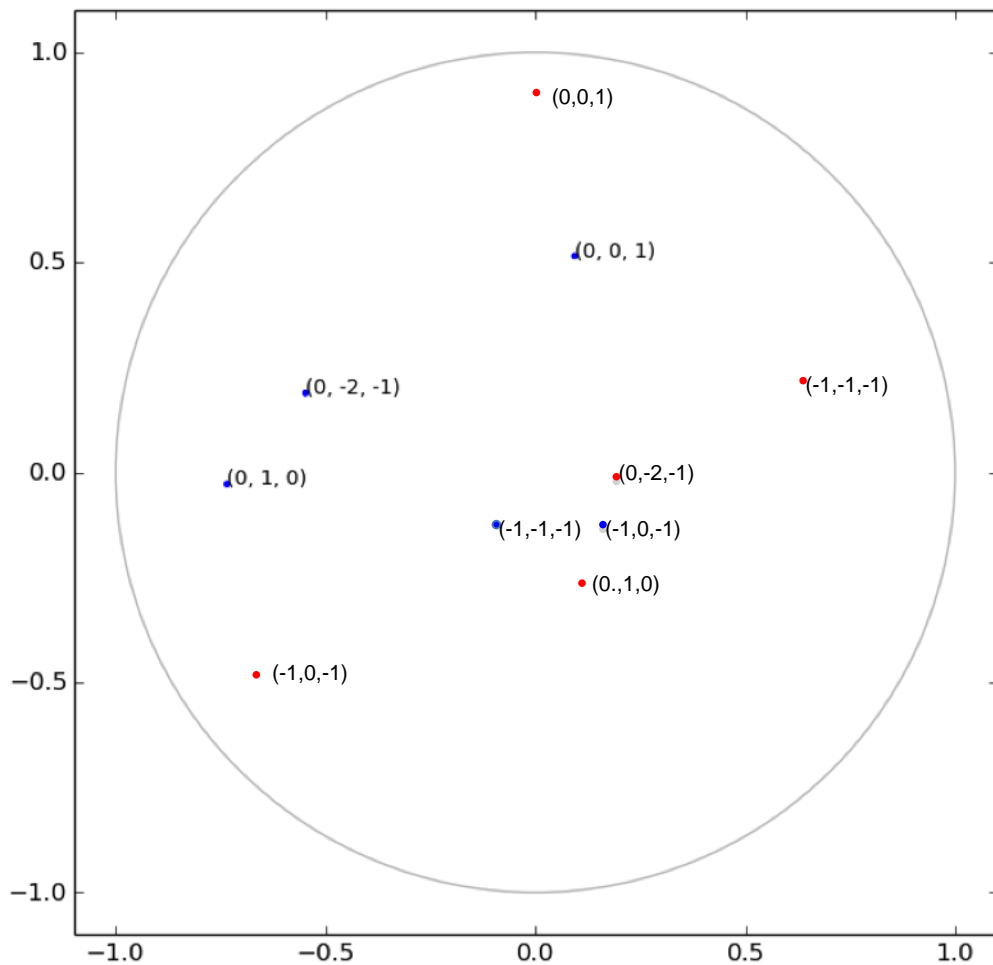


Figure 6.28: Stereographic projection plots of two agglomerated α -LGA. Blue dots represent crystal a and red dots represent crystal b.

The angle calculation results in table 6.32 of two agglomerated α -LGA is compared between both methods. The results given in table 6.32 does not give good agreement between both method. It is because in vector calculation, it considers the three basic direction of unit cell axis, a,b,c, [100], [010], and [001] while the important planes of the crystals (101), (111) and (021). However, in this carried out experiment, the objective is to assess the capability the combined method of X-ray microdiffraction and X-ray microtomography. In this work, this is the only experiment that can be done

for the combined technique. It needs more analysis on different samples to evaluate further the relationship between the agglomerated samples.

6.7 Discussion

In XMD and XMT works, the development of this methods gives understanding in the surface properties of the inter-particles, particularly in this study is agglomerated materials. The first attempt to do is the combined technique of the XMD and XMT at the same microfocus beamline I24. However, because of the stability of the beam for the tomography still under development to achieve high stability in order to produce good result of imaging, the XMT only could be done on I04 macrocrystallography beamline. Only one sample of agglomerated α -LGA was done for combined XMD and XMT technique. However, further experiments need to be carried out in order to get full understanding of the inter-particle relationships between the agglomeration. In tomography imaging technique, the challenging issue is to do with the absorption contrast in which as using micron-sized particles, the absorption contrast plays the important roles to achieve the good quality data. Further studies are clearly needed, notably using wavelength dispersion technique to achieve the best tomographic contrast.

6.8 Closing Remarks

The approach of simultaneous X-ray microdiffraction and microtomography experiments. These techniques offer promise for the study of micron-sized particles and future improvement during data collection in order to produce good quality results. By determination of orientation relationship between agglomerates using XMD and the 3D imaging technique of XMT, the understanding on molecular surface properties of crystals and the crystal morphology from the 3D image can be achieved opening the way to a more molecular centred science in terms of the agglomeration of micro-crystals.

References

1. Aubrey-Medendorp, C., Parkin, S., Li, T., (2007). The Confusion of Indexing Aspirin Crystals. *J. Pharm.Sci.* (97) 1361-1367.
2. Chemla, D.S., (2012). Nonlinear Optical Properties of Organic Molecules and Crystals. Vol.1. *Academic Press, Inc.*, Orlando.
3. Dechamps, M., de Leon Guevara, A.M., Pinsard, L., Revcolevschi, A., (2000). Twinned microstructure of $\text{La}_{1-x}\text{Sr}_x\text{MnO}_3$ solid solutions, *Philosophical Magazine A*: (80) 119-127.
4. Dharmayat, S., J. C. De Anda, et al., (2006). "Polymorphic transformation of L-glutamic acid monitored using combined on-line video microscopy and X-ray diffraction." *J. Cryst. Growth.* (294) 35-40.
5. Docherty, R., Roberts, K.J., Dowty, E., (1988). MORANG-A Computer Program Designed to Aid in the Determinations of Crystal Morphology. *Comput. Phys. Commun.* (51) 423-430.
6. Docherty, R., Clydesdale, G., Roberts, K.J., Bennema, P., (1991). Application of Bravais-Freidel-Donnay-Harker, Attachment Energy and Ising Models to Predicting and Understanding the Morphology of Molecular Crystals. *J. Phys. D: Appl. Phys.* (24) 89-99.
7. Evans, P.R., (1999). Some Notes on Choices in Data Collection. *Acta Cryst. D* (55): 1771-1772
8. Farrugia, L.J., (2012). WinGX and ORTEP for Windows: an update. *J. Appl. Crystallogr.* (45):849-854.
9. Ferreira, T., Rasband, W., 2012. ImageJ User Guide (*Revised Edition*).
10. Ferrari, E. S.; Davey, R. (2001). Solution-Mediated Transformation of L-glutamic acid: Rate Enhancement Due to Secondary Nucleation. *J. Cryst. Growth Des.* (4) 1061.

11. Hammond, R. B., K. Pencheva, Robert, K.J., (2007). "Molecular modeling of crystal-crystal interactions between the alpha- and beta-polymorphic forms of L-glutamic acid using grid-based methods." *J. Cryst. Growth Des.* (7): 875-884.
12. Harrison, A. Ibberson, R., Robb, G., Whittaker, G., Wilson, C., Youngson, D. (2002). In-situ Neutron Diffraction Studies of Single Crystals and Powders during Microwave Irradiation. *Faraday Discuss.* (122) 363-379.
13. Kim, Y., Machida, K., Taga, T., (1985). Structure Determination and Packing Analysis of Aspirin Crystal. *Chem. Pharm. Bull.* (33) 2641-2647.
14. Lehmann, M.S., Nunes, A.C., (1980). A Short Hydrogen Bond between Near Identical Carboxyl Groups in the α Modification of L-Glutamic Acid. *Acta Crystallogr. B.* (36) 1621-1625.
15. Pile, K., X. Lai, et al., (2006). "An investigation of crystallite alignment and polymorphic interaction of glutamic acid using an in situ synchrotron X-ray diffraction tomographic technique." *J. Cryst. Growth.* (294) 41-45.
16. Salje, E.K.H., (1995). A novel 7-circle diffractometer for the rapid analysis of extended defects in thin films, single crystals, and ceramics. *Phase Transitions: A Multinational Journal.* (55) 37-56.
17. Stokes, G.K., Keown, S.R., Dyson, D.J., (1968). The Construction of Stereographic Projections by Computer. *J. Appl. Crystallogr.* (1) 68-70.
18. Umiyama, H., Nakagawa, S., Moriguchi, I., (1979). Molecular Orbital Study of the Cleavage of Aspirin Crystals. *The J. Phys. Chem.* (83) 2048-2052.
19. Wheatley, P.J., (1964). The Crystal and Molecular Structure of Aspirin. *J. Chem. Soc.* 6036-6048.

CHAPTER VII

CONCLUSION & FUTURE WORKS

7.1 Introduction

In this chapter the main results are summarised in section 7.2 together with a re-appraisal of the thesis aims and objectives in 7.3, as described in section 1.2. The suggestion for future work is described in section 7.4.

7.2 Conclusion of this Study

This work included the bulk properties of the crystals, the internal atomic information of the single micro-crystals, together with an understanding of the external shape of the crystals, and molecular modelling analysis from the crystal structure information. This thesis involved a combination of experimental analysis carried out in the laboratory, molecular modelling analysis and XMD and XMT studies at the synchrotron radiation source. The research concluded that the bulk properties of crystalline powders can be represented by their analysis at single micro-crystals level and that correlation of the bulk powders and the single micro-crystals can be understood by integrate these three analysis together.

7.2.1 Influence of Crystallisation Environment the Physico-chemical Properties of Urea Crystals

Crystallisation of urea in 99% ethanol produced long needle-like crystals. The addition of 4% of biuret modified the original morphology of urea from this morphology to a more prismatic shape. The difference in cooling rates for crystallisation was also found to affect the crystals size produced. At lower cooling rates, larger crystals were produced whilst at higher cooling rates, smaller sizes of crystals were produced. This is reflection of the higher cooling rates where supersaturation is higher and hence the nucleation occurs at a faster rate, therefore there is a greater number of the crystals which do not grow to its some extent. The effect of biuret on urea

morphology and cooling rates effect was also studied using surface energy analysis. From this study, the needle-like unmodified urea was found to have a lower dispersive surface energy than the urea crystals modified by which when modified by the presence of biuret. This is because when the crystals become prismatic in shape, the fraction of the surface area of the {111} faces increases with respect to that of the {110} faces. The small size of the crystals prepared at higher cooling rates were also found to have higher dispersive surface energy values than the larger size crystals, consistent with the latter having larger surface area per volume. Therefore, increasing surface area increased the numbers of surface energetic sites on the crystal surface hence yielding a higher surface energy. Molecular modelling also was carried out to validate the experimental results and the dispersive surface energy of the particle was calculated from first principles based on morphology predictions. In this, the face-specific surface energies were weighted with respect to their fractional surface areas in the observed morphologies. The resultant dispersive surface energies were found to give good agreement with the experimental results. In the other experiment using dynamic vapour sorption method to evaluate the adsorption of water on unmodified urea and urea modified by biuret samples in order to observe the effect of addition of biuret on the water adsorption on the urea samples, it shows that at lower relative humidity, less than 70% RH, the water adsorption on both samples are slow, but above this RH, the mass changed increased rapidly, showing that the samples absorbed water rather than only adsorption. However, the adsorption occurred faster in unmodified urea as the large surface of hydrophilic {110} but, lower adsorption in urea modified by biuret as the addition of biuret made the {110} shrunk, thus, less hydrophilic surface, hence, lower adsorption can be seen.

7.2.2 XMD and XMT Studies of the Structure and Orientation of Single Agglomerated Micro-crystals

This work demonstrated the capability of the microfocus synchrotron radiation beamlines and facilities to measure the atomic arrangement of the

agglomerated micron- sized crystals (20-50 μ m). The analysed data showed the variability of powdered samples of their unit cell parameters and the crystal perfection. This was done by using XMD technique. Using XMT, it was demonstrated that of micro-crystal agglomeration the 3-dimensional imaging can be obtained to demonstrating that the interfaces between agglomerated particles can be characterised. However, as the absorption contrast is the limitation in this study, it needs more improvement in the absorption contrast, for example the distance between sample and the detector, and the wavelength used for future study.

7.3 Re-appraisal of Thesis Objectives

The main objective of this PhD work is to understand the surface properties of micro-crystalline particles with the effect of process conditions such as impurities and cooling rate to the crystal size and shape using surface analysis methods and synchrotron radiation source to study the relative orientation of the agglomerated micro-crystals. Molecular modelling analysis used to correlate the bulk properties of powdered samples and the single crystals. The examination on crystal size and shape produced at different process conditions has successfully done by experimental analysis. The study on the micro-crystals samples on XMD and XMT has several limitations in which these techniques only available at the synchrotron radiation source facilities, there was a limit in collecting enough data to be analysed. The combined technique of XMD and XMT also still in development stage. However, the results obtained in this PhD work using these techniques shows a good start to continue for the combined technique. However, it is a challenging work to correlate between bulk crystalline powder samples with single particles. There is no direct method to correlate between samples, powder and single particles. As mentioned in above statement, the objective of this research is to understand the surface properties of micro-particles with the effect of the additive. Therefore, the surface energy analysis using inverse gas chromatography correlates particle characterisation using Morphologi G3 together with molecular

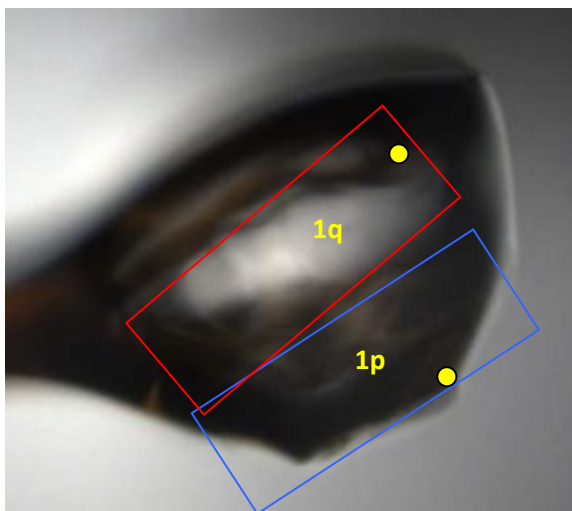
modelling. Also, the correlation between inter-particle analysis on agglomerates need to be work together with stereographic projection method and molecular modelling. Nevertheless, more future works need to be done to make this research become clearer to be understood.

7.4 Suggestion for Future Work

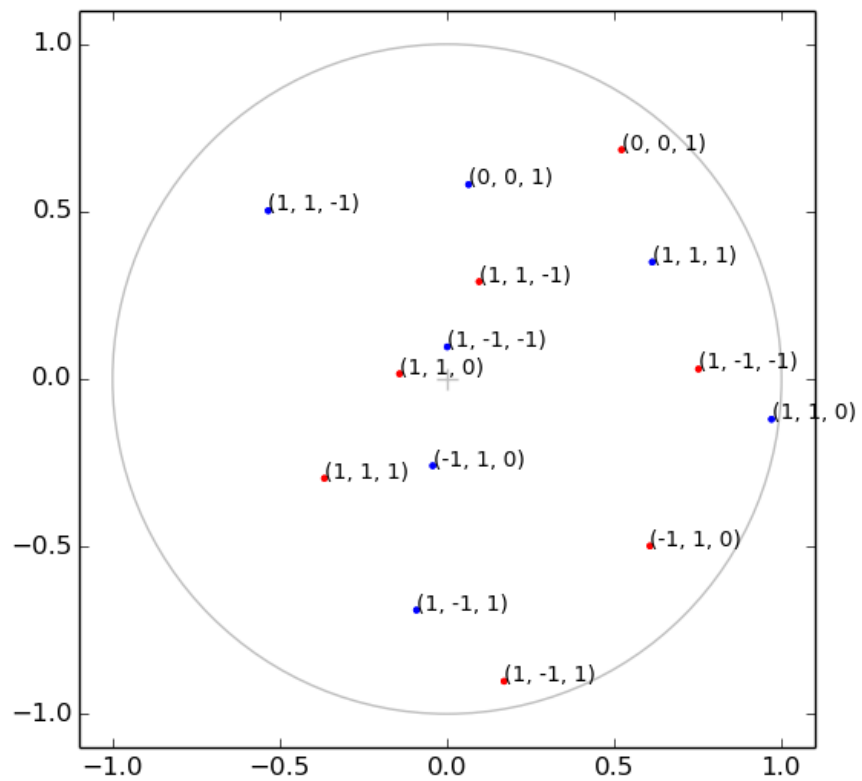
There are several recommendations for the extensive study from this work that should be considered:

- Crystallisation of urea at different process conditions, such as different types of solvents to be used for crystallisation to observe the morphological changes of urea and different percentage of impurities to observe whether there is any changes could occur.
- The robotic automatic handling for mounting micro-crystals is being developed. Therefore, it could be used for future work for understanding different micro-crystals type. The robotic handling also can reduce time consume when selecting the crystals to be mounted for data collection.
- As agglomerated micro-crystals are the same type of materials stack together, the phase contrast is low. Therefore it is recommended to improve the absorption contrast of the XMT work in order to produce high quality 3D tomography image.
- The combined technique of XMD and XMT to be carried out for more samples for repeatability and concise results. Therefore, if more samples and data can be obtained, clear analysis can be done.
- Futher work on molecular modelling such as using other modeliing method (such as Systematic Search method) to evaluate the molecule to surface interactions.

APPENDIX

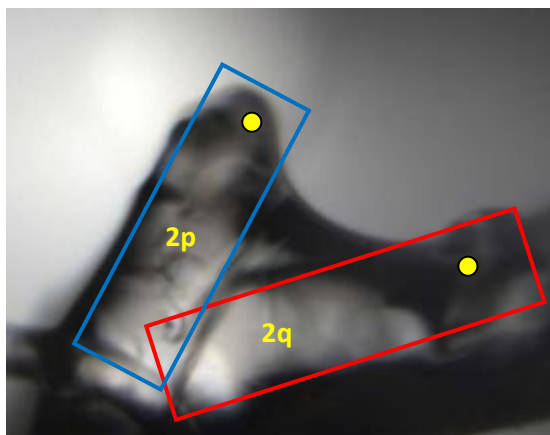


(a)

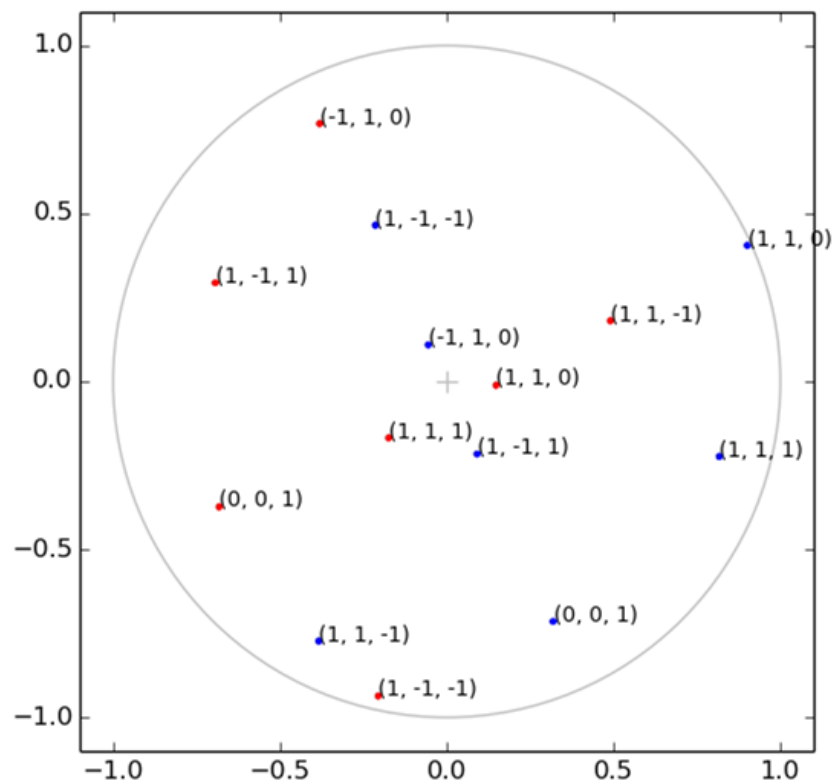


(b)

Figure 1: (a) Image of unmodified urea crystals recrystallised at $0.1^{\circ}\text{C}/\text{min}$ (sample no.1 in table 6.16 and 6.17 in page 148 and 149) (b) stereographic projections plotted for sample no.1 (blue: crystal 1p & red: crystal 1q)

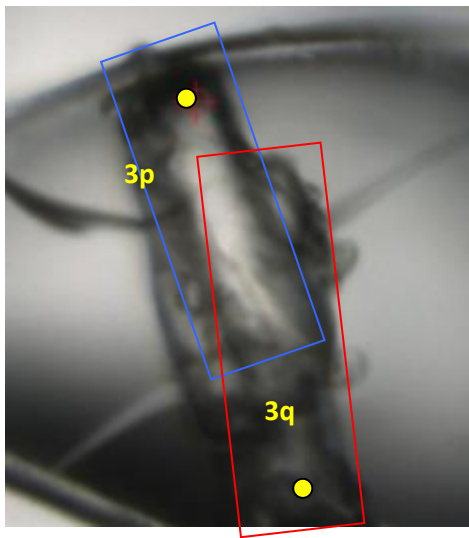


(a)

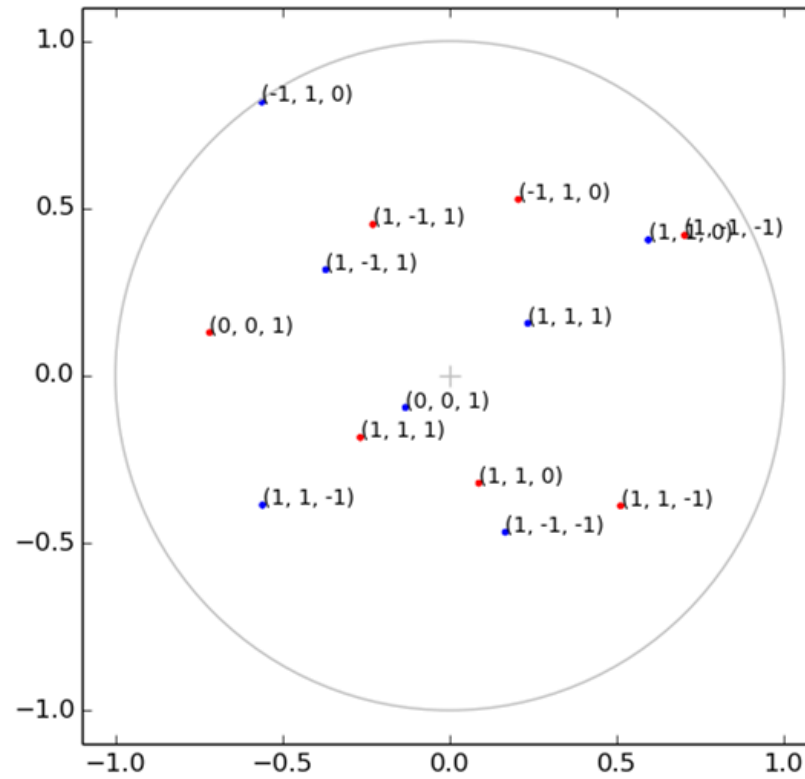


(b)

Figure 2: (a) Image of unmodified urea crystals recrystallised at $0.1^{\circ}\text{C}/\text{min}$ (sample no.2 in Table 6.16 and 6.17 in page 148 and 149), (b) stereographic projections plotted for sample no.2 (blue: crystal 2p & red: crystal 2q). Yellow dots represent the beam hits the sample.

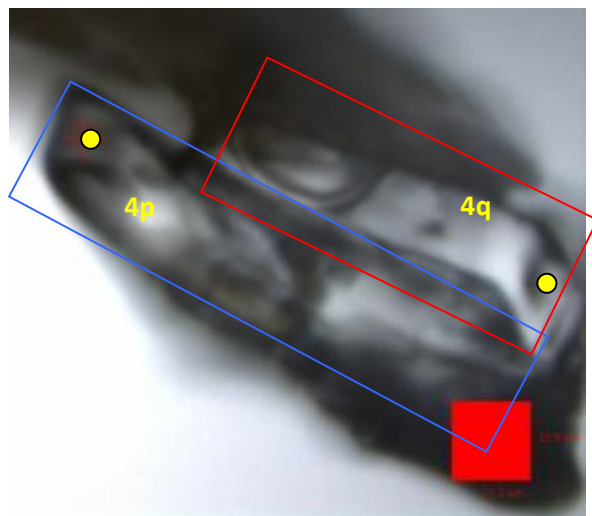


(a)

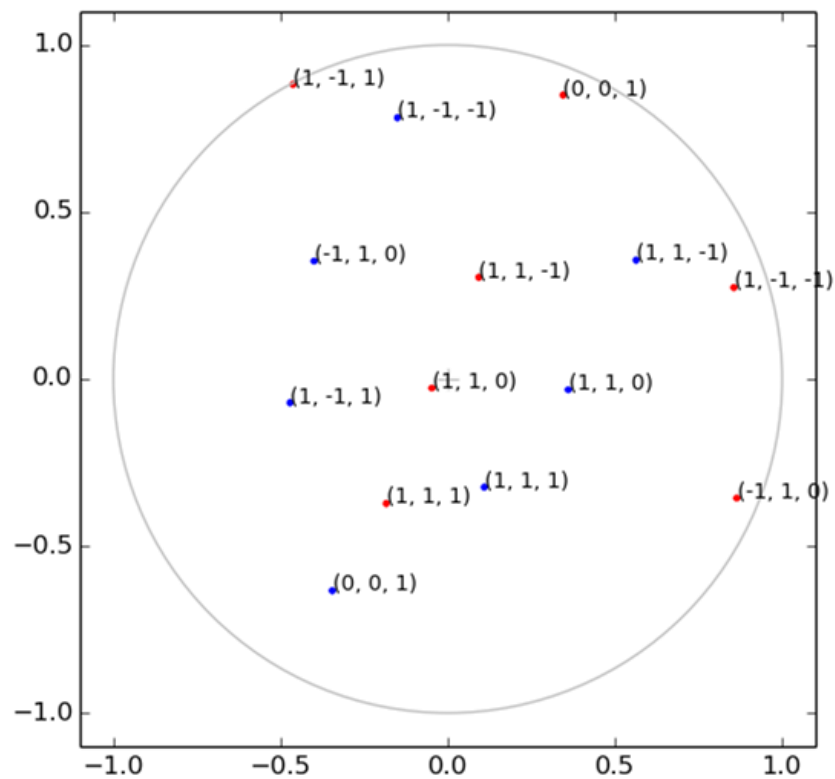


(b)

Figure 3: (a) Image of unmodified urea crystals recrystallised at 0.1°C/min (sample no.3 in table 6.16 and 6.17 in page 148 and 149) (b) stereographic projections plotted for sample no.3 (blue: crystal 3p & red: crystal 3q). Yellow dots represent the beam hits the sample.

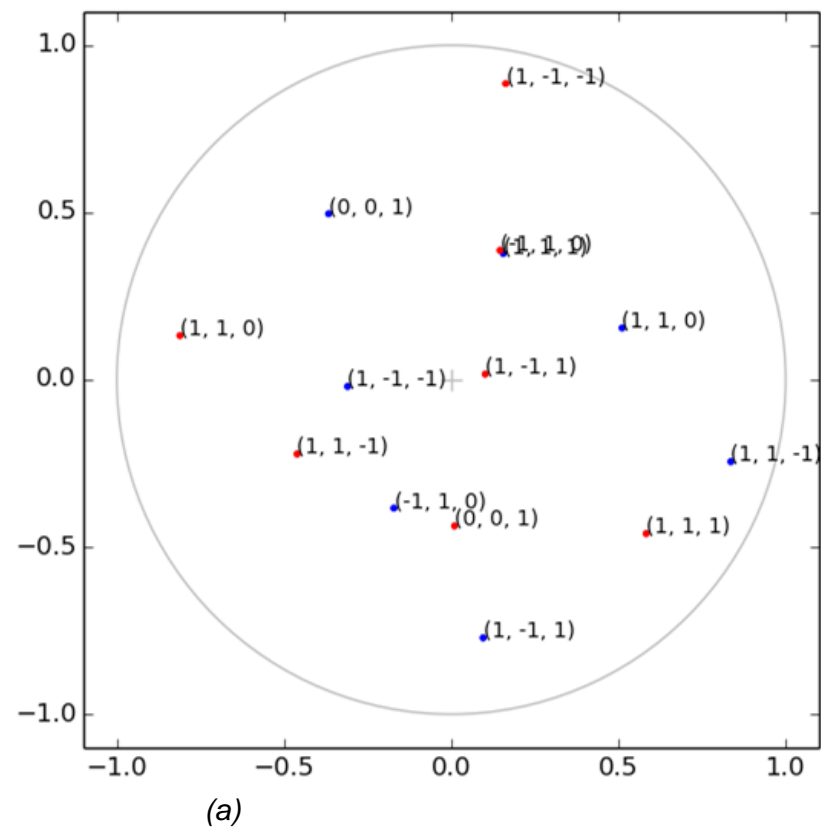
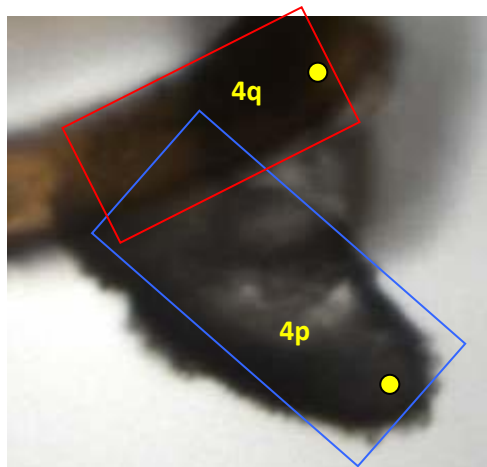


(a)



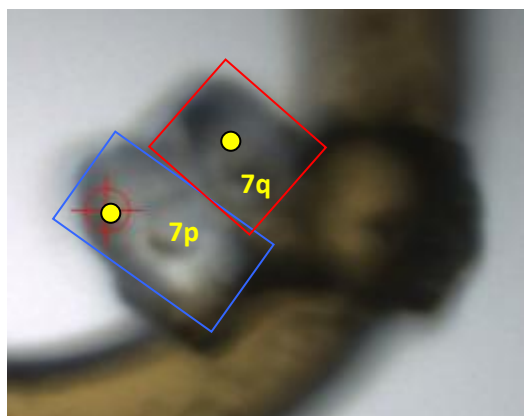
(b)

Figure 4: (a) Image of unmodified urea crystals recrystallised at $0.1^{\circ}\text{C}/\text{min}$ (sample no.4 in table 6.16 and 6.17 in page 148 and 149), (b) stereographic projections plotted for sample no.4 (blue: crystal 4p & red: crystal 4q). Yellow dots represent the beam hits the sample.

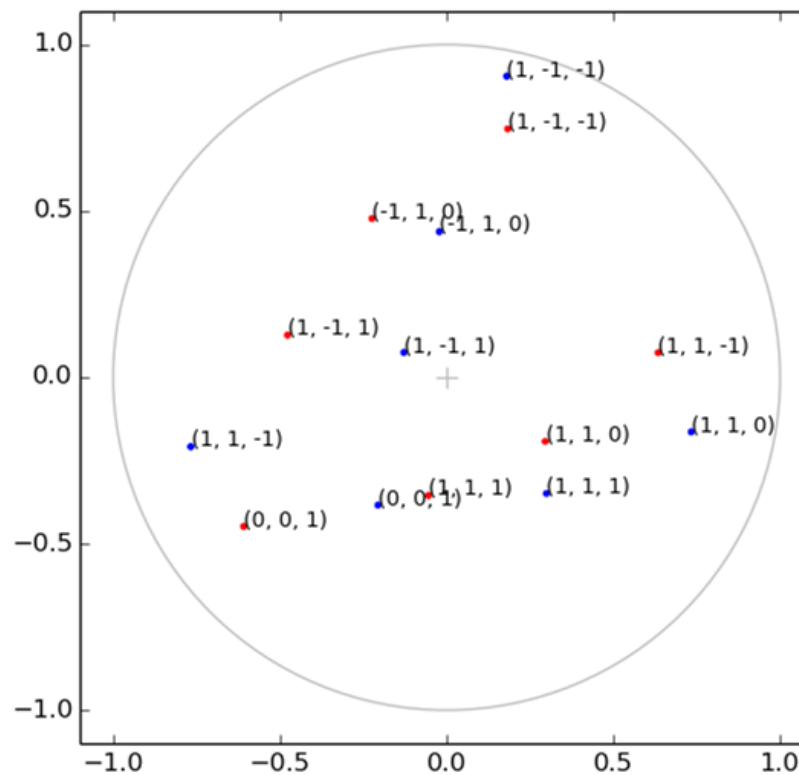


(b)

Figure 5: (a) Image of urea modified by biuret crystals recrystallised at $0.1^{\circ}\text{C}/\text{min}$ (sample no.6 in table 6.18 and 6.19 in page 151), (b) stereographic projections plotted for sample no.6 (blue: crystal 6p & red: crystal 6q). Yellow dots represent the beam hits the sample.

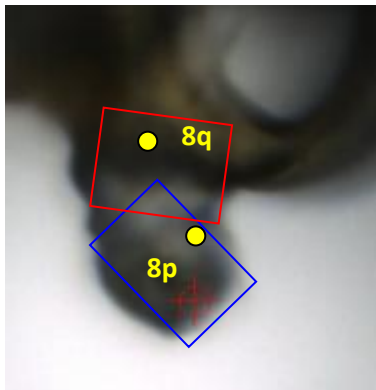


(a)

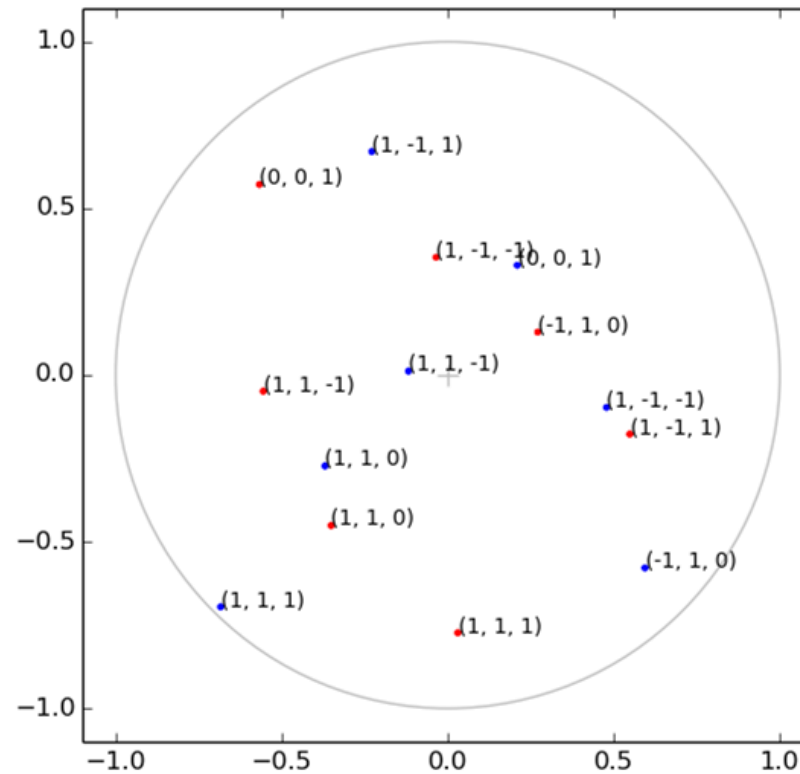


(b)

Figure 6: (a) Image of urea modified by biuret crystals (0.1degC/min) (sample no.7 in Table 6.18 and 6.19 in page 151), (b) stereographic projections plotted for sample no.7 (blue: crystal 7p & red: crystal 7q). Yellow dots represent the beam hits the sample.



(a)



(b)

Figure 7: (a) Image of urea modified by biuret crystals recrystallised at $0.1^{\circ}\text{C}/\text{min}$ (sample no.9 in table 6.16 and 6.17 in page 151) (b) stereographic projections plotted for sample no.9 (blue: crystal 9p & red: crystal 9q). Yellow dots represent the beam hits the sample.

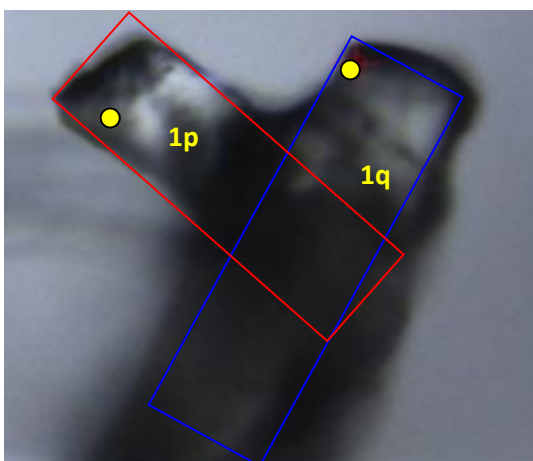
Table 1 and 2 are the results of angle calculations of unmodified urea recrystallised at 0.25°C/min using vector equation and stereographic projection method respectively.

Table 1: Angle calculations between agglomerated unmodified urea 0.25°C/min using vector equation

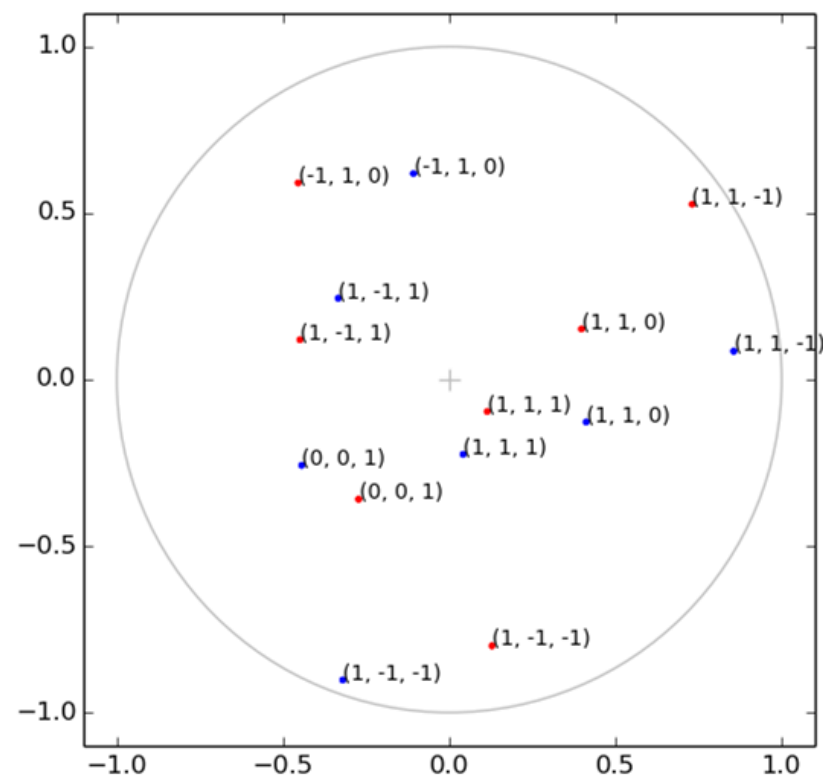
Agglomerated Urea Sample No.	Angle between crystals :	Angle in Unit Cell Axis		
		a (°)	b (°)	c (°)
1 (2 crystals)	1p & 1q	23.9	30.4	18.6
2 (2 crystals)	2p & 2q	54.6	53.7	22.3
3 (2 crystals)	3p & 3q	60.3	65.5	57.9

Table 2: Angle calculations between agglomerated unmodified urea 0.25°C/min using stereographic projection

Planes for crystals		Samples (angle, θ (°))		
P	q	1	2	3
(0 0 1)	(0 0 1)	18	20	58
(1 1 0)	(1 1 0)	26	52	104 (76)
(0 0 1)	(1 1 0)	100	100	26
(1 1 1)	(1 1 1)	16	54	72
(1 1 1)	(1 1 0)	54	68	44
(0 0 1)	(1 1 1)	60	62	26

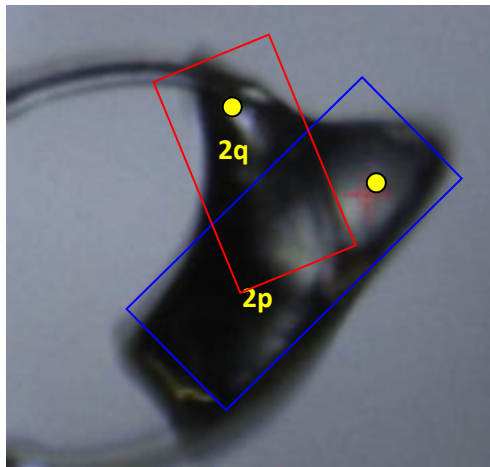


(a)

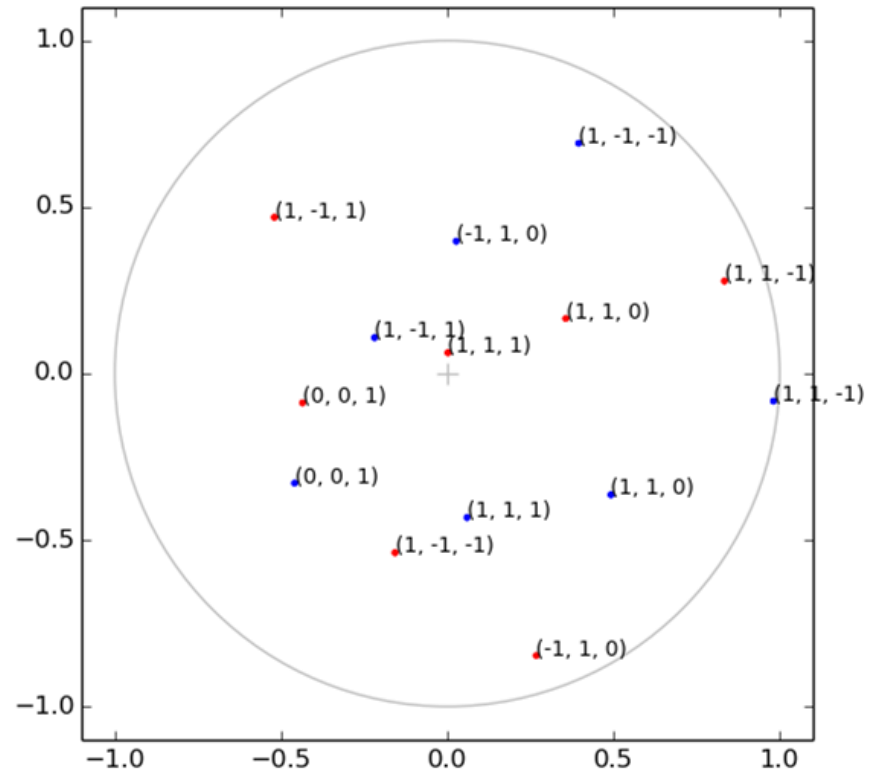


(b)

Figure 8: (a) Image of unmodified urea crystals recrystallised at 0.25°C/min (sample no.1 in Table 1 and 2), (b) stereographic projections plotted for sample no.1 (blue: crystal 1p & red: crystal 1q). Yellow dots represent the beam hits the sample.

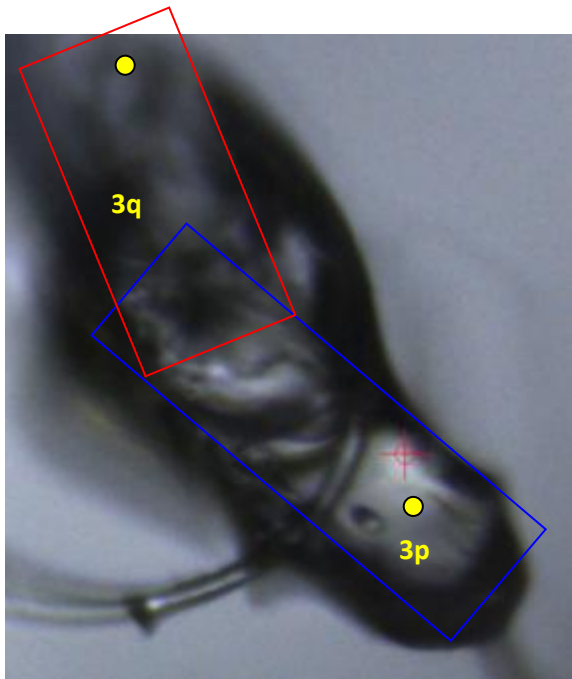


(a)

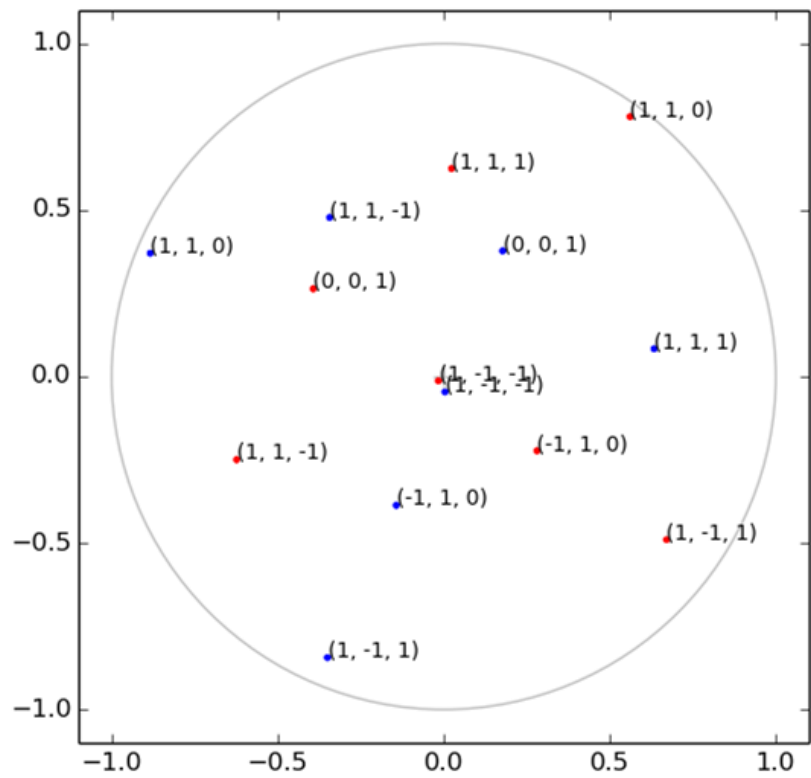


(b)

Figure 6: (a) Image of unmodified urea crystals recrystallised at 0.25°C/min (sample no.2 in table 1 and 2) (b) stereographic projections plotted for sample no.2 (blue: crystal 2p & red: crystal 2q). Yellow dots represent the beam hits the sample.



(a)



(b)

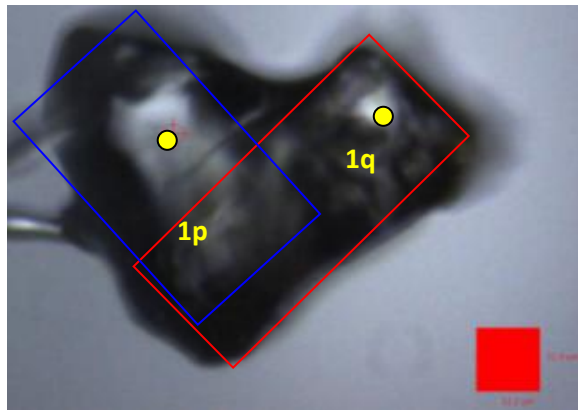
Figure 7: (a) Image of unmodified urea crystals recrystallised at 0.25°C/min (sample no.3 in table 1 and 2), (b) stereographic projections plotted for sample no.3 (blue: crystal 3p & red: crystal 3q). Yellow dots represent the beam hits the sample.

Table 3: Angle calculations between agglomerated urea modified by biuret 0.25°C/min using vector equation

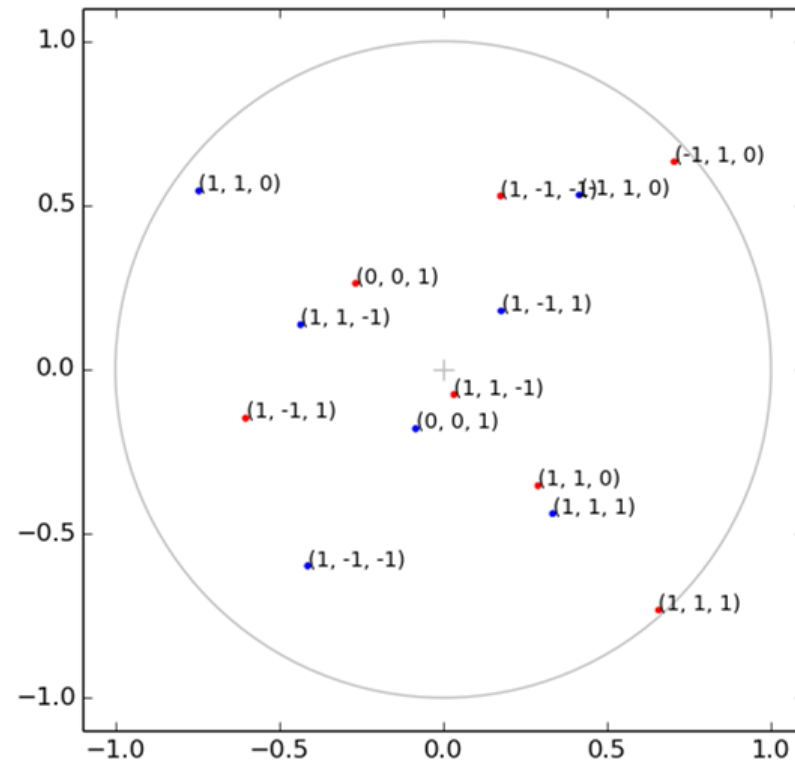
Agglomerated Urea Biuret Sample No.	Angle between crystals :	Angle in Unit Cell Axis		
		a (°)	b (°)	c (°)
1 (2 crystals)	1p & 1q	17.5	28.3	31.7
2 (2 crystals)	2p & 2q	18.2	48.7	52.1

Table 4: Angle calculations between agglomerated urea modified by biuret 0.25°C/min using stereographic projection

Planes for crystals		Samples (angle, θ (°))	
p	q	1	2
(0 0 1)	(0 0 1)	52	92
(1 1 0)	(1 1 0)	133 (47)	72
(0 0 1)	(1 1 0)	45	34
(1 1 1)	(1 1 1)	32	80
(1 1 1)	(1 1 0)	10	40
(0 0 1)	(1 1 1)	80	52

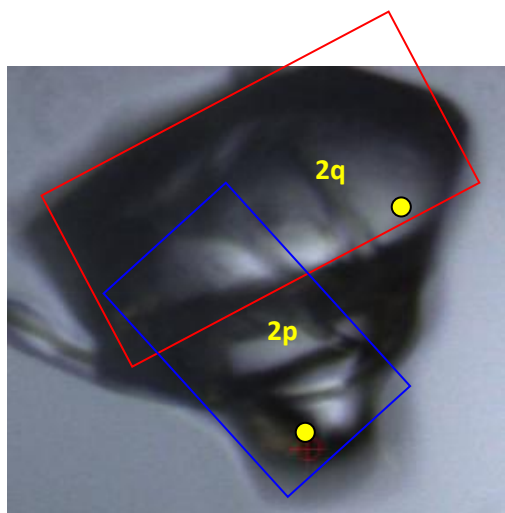


(a)

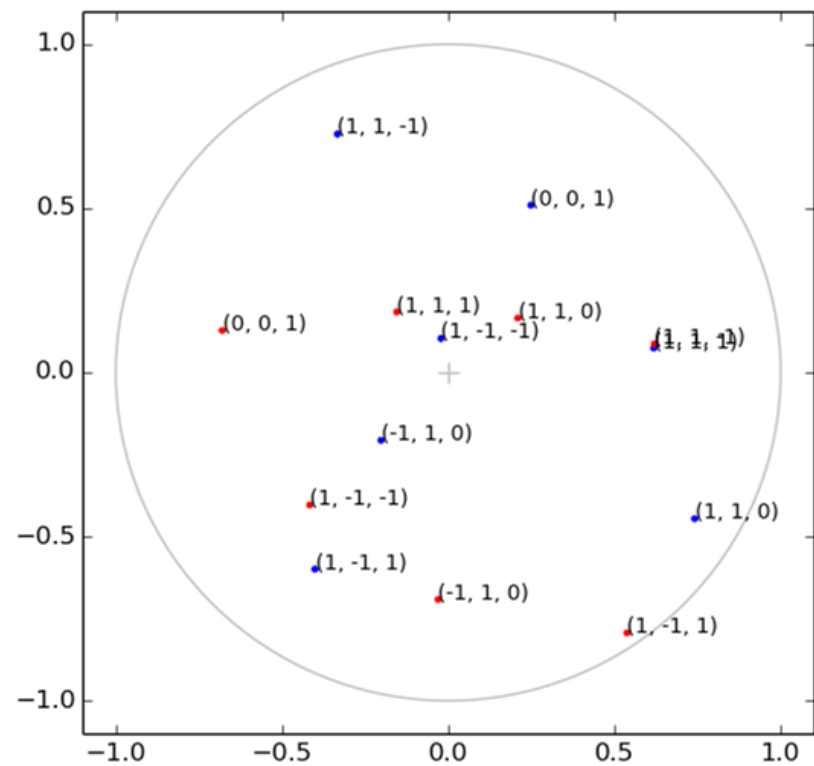


(b)

Figure 8: (a) Image of urea modified by biuret crystals recrystallised at 0.25°C/min (sample no.1 in Table 3 and 4), (b) stereographic projections plotted for sample no.1 (blue: crystal 1p & red: crystal 1q). Yellow dots represent the beam hits the sample.

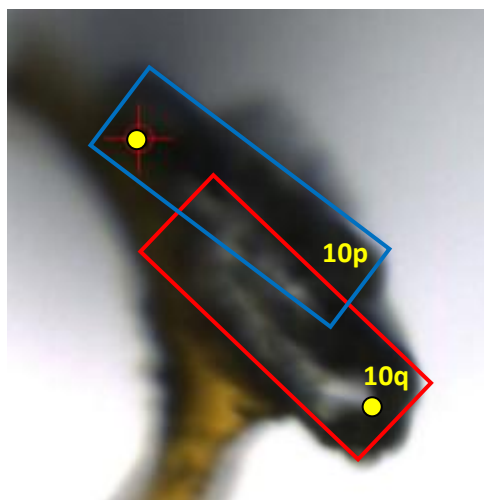


(a)

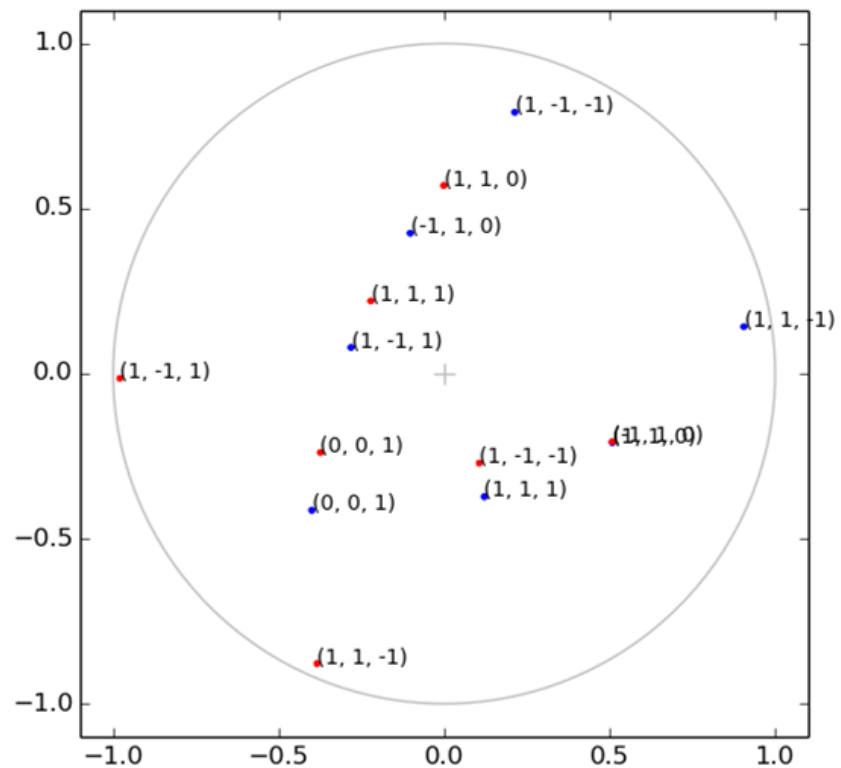


(b)

Figure 9: (a) Image of urea modified by biuret crystals recrystallised at 0.25°C/min (sample no.2 in Table 3 and 4), (b) stereographic projections plotted for sample no.2 (blue: crystal 2p & red: crystal 2q). Yellow dots represent the beam hits the sample.



(a)



(b)

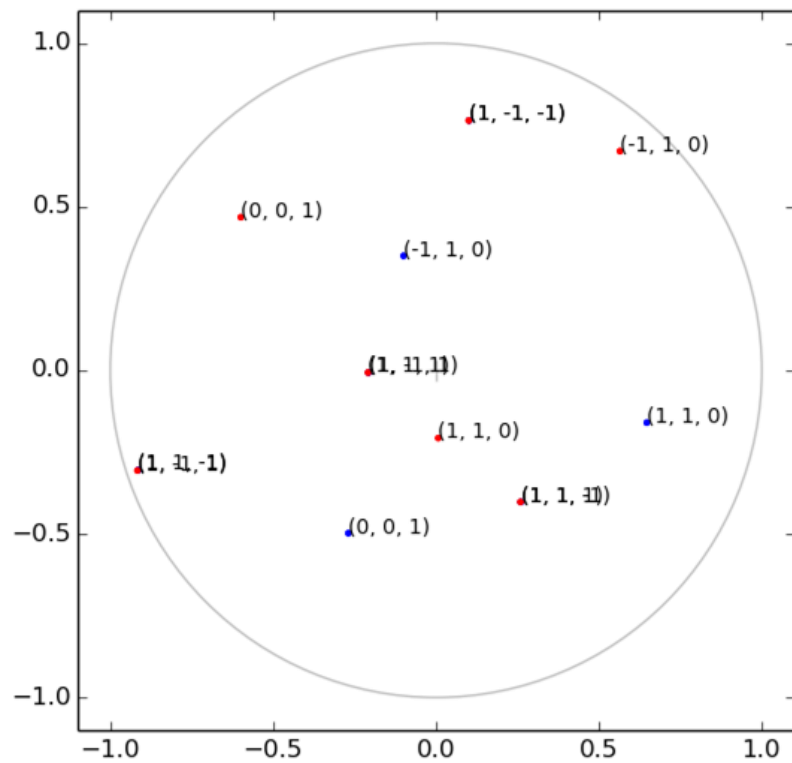
Figure 10: (a) Image of unmodified urea crystals recrystallised at $0.5^{\circ}\text{C}/\text{min}$ (sample no.10 in Table 6.20 and 6.21 in page 153). Blue and red boxes indicate the position of the agglomerated crystals. The yellow spots indicate the point where the beam hits the crystal during data collection, (b) stereographic projections plotted for sample no.10 (blue: crystal 10p & red: crystal 10q).

Table 5: Angle calculations between agglomerated urea modified by biuret 0.5°C/min using vector equation

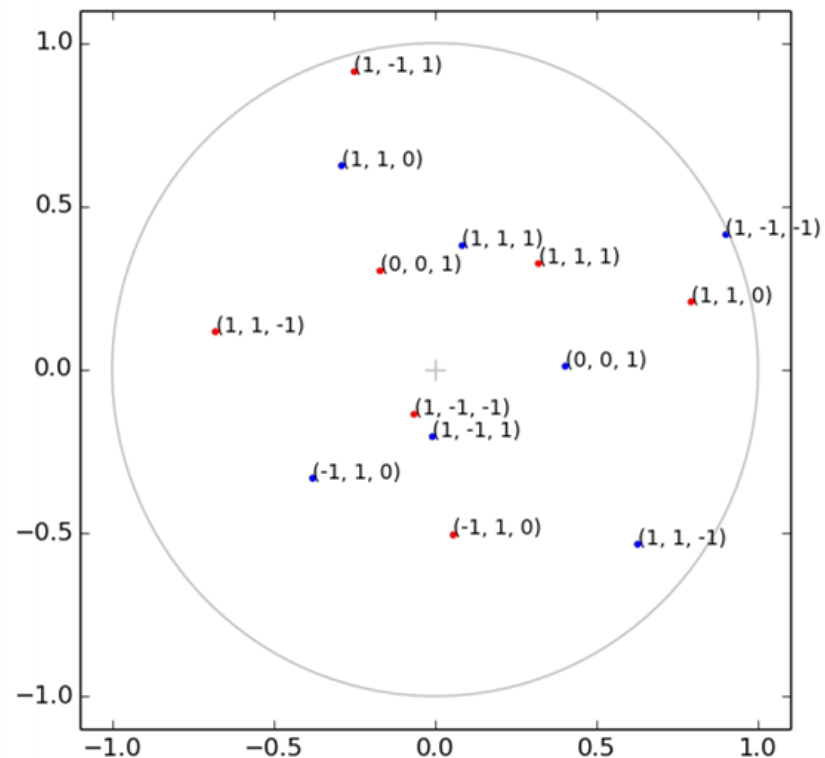
Agglomerated Urea Biuret Sample No.	Angle between crystals :	Angle in Unit Cell Axis		
		a (°)	b (°)	c (°)
1 (2 crystals)	1p & 1q	75.4	114.8	85.7
2 (2 crystals)	2p & 2q	63.4	68.5	68.7

Table 6: Angle calculations between agglomerated urea modified by biuret 0.5°C/min using stereographic projection

Planes for crystals		Samples (angle, θ (°))	
p	q	1	2
(0 0 1)	(0 0 1)	90	68
(1 1 0)	(1 1 0)	62	95
(0 0 1)	(1 1 0)	40	34
(1 1 1)	(1 1 1)	66	25
(1 1 1)	(1 1 0)	34	64
(0 0 1)	(1 1 1)	50	30



(a)



(b)

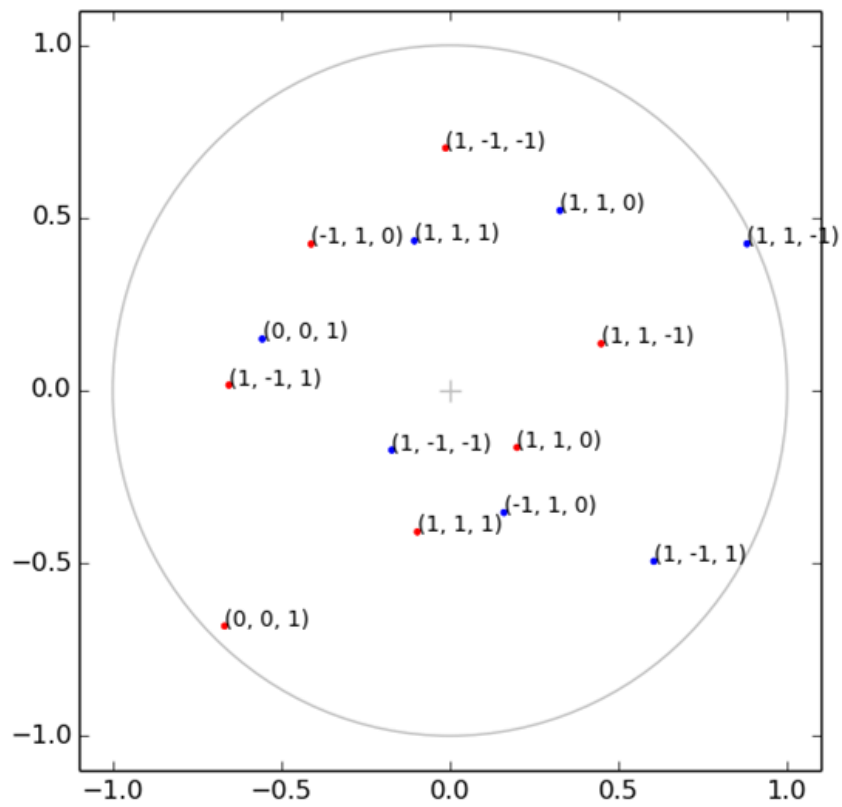
Figure 11: Stereographic projection plotted for samples in Table 5 and 6 (blue: crystal p & red: crystal q) (a) sample no.1 (b) sample no.2

Table 7: Angle calculations between agglomerated unmodified urea 0.75°C/min using vector equation

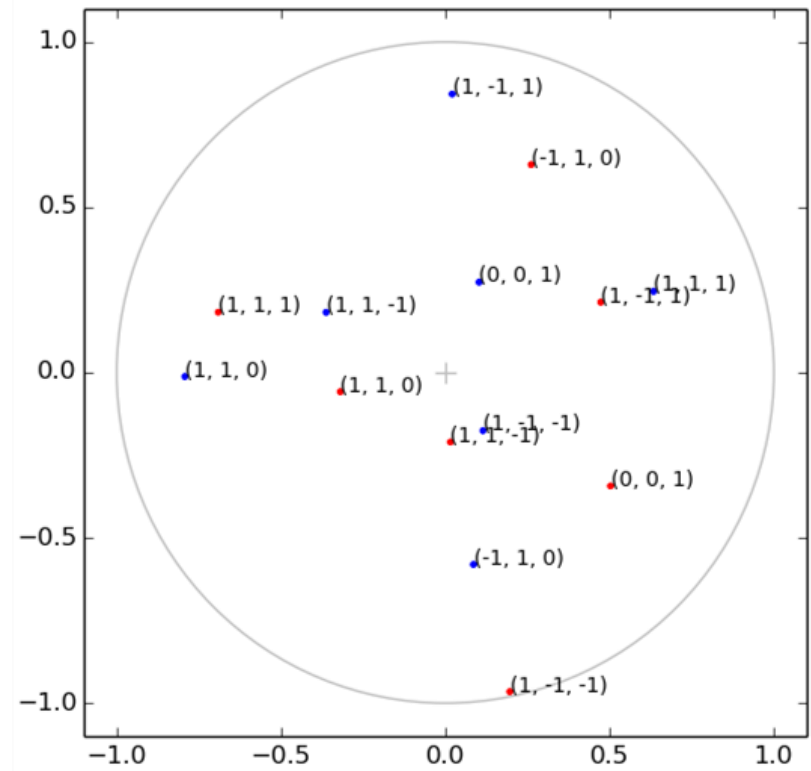
Agglomerated Urea Sample No.	Angle between crystals :	Angle in Unit Cell Axis		
		a (°)	b (°)	c (°)
1 (2 crystals)	1p & 1q	89.9	57.5	63.4
2 (2 crystals)	2p & 2q	12.1	73.1	74.1

Table 8: Angle calculations between agglomerated unmodified urea 0.75°C/min using stereographic projection

Planes for crystals		Samples (angle, θ (°))	
p	q	1	2
(0 0 1)	(0 0 1)	64	76
(1 1 0)	(1 1 0)	70	42
(0 0 1)	(1 1 0)	86	58
(1 1 1)	(1 1 1)	90	126
(1 1 1)	(1 1 0)	72	104
(0 0 1)	(1 1 1)	70	76



(a)



(b)

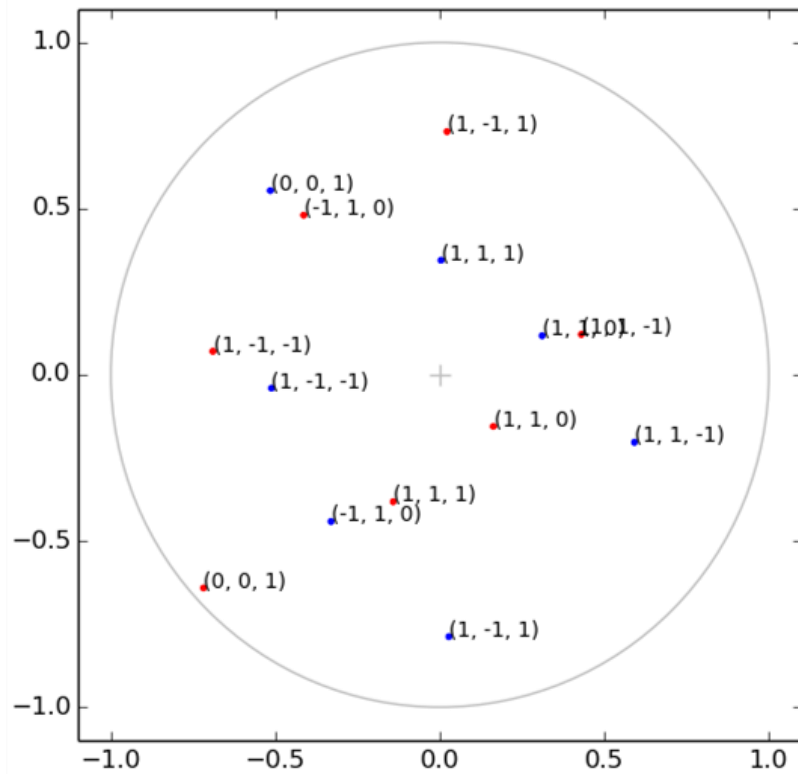
Figure 12: Stereographic projection plotted for samples in Table 7 and 8 (blue: crystal p & red: crystal q) (a) sample no.1 (b) sample no.2

Table 9: Angle calculations between agglomerated urea modified by biuret 0.75°C/min using vector equation

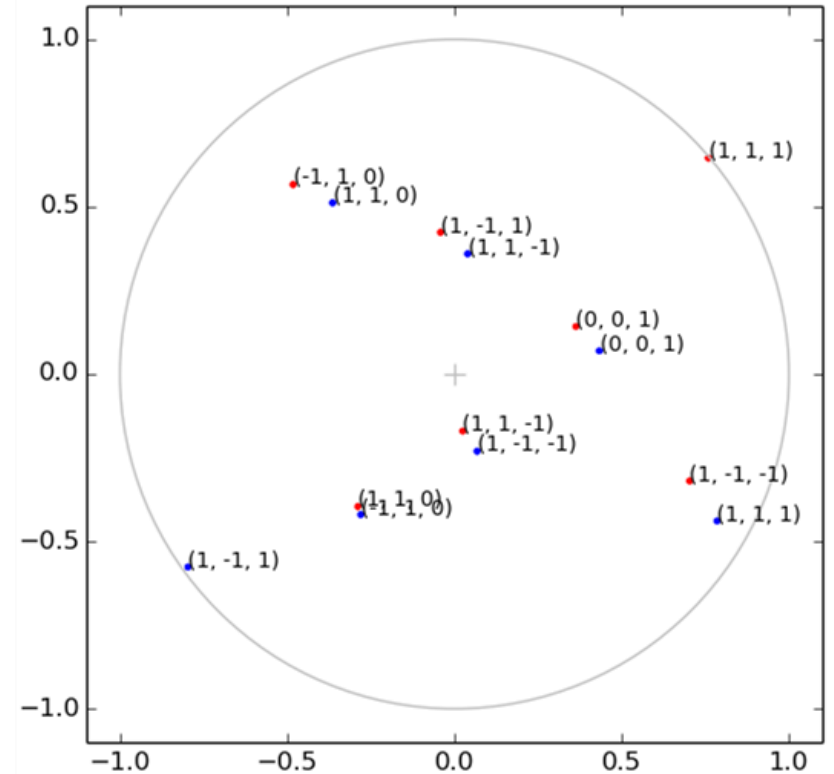
Agglomerated Urea Sample No.	Angle between crystals :	Angle in Unit Cell Axis		
		a (°)	b (°)	c (°)
1 (2 crystals)	1p & 1q	83.1	38	91.1
2 (2 crystals)	2p & 2q	89.2	90.3	11.2

Table 10: Angle calculations between agglomerated urea modified by biuret 0.75°C/min using vector equation

Planes for crystals		Samples (angle, θ (°))	
p	q	1	2
(0 0 1)	(0 0 1)	90	8
(1 1 0)	(1 1 0)	32	88
(0 0 1)	(1 1 0)	100	90
(1 1 1)	(1 1 1)	82	70
(1 1 1)	(1 1 0)	58	90
(0 0 1)	(1 1 1)	98	50

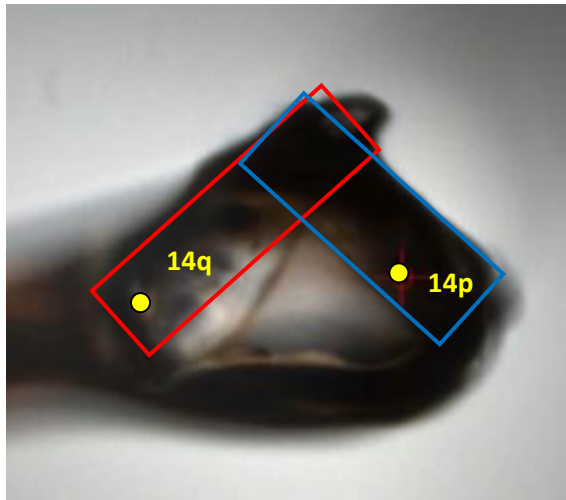


(a)

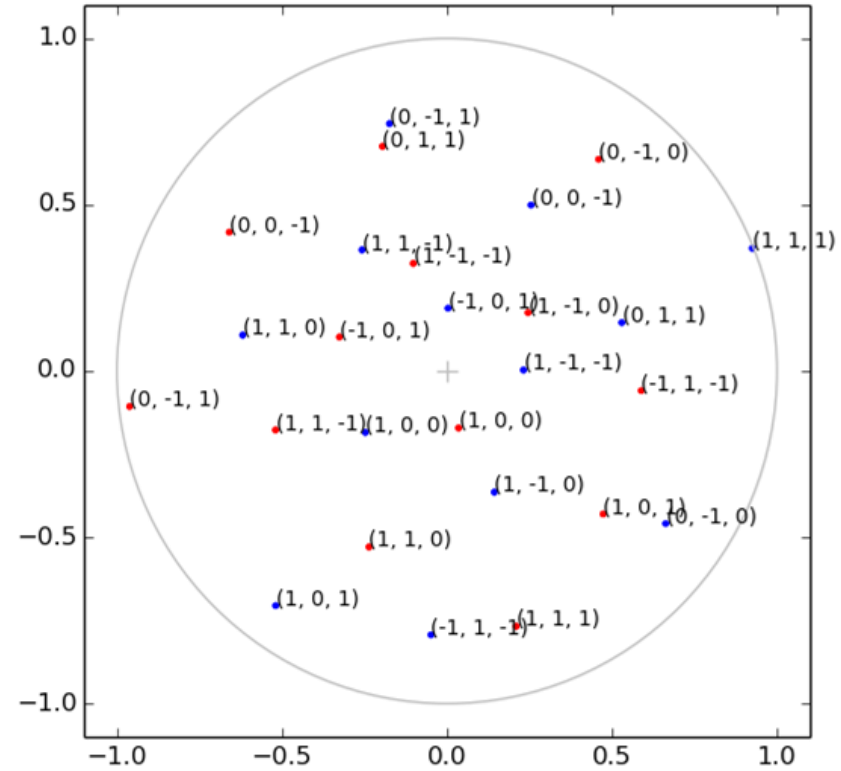


(b)

Figure 13: Stereographic projection plotted for samples in Table 9 and 10 (blue: crystal p & red: crystal q) (a) sample no.1 (b) sample no.2

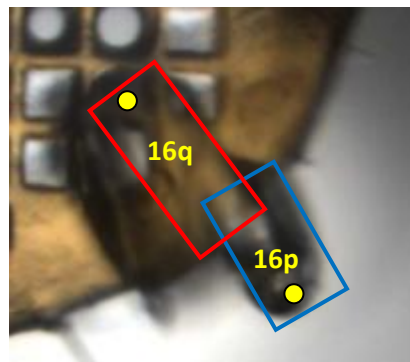


(a)

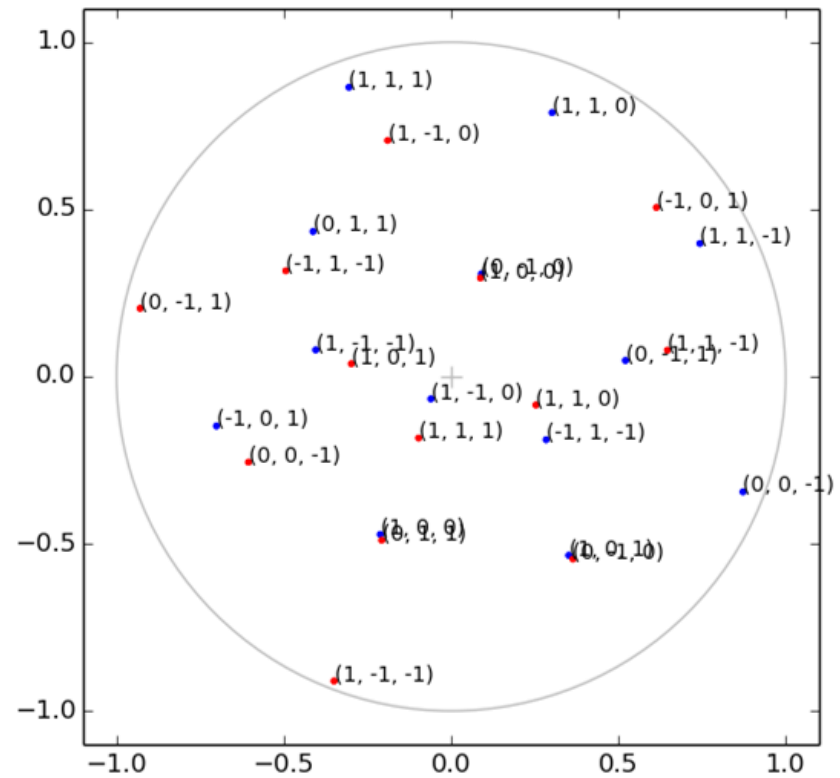


(b)

Figure 14: (a) Image of unmodified urea crystals recrystallised at $1.0^{\circ}\text{C}/\text{min}$ (sample no.14 in table 6.22 and 6.23 in page 155). Blue and red boxes indicate the position of the agglomerated crystals. The yellow spots indicate the point where the beam hits the crystal during data collection, (b) stereographic projections plotted for sample no.14 (blue: crystal 14p & red: crystal 14q)



(a)



(b)

Figure 15: (a) Image of urea modified by biuret crystals recrystallised at 1.0°C/min (sample no.16 in Table 6.22 and 6.23 in page 155). Blue and red boxes indicate the position of the agglomerated crystals. The yellow spots indicate the point where the beam hits the crystal during data collection, (b) stereographic projections plotted for sample no.16 (blue: crystal 16p & red: crystal 16q).

